Spectroscopic Investigation of Photo-Induced Proton-Coupled Electron Transfer and Dexter Energy Transfer in Model Systems

Elizabeth R. Young

B.S., Haverford College (2002)

Submitted to the Department of Chemistry
In Partial Fulfillment of the Requirements
For the Degree of
DOCTOR OF PHILOSOPHY IN PHYSICAL CHEMISTRY
at the
MASSACHUSETTS INSTITUTE OF TECHNOLOGY
April 2009

Signature of Author: ______________________
Department of Chemistry
April 19, 2009

Certified by: ______________________
Daniel G. Nocera
The Henry Dreyfus Professor of Energy and Professor of Chemistry
Thesis Supervisor

Accepted by: ______________________
Robert W. Field
Haslam and Dewey Professor of Chemistry
Chairman, Department of Chemistry on Graduate Studies

This doctoral thesis has been examined by a Committee of the Department of Chemistry as follows:

Professor Moungi G. Bawendi ________________________________
Lester Wolfe Professor of Chemistry
Chairman

Professor Daniel G. Nocera ________________________________
The Henry Dreyfus Professor of Energy and Professor of Chemistry
Thesis Supervisor

Professor Vladimir Bulović ________________________________
Professor of Electrical Engineering and Computer Science

To my family,
in gratitude for their understanding and patience.

And, in memory of Pop-pop. I will miss his fiery obstinance and boundless compassion.

Spectroscopic Investigation of Photo-Induced Proton-Coupled Electron Transfer and Dexter Energy Transfer in Model Systems

By Elizabeth R. Young

Submitted to the Department of Chemistry
on May 19, 2009 in partial fulfillment of
the requirements for the degree of
Doctor of Philosophy in Physical Chemistry

Abstract

Spectroscopic investigations of systems designed to advance the mechanistic interrogation of photo-induced proton coupled electron transfer (PCET) and proton-coupled (through-bond) energy transfer (PCEnT) are presented. PCET is ubiquitous in Nature, where it is at the heart of bioenergy conversion and catalysis (Chapter I). Systems of relevance to mechanistic studies of PCET and PCEnT are the central tenet of this work. In uni-directional PCET, electron transfer (ET) occurs from an electron donor (De) to an electron acceptor (Ae) through a hydrogen bonded proton interface. The proton interface plays a vital role in mediating ET. Thus, the exact ionization configuration of the interface must be uncovered to fully realize the influence of the interface. Specifically, does the interface exists in the *non-ionized* (i.e. amidine-carboxylic acid) or *ionized* (i.e. amidinium-carboxylate) form. Strategies to spectrally monitor the interface ionization state by extending electronic communication from a porphyrinic chromophore to its pendant amidinium functionality are pursued through examination of an alkynylamidinium Ni(II) porphyrin (Chapter II) and an amidinium appended Zn(II) purpurin (Chapter III). With the ionization state of the interface resolved, mechanistic studies of photo-induced PCET between an identical De and Ae pair juxtaposed by a *non-ionize*d (amidine-carboxylic acid) and an ionized (amidinium-sulfonate) interface are undertaken to reveal that PCET occurring through an *ionized* interface is more strongly coupled to the surrounding solvent environment (Chapter IV). Work on this system is extended to a second solvent of similar dielectric constant to establish that molecular variation of the solvent environment impacts PCET, likely through its interaction with the proton interface (Chapter V). Two water-soluble amidinium-appended ferrocene moieties are presented as building blocks for aqueous bi-directional PCET in which PT occurs to the bulk and ET occurs along a covalently bound coordinate (Chapter VI). ET and through-bond EnT are described by the semi-classical nonradiative decay formalism, meaning both processes should be sensitive to an intervening proton network. For the first time, PCEnT is established using ferrocenyl-amidine moieties bound through an amidine-carboxylic acid interface to Ru(II) polypyridyl complexes (Chapter VII).

Thesis Supervisor: Daniel G. Nocera
The Henry Dreyfus Professor of Energy and Professor of Chemistry

Abstracts

Chapter I

Building on electron transfer to uncover the increased complexity of proton-coupled electron transfer

The case for understanding the increased complexity of PCET reactions is motivated by placing these reactions in the context of bioenergy conversion and catalysis. The applicability of PCET to catalysis of O—O bond formation from water is presented along with a newly discovered water splitting catalyst. The mechanistic study of PCET is critical to understanding the multi-proton, multi-electron transformations involved in these processes. Because these complex processes of consequence do not occur through simple one-electron ET steps, a thorough understanding of PCET is necessary. Simple one-electron ET transformations are addressed in ET theory. Marcus Theory for ET is introduced as the foundation for PCET theory. Development of PCET theory beckons careful design of model systems for which specific parameters and variables can be precisely controlled. Two architectural paradigms for PCET model systems are presented that speak to the needs of PCET theory development guided by experimental results. The particular focus of mechanistic studies in this Thesis is a co-linear PCET motif to study ET mediated by an intervening hydrogen bonded interface. The significance of the particular static ionization state within the interface is presented and discussed with respect to mechanistic studies. The case for application of the co-linear PCET model system motif to studies of through-bond EnT is developed as an outgrowth of PCET studies, as both mechanisms are governed by the semi-classical formalism for nonradiative decay.

Chapter II

Spectroscopic characterization of structurally homologous *β*- and *meso-alkynylamidinium* porphyrins

Alkynylamidinium groups have been synthetically introduced at the *β* and *meso* positions of a Ni(II) porphyrin framework. The modification permits the distance between the amidinium-amidine acid-base group and porphyrin to be increased while effectively maintaining π-conjugation between the porphyrin macrocycle and the acid-base functionality. Use of an ethynyl spacer as a linker (i) extends the amidinium functionality away from the sterically bulky mesityl groups of the porphyrin, allowing it to be nearly planar with respect to the porphyrin ring, and (ii) draws the π-orbital character of the porphyrin out towards the amidinium functionality, thereby engendering sensitivity of the electronic properties of the porphyrin macrocycle to the protonation state of the amidinium. Analysis of UV-vis absorption profiles for the *β*- and *meso*-alkynylamidinium Ni(II) porphyrin upon deprotonation of the amidinium functionality reveals sensitivity of the spectral bands to the protonation state of the amidinium-amidine functionality and enables accurate determination of the amidinium acidity constants for the ground and excited state. The excited state acidity constants reveal that the *β*-alkynylamidinium Ni(II) porphyrin is a photoacid, while the *meso*-alkynylamidinium Ni(II) is a photobase. These divergent behaviors are supported by analysis of the frontier MOs of the homologous pair with TD-DFT. The barrier

for rotation of the amidinium group is obtained from a series of TD-DFT calculations. Experimental and computational methods confirm that the ethynyl spacer imparts significant electronic communication between the amidinium-amidine acid-base group and porphyrin.

Chapter III

Steady-state absorption spectroscopy of amidinium appended purpurin to determine proton interface configuration

A porphyrin derivative possessing a highly conjugated isocyclic five-membered ring appended with an amidinium functionality has been used to examine the ionization configuration within hydrogen bonded PCET interfaces. The highly conjugated amidinium-purpurin displays large spectral shifts in the visible region upon alteration of the amidinium-amidine protonation state. Analysis of the UV-vis absorption profiles of the amidinium-purpurin upon deprotonation allows for measurement of the ground and excited state amidinium acidity constants. Through the excellent sensitivity of the purpurin chromophore to the protonation state of the amidinium, the absorption spectrum of the purpurin can be used to distinguish between the unbound amidinium, the bound amidinium (in the ionized interface) and the bound amidine (in the non-ionized interface), thus providing a convenient spectroscopic handle for determining the static ionization state of assembled two-point hydrogen bonded interfaces. A series of BMs with pendant acid-base functionalities of known pK_a are bound to the amidinium-purpurin and the static ionization configuration of each interface is determined as a function of pK_a of the BM. A non-ionized interface is observed for electron rich BMs, whereas an ionized interface is observed for electron poor BMs. The series is performed in three solvents of relevance to PCET studies (ACN, THF, DCM) to allow the static ionization configuration of the interface to be assigned in subsequent PCET dyads. Solvents of lower dielectric constant are shown to be less tolerant of formation of the ionized interface.

Chapter IV

Comparison of ionized versus non-ionized interface architecture in uni-directional PCET systems

A Zn(II) porphyrin-amidinium functions as the excited state De to a naphthalene diimide, NI, Ae. The NI is appended with either a carboxylate or a sulfonate functionality. The two-point hydrogen bonded interface formed between the amidinium and carboxylate or the amidinium and sulfonate establishes a co-linear PCET pathway for CT. The two D---[H^+]---A assemblies differ only by the proton configuration within the hydrogen bonding interface. Specifically, the amidinium transfers a proton to the carboxylate to form a *non-ionized* amidine-carboxylic acid network, whereas the amidinium maintains both protons when bound to the sulfonate functionality forming an *ionized* amidinium-sulfonate network. These two interface configurations within the dyads allow for a direct comparison of PCET kinetics between the same De and Ae juxtaposed by an *ionized* and a *non-ionized* hydrogen-bonded interface. Analysis of PCET kinetics ascertained from TA and TE spectroscopy reveal that PCET through the ionized interface is more strongly impacted by the local solvent environment, thus establishing that the initial static configuration of the proton interface is indeed a critical determinant to the kinetics of PCET.

Chapter V

Molecular variation to the solvent influences PCET: Comparison of ionized versus non-ionized interfaces

The role of molecular variation in the local solvent environment towards influencing PCET dynamics is explored. THF and 2-MeTHF comprise a solvent pair with similar dielectric constants. The two solvents, however, contain non-trivial molecular variation in the absence or presence of a methyl group on the five-membered ring. These studies explore on the influence of the solvent interaction with the proton interface. Variable-temperature and kinetic isotope studies are carried out on the De-Ae pair introduced in Chapter IV. PCET through the *non-ionized* amidine-carboxylic acid network is compared to PCET through the *ionized* amidinium-sulfonate network, thereby enabling direct solvent-dependent comparison of PCET kinetics for the same D---[H^+]---A pair juxtaposed by hydrogen-bonded interfaces of differing static ionization state. PCET through the ionized interface is more sensitive to molecular variations to the solvent as reflected by divergent PCET dynamics for the two systems.

Chapter VI

Ferrocenyl-amidinium compounds as building blocks for aqueous PCET systems

Two water-soluble amidinium-appended ferrocene moieties are characterized and presented as building blocks for aqueous bi-directional PCET studies. The amidinium functionality is either fused directly to the ferrocene ring or is connected via an ethynyl spacer. Description of the ferrocenyl-amidinium moieties includes characterization of pH-dependent electronic absorption band shifts, pH-dependent electrochemical oxidation potentials, and spectral observation of the oxidized ferrocenyl-amidinium moiety during bulk electrolysis. pH-dependent absorption spectroscopy is utilized to determine pK_a values for the amidinium functionality in water, while pH-dependent electrochemistry reveals that the electrochemical potential of the compounds is intimately linked to the protonation state of the amidinium functionality. Formation of the oxidized species is monitored by electronic absorption spectroscopy during bulk electrolysis experiments and is evidenced by red-shifted peaks for both compounds. Proof-of-concept diffusion controlled ground-state ET studies (Ae = hexamine ruthenium(III) chloride) are presented using steady-state electronic absorption spectroscopy to detect formation of ET products. As expected, an increase in pH drives increased formation of ET products. The ferrocenyl-amidinium species are compelling as building blocks for aqueous PCET systems for which PT occurs to the bulk and ET occurs along a covalently bound coordinate.

Chapter VII

Dexter energy transfer through asymmetric hydrogen-bonded interfaces of ferrocenyl-amidinium compounds

Three amidine-appended ferrocene derivatives and two Ru(II) polypyridyl complexes have been assembled via an amidine-carboxylic acid interface to study proton-coupled quenching dynamics. Extensive characterization of quenching via ambient- and variable-temperature steady-state and time-resolved spectroscopies reveal that the dominant quenching mechanism in these systems is Dexter energy transfer, which yields the first report of proton-coupled energy transfer (PCEnT). Further, isotopic labeling of the proton interface establishes the importance of the intervening hydrogen bonds and reveals an inverted KIE for dyads containing one of the Ru(II) polypyridyl complexes and a normal KIE for dyads containing the other. The Ru(II) polypyridyl complexes introduce two distinct PCEnT mechanisms based on the position of the hydrogen-bonded interface relative to the bipyridine ligand bearing the ^{3}MLCT excited state. Effects of excited state localization onto or ancillary to the bipyridine bearing the interface are discussed under the framework of PCET to understand the reported KIE. Parameters affecting PCEnT, specifically electronic coupling $|V|$, are extracted and compared to values for similar, covalently bound systems.

Table of contents

Contents

List of figures

Chapter I

Chapter II

Contents

Chapter III

Chapter IV

Chapter V

Chapter VI

Chapter VII

List of schemes

Chapter II

Chapter III

Chatper IV

Chapter V

Chatper VI

Chapter VII

List of tables

Chapter III

Chapter IV

Chapter V

Chapter VI

Chapter VII

List of abbreviations

Å	Ångstrom (1 Å = 10^{-10} m)
A	absorbance
Ae	acceptor
A,mA μA	Amperes, milliampere, microampere
ACN	acetonitrile
ADF	Amsterdam Density Functional^{TM}
AU	absorption unit
BM	binding moiety
bpy	bipyridine
c	concentration
cal, kcal	calorie, kilocalorie
CCD	charge-coupled device
cm^{-1}	wavenumber
Cp^-	cyclopentadienyl anion
CR	charge recombination
CS	charge-separated
CT	charge transfer
CV	cyclic voltammetry
De	donor
d_{DA}	De-Ae separation
DCM	dichloromethane
DEnT	Dexter energy transfer
DFT	density functional theory
G	Gibbs free energy
$\Delta G(\varepsilon_S)$	solvent-dependent Coulombic term
DMAP	4-dimethylaminopyridine
DPV	differential pulse voltammetry
ε	extinction coefficient or solvent dielectric constant

ε_s	solvent dielectric constant
E	energy
$E°$	electrochemical potential
E_{00}	zero-point energy
E_a	activation energy
E. Coli	*Escherichia Coli*
E_p	peak potential from DPV
EnT	energy transfer
es	excited state
ET	electron transfer
eV	electron volt
EXAFS	extended X-ray absorption fine structure
FRET	Förster resonance energy transfer
η	refractive index
$[H^+]$	hydrogen bonding interface
Hz, kHz	Hertz, kilohertz
h	Planck's constant
HOMO	highest occupied molecular orbital
H_{RP}	electronic coupling matrix element
I	intensity
J, kJ, nJ	Joule, kilojoule, nanojoule (1 J = 1 Nm)
K	Kelvin
K_a'	acidity constant
K_{assoc}	association constant
k_B	Boltzmann constant
K_{eq}	equilibrium constant
KIE	kinetic isotope effect (KIE = k_H/k_D)
ℓ	pathlength
λ	wavelength or solvent reorganization energy
L, mL	liter, milliliter
LUMO	lowest unoccupied molecular orbital
m, mm, nm	meter, millimeter, nanometer

M, mM, uM	molar
Mes	mesityl (2,4,6-trimethylphenyl)
2-MeTHF	2-methyltetrahydrofuran
MO	molecular orbital
mol	mole (1 mol = 6.022 × 1023 units)
MLCT	metal-to-ligand charge transfer
N	Avogadro's number
NADP	nicotinamide adenine dinucleotide phosphate
NADPH	reduced form of NADP
NI	naphthalene diimide
NMR	nuclear magnetic resonance
OEC	oxygen evolving complex
OD	optical density
$^{-}$OH	hydroxide
OPA	optical parametric amplifier
PSII	Photosystem II
PCET	proton-coupled electron transfer
PCEnT	proton-coupled energy transfer
PL	photoluminescence
ppm	part(s) per million (1ppm = 10^{-6})
PT	proton transfer
q	point charge
r	radius
R	gas constant (R = 8.314 J $K^{-1}M^{-1}$)
RNR	ribonucleotide reductase
s, μs, ns, ps, fs	second, microsecond, nanosecond, picosecond, femtosecond
S_0, S_1, S_2	singlet; ground state-, first excited-, second excited-
SCE	standard calomel electrode
τ	time constant
T	temperature
T_1	triplet excited state
TA	transient absorption

t-Bu	*tert*-butyl (1,1-dimethylethyl)
TD-DFT	time-dependent DFT
TE	transient emission
THF	tetrahydrofuran
TMP	tetramesityl porphyrin
Torr	torr (1 torr = 1 mmHg = 1.3158×10^{-3} atmosphere)
TST	transition state theory
θ_m	magic angle
UV	ultraviolet
$\lvert V \rvert$	electronic coupling constant
V, mV	volts, millivolts
vis	visible

Chapter I

Building on electron transfer to uncover the increased complexity of proton-coupled electron transfer

Chapter I

I.1. Motivation and overview

Proton-coupled electron transfer (PCET) is the fundamental process at the heart of bioenergy and chemical energy conversion. Movement of electrons, which are necessary to perform a catalytic function, is intimately coupled to the molecular motions of surrounding protons via the polarization of the surrounding environment. This coupling of proton to the electron is the mechanistic differentiation between electron transfer (ET) and PCET.

This Thesis interrogates PCET in model systems. The model systems are pared down from the complex systems found in biology and for this reason they are (i) specifically tailored to isolate the PCET event (ii) are rigidly constructed to avoid ill-defined bi-molecular side reactions and (iii) allow for mechanistic study of PCET between different moieties that are designed to control ET and proton transfer (PT) architecture and thermodynamics. By examining PCET networks in model systems, this Thesis aims to develop a mechanistic framework with which to interpret coupled charge transfer (CT) processes. The aim is to contribute to an understanding of the structure and functional relations of a variety of enzymes, proteins and catalysts for small molecule activation, and especially those pertaining to water splitting.

The kinetics and mechanisms of PCET in these model systems are determined by time-resolved laser spectroscopy of assemblies comprising an electron donor (De) and an electron acceptor (Ae) juxtaposed by a PT interface (---[H^+]---). The nature of the intervening proton interface is of paramount importance to mediating CT and is therefore of special interest in mechanistic studies. Specifically, the constituent components of the interface and the static ionization configuration of the proton interface with respect to the ET pathway are a primary focus of the work presented in this Thesis.

I.2. PCET in Nature

Nearly fifty years ago, Mitchell first recognized the importance of electron/proton coupling in biology with his proposal of proton translocation driven by ET.[1] Since this seminal work, PCET has been recognized as a critical component in small-molecule activation and redox-driven proton pumps as well as radical initiation and transport processes in biology.[2-6]

In the realm of biological PCET, ribonucleotide reductase (RNR) has received a great deal of attention.[2-9] RNR, which is composed of two subunits, converts ribonucleotides to deoxyribonucleotides necessary for DNA synthesis through a radical-dependent mechanism. The subunit R1 contains the enzyme active site and the subunit R2 contains the assembled diiron-tyrosyl radical cofactor. The active site in R1 is more than 35 Å away from the tyrosyl radical formation site in R2. Because direct CT over such long distances is disfavored within the protein manifold, a PCET radical hopping pathway (Figure I.1) connecting the radical generation site and the active site has been proposed. With guidance from the protein crystal structure and consideration of possible PCET mechanisms, the pathway contains several amino acids residues, such as tyrosine (Y) and tryptophan (W), which possess redox characteristics that are highly dependent on the protonation state of the residue. Within the R2 subunit, long distance electron transport is coupled to short distance, bi-directional PT within hydrogen bonds, while in the R1 subunit radical hopping appears to occur along a uni-directional PCET pathway.

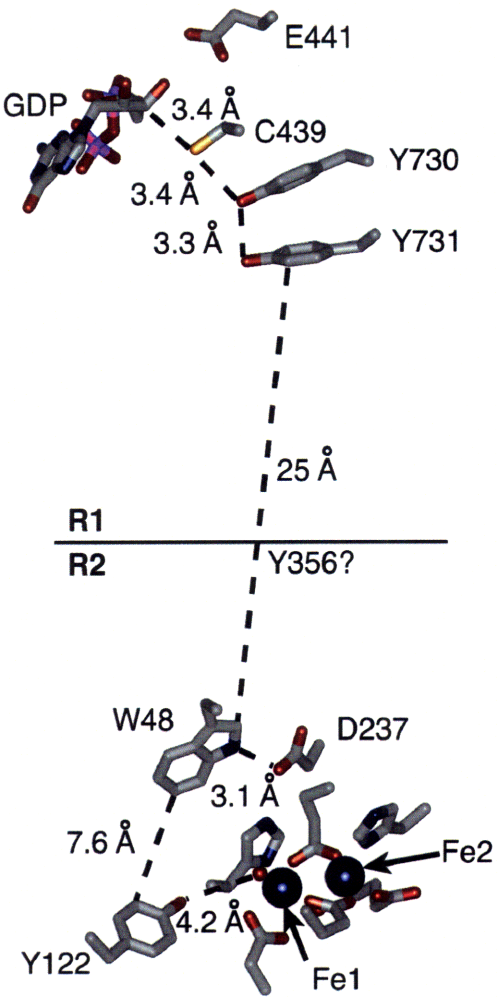

Figure I.1. Proposed PCET pathway in E. coli RNR. The pathway is based on a docking model between the R1 and R2 subunit structures.

Of further relevance to the Nocera group is the implication that PCET drives the water-splitting engine of Nature.[10, 11] The Oxygen-Evolving Complex (OEC) of Photosystem II (PS II) is thought to effect O—O bond coupling by PCET, which couples ET to protonation/deprotonation events within the surrounding amino acid network.[12] Light is collected and converted by PS II into a wireless current. The holes of this current are fed to the OEC where water is oxidized to O_2 and the electrons are fed to Photosystem I where additional light capture occurs to provide sufficient reducing power for the reduction of NADP to NADPH by ferredoxin NADP reductase. Through efficient management of protons and electrons, the OEC stores oxidizing equivalents in its metal-oxide core to build up the oxidizing power necessary to achieve the four-electron/four-hole process of water splitting.[13] Several additional key characteristics of the OEC facilitate successful water-splitting.

Recently, a catalyst that effects O—O bond formation from water at neutral pH has been discovered.[14] The catalyst, formed from cobalt ions (Co(II)) and phosphate (Pi) buffered solutions, is capable of managing the multi-electron, multi-proton catalysis of water. Parallel factors emerge between the structure and

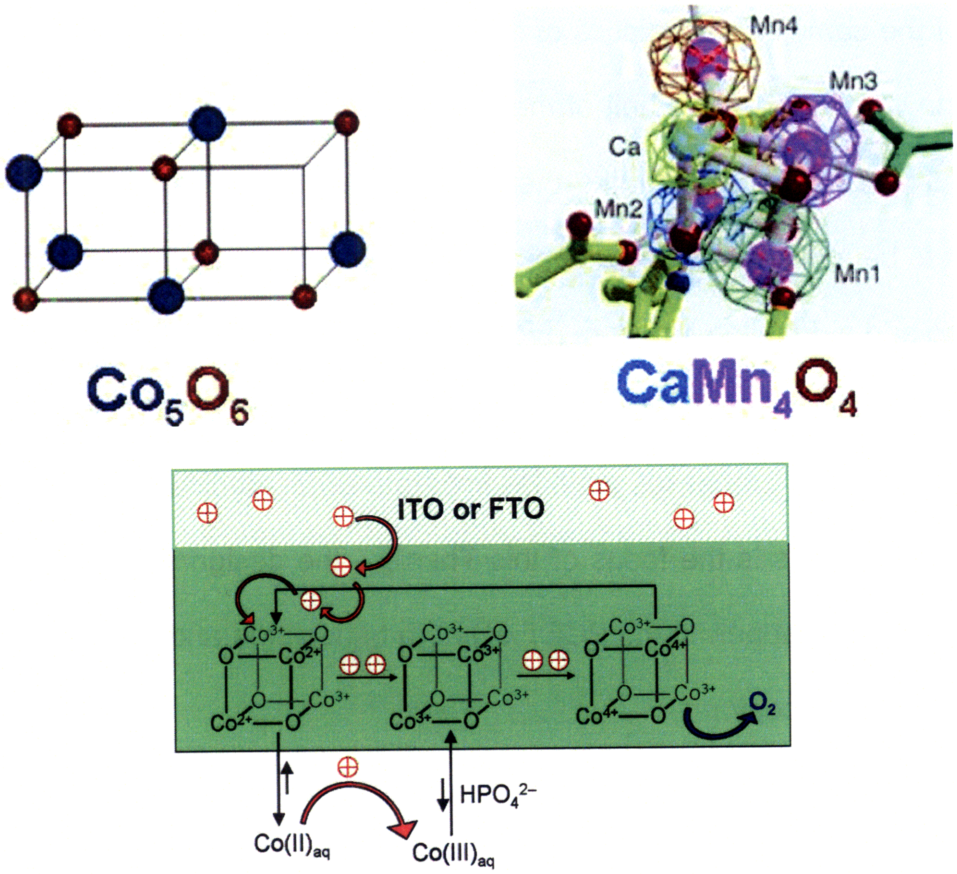

Figure I.2. Comparison of proposed Co-Pi catalyst structure with the OEC of PSII. Top: In situ EXAFS of the Co-Pi oxidation catalyst during water oxidation reveals a Co-O double cubane structure (left). The EXAFS spectrum is nearly identical to that of the OEC complex indicating that the structure closely resembles that of the OEC (right). Bottom: The proposed mechanism for operation of the Co-Pi catalyst shows that the catalyst in its active state is in dynamic equilibrium with the oxidized Co(III) and is continually repaired as water activation occurs.

function of the OEC and the catalyst (Co-Pi). The OEC consists of an all-inorganic metal oxide core[15-19] and self-assembles upon oxidation of incoming metal ions[20]. Because the OEC produces highly reactive oxygen species, it has a built-in repair mechanism that replaces the proteins associated with the PSII complex nearly every 30 minutes.[21] Proton management is required for water oxidation catalysis in aqueous solutions at pH = 7 and in the OEC is accomplished along water channels lined by Lewis basic amino acid side chains.[22,23] Characterization of the Co-Pi catalyst reveals that catalyst embodies many of the same characteristics of the OEC.[24,25] Indeed, recent EXAFS studies have shown that the basic unit of the catalyst active site is a cubane composed of cobalt and oxygen, much like the postulated structure of the OEC, which is thought to be a distorted Mn_3Ca cube with oxygen atoms at alternating corners of the cube and a dangling Mn atom (Figure I.2).[18,19,26]

The prevalence of PCET in many biological and chemical catalytic and energy conversion processes provides imperatives for elucidating the factors that govern PCET. This is the focus of this Thesis – the design and investigation of model systems that permit the PCET event to be isolated and examined by time-resolved spectroscopy.

I.3. ***Marcus Theory for ET as the basis for PCET***

ET Theory provides a suitable starting point for the considering PCET. ET Theory developed by Marcus and Hush utilizes the concept of a special, collective solvent coordinate that drives coupling between a De and an Ae.[27-35]

The polarization of the solvent is intimately tied to the De and Ae moieties in both their equilibrium states as well as the charge-separated (CS) state. In order for facile ET to occur between De and Ae, the dipoles of the solvent molecules must reorient to assist CT by accommodating the redistributed charge resulting from the charge transfer event (Figure I.3). Marcus represented the reactants and the CS products states with intersecting parabolas defined by a solvent reaction coordinate. The ET reaction progresses from reactants to products by traversing the parabolic reaction wells. When the ET process occurs, (Figure I.3) an energetic penalty in the form of the solvent reorganization energy (λ_s) must be paid that represents the fluctuation of solvent dipoles to an orientation that enables ET. The nature of the parabolas (depth of the wells, relative off-set, and crossing-point) reflects specific thermodynamic and electronic properties of the donor-acceptor (De-Ae) system, which varies depending on the constituent components. The crossing of the wells represents the De-Ae coupling matrix element, $|V|$. The driving force for ET (ΔG^o) is represented by the vertical offset of the bottom of the parabolic wells. The Marcus-Levich equation for the rate of ET is described in terms of these thermodynamic parameters as outlined in equation I.1.[36] Subsequent expansion of Marcus Theory has lead to incorporation of quantum mechanical corrections.[37-40]

$$k_{\mathrm{ET}} = \frac{2\pi}{\hbar}|V|^2 \sqrt{\frac{1}{4\pi\lambda_s k_B \mathrm{T}}} \exp\left[\frac{(\Delta G^o + \lambda_s)^2}{4\lambda_s k_B \mathrm{T}}\right] \qquad (\mathrm{I.1})$$

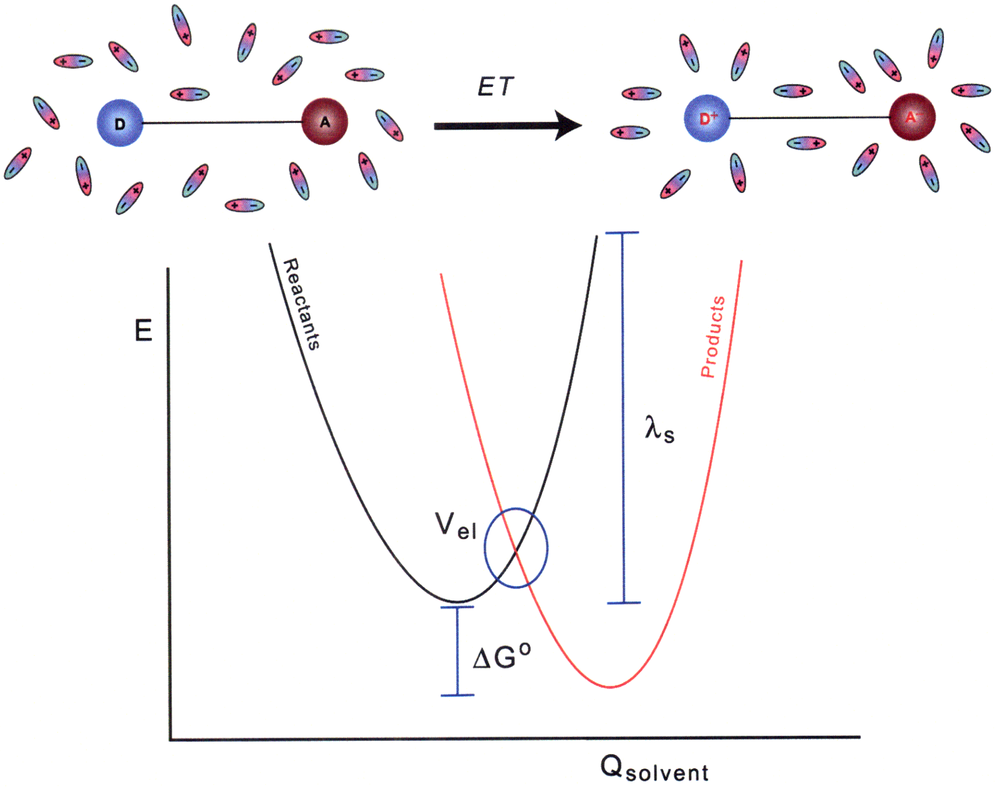

Figure I.3. Marcus theory for ET represented with a single solvent coordinate. Top: Solvent dipoles orientated around a De-Ae pair must rearrange upon CT to accommodate the charge buildup in solution. Bottom: The reactant and product state of ET are represented by parabolic wells and progress towards the CS products is plotted along a generalized solvent coordinate, Q.

Marcus Theory has been experimentally demonstrated over the decades by numerous mechanistic studies of ET in model systems including the verification of the inverted region, which describes the regime of ET for which the rate of ET decreases with increasing values of ΔG.[41-45] In addition , twenty years of intense investigations of biological ET have verified that Marcus theory aptly describes electron transport in proteins and enzymes[46-48] protein-protein systems[49-52] and de novo designed proteins[53-60].

PCET, however, steps beyond conventional Marcus treatment because both electron and proton displacements in PCET affect the $|V|$, λ_s, ΔG terms of

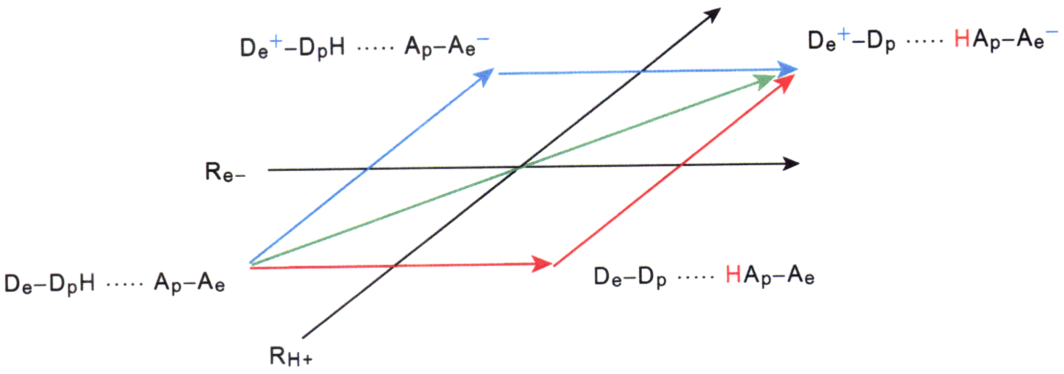

Figure I.4. Square scheme for PCET. Three PCET pathways exist to reach the CS product state during a PCET reaction. The blue line describes the transfer of the electron followed by the proton. The red line describes PT followed by ET. All other possible PCET pathways are confined within the space of the red and blue paths. One especially important pathway is along the diagonal that describes concerted electron and PT.

equation I.1. As the electron moves, pK_a values of redox cofactors change; and conversely at the proton fluctuates, the electrochemical potentials of the redox cofactor are modulated. Even if the thermodynamic driving force could be sufficiently mapped out during the electron and proton displacements, knowledge of the driving force of the reaction alone is insufficient. The $|V|$ and λ_s terms will be affected by the charge redistribution resulting from electron and proton motion.

When considering the PCET reaction, an added level of complexity arises. The two-state model operative for ET, represented by the 2-dimensional parabolic wells (Figure I.3), is augmented to a four-state model in PCET that leads to a more complex reaction surface. Whereas in ET, there is one initial state, De-Ae, and one final state, De^+-Ae^-, with no intermediates, several possible mechanisms and intermediates arise for reaching the products state in PCET. Simply speaking, the product state can be reached by an ET then PT process, a PT then ET process or a concerted PCET process. These three reaction pathways are depicted in a square scheme in Figure I.4. Within this square scheme framework, theoretical treatments of PCET rate expressions have been developed by several groups.[61-74] These theoretical models are two-dimensional quantum mechanical adaptations of Marcus Theory of ET that include the contributions of the proton component on the thermodynamic and electronic parameters governing CT. The values of ΔG and λ_s depend on the charge distribution of the electron *and the proton* and as a result are dependent on whether the process corresponds to ETPT, PTET or PCET. Further, the two factors that determine the rate of a CT reaction, ΔG and V, depend on the reaction pathway. The coupling of the charge shift resulting from electron *and* proton motion to the polarization of the surrounding environment embodies the essential distinguishing characteristic of a PCET reaction.

I.4. Architectural paradigms for PCET in model systems

The need to account for both proton and electron motion in PCET requires development of model system architectures to specifically position donor and acceptor moieties relative to each other to achieve specific distances and orientations throughout the mechanistic studies. This need has driven development of various model systems and has fueled to the emergence of PCET as a rich field of study.

Two relevant design paradigms have emerged in the field of mechanistic study of PCET. The paradigms speak to the position of the De/Ae pair relative to the proton donor/acceptor (Dp/Ap) pair and to the pathway of ET and PT. The two design paradigms for mechanistic study of PCET are uni-directional and bi-directional PCET (Figure I.5). In uni-directional PCET, the electron and proton move along the same coordinate, whereas in bi-directional PCET, ET and PT occurs to distinct De/Ae and Dp/Ap sites.

Initial studies of PCET at the mechanistic level have utilized uni-directional PCET (Figure I.7, Top).[75,76] For those systems, photoinitiated PCET occurs between a De and an Ae juxtaposed by a hydrogen bonded interface, De---$[H^+]$---

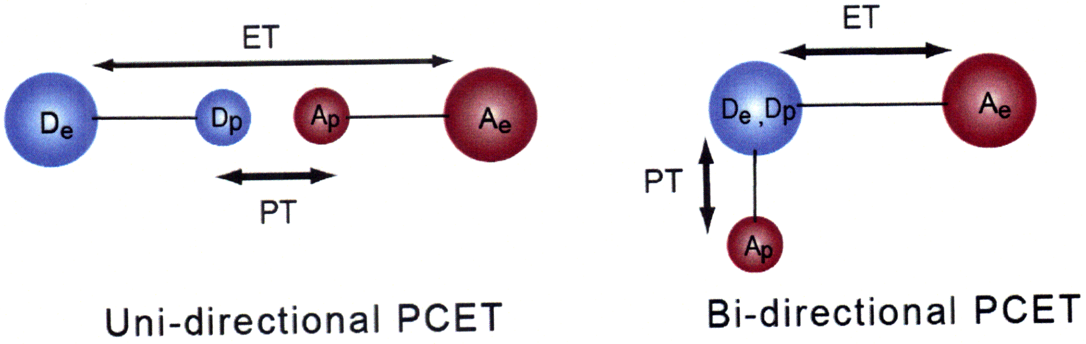

Figure I.5. Representation of uni-directional and bi-directional PCET.

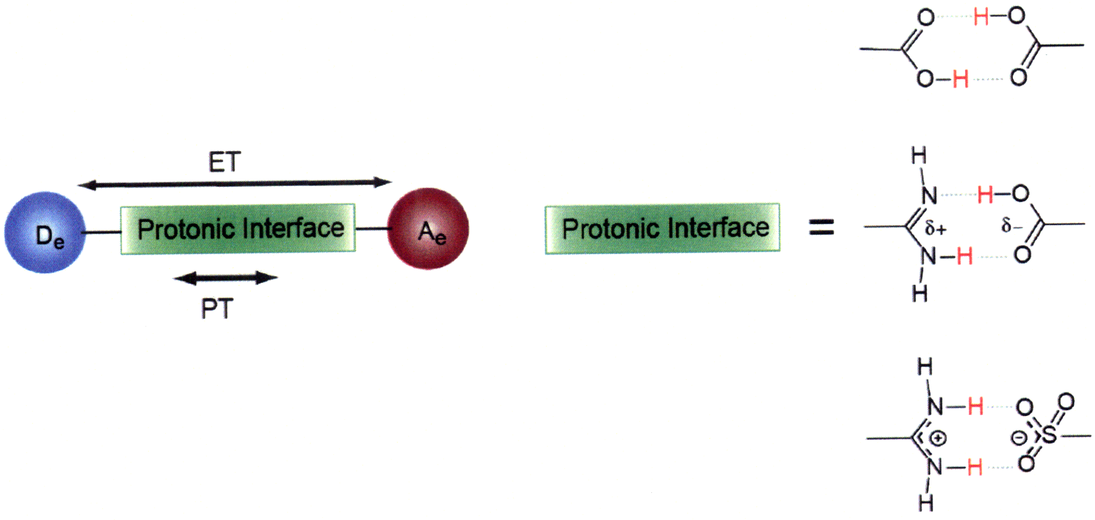

Figure I.6. The proton interface of uni-directional PCET. In uni-directional PCET, the intervening proton interface can be formed by a variety of constituent handles as depicted here.

Ae. The initial De---[H$^+$]---Ae construction exploited the propensity of carboxylic acids to form cyclic dimers ([H$^+$] = [$(COOH)_2$]) in low-polarity, non-hydrogen bonding solvent.[77] Within the interface, proton displacement on one side of the dicarboxylic acid interface is compensated by the concomitant displacement of a proton from the other side. In these systems, coupling of ET to proton motion occurs by virtue of the hydrogen bonds of the interface mediating ET. The PCET mechanism arises from the dependence of the electronic coupling on the position of the protons within the interface.[78,79]

To further understand charge transport in biologically relevant systems, mechanistic studies have been extended to include salt-bridge interfaces formed from the association of an amidinium and carboxylate functionalities.[80-86] The two-point binding motif of the amidinium-carboxylate proton interface presents a significant improvement over the symmetric interfaces and interfaces such as guanine-cytosine base pairs[87-91] and related interfaces[92] because significant proton motion within the interface is accommodated by the inteface.[77, 93] In addition, the amidinium-carboxylate avoids multiple available binding orientations within the interface.

PCET in model systems bridged by the asymmetric amidinium-carboxylate interface has been previously explored by a comparative kinetics study of a De---[amidine-carboxylic acid]---Ae complex and its inverted interfacial De---[amidine-carboxylic acid]---Ae counterpart (Figure I.7, Bottom).[82,83] Differences between the rates of charge transport of 10^2-10^3 s^{-1} have been observed for the two

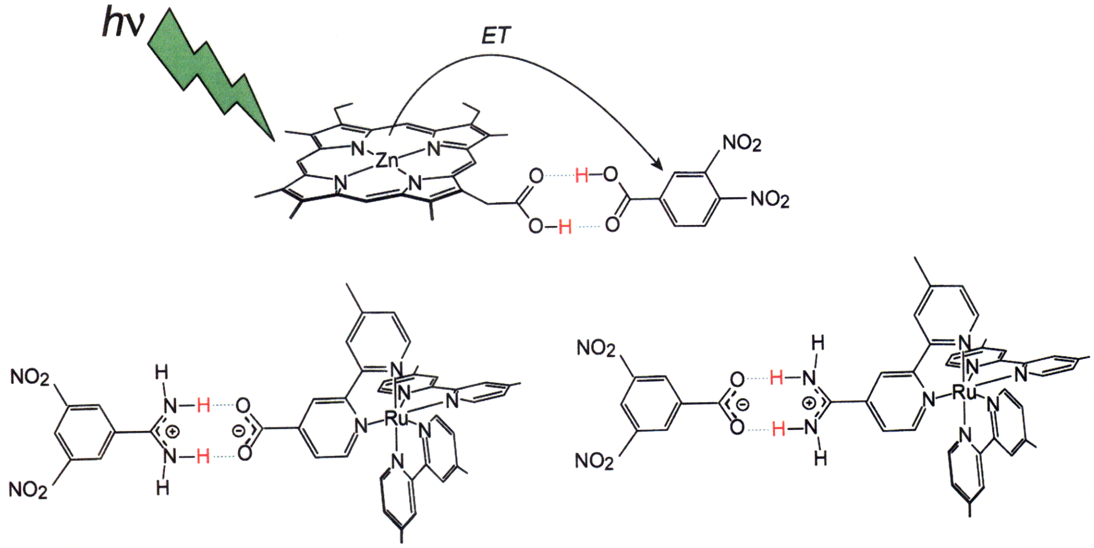

Figure I.7. Model systems for mechanistic study of photoinitiated PCET.

.

systems, which demonstrate that the direction of the pre-existing dipole moment of the interface strongly influences the ET process through the interface.

In asymmetric interfaces, the pre-existing equilibrium configuration of the interface can take two forms. The uncertainty in interface configuration occurs in the formal bonding of the protons within the interface. Depending on the pK_a values of the constituent components relative to the electrostatic stabilization imparted by formation of the interface in a low-dielectric environment, the constituent components can form an *ionized* or a *non-ionized* interface (Figure I.8). If a non-ionized interface is formed, for which the dipole moment points in the direction of ET (corresponding to ET from a De on the left of the interface in Figure I.8 to an Ae on the right side of the interface), then the possibility of PT concomitant with ET is negligible, as the proton will remain localized in its original

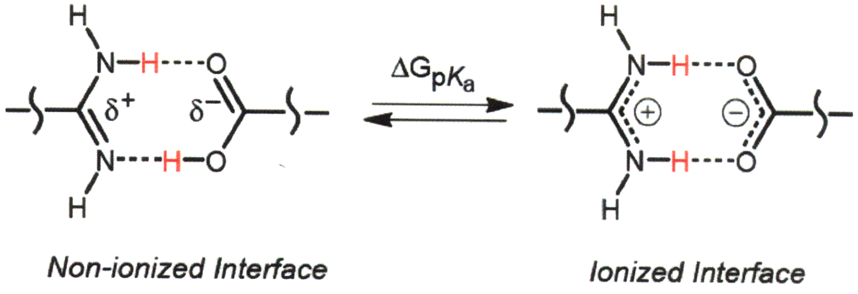

Figure I.8. Representation of an ionized and a non-ionized interface for the proton interface formed from amidinium and carboxylate appended moieties. The nature of the interface is dictated by the respective pK_a values of the acid groups and the electrostatic stabilization of the interface within the solvent dielectric environment.

position. However, if an ionized interface is formed for which the dipole moment matches the direction of ET, then PT or significant proton fluctuations within the interface are possible upon ET. In this case, the charge within the interface shifts to accommodate the ET process between the De and Ae moieties. For analysis of these PCET systems, direct knowledge of the ionization state of the interface with respect to the direction of ET is absolutely critical to analyzing mechanistic studies of PCET through hydrogen bonded interfaces.

I.5. Proton interface ionization state for uni-directional PCET

As introduced in Section I.4, the asymmetric nature of the amidine-carboxylic acid interface underscores the importance of the proton configuration on PCET by adding a dipole component to the proton interface.[94] Proton fluctuations within the hydrogen-bonding interface couple to the charge shift accompanying the ET through the polarization of the surrounding environment.

Even in the absence of formal PT, fluctuations of the proton position within the interface profoundly influence the kinetics of the ET component.[3,95] The issues addressed by these mechanistic PCET studies are especially relevant to biology where ionization states within a protein or peptide effect charge transport rates. ET may be dramatically altered by the direction of the transferring electron with regard to the orientation of electrostatic and polar fields within the biological milieu.[96-99] In addition, amino acid radical transport rates and yields depend on the ionization state of the amino acid.[3,4,100] The issue of interface ionization on mediating PCET has not been isolated owing to the inability to perform comparative PCET rate measurements on a homologous system that features ionized and non-ionized proton interfaces.

A primary thrust of the model systems developed and studied in this Thesis is to elucidate the equilibrium configuration of the assembled, asymmetric interface and to determine how the interface influences ET through the hydrogen bonds of the interface. Only with a clear understanding of the interface ionization state, can mechanistic study of PCET progress. As depicted is Figure I.9, solvent pre-organization exists to a greater extent for a PCET system compared to an ET system. Indeed, this has been a primary distinction between PCET studies and ET studies. By virtue of the interface, the greater solvent pre-organization, and the more substantive charge shifts between the De/Ae and Dp/Ap moieties, a higher solvent reorganization penalty is paid in the case of PCET. Extending this line of reasoning, proton interfaces of differing ionization states will elicit stronger or weaker pre-organization of the solvent diploes.

The extent of solvent pre-organization establishes the dipole environment through which PCET proceeds and thereby modulates the rate of ET between De and Ae moieties joined by ionized and non-ionized interfaces. The effects of this ionization state configuration on ET is borne out in the experimental solvent reorganization energy which reflects the coupling of the De-Ae model system to the solvent environment.

I.6. Dexter energy transfer coupled to the proton interface

To date, experimental investigations concerning the effect of proton motion on through-bond deactivation mechanisms have been explored for charge transfer. However, because ET and through-bond Dexter energy transfer (DEnT)

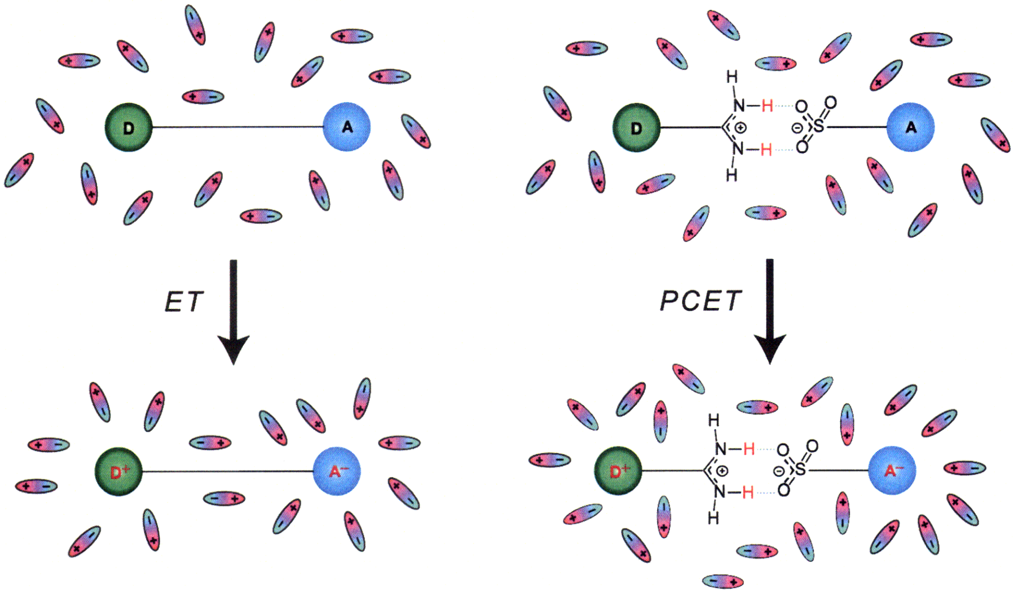

Figure I.9. Solvent dipoles couple to the reactants and CS states of ET and PCET. The solvent dipole pre-orientation for ET and PCET must undergo reorientation upon CT that is more complex for PCET systems compared to ET systems. The solvent dipoles pre-organize around the charged proton interface. Upon CT the solvent reorganizes to accommodate additional charge build up generated by the oxidized donor and reduced acceptor moiety.

are described by the semi-classical nonradiative decay formalism, it follows that the Dexter energy transfer mechanism should likewise be influenced by intervening proton networks. The nonradiative decay formalism includes a coupling constant (|*V*|) that is attenuated in PCET when compared to similar covalently bound systems.[86] Coupling in through-bond EnT systems should likewise be attenuated upon incorporation of an intervening proton interface. For DEnT systems joined by a proton interface, not only will the coupling term be attenuated, but additionally the hydrogen bonds will modulate the kinetics of DEnT and thus will be sensitive to protonation or deuteration of the interface, as is the case in PCET. In the final Chapter of this Thesis, a De-Ae system is constructed around a proton interfaces for which DEnT is the quenching mechanism. In these studies, modulation of the kinetics and nonradiative decay parameters by the proton interface is defined within the construct of a proton-coupled energy transfer (PCEnT) mechanism.

I.7. Thesis outline

This Thesis aims to identify model systems in which spectroscopic determination of the proton interface is facile, and to subsequently perform mechanistic studies of PCET kinetics on systems for which the precise ionization interface is known. Chapter II describes a homologous pair of amidinium appended porphyrin chromophores with the purpose of characterizing electronic coupling between the appended amidinium and the porphyrin chromophore. Chapter III extends previously published work on an amidinium appended purpurin chromophore. Due to excellent electronic communication between the amidinium functionality and purpurin chromophore, the ionization state of the proton interface may be defined with steady-state absorption spectroscopy. Chapter IV entails time-resolved spectroscopy on two homologous uni-directional PCET model systems that differ only by the ionization state of the interface. Chapter V extends spectroscopic investigation of these systems to second-sphere solvent environment to demonstrate that this shell of solavtion can modulate PCET behavior. Chapter VI explores a pair of amidinium appended ferrocene moieties that are potential PCET components suitable for aqueous PCET studies. Novel demonstration and analysis of proton-coupled energy transfer (PCEnT) is presented in Chapter VII.

I.8. References

1 Mitchell, P. *Nature* **1961**, *191*, 144-148.

2. Reece, S. Y.; Hodgkiss, J. M.; Stubbe J.; Nocera, D. G. *Phil. Trans. Royal Soc. B* **2006**, *361*, 1351-1364.

3. Seyedsayamdost, M. R.; Yee, C. S.; Reece, S. Y.; Nocera, D. G.; Stubbe, J. *J. Am. Chem. Soc.* **2006**, *128*, 1562-1568.

4. Seyedsayamdost, M. R.; Reece, S. Y.; Nocera, D. G.; Stubbe, *J. Am. Chem. Soc.* **2006**, *128*, 1569-1579.

5. Reece, S. Y.; Seyedsayamdost, M, R.; Stubbe, J.; Nocera, D. G. *J. Am. Chem. Soc.* **2007**, *129*, 8500-8509.

6. Reece, S. Y.; Seyedsayamdost, M, R.; Stubbe, J.; Nocera, D. G. *J. Am. Chem. Soc.* **2007**, *129*, 13828-13830.

7. Yee, C. S.; Chang, M. C. Y.; Ge, J.; Nocera, D. G.; Stubbe, J. *J. Am. Chem. Soc.* **2003**, *125*, 10506-10507.

8. Stubbe, J.; Nocera, D.G.; Yee, C. S.; Chang, M. C. Y. *Chem. Rev.* **2003**, *103*, 2167-2202.

9. Chang, C. J.; Chang, M. C.Y.; Damrauer, N. H.; Nocera, D. G. *Biochim. Biophys. Acta* **2004**, *1655*, 13-28.

10. Lewis, N. S.; Nocera, D. G. *Proc. Natl. Acad. Sci. U.S.A.* **2006**, *103*, 15729-15735

11. Dempsey, J. L.; Esswein, A. J.; Manke, D. R.; Rosenthal, J.; Soper, J. D.; Nocera, D. G. *Inorg. Chem.* **2005**, *44*, 6879-6892.

12. Ferreira, K. N.; Iverson, T. M.; Maghlaoui, K,; Barber, J.; Iwata, S. *Science* **2004**, *303*, 1831-1838.

13. Betley, T. A.; Wu, Q.; Van Voorhis, T.; Nocera, D. G. *Inorg. Chem.* **2008**, *47*, 1849-1861.

14. Kanan, M. W.; Nocera, D. G. *Science* **2008**, *321*, 1072-1075.

15. Ferreira, K. N.; Iverson, T. M.; Maghlaoui, K.; Barber, J.; Iwata, S. *Science* **2004**, *303*, 1831-1838.

16. Loll, B.; Kern, J.; Saenger, W.; Zoun, A.; Biesiadka, J. *Nature* **2005**, *438*, 1040-1052.

17. Yano, J.; Kern, J.; Sauer, K.; Latimer, M. J.; Pushkar, Y.; Biesiadka, J.; Loll, B.; Saenger, W.; Messinger, J.; Zouni, A.; Yachandra, V. K. *Science* **2006**, *314*, 821-825.

18. Barber, J. *Inorg. Chem.* **2008**, *47*, 1700-1710.

19. Peloquin, J. M.; Campbell, K. A.; Randall, D. W.; Evanchik, M. A.; Pecoraro, V. L.; Armstrong, W. H.; Britt, R. D. *J. Am. Chem. Soc.* **2000**, *122*, 10926-10942.

20. Burnap, R. L. *Phys. Chem. Chem. Phys.* **2004**, *6*, 4803-4809.

21. Aro, E.-M.; Suorsa, M.; Rokka, A.; Allahverdiyeva, Y.; Paakkarinen, V.; Saleem, A.; Battchikova, N.; Rintamaki, E. *J. Exp. Bot. E* **2005**, *56*, 347-356.

22. Murray, J. W.; Barber, J. *J. Struct. Biol.* **2007**, *159*, 228-237.

23. Ishikita, H.; Saenger, W.; Loll, B.; Biesiadka, J.; Knapp, E.-W. *Biochemistry* **2006**, *45*, 2063-2071.

24. Surendranath, Y.; Dinca, M.; Nocera, D. G. *J. Am. Chem. Soc.* **2009**, *131*, 2615-2620.

25. Lutterman, D. A.; Surendranath, Y.; Nocera, D. G. *J. Am. Chem. Soc.* **2009**, *131*, 3838-3839.

26. Risch, M.; Khare, V.; Zaharieva, I.; Gerencser, L.; Chernev, P.; Dau, H. *J. Am. Chem. Soc.* **2009**, ASAP article.

27 . Marcus, R. A. *J. Chem. Phys.* **1956**, *24*, 966-976.

28. Marcus, R. A. *J. Chem. Phys.* **1957**, *26*, 867-871.

29. Marcus, R. A. J. Chem. Phys. **1957**, *26*, 872-877.

30 Marcus, R. A.; Sutin, N. *Biochim. Biophys. Acta* **1985**, *811*, 265-322.

31. Marcus, R. A. *Angew. Chem., Int. Ed. Engl.* **1993**, *32*, 1111-1121.

32. Marcus, R. A. *Rev. Mod. Phys.* **1993**, *65*, 599-610.

33. Marcus, R. A. *Adv. Chem. Phys.* **1999**, *106*, 1-6.

34. Hush, N. S. *J. Chem. Phys.* **1958**, *28*, 962-972.

35. Hush, N. S. *Trans. Faraday Soc.* **1961**, *57*, 557-580.

36. Levich, V. G.; Dogonadze, R. R. *Dokl, Akad. Nauk SSSR* **1959**, *124*, 123-126.

37. Ulstrup, J.; Jortner, J. *J. Chem. Phys.* **1975**, *63*, 4358-4368.

38. Jortner, J. *J. Chem. Phys.* **1976**, *64*, 4860-4867.

39. Efrima, S.; Bixon, M. *Chem. Phys.* **1976**, *13*, 447-460.

40. Sarai, A. *Chem. Phys. Lett.* **1979**, *63*, 360-366.

41. Creutz, C.; Sutin, N. *J. Am. Chem. Soc.* **1977**, *99*, 241-243.

42. Miller, J. R.; Calcaterra, L. R.; Closs, G. L. *J. Am. Chem. Soc.* **1984**, *106*, 3047-3049.

43. Wasielewski, M. R.; Niemczyk, M. P.; Svec, W. A.; Pewitt, E. B. *J. Am. Chem. Soc.* **1985**, *107*, 1080-1082.

44. Irvine, M. P.; Harrison, R. J.; Beddard, G. S.; Leighton, P.; Sanders, J. K. M. *Chem. Phys.* **1986**, *104*, 315-324.

45. Fox, L. S.; Kozik, M.; Winkler, J. R.; Gray, H. B. *Science*, **1990**, *247*, 1069-1071.

46. Gray, H. B.; Winkler, J. R. *Annu. Rev. Biochem.* **1996**, *65*, 537-61.

47. Gray, H. B.; Winkler, J. R., In *Electron Transfer in Chemistry*; V. Balzani, Ed.; Wiley-VCH: Weinheim, Germany, 2001; Vol. 3.1.1; pp 3-23.

48 Wright, J. L.; Wang, K.; Geren, L.; Saunders, A. J.; Pielak, G. J.; Durham, B. Millett, F. *Adv. Chem. Ser.* **1998**, *254*, 99-110.

49 Tollin, G. In *Electron Transfer in Chemistry*; V. Balzani, Ed.; Wiley-VCH: Weinheim, Germany, 2001; Vol. 4.1.5; pp 202-231.

50 Davidson, V. L. *Acc. Chem. Res.* **2000**, *33*, 87-93.

51 Nocek, J. M.; Zhou, J. S.; Forest, S. D.; Priyadarshy, S.; Beratan, D. N.; Onuchic, J. N.; Hoffman, B. M.; *Chem. Rev.* **1996**, *96*, 2459-2489.

52 McLendon, G. L.; Hake, R. *Chem. Rev.* **1992**, *92*, 481-490.

53. Shifman, J. M.; Moser, C. C.; Kalsbeck, W. A.; Bocian D. F.; Dutton, P. L. *Biochemistry* **1998**, *37*, 16815-16827.

54. Sharp, R. E.; Moser, C. C.; Rabanal F.; Dutton, P. L.; *Proc. Natl. Acad. Sci. U.S.A.* **1998**, *95*, 10465-10470.

55. Tommos, C.; Skalicky, J. J.; Pilloud, D. L.; Wand, J. A.; Dutton, P. L. *Biochemistry* **1999**, *38*, 9495-9507.

56. Dai, Q.-H.; Tommos, C.; Fuentes, E. J.; Blomberg, M. R. A.; Dutton P. L.; Wand, A. J. *J. Am. Chem. Soc.* **2002**, *124*, 10952-10953.

57 Mutz, M. W.; McLendon, G. L.; Wishart, F. J.; Gaillard E. R.; Corin, A. F.; *Proc. Natl. Acad. Sci. U.S.A.* **1996**, *93*, 9521-9526.

58. Case, M. A.; Ghadiri, M. R.; Mutz M. W.; McLendon, G. L.; *Chirality* **1998**, *10*, 35-40.

59. Mutz, M. W.; Wishart J. F.; McLendon, G. L. *Adv. Chem. Ser.* **1998**, *254*, 145-159.

60 Kozlov G. V.; Ogawa, M. Y. *J. Am. Chem. Soc.* **1997**, *119*, 8377-8378.

61 Hammes-Schiffer, S. In *Electron Transfer in Chemistry*; V. Balzani, Ed.; Wiley-VCH: Weinheim, Germany, 2001; Vol. 1.1.5; pp 189-237.

62 . Cukier, R. I. *J. Phys. Chem.***1996**, *100*, 15428-15443.

63. Cukier, R. I. *J. Phys. Chem.* **1994**, *98*, 2377-2381.

64. Zhau, X. G. Cukier, R. I. *J. Phys. Chem.* **1995**, *99*, 945-954.

65. Cukier, R. I. *J. Phys. Chem. A* **1999**, *103*, 5989-5995.

66. Soudackov, A. Hammes-Schiffer, S. *J. Chem. Phys.* **1999**, *111*, 4672-4687.

67. Soudackov, A.; Hammes-Schiffer, S. *J. Chem. Phys.* **2000**, *113*, 2385-2396.

68. Decornez, H.; Hammes-Schiffer, S. *J. Phys. Chem. A.* **2000**, *104*, 9370-9384.

69 Shin S.; Cho, S. I. *Chem. Phys.* **2000**, *259*, 27-38.

70 Soudackov A.; Hammes-Schiffer, S. *J. Chem. Phys.* **2000**, *113*, 2385-2396.

71. Hammes-Schiffer, S. *Acc. Chem. Res.* **2001**, *34*, 273-281.

72 Cukier, R. I. *J. Phys. Chem. B* **2002**, *106*, 1746-1757.

73. Cukier, R. I. *Biochim. Biophys. Acta* **2004**, *1655*, 37-44.

74. Hammes-Schiffer, S. Iordanova, N. *Biochim. Biophys. Acta* **2004**, *1655,* 29-36.

75 Chang, C. J.; Brown, J. D. K. ; Chang, M. C. Y. ; Baker E. A. ; Nocera, D. G. In *Electron Transfer in Chemistry*; V. Balzani, Ed.; Wiley-VCH: Weinheim, Germany, 2001; Vol. 3.2.4; pp 409-461.

76 Cukier R. I. ; Nocera, D. G. *Annu. Rev. Phys. Chem.* **1998**, *49*, 337-369.

77 Turró, C. ; Chang, C. K. ; Leroi, G. E. ; Cukier R. I. ; Nocera, D. G. *J. Am. Chem. Soc.* **1992**, *114*, 4013-4015.

78. Zhao, X. G.; Cukier, R. I. *J. Phys. Chem.* **1995**, *99*, 945-954.

79. Cukier, R. I.; Daniels, S.; Vinson E.; Cave, R. J. *J. Phys. Chem. A* **2002**, *106*, 11240-11247.

80. Roberts, J. A.; Kirby, J. P.; Nocera, D. G. *J. Am. Chem. Soc.* **1995**, 117, 8051-8052.

81. Kirby, J. P. ; van Dantzig, N. A. ; Chang C. K. ; Nocera, D. G. *Tetrahedron Lett.* **1995**, *36*, 3477-3480.

82. Roberts, J. A.; Kirby, J. P.; Wall, S. T.; Nocera, D. G. *Inorg. Chim. Acta*, **1997**, *263*, 395-405.

83. Roberts, J. A.; Kirby, J. P.; Nocera, D. G. *J. Am. Chem. Soc.* **1997**, *119*, 9230-9236.

84. Damrauer, N. H.; Hodgkiss, J. M.; Rosenthal, J.; Nocera, D. G. *J. Phys. Chem. B* **2004**, *108*, 6315-6321.

85. Yeh, C.-Y. ; Miller, S. E. ; Carpenter S. D. ; Nocera, D. G. *Inorg. Chem.* **2001**, *40*, 3643-3646.

86. Hodgkiss, J. M.; Damrauer, N. H.; Pressé, S.; Rosenthal, J.; Nocera, D. G. *J. Phys. Chem. B.* **2006**, *110*, 18853-18858.

87 Sessler, J. L. ; Wang, B.; Springs, S. L.; Brown, C. T. In *Comprehensive Supramolecular Chemistry*; Murakami, Y., Ed.; Pergamon Press: Oxford, 1996; Vol. 4; pp 311-336.

88. Berg, A.; Shuali, Z.; Asano-Someda, M.; Levanon, H.; Fuhs, M.; Moebius, K.; Wang, R.; Brown C.; Sessler, J. L. *J. Am. Chem. Soc.* **1999**, *121*, 7433-7434.

89. Sessler, J. L.; Sathiosatham, M.; Brown, C. T.; Rhodes T. A.; Wiederrecht, G. *J. Am. Chem. Soc.* **2001**, *123*, 3655-3660.

90 Ward, M. D. *Chem. Soc. Rev.* **1997**, *26*, 365-376.

91 Shafirovich, V. Y.; Courtney, S. H.; Ya, N. ; Geacintov, N. E. *J. Am. Chem. Soc.* **1995**, *117*, 4920-4929.

92 Ghaddar, T. H.; Castner E. W.; Isied, S. S. *J. Am. Chem. Soc.* **2000**, *122*, 1233-1234.

93. de Rege, P. J. F.; Williams, S. A.; Therien, M. J. *Science* **1995**, *269*, 1409-1413.

94. Hodgkiss, J. M.; Rosenthal, J.; Nocera, D. G. In *Hydrogen-Transfer Reactions*; Hynes, J. T.; Klinman, J. P.; Limbach, H.-H.; Schowen, Eds; Wiley-VCH: Weinheim, Germany, 2007; Vol 2.17, pp 503-561.

95. Pressé, S.; Silbey, R. *J. Chem Phys.* **2006**, 124, 164504-164511.

96. Galoppini, E.; Fox M. A. *J. Am. Chem. Soc.* **1996**, *118*, 2299-2300.

97. Suydam, I. T.; Snow, C. D.; Pande, V. S.; Boxer, S. G. *Science*, **2006**, *313*, 200-204.

98. Steffen, M. A.; Kaiqin, L.; Boxer, S. G. *Science*, **1994**, *264*, 810-816.

99. Shin, Y.-G. K.; Newton, M. D.; Isied, S. S. *J. Am. Chem. Soc.* **2003**, *125*, 3722-3732.

100. Sibert, R.; Josowicz, M.; Porcelli, F.; Veglia, G.; Range, K.; Barry, B. A. *J. Am. Chem. Soc.* **2007**, *129*, 4393-4400.

Chapter II

Spectroscopic characterization of structurally homologous β- and *meso*-alkynylamidinium porphyrins

Parts of this Chapter have been published:
Rosenthal, J.; Young, E. R.; Nocera, D. G. *Inorg. Chem.* **2007**, *46*, 8668-8675.

Chapter II

II.1. Introduction

Supramolecular porphyrin assemblies constructed from De and Ae termini bridged by a hydrogen-bond network (---[H^+]---) are used for the study of photo-induced PCET. [1] A Zn(II) porphyrin appended with a hydrogen bonding functionality is utilized as a photo-reductant towards the goal of probing photo-induced CT mediated by hydrogen bonded interfaces in which the influence of the ionization state of the interface on ET is clearly resolved.[2] The amidine-carboxylic acid and the amidinium-sulfonate bridges utilized in these PCET studies take advantage of the dipole of an electrostatic ion pair interaction within a hydrogen-bonding scaffold and allow for investigation into the manner in which proton motion within a hydrogen-bond interface affects the rate, energetics and electronic coupling of electron transport.[1-4]

The kinetics for the individual PT and ET steps of the photo-induced PCET event may be probed by transient spectroscopy provided that the PT and ET are spectroscopically distinguishable. This task is not particularly onerous for ET, but does present challenges for PT. One strategy for monitoring PT may be to incorporate a spectral shift in the absorption spectrum of the porphyrin chromophore, which depends on the protonation state of the amidinium functionality. The absorption shift requires strong ground and excited state communication between the protonic functionality and the redox chromophore.[5] Such communication is mitigated by a saturated bridge or by canting of the amidinium functionality out of the porphyrin plane.[6-8] In order to circumvent the attenuation of the electronic communication between these two sites, a set of homologous *β*- and *meso*-alkynylamidinium porphyrin derivatives are presented. Scheme II.1 depicts the amidinium functionality extended away from the macrocycle. The cylindrical symmetry of the alkynyl spacer preserves the electronic communication between protonic interface and the porphyrin. The benefit of an interposed alkynyl spacer between the amidine and porphyrin is revealed by the pronounced wavelength dependence of the porphyrin electronic properties on the amidinium-amidine protonation state. Communication between the porphyrin and amidinium-amidine acid-base functionality are probed in both the porphyrin ground and excited electronic states to establish viability of this strategy for increasing electronic communication between the two sites.

II.2. A homologous pair: The β- and meso-alkynylamidinium porphyrins

Alkynylamidinium functionalities were fused to either the *β* (**AP-1**) or *meso* (**AP-2**) position (Scheme II.2) of the mesityl porphyrin macrocycle by Dr. Joel Rosenthal following the synthetic protocol outlined in the publication based on

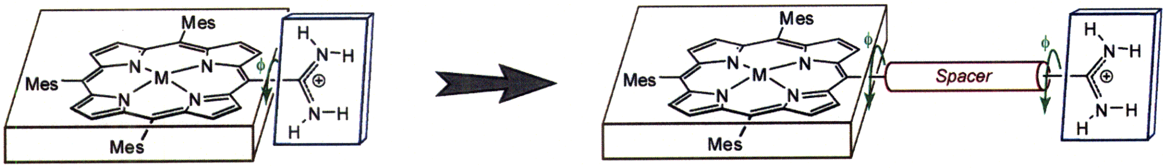

Scheme II.1. Extension of the amidinium functionality away from the porphyrin macrocycle using a spacer. The extension is achieved by an alkynylamidinium functionality that effectively decreases the cant angle between the porphyrin and the amidinium, thus increasing the electronic communication between the two components.

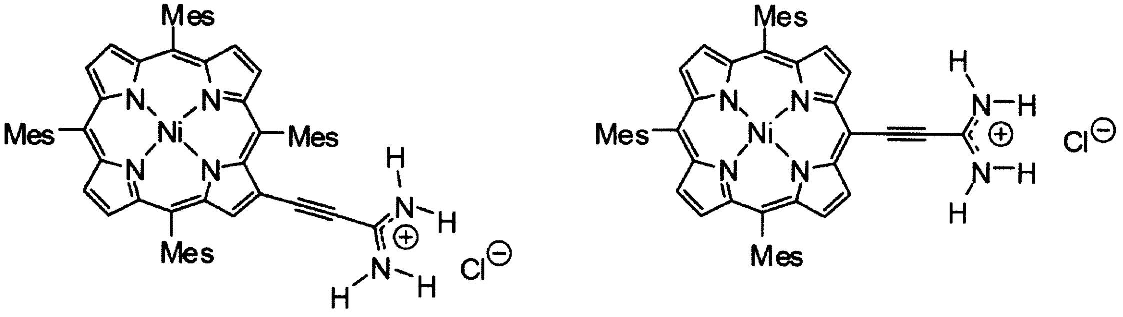

AP-1: β-amidinium porphyrin

AP-2: *meso*-amidinium porphyrin

Scheme II.2. Alkynylamidinium porphyrins **AP-1** and **AP-2**.

this work.[9] Dr. Joel Rosenthal furnished **AP-1** and **AP-2** for the further spectroscopic characterization presented in this Thesis.

II.3. Characterization of AP-1 and AP-2

*II.3.1. Electronic absorption spectroscopy of **AP-1** and **AP-2***

Electronic coupling between the amidinium functionality and the porphyrin macrocycle is revealed by pH-dependent electronic absorption spectra for both the *β*- and *meso*-alkynylamidinium porphyrin. Figure II.1A shows a pronounced perturbation of the electronic absorption profile of **AP-1** upon deprotonation of the amidinium group. A bathochromic shift is observed for the Soret band from 432 nm to 435 nm upon deprotonation. Well-anchored isosbestic points are maintained at 425 nm, 564 nm and 602 nm between the spectra of the protonated (amidinium) and deprotonated (amidine) forms of the proton interface. The red shift in the Soret band is accompanied by similar spectral shifts in the Q-band region. Similarly, the absorption spectrum of **AP-2** displays considerable

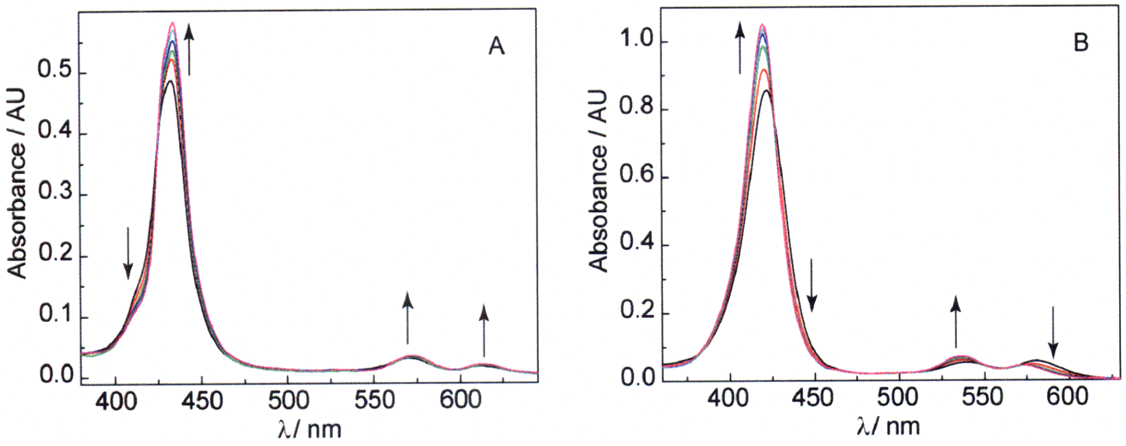

Figure II.1. Spectral changes associated with deprotonation the amidinium functionality of **AP-1** and **AP-2**. The base DMAP was used to deprotonate the amidinium functionality of (A) **AP-1** and (B) **AP-2** in ACN.

absorption shifts upon deprotonation of the amidinium functionality. However, as shown in Figure II.1B, a hypsochromic shift is observed upon conversion of amidinium to amidine. The maximum of the Soret band shifts from 422 nm to 420 nm while maintaining well-anchored isosbestic points at 428 nm, 550 nm and 568 nm. Similar modulation of the absorption profile is observed in the Q-band region of **AP-2** upon deprotonation.

II.3.2. Determination of pK_a and pK_a for **AP-1** and **AP-2***

Spectral shifts in the electronic absorption spectra of the alkynylamidinium porphyrins that accompany deprotonation of the amidinium functionalities provide spectroscopic observables that can be used to determine the pK_a of the amidinium functionality of **AP-1** and **AP-2** in the ground and excited electronic states. Titration of **AP-1** and **AP-2** in ACN with the base, 4-dimethylaminopyridine (DMAP), produces the spectral series shown in Figure II.1.

Benesi-Hildebrand plots of the spectral shifts for both alkynylamidinium porphyrins are shown in Figure II.2 and yield deprotonation constants (K_a'), from which the pK_as of **AP-1** and **AP-2** are determined according to the relation,

$$\text{p}K_a(\textbf{AP}) = \text{p}K_a(\text{DMAP}) - \log [K_a'(\textbf{AP})] \qquad \text{(II.1)}$$

The pK_a of DMAP in ACN is 12.33,[10] yielding a pK_a = 7.03 ± 0.10 for the ground state of **AP-1** and similarly pK_a = 7.74 ± 0.10 for the ground state of **AP-2**.

The excited state pK_a (pK_a*) of the alkynylamidinium porphyrin chromophore can be determined when the ground state pK_a and the magnitude of spectral shift of accompanying deprotonation is known. The excited state acidity constant, pK_a*, is formalized by the Förster equation, [11,12]

$$\text{p}K_a^* = \frac{\Delta G_a^*}{2.3RT} = \frac{\text{p}K_a - (h\nu_1 - h\nu_1)}{2.3RT} \qquad \text{(II.2)}$$

For equation II.2, $h\nu_1$ and $h\nu_2$ represent the energies of the 0-0 electronic

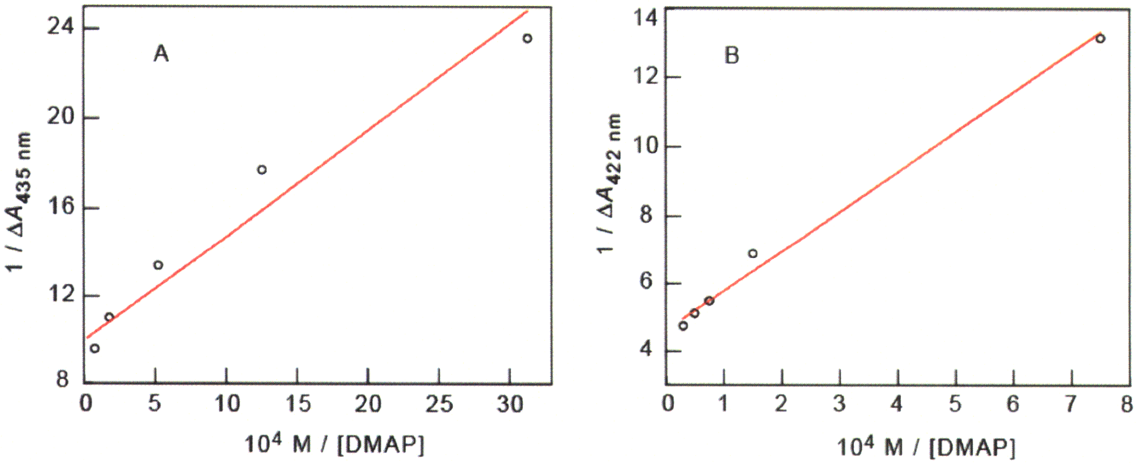

Figure II.2. Benesi-Hildebrand plots developed for **AP-1** and **AP-2**. Amidinium deprotonation is achieved for (A) **AP-1** and (B) **AP-2** upon titration with DMAP.

transitions for the conjugate acid and base, respectively. Thus, a chromophore for which the conjugate base displays a bathochromic shift relative to the conjugate acid ($h\nu_1 > h\nu_2$) is predicted to be a stronger acid in its excited state, or a photoacid. In contrast, a chromophore that demonstrates a hypsochromic shift between its conjugate base and conjugate acid is predicted to be more basic in its excited state, or a photobase. This explanation is depicted in a simplified Jablonski diagram shown in Scheme II.3. The thermodynamic relation can be alternately summarized in terms of the free energy change associated with deprotonation of the molecule in the ground state (ΔG_a) and excited state (ΔG_a^*) of the chromophore. When $\Delta G_a > \Delta G_a^*$, the compound is a photoacid; when $\Delta G_a > \Delta G_a^*$ the compound is a photobase.

Analysis of the electronic absorption spectra associated with deprotonation of **AP-1** and **AP-2** yield a $pK_a^* = 6.89 \pm 0.10$ and $pK_a^* = 8.37 \pm 0.10$ in ACN at 23 °C, respectively. These results demonstrate that the acidity of **AP-1** is greater in its excited state as compared to its ground state ($pK_a = 7.03 \pm 0.10$), while the acidity of **AP-2** is lower in its excited state relative to its ground state ($pK_a = 7.74 \pm 0.10$). Thus, in contrast to **AP-1**, which is a photoacid, **AP-2** is a photobase. The observed results obtained from electronic absorption spectroscopy are confirmed by the energy levels of the frontier MOs for both compounds as determined by DFT and TD-DFT calculations described in Section II.4. The calculated MOs and relative energy levels for **AP-1** and **AP-2** are shown in Figure II.3.

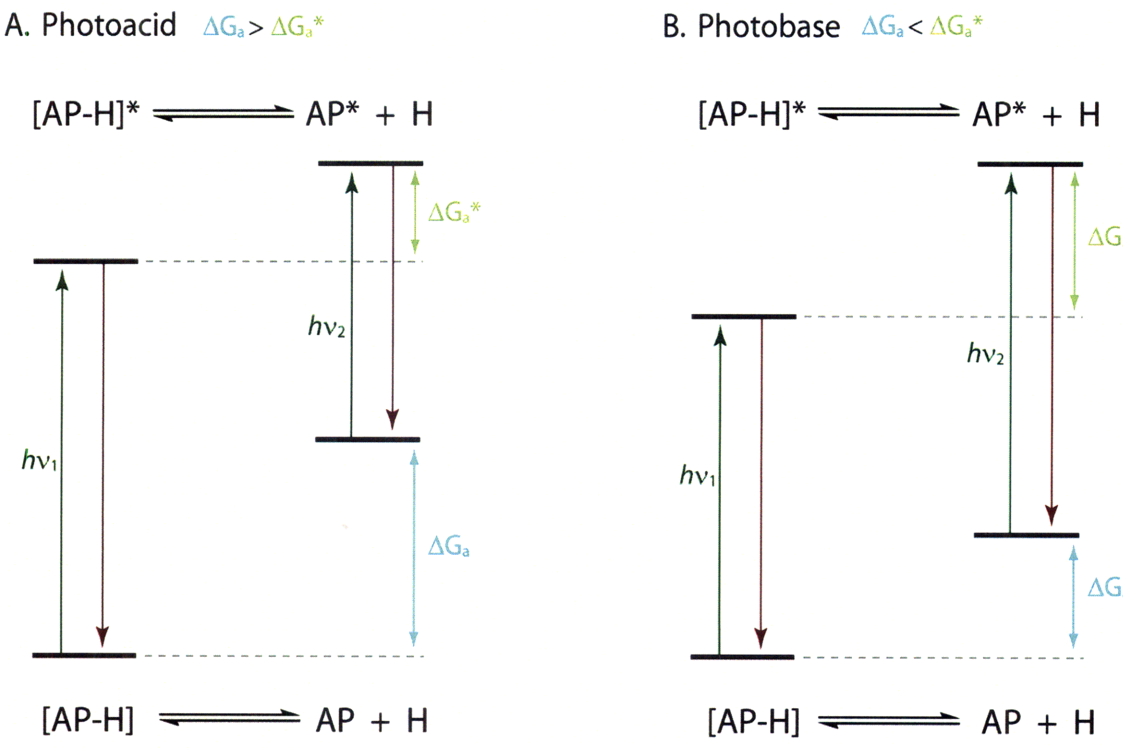

Scheme II.3. Generalized Jablonski diagrams of a photoacid and photobase. (A) Generalization for molecular species that behave as photoacids and (B) molecular species that behave as photobases.

II.4. Density functional theory calculations

The electronic coupling responsible for spectral shifts observed in steady state electronic absorption spectroscopy as a function of protonation state of the amidinium-amidine functionality are further elucidated by geometry optimized density functional theory (DFT) and time-dependent density functional theory (TD-DFT) calculations. Two factors are determinant in the electronic coupling responsible for the observed spectral shifts: the electronic structure of the frontier MOs of the porphyrin ring at the *meso*- and *β*- positions and the twist angle of the amidinium-amidine group with respect to the porphyrin macrocycle. DFT and TD-DFT are employed to gain further insight to these factors.

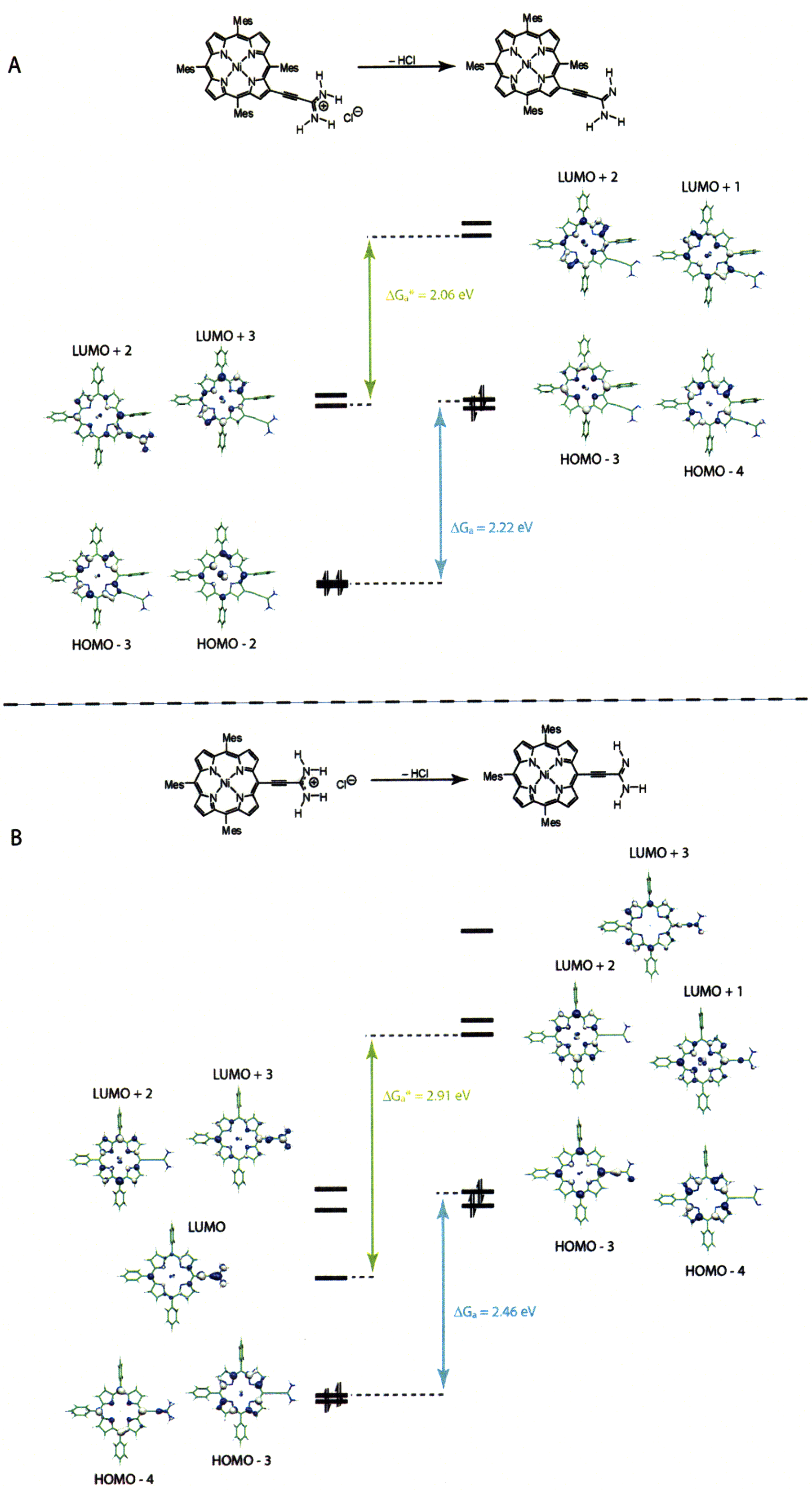

Figure II.3. Frontier MOs for **AP-1** and **AP-2**. The frontier MOs that contribute to the observed electronic transitions for both the amidinium and amidine forms are depicted in (A) **AP-1**, which is a photoacid and in (B) **AP-2**, which is a photobase.

II.4.1. Frontier MOs calculated by DFT

The calculated porphyrin frontier orbitals of **AP-1** and **AP-2** are shown in Figure II.3 for both the alkynylamidinium acid (left) and the corresponding conjugate alkynylamidine base (right). MOs lacking significant porphyrin π-orbital character are omitted for clarity, as they are not responsible for the porphyrin transitions observed in the absorption profiles of Figure II.1. Electronic absorption spectra of porphyrin-based macrocycles are addressed by the Gouterman model, which describes the electronic absorption spectrum in terms of transitions that arise between the frontier MOs of the porphyrin.[13]

DFT and TD-DFT calculations have been shown to reasonably predict electronic transition wavelengths for optical absorptions in porphyrins with β- and *meso*-substituents.[14-19] Considering the electronic distribution of the MOs about the porphyrin ring, it has been shown that HOMOs of a_{2u} and a_{1u} symmetries result in maximal orbital overlap with alkyne groups in *meso*- and β- positions of the porphyrin macrocycle, respectively.[20-22] In the systems described here, these orbitals are the parents of the HOMO-3 (a_{1u}, **AP-1**) and HOMO-4 (a_{2u}, **AP-2**) orbitals shown for the protonated amidinium species (Figure II.3). Geometry optimized calculations were performed with both DFT and TD-DFT for **AP-1** and **AP-2**. The highest occupied porphyrin-based MOs provide the linchpin for electronic coupling between the alkynyl group and the porphyrin ring. The energy gap is affected not only by the sensitivity of the aforementioned porphyrin-based HOMO levels on protonation state, but depends also on the LUMO energy levels. The LUMO+2 (protonated) and LUMO+1 (deprotonated) of **AP-1** (Figure II.3A) and the LUMO, LUMO+3 (protonated) and the LUMO+1, LUMO+3 (deprotonated) of **AP-2** (Figure II.3B) reveal orbital density on both the porphyrin macrocycle and the alkynylamidinium functionality. This electronic redistribution between the HOMOs and LUMOs is responsible for the spectral sensitivity of the porphyrin to the amidinium protonation state. Additionally, the relative energies of the calculated orbitals justify the divergent excited state behavior for the acidity constants of **AP-1** and **AP-2**. Specifically, the low lying LUMO of **AP-2** produces $\Delta G^* > \Delta G$ (predicting a photobase). In contrast, the absence of the lower lying LUMO in **AP-1** yields $\Delta G > \Delta G^*$ (predicting a photoacid).

II.4.2. Fixed dihedral angle calculations by DFT

The geometry optimized DFT calculations described above (Figure II.3) predict a $\theta_{\text{dihedral}} = 14°$ for **AP-1** and a $\theta_{\text{dihedral}} = 12°$ for **AP-2**, where the dihedral angle (θ_{dihedral}) is defined by the N–$C_{\text{amH+}}$ bond of the amidinium and the C_β–C_α or C_{meso}–C_α bonds on the porphyrin ring. These relatively small cant angles contrast sharply with the roughly 75° cant angle calculated for porphyrin-amidinium compounds in which the amidinium is directly linked to the porphyrin.[6,8] The steric clashing between the amidinium and the hydrogens of the porphyrin ring present in the direct linkage is avoided by poising the amidinium at the end of the alkynyl linker of **AP-1** and **AP-2**.

The structure of the alkynyl spacer is cylindrically symmetric and hence the electronic communication between the amidinium-amidine functionality and porphyrin macrocycle should be perturbed minimally upon rotation. TD-DFT calculations are presented to confirm this assertion. Systematic variation of θ_{dihedral} to span dihedral angles between 0° and 180°, performed for both **AP-1** and **AP-2**, confirms the intuition that conjugation persists upon amidinium rotation and that the barrier for rotation is minimal. Visualized MOs and relative orbital energies for rotational calculations on **AP-1** and **AP-2** are presented in Figure II.4 and Figure II.5, respectively.

II.4.3. Determining barrier of rotation for alkynylamidinium functionality

With results of the variable angle DFT calculations in hand, the calculated total potential energy is extracted in order to determine the barrier of rotation for the alkynylamidinium functionality.[23, 24] The potential energy change upon variation of θ_{dihedral} relative to the potential energy of geometry optimized calculation in terms of kT varies as,

$$\Delta U(\theta) = U(\theta) - U(\theta_i) \tag{II.3}$$

where $U(\theta) = A \sin[\omega(\theta - \theta_c)]$ and θ_i is the initial cant angle for the system, θ_i = 14.4 for **AP-1** and θ_i = 12.7 for **AP-2**. A is the amplitude of the sine curve, ω is related to the period of oscillation and θ_c is the offset angle. Fitted values for **AP-1** are A = 4.21 kT, ω = 2.11, and θ_c = 50.7° and **AP-2** are A = 4.27 kT, ω = 2.42, and θ_c = 54.7°. The calculated potential energies of **AP-1** and **AP-2** are plotted in Figure II.6 in terms of relative kT with the geometry optimized calculation set as the baseline energy value.

Two times the fitted amplitude (2*A*) represents the barrier height for rotation of the alkynylamidinium functionality relative to the plane of the porphyrin macrocycle. The barrier height for **AP-1** is 8.42 *k*T (4.99 kcal/mol) and for **AP-2** is 8.54 *k*T (5.05 kcal/mol). The rate for rotation of the amidinium functionality about the alkynyl spacer is described using transition state theory,

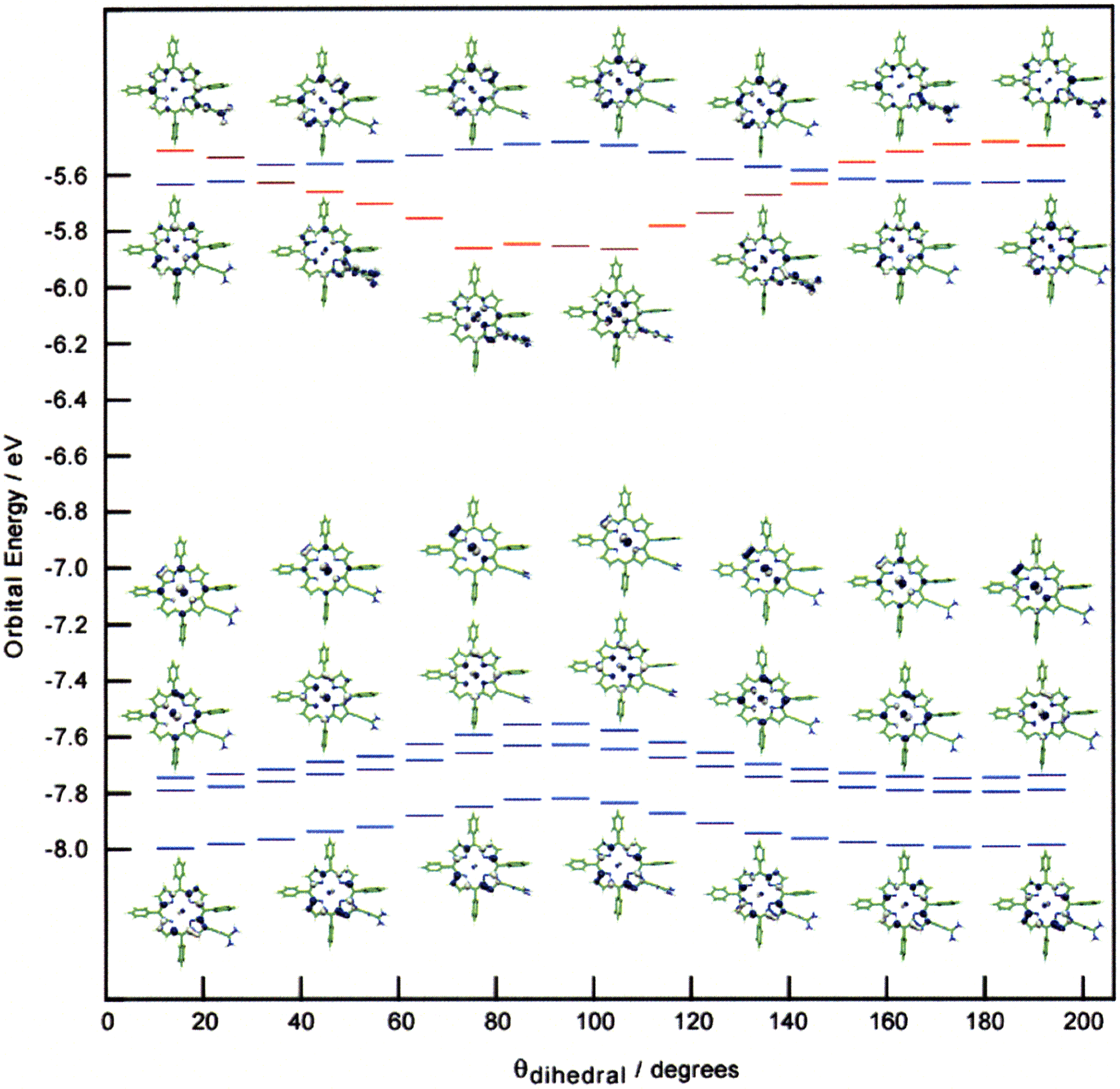

Figure II.4. Porphyrin-based MOs and energy levels for **AP-1** upon rotation of amidinium functionality. DFT calculations demonstrate that conjugation between the amidinium functionality and porphyrin macrocycle persist upon rotation and the barrier for rotation is low.

$$k_{TST} = \frac{k_B T}{h} e^{\frac{-\Delta G}{kT}} \tag{II.4}$$

where the barrier height for alkynylamidinium rotation is ΔG, T is temperature, k_B is the Boltzmann constant, *h* is the Planck constant and *k* is the gas constant. For **AP-1**, the rotational constant is calculated to be $k_{rot} = 6 \times 10^{-10}\ s^{-1}$, or one

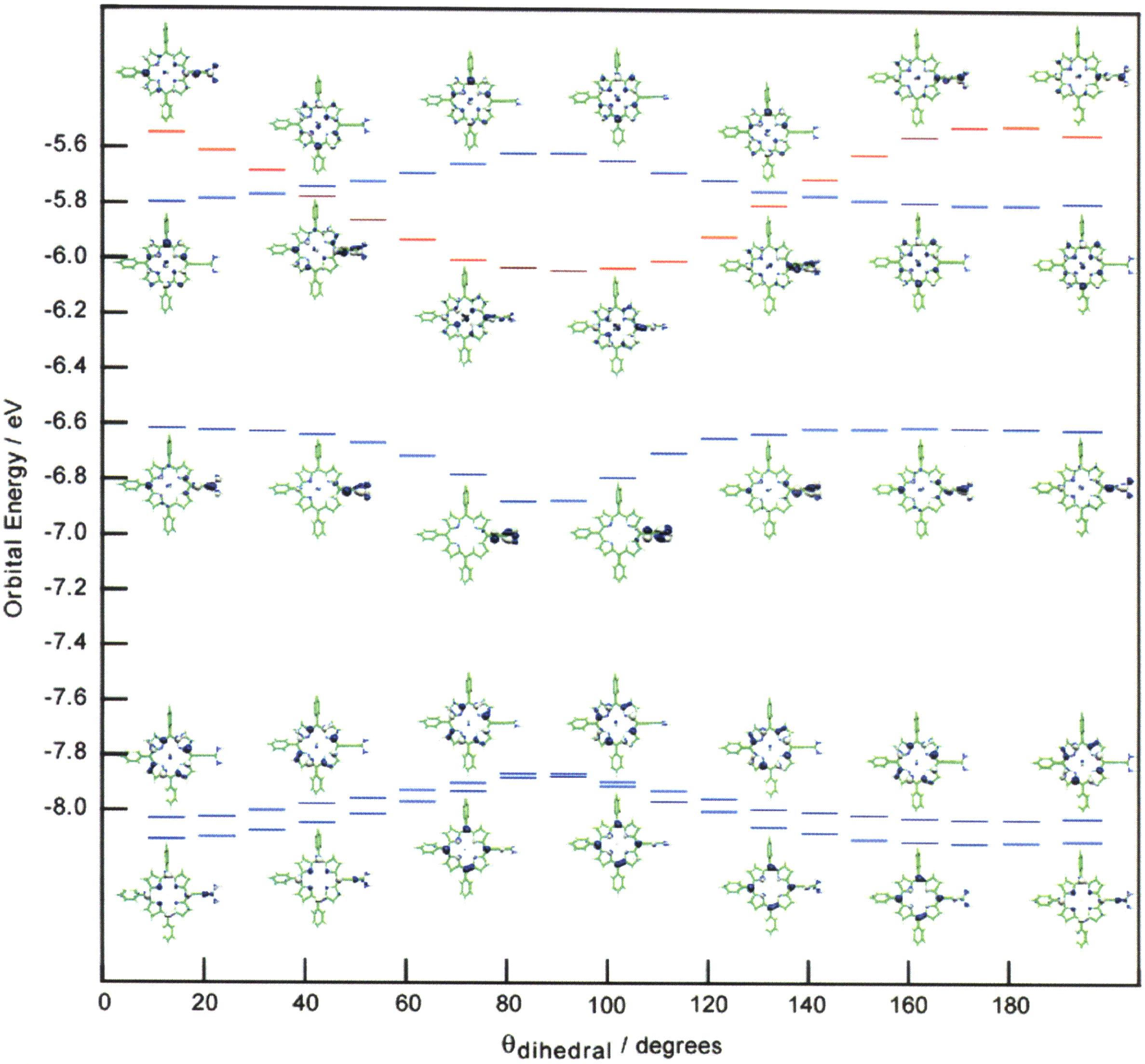

Figure II.5. Porphyrin-based MOs and energy levels for **AP-2** upon rotation of amidinium functionality. DFT calculations demonstrate that conjugation between the amidinium functionality and porphyrin macrocycle persist upon rotation and the barrier for rotation is low.

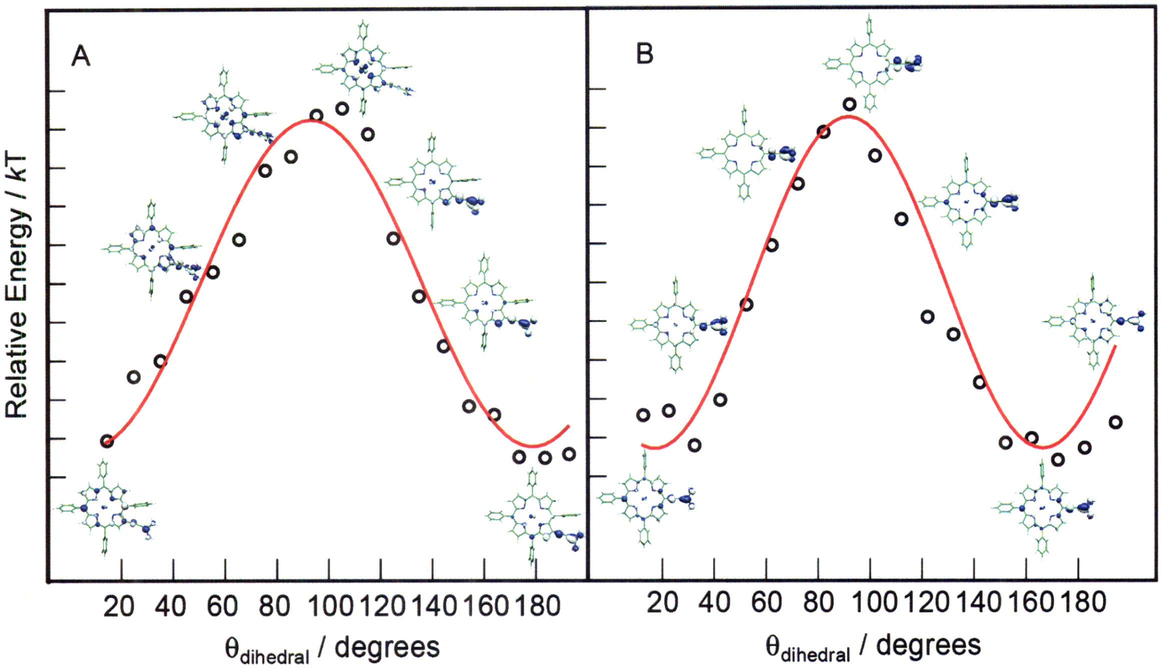

Figure II.6. Relative potential energies of **AP-1** and **AP-2** as a function of the dihedral angle between the porphyrin and the amidinium. (A) The LUMO+3 of **AP-1** and (B) the LUMO of **AP-2** are the two lowest lying unoccupied orbitals bearing significant electronic density on the porphyrin macrocycle and the amidinium functionality. The energy values are plotted at θ (relative to θ_i) = 0, 30, 60, 90, 120, 165, 180°.

rotation every 0.6 ns. For **AP-2**, the rotational constant is calculated to be $k_{\mathrm{rot}} = 7 \times 10^{-10}\ \mathrm{s}^{-1}$, or once every 0.7 ns. The rotational constants determined from TD-DFT calculations indicate that relative to typical singlet excited state lifetimes of these and similar porphyrin systems (~2-3 ns), the alkynylamidinium functionality is freely rotating.

II.5. Discussion and conclusion

II.5.1. Experiment and theory: A united front

Steady state absorption spectroscopy and DFT calculations provide a unified front in characterization of **AP-1** and **AP-2**. The disparate behavior of the p*K*a and p*K*a* values for **AP-1** and **AP-2** is reflected in the energy levels of the MOs of the protonated versus deprotonated amidinium functionality for AP-1 and AP-2, and for the overlap of the frontier MOs with the *β*- and *meso*-alkynylamidinium substitution pattern. The energy differences between HOMOs of the protonated and deprotonated forms of **AP-1** in Figure II.3A is $\Delta G_a = 2.22$ eV whereas the LUMOs energy difference is $\Delta G_a{}^* = 2.06$ eV, respectively. Given that $\Delta G_a > \Delta G_a{}^*$, **AP-1** is predicted by TD-DFT to be a photoacid in accordance with the experimentally observed bathochromic shift observed upon deprotonation. In contrast to **AP-1**, **AP-2** shows the opposite trend for the relative values of ΔG_a and $\Delta G_a{}^*$ as determined by TD-DFT calculations presented in Figure II.3B. In the case of **AP-2**, a third low lying LUMO orbital with significant alkynylamidinium and porphyrin π-orbital density is evident in the protonated **AP-2** MOs resulting in an increased $\Delta G_a{}^*$ value. Values of $\Delta G_a = 2.46$ eV and $\Delta G_a{}^* = 2.91$ eV are found for **AP-2**. As a result, $\Delta G_a < \Delta G_a{}^*$ and **AP-2** is predicted to be a photobase, in agreement with the observed absorption shifts.

II.5.2. Summary

As demonstrated by steady state absorption spectroscopy and accompanying DFT calculations, an alkynylamidinium functionality substituted at the *β*- or *meso*- position of a porphyrin maintains electronic communication with the macrocycle via an alkynyl spacer. Both **AP-1** and **AP-2** display similar ground state acidity constants, but exhibit opposite trends in terms of relative acidity in their excited states. **AP-1** behaves as a photoacid whereas the **AP-2** behaves as a photobase.

AP-1 and **AP-2** serve as excellent examples for designing molecular architecture to maintain electronic communication between the hydrogen bonding functionality (amidinium-amidine functionality) and the porphyrin macrocycle. Indeed, electronic communication between the two sites is proven both by experimental observation and theoretical calculation. The primary shortcomings of **AP-1** and **AP-2** lie in the relatively small, 2-3 nm, shifts in the electronic absorption spectrum for protonation versus deprotonation of the amidinium functionality. In order to further develop an understanding of the hydrogen bonded interface configuration and to provide an adequate spectroscopic handle for observation of PT, larger absorption shifts are necessary and are further pursued in Chapter III.

II.6. Experimental section

II.6.1. Materials

AP-1 and **AP-2** were synthesized by Dr. Joel Rosenthal as described in the publication that forms the basis of this Chapter.

II.6.2. Spectroscopy

Steady-state absorption spectra were obtained using a Spectral Instruments 440 Series spectrophotometer.

Absorption spectroscopy on samples of **AP-1** and **AP-2** was performed in a high-vacuum cell comprised of a 1-cm pathlength clear fused-quartz cuvette (purchased from Starna cells) connected to a 10-cm^3 solvent reservoir via a graded seal. High-vacuum Teflon valves were used to seal the cell from the environment and the cuvette from the solvent reservoir. Samples were prepared at concentrations of 16 μM (**AP-1**) and 9 μM (**AP-2)** in ACN, to give an optical density of ~0.48 AU (**AP-1**) and ~0.85 AU (**AP-2**) at the Soret absorption band and ~0.03 AU (**AP-1**) and ~0.07 AU (**AP-2**) at the Q_{10} absorption band. Sample preparation was performed under high-vacuum. An aliquot of **AP** (4.6×10^{-8} (**AP-1**) and 2.7×10^{-8} mol (**AP-2**) was added to the cuvette and the cell was evacuated under high-vacuum (10^{-5} Torr) to remove the transferring solvent. Three milliliters of dry ACN were vacuum transferred to the solvent reservoir where it was subject to three freeze-pump-thaw cycles. The cell was sealed to the environment and removed from the high vacuum manifold. A titration with DMAP was performed to monitor the spectral shifts associated with deprotonation of the amidinium functionality. Prior to each DMAP addition, ACN was vacuum transferred to the cuvette with a dry ice/acetone bath and sealed from the solvent reservoir and environment. This procedure ensured that the solvent volume remained constant throughout the course of the experiment. A stock solution of DMAP was added to the open solvent reservoir, while preserving the vacuum in the cuvette, and the transferring solvent was removed with a high vacuum manifold (10^{-5} Torr). The solvent reservoir was then sealed from the environment and opened to the cuvette compartment to introduce each new DMAP addition.

A Benesi-Hildebrand plot ($1/\Delta A$ vs. 1/[DMAP]) was developed for the spectral shift of the Soret band of **AP-1** and **AP-2** upon titration with DMAP. The Soret band of **AP-1** is observed at 432 nm with an extinction coefficient of 32,500 M^{-1} cm^{-1}, while the Soret band of **AP-2** is observed at 422 nm with a measured extinction coefficient of 94,000 M^{-1} cm^{-1}. Titration with DMAP yields strong isosbestic points for both **AP-1** and **AP-2**. Because an isosbestic point occurs near the Soret peak of the amidinium, as opposed to that of the amidine porphyrin, the absorption changes associated with the Soret band of the latter ($\Delta A_{\mathrm{Soret}}$) were used in the Benesi-Hildebrand analysis. The **AP-1** Soret undergoes a 3-nm red shift to 435 nm, while a 2-nm blue shift is observed in the **AP-2** spectra to a final Soret peak position at 420 nm. An acidity constant, K_a, for **AP-1** and **AP-2** is obtained from the ratio of the *y*-intercept and slope of linearly fit data.[25]

II.6.3. Computational methods

DFT and TD-DFT were performed using the Amsterdam Density Functional (ADF2006.01, TD-DFT; ADF2004.01, DFT) program[26-28] on a home-built Linux cluster comprising 60 Intel processors organized in groups of 12 running in parallel. The generalized gradient approximation was used as implemented in ADF by the Becke exchange functional,[29] and the PW91c correlation functional.[30] Convergence criteria tolerance for DFT were altered from default and set as follows: energy: 1 × 10^{-4} Hartrees; gradients: 1 × 10^{-3} Hartrees; coordinates: 1 × 10^{-3} Å; bond angles; 0.5°. Relativistic corrections were included using the scalar zero-order regular approximation (ZORA).[31,32] A basis set of triple-ζ Slater-type functions augmented by a polarization set (TZP) was used for Zn and N atoms and double-ζ with polarization (DZP) was used for C and H. Relativistic frozen core approximation was used to treat shells up to 2p for Zn and 1s for C and N as core shells. The input coordinates for **AP-1** and **AP-2** were obtained from a Chem2D model. Orbitals were visualized using the Molekel v.4.2 Linux-mesa software.[33,34]

TD-DFT was utilized for calculations on the protonated (amidinium) and deprotonated (amidine) functionalities of both Ni(II) porphyrins. Calculations were performed in which the plane of the amidinium functionality was rotated with respect to the porphyrin plane. The final coordinates of an initial DFT geometry optimization were utilized as the input coordinates. The dihedral angle (θ_{dihedral}), defined by the N–$C_{\text{amH+}}$ bond of the amidinium and the C_{β}–C_{α} or C_{meso}–C_{α} on the porphyrin ring, was rotated by intervals of 10 degrees and restrained. Default convergence criteria were used for TD-DFT calculations.

II.7. References

1. Chang, C. J.; Brown, J. D. K.; Chang, M. C. Y.; Baker, E. A.; Nocera, D. G. In *Electron Transfer in Chemistry*; Balzani, V., Ed.; Wiley-VCH: Weinheim, Germany, 2001; Vol. 3.2.4, pp 409-461.
2. Damrauer, N. H.; Hodgkiss, J. M.; Rosenthal, J.; Nocera, D. G. *J. Phys. Chem. B* **2004**, *108*, 6315-6321.

3. Chang, C. J.; Chang, M. C. Y.; Damrauer, N. H.; Nocera, D. G. *Biophys. Biochim. Acta* **2004**, *1655*, 13-28.

4. Hodgkiss, J. M.; Damrauer, N. H.; Pressé, S.; Rosenthal. J.; Nocera, D. G. *J. Phys. Chem. A* **2006**, *110*, 18853-18858.

5. Rosenthal, J.; Hodgkiss, J. M.; Young, E. R.; Nocera, D. G. *J. Am. Chem. Soc.* **2006**, *128*, 10474-10483.

6. Yeh, C.-Y.; Miller, S. E.; Carpenter S. D.; Nocera, D. G. *Inorg. Chem.* **2001**, *40*, 3643-3646.

7. Deng, Y.; Roberts, J. A.; Peng, S.-M.; Chang, C. K.; Nocera, D. G. *Angew. Chem. Int. Ed.* **1997**, *36*, 2124-2127

8. Kirby, J. P.; van Dantzig, N. A.; Chang, C. K.; Nocera, D. G. *Tetrahedron Lett.* **1995**, *36*, 3477-3480.

9. Rosenthal, J.; Young, E. R.; Nocera, D. G. *Inorg. Chem.* **2007**, *46*, 8668-8675.

10. Izutsu, K. *Acid-Base Dissociation Constants in Dipolar Aprotic Solvents*; Blackwell Scientific: Cambridge, USA, 1990.

11. Tolbert, L. M.; Solntsev, K. M. *Acc. Chem. Res.* **2002**, *35*, 19-27.

12. Weller, A. *Z. Elektrochem.* **1952**, *56*, 662-668

13. Gouteraman, M. In *The Porphyrins*; D. Dolphin, Ed.; Academic Press: New York, 1978; Vol. III.

14. Walsh, P. J.; Gordon, K. C.; Officer, D. L.; Campbell, W. M. *Theochem.* **2006**, *759*, 17-24.

15. Liao, M-S.; Scheiner, S. *Chem. Phys. Lett.* **2003**, 367, 199-206.

16 . Cramariuc, O.; Hukka, T. I.; Rantala, T. T. *Chem. Phys.* **2004**, *305*, 13-26.

17. Nguyen, K. A.; Day, P. N.; Pachter, R. *J. Phys. Chem. A.* **2000**, *104*, 4748-4754.

18. van Gisberg, S. J. A.; Rosa, A.; Ricciarde, G.; Baerends, E. J. *J. Chem. Phys.* **1999**, *111*, 2499-2506.

19 . Sundholm, D. *Phys. Chem. Chem. Phys* **2000**, *2*, 2275-2281.

20. Strachan, J. –P.; Gentemann, S.; Seth, J.; Kalsbeck, W. A.; Lindsey, J. S.; Holten, D.; Bocian, D. F. *J. Am. Chem. Soc.* **1997**, *119*, 11191-11201.

21. Yang, S. I.; Seth. J.; Balasubramanian, T.; Kim, D.; Lindsey, J. S.; Holten, D.; Bocian, D. F. *J. Am. Chem. Soc.* **1999**, *121*, 4008-4018.

22. Holten, D.; Bocian, D. F.; Lindsey, J. S. *Acc. Chem. Res.* **2003**, *35*, 57-69.

23 . Okuno, Y.; Kamikado, T.; Yokohama, S.; Mashiko, S. *Theochem.* **2002**, *594*, 55-60.

24 . Crossely, M. J.; Field, L. D.; Forster, A. J.; Harding, M. M.; Sternhell, Sever. *J. Am. Chem. Soc.* **1987**, *109*, 341-348.

25. Connors, K. A. In *Binding Constants: A Measurement of Molecular Complex Stability*; Wiley: New York, 1987.

26. ADF2004.01, SCM, Theoretical Chemistry, Vrije Universiteit, Amsterdam, The Netherlands, http://www.scm.com.

27. te Velde, G.; Bickelhaupt, F. M.; van Gisbergen, S. J. A.; Fonseca Guerra, C.; Baerends, E. J.; Snijders, J. G.; Ziegler, T. *J. Comput. Chem.* **2001**, *22*, 931-967.

28. Fonseca Guerra, C.; Snijders, J. G.; te Velde, G.; Baerends, E. J. *Theor. Chem. Acc.* **1998**, *99*, 391- 403.

29. Becke, A. D. *Phys. Rev. A* **1988**, *38*, 3098-3100.

30. Perdew, J. P.; Chevary, J. A.; Vosko, S. H. ; Jackson, K. A.; Pederson, M. R.; Singh, D. J.; Fiolhais, C. *Phys. Rev. B* **1992**, *46*, 6671-6687.

31. Van Lenthe, E.; Baerends, E. J.; Snijders, J. G. *J. Chem Phys.* **1993**, 99, 4597-4610.

32. Van Lenthe, E.; Ehlers, A.; Baerends, E. J. *J. Chem. Phys.* **1999**, *110*, 8943-8953.

33. Molekel v.4.2/3, Flükiger, P.; Lüthi, H. P.; Portmann, S.; Weber, J., Swiss Center for Scientific Computing, Manno (Switzerland), 2000-2002.

34. Portmann, S.; Lüthi, H. P. *Chimia* **2000**, *54*, 766-769.

Chapter III

Steady-state absorption spectroscopy of amidinium appended purpurin to determine proton interface configuration

Parts of this Chapter have been published:

Young, E. R.; Rosenthal, J.; Nocera, D. G. *Chem. Commun.* **2008**, 2322-2324.

Rosenthal, J.; Hodgkiss, J. M.; Young, E. R.; Nocera, D. G. *J. Am. Chem. Soc.* **2006**, *128*, 10474-10483.

Chapter III

III.1. Introduction and goals

An absorption shift is observed upon deprotonation of the amidinium functionality affixed to the porphyrin chromophore through an alkynyl spacer linking the two sites. The alkynylamidinium functionality of the previous Chapter successfully maintains ground and excited state communication between the protonic functionality and the redox chromophore in **AP-1** and **AP-2**, which is attenuated in other systems by a saturated bridge or by canting of the amidinium out of the porphyrin plane.[1-7] Although electronic communication is clearly maintained for **AP-1** and **AP-2**, the electronic absorption spectrum of each porphyrin show relatively small shifts upon protonation or deprotonation of the amidinium functionality. Larger spectral shifts are necessary in order to more accurately determine and monitor the protonation state of the amidinium functionality affixed to a porphyrin macrocyclic ring. A purpurin macrocycle is employed towards the goal of increasing electronic communication between the proton interface and chromophore via addition of an amidinium functionality to a fused 5-member ring. Conjugation between the purpurin macrocycle and the amidinium functionality is maintained by the unsaturated 5-membered ring joining the two sites (Scheme II.1). More dramatic spectral shifts than those reported for **AP-1** and **AP-2** are obtained for amidinium purpurin, **P**, upon protonation or deprotonation of the amidinium functionality. Spectral characterization of **P** yields a general tool for PCET studies. The spectral shifts of **P** are used to probe the location of the proton within the interface in order to determine which tautomer (non-ionized or ionized) prevails when carboxylate or sulfonate appended binding moieties are associated to the amidinium handle of **P**. Extensive characterization of **P** upon coordination of a series of binding moieties (**BM**) is performed in order to fully characterize the ionization state of the interfaces formed for each **BM** as a function of pK_a value. The goal is to develop a tool for assigning the ionization state of the proton interface in future PCET studies of D---[H$^+$]---A dyads.

III.2. Amidinium purpurin: Sensitivity of the macrocycle chromophore to the amidinium functionality

III.2.1. Amidinium purpurin

The amidinium functionality was appended to a purpurin macrocycle (Scheme III.1) by Dr. Joel Rosenthal following the synthetic protocol outlined his Thesis and the publication that forms the basis of this Chapter.[8] Dr. Joel Rosenthal synthesized and performed initial characterization of **P**, and furnished

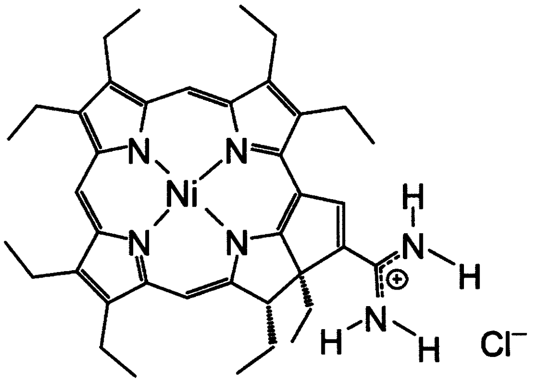

P

Scheme III.1. Amidinium purpurin, **P**. **P** provides excellent electronic communication between the amidinium functionality and the porphyrinic macrocycle in the form of the unsaturated five-membered ring joining the two sites.

them for the further characterization presented in this Thesis.

*III.2.2. Deprotonation titrations of **P** yield acidity constants*

The spectral signatures accompanying deprotonation-protonation of the amidinium-amidine functionality in **P** provides a spectroscopic observable that is used to determine the acidity constant of the amidinium functionality in both the ground and excited states. Titration of the amidinium purpurin in ACN with the base DMAP produces the spectral series shown in Figure III.1. A Benesi-Hildebrand plot of the spectral shifts shown (Figure III.1, inset) yields a deprotonation constant (K_a'), which allows for the pK_a of **P** to be determined by the relation,

$$\mathrm{p}K_a(\mathbf{P}) = \mathrm{p}K_a(\mathrm{DMAP}) - \log\,[K_a'(\,\mathbf{P})] \qquad \text{(III.1)}$$

The pK_a of DMAP in ACN is 12.33,[9] yielding a pK_a = 9.55 ± 0.10 for the ground state of **P**. The excited state is predicted to be a weaker acid than the ground state since the absorption spectrum of the conjugate base, **P-amH**, displays a hypsochromic shift relative to that of the conjugate acid, **P-amH$^+$**, ($h\nu_1 < h\nu_2$).[10-13] The excited state acidity constant, pK_a*, is readily expressed by the Förster equation,[14]

$$\mathrm{p}K_a{}^{*} = \frac{\Delta G_a\,{}^{*}}{2.3\mathrm{RT}} = \frac{\mathrm{p}K_a - (h\nu_1 - h\nu_1)}{2.3\mathrm{RT}} \qquad \text{(III.2)}$$

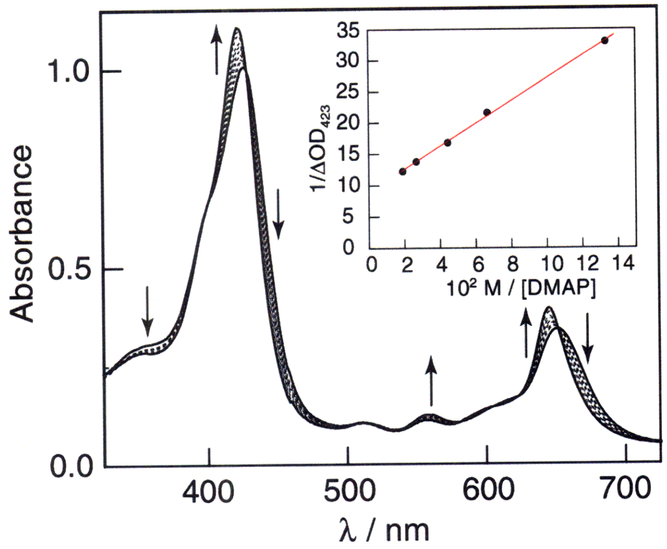

Figure III.1. Spectral evolution **P** upon deprotonation of the amidinium functionality.

For equation III.2, $h\nu_1$ and $h\nu_2$ represent the energies of the 0-0 electronic transitions for the conjugate acid and base, respectively. Using the electronic absorption spectra corresponding to amidinium purpurin **P-amH⁺** and the corresponding deprotonated amidine, **P-amH**, furnishes $pK_a^* = 10.40 \pm 0.1$ in ACN at 23 °C. These results indicate that upon excitation, **P** is nearly ten times more basic than in the ground state ($pK_a = 9.55 \pm 0.1$).

*III.2.3. Spectral shifts of **P** to characterize proton interfaces*

The spectra of **P-amH⁺** and **P-amH** provide reference points for the direct evaluation of the nature of the hydrogen bonding interface formed from the association of the **P** to carboxylic acid or sulfonic acid containing compounds of varying acidity. A series of spectra for **P** associated to benzoate (**1**), 3,5-dinitrobenzoate (**2**) (2,4-dinitrobenzoate gives the same result and is not shown for the sake of clarity), and phenyl sulfonate (**3**) are displayed in Figure III.2 and reveal unique spectral shifts associated with binding of moieties of different pK_as. The absorption spectra of the **P**:**1** assembly closely matches that of **P** when it has been deprotonated with DMAP. Conversely, the absorption spectra of **P:2** and **P:3** are red-shifted considerably from **P-amH**, displaying Soret peak maxima approaching that of **P-amH$^+$**. Some deviation from the spectrum of **P** is expected to result from association of a **BM**, even if the interface is best described as the ionized interface. The small spectral deviation in the case of the bound, ionized interface reflects that amidinium functionality is hydrogen bound by the **BM**. Comparison of these spectra leads to the following assignment: the proton interface is best described as a *non-ionized* amidine-carboxylic acid when **P** is bound to **1**, and as an *ionized* amidinium-carboxylate/sulfonate salt bridge when **P** is bound to **2** or **3**, respectively.

III.3. Solvent-dependent binding studies

III.3.1. Examination of ΔG and pK_a to determine proton interface configuration

The spectral sensitivity of **P** to a variety of **BM**s enables the configuration of the proton interface to be determined in a variety of different dielectric environments. Two primary factors at play in dictating the configuration of the interface are electrostatics within the interface and the pK_a difference between the constituent protonic interface functionalities. The amidinium-carboxylate and amidinium-sulfonate interfaces combine the dipole of an electrostatic ion pair interaction, a two-point hydrogen bond, and secondary electrostatic interactions to produce a highly stable proton interface.[15-19] These electrostatic factors favor formation of an ionized proton interface. The relative pK_a values of the amidinium, the carboxylic acid and the sulfonic acid functionalities that comprise the proton interface also conspire to determine the extent to which the interface configuration is ionized.[20] In many cases, the difference in acidity between the amidinium and carboxylic acid or the amidinium and sulfonic acid functionalities drives the formation of a non-ionized interface as the more acidic amidinium drives donation of its proton to the partner interface moiety. However, the electrostatic interactions within the interface stabilize charge accumulation, leading in some cases to an ionized interface even when a simple ΔpK_a calculation predicts formation of a non-ionized interface.[21] The ΔpK_a difference needed to achieve the ionized over the non-ionized interface, thereby overcoming the electrostatic contributions to the contrary, must be determined experimentally and is pursued in this Chapter by stepping through a series of **BM**s with different acidity constants. The transition from a *non-ionize*d to *ionized* interface occurs as the acidity of the **BM** increases. Binding studies of **P**:**BM** yield experimental insight to the configuration of the proton interface, and in doing so resolve the question of whether electrostatics or pK_a driving force imparted by the acidity constants of the constituent functionalities (ΔpK_a) prevails within a given interface.

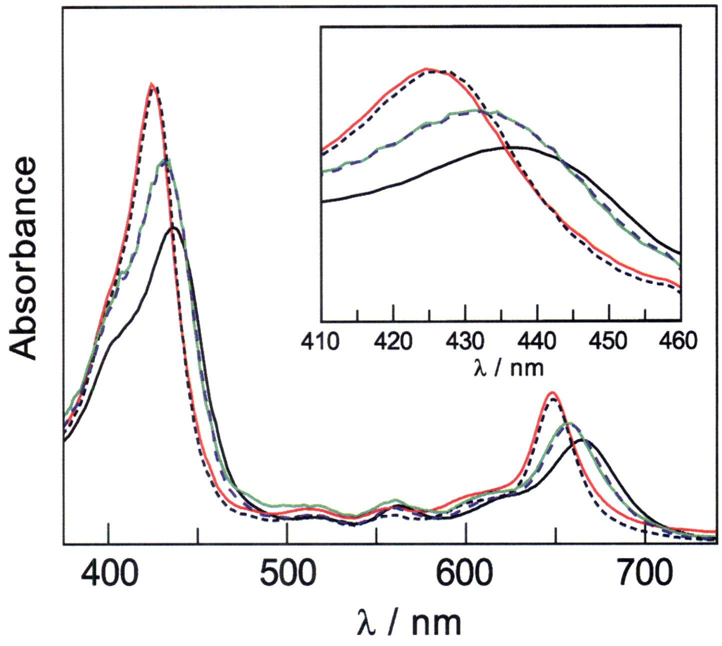

Figure III.2. Absorption spectra of **P** upon binding of various moieties. Protonated purpurin **P-amH$^+$** (0.63 × 10^{-6} M) (black, solid line, λ_{max} = 435 nm) and deprotonated purpurin **P-amH** (red, solid line, λ_{max} = 424 nm) are shown along with **P** upon addition of a large excess of benzoate, **1** (8.5 × 10^{-2} M) (blue, dashed, λ_{max} = 424 nm), 3,5-dinitrobenzoate, **2** (3.12 × 10^{-4} M) (purple, long dashed, λ_{max} = 432 nm), and phenyl sulfonate, **3** (4.0 × 10^{-2} M) (green, solid line, λ_{max} = 432 nm) in DCM.

III.3.2. Determination of binding constants in various solvents

The absorption spectrum of **P** is sensitive to protonation state of the appended amidinium functionality. Figure III.1 shows large spectral shifts in the electronic absorption spectrum of **P** before (**P-amH$^+$**) and after (**P-amH**) addition of the base DMAP in ACN. Deprotonation of the amidinium functionality in ACN, is indicated by a shift in the absorption maximum of the Soret band from 428 nm to 423 nm. Deprotonation of the amidinium functionality shifts the Soret band from 430 nm to 426 nm in THF and from 436 nm to 426 nm in DCM. The endpoints of these titrations are shown in Figure III.3. A 1:1 binding motif between **P**:**BM** is signified by a Benesi-Hildebrand analysis of the titration data

(1/ΔA vs. 1/[**BM**]).[22] The binding constant, K_{assoc}, for **P**:**2** is found to be ~ 4.5 × 10^4 M^{-1} and for **P**:**3** is ~ 1.5 × 10^2 M^{-1} in ACN. The K_{assoc} for **4**, **5** and **6** are all the same within error and are measured to be ~ 9.9 × 10^3 M^{-1}.

III.3.3. Assignment of proton interface configuration in various dielectric environments

A series of **BM**s of varying pK_a values in ACN is presented as summarized in Table III.1.[23,24] The dependence of the **P**:**BM** association and interface configuration on the dielectric constant of the solvent is probed along the series THF (ε_s = 7.58), DCM (ε_s = 8.93) and ACN (ε_s = 37.5).[25] Absorption spectra of **P** in ACN, THF, and DCM demonstrate analogous spectral shifts with each **BM** and exhibit well-anchored isosbestic points during the titration of the **BM** with **P-amH⁺**. The endpoint spectrum of each titration reveals the configuration of the proton interface as indicated by the final position of the Soret ($S_2 \leftarrow S_0$ transition at ~ 430 nm) or Q-band ($S_1 \leftarrow S_0$ transition at ~ 650 nm) maximum. Conversion of **P-amH⁺** to **P-amH** in the *non-ionized* interface is indicated by a shift of the

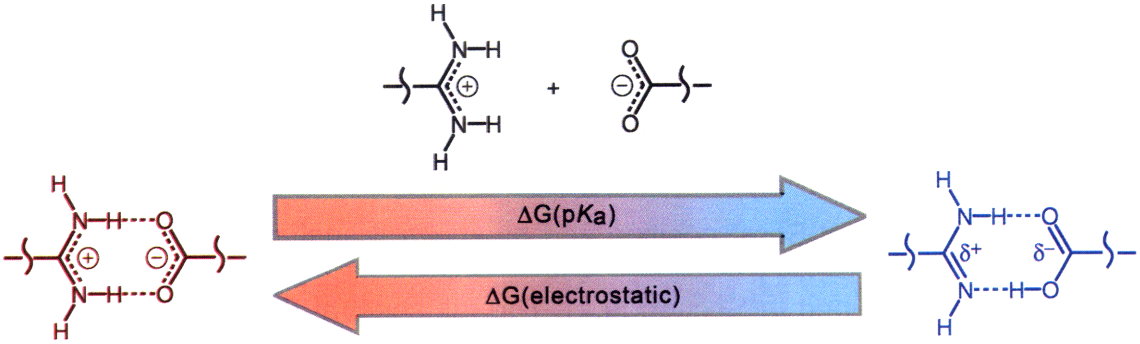

Scheme III.2. Role of pK_a and electrostatics in dictating interface ionization. Relative acidity constants of component moieties and electrostatic contributions conspire to determine the proton interface configuration: non-ionized or ionized

Table III.1. ΔG_{pK_a} and interface configuration for **P**:**BM** complexes.

	Binding Moiety	pK_a[a]	ΔG_{pK_a} /eV[b]	Ionized Interface?		
				THF	DCM	ACN
P	Purpurin-am$^+$	9.55				
2	3,5-Dinitrobenzoate	17	−0.44	✓	✓	✓
3	Phenylsulfonate	7	0.15	✓	✓	✓
4	Acetate	21	−0.68			
5	Chloroacetate	18	−0.50		✓	✓
6	Dichloroacetate	14	−0.26	✓	✓	✓

[a] in ACN from ref. 23. [b] at 298 K, calculated from pK_a values recorded in ACN, $\Delta G_{pK_a} = -RT\,[pK_a(\mathbf{BM})/pK_a(\mathbf{P\text{-}am^+})]$

peak maxima to wavelengths nearly coincident with that observed for **P-amH** upon deprotonation of **P-amH$^+$** with DMAP. The small 1-2 nm shifts of the Soret band of **P-amH$^+$** in the presence of **BM** are interpreted as the establishment of an *ionized* interface.[21]

The insets of Figure III.3 show the final Soret peak position of **P** in each solvent for all **BMs** studied. The solid data points at each end represent the peak position of **P-amH$^+$** (highest wavelength, black circle) and **P-amH** (lowest wavelength, red circle). The dotted line in each plot denotes an approximate boundary for the transition between the *ionized* and *non-ionized* interface as determined by the final Soret position and by spectral analysis of the initial and final spectra (as outlined in Section III.4). The full spectral development of each titration and accompanying Benesi-Hildebrand plot are shown in Appendix A.

Table III.1 summarizes the **BM**, the pK_a of each **BM** and the ionization state of the interface formed for association of **P** with each **BM**.

III.4. *Analysis and discussion*

Experimental observation of the proton interface configuration for each **P**:**BM** dyad and determination of K_{assoc} for each interface enables the construction of a thermodynamic cycle as shown in Scheme III.3. Studies of the proton interface configuration upon variation of the **BM** acidity constant provide a means to quantify the relative contributions of pK_a and the interface electrostatics so that a metric can be developed to predict the configuration of a bound proton interface with knowledge of only the pK_a values of the constituent moieties. By utilizing a series of solvents with differing dielectric constants, this metric can be

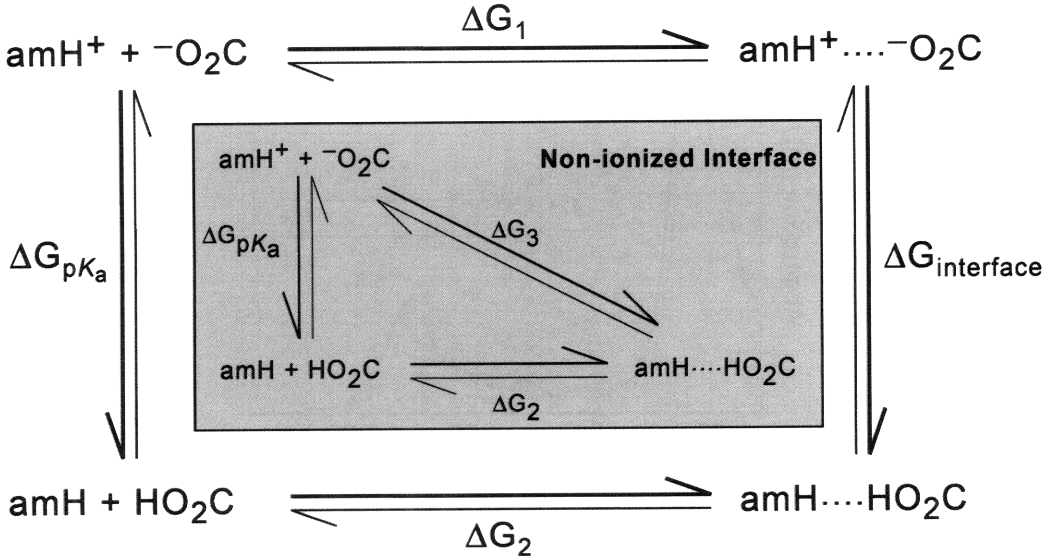

Scheme III.3. Square scheme representation of free energies involved in determining the tautomeric form of the proton interface.

developed, as the electrostatic contribution to stabilization of the interface will vary with the dielectric continuum experienced by the system.

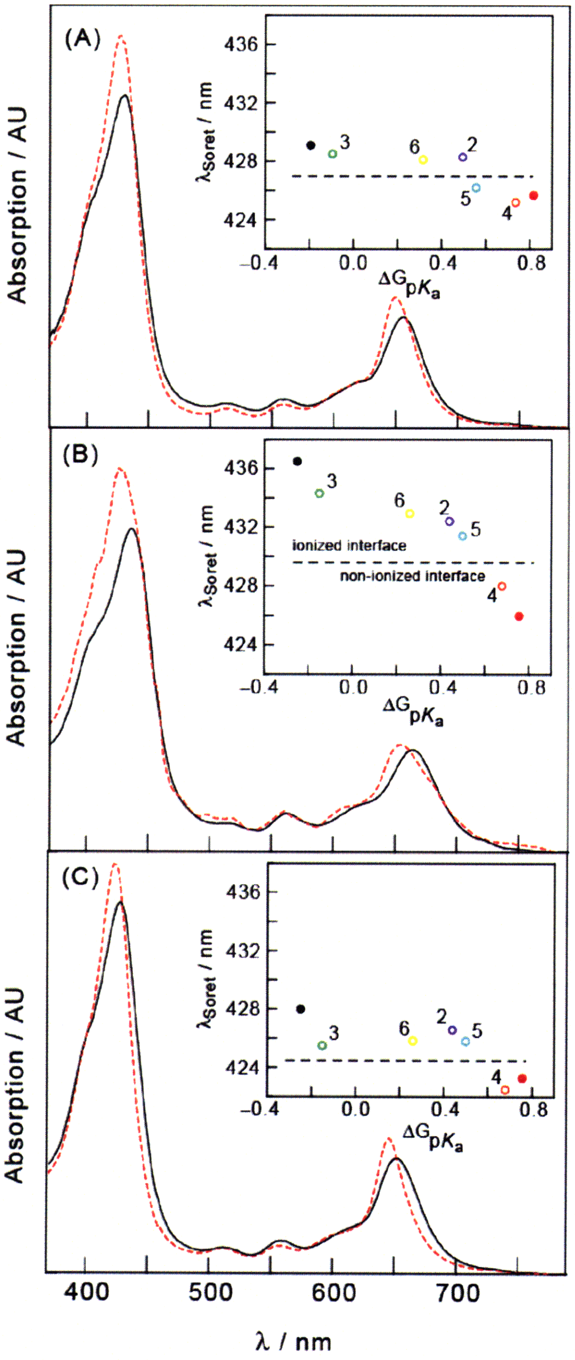

Figure III.3. UV-vis profiles and Soret peak positions for **P** bound by various moieties in THF, DCM and ACN. The absorption spectra of **P-am**$^+$, solid black line; and **P-am**^{0} formed by deprotonated of **P-am**$^+$ with DMAP, red dotted line are shown (a) in THF, 2000 eq DMAP, (b) in DCM, 550 eq DMAP and (c) in ACN, 950 eq DMAP. Inset: Soret peak position of **P** vs. ΔG_{pKa} for each **P**:**BM** complexes. The highest and lowest peak maxima (solid circles) represent **P-am**$^+$, and **P-am**^{0}, respectively.

Since the interface under consideration is formed from a protonated amidinium purpurin, amH$^+$, and a deprotonated carboxylate (or sulfonate) appended **BM**, ^-O_2C, as the reactants (Scheme III.3 top, left), either an ionized **amH$^+\cdots{}^-$O$_2$C** or an non-ionized **amH···HO$_2$C** interface is produced. The driving force for formation of the former (ΔG_1) is determined directly from the measurement of K_{assoc} for **P**:**BM** that leads to formation of the ionized **P-amH$^+\cdots{}^-$O$_2$C** complex (Scheme III.3, inset). The bottom horizontal equilibrium relation of the square scheme addresses the driving force for formation of the non-ionized interface **P-amH···HO$_2$C** from the neutral analogues (ΔG_2), and is determined by finding the difference between the ΔG_3 and ΔG_{pKa} as shown by the inset in Scheme III.3, where ΔG_3 is measured experimentally for the case in which the amidinium and carboxylate functionalities combine to form a non-ionized interface,

$$\Delta G_2 = \Delta G_3 - \Delta G_{pKa} \qquad \text{(III.3)}$$

Accordingly, the stabilization imparted by PT within the interface ($\Delta G_{interface}$) can be determined from the free energies of the square scheme and the pK_a values of the constituent moieties (ΔG_{pKa}). The various ΔG values in the square scheme are summarized in Table III.2.

Although the binding of the various **BM**s listed in Table III.1 to **P-amH$^+$** is presented in ACN, DCM and THF, the thermodynamic description and stabilization energy of the interface can only be determined rigorously for ACN since pK_a values for the **BM**s used in this study have been determined only in this solvent. Inspection of Figure III.3 reveals that conversion between the tautomeric forms of the interface occurs for pK_a values between those of **4** and **5** in ACN (Figure III.3 C).

Thus, Scheme III.3 is analyzed for these two **BM**s as they most closely define the razor's edge between formation of the *ionized* and *non-ionized* proton interface. Accordingly, these two points allow for the determination of the minimum interface stabilization necessary to obtain an ionized interface as per equation III.4:

$$\Delta G_{interface} = (\Delta G_2 + \Delta G_{pKa}) - \Delta G_1 \qquad \text{(III.4)}$$

Upon association of **P-amH$^+$** with **4**, the am···HO_2C tautomer is formed, allowing for the determination of ΔG_2 via equation III.3. ΔG_1 is obtained from K_{assoc} of **P**:**5**, since association of **P-amH$^+$** with **5** generates the ionized **amH$^+$···^-O_2C** complex. That the ionized interface for **P**:**5** persists when the pK_a difference predicts formation of the am···HO_2C interface reveals the importance of electrostatic contributions to the interface configuration. The electrostatic stabilization of the interface imparted by formation of the ionized **amH$^+$···^-O_2C** complex ($\Delta G_{interface}$) can be determined using equation III.4 and is minimally 0.18 eV in ACN. This electrostatic interaction energy can be calculated for point charges, q_1 and q_2, according to $V = (q_1q_2)/(4\pi\varepsilon_s r)$ where ε_s is the dielectric constant of the medium.[26] An electrostatic stabilization energy of 0.10 eV is calculated for the amidinium-carboxylate salt bridge at a distance of r = 3.9 Å in THF. This distance is measured between the central carbon atoms of the

Table III.2. Free energy values for thermodynamic assignment of $\Delta G_{Interface}$ in ACN.

	Binding Moiety	pK_a[a]	ΔG_1 /eV[b]	ΔG_2 /eV	ΔG_3 /eV[b]	ΔG_{pK_a} /eV[c]	$\Delta G_{interface}$ /eV
P	Purpurin-am$^+$	9.55					
2	3,5-Dinitrobenzoate	17	−0.28			−0.44	
3	Phenylsulfonate	7	−0.13			0.15	
4	Acetate	21		0.44	−0.24	−0.68	0.18
5	Chloroacetate	18	−0.24			−0.50	
6	Dichloroacetate	14	−0.24			−0.26	

[a] in ACN, from ref. 23. [b] $\Delta G = -RT \ln K_{assox}$(**P**:**BM**) [c] at 298 K, calculated from pK_a values recorded in ACN, $\Delta G_{pKa} = -RT\ [pK_a(\mathbf{BM})/pK_a(\mathbf{P\text{-}am}^+)]$

amidinium and carboxylate groups from the energy optimized structure.[2] The experimental results of these studies are in reasonable agreement with a simple ion solvation model. The discrepancy most likely arises from the approximation that the electrostatic charge within the interface is confined to a point-dipole.

While the dearth of known pK_a values in DCM and THF preclude a similar thermodynamic analysis in those solvents, a qualitative understanding of interface behavior is inferred from experimental results. In the dielectric environment of DCM, the proton interface maintains the ionized configuration at the same ΔpK_a difference as ACN, however in the lower dielectric environment of THF conversion to the ionized tautomer shifts to lower ΔpK_a. THF does not tolerate charge build-up to the extent that ACN and DCM do, and thereby favors a *non-ionized* interface configuration at a lower free energy.

III.5. Conclusion

The excellent electronic communication between the purpurin chromophore and appended amidinium functionality in **P** yields clear insight to the static configuration of the bound protonic interface through steady-state electronic absorption spectroscopy. The distinct spectral shifts that accompany **BM** association to the amidinium to form an ionized interface differ from the spectrum of the unbound amidinium and also from the spectrum of the bound amidine functionality in the non-ionized interface form. The spectral characterization of the three amidinium functionality states (unbound; bound ionized interface; bound non-ionized interface) enable the proton interface configuration to be assigned for De-Ae dyads in mechanistic studies of PCET. Of particular interest to the studies presented in Chapter IV and V is the assignment of a non-ionized amidine-carboxylic acid formed between an amidinium appended Zn(II) porphyrin De and an carboxylate appended NI Ae. When the Ae is replaced with a sulfonate appended NI, the interface ionization when bound to the amidinium appended Zn(II) porphyrin is established as an ionized amidinium-sulfonate interface.

III.6. Experimental

II.6.1. Materials

P was synthesized by Dr. Joel Rosenthal as described in the publication that forms the basis of this Chapter.[27] Tetrabutylammonium phenylsulfonate (**3**) was prepared as described previously.[21] Tetrabutylammonium 3,5-

Dinitrobenzoate (**2**), tetrabutylammonium chloroacetate (**5**) and tetrabutylammonium dichloroacetate (**6**) were prepared as described previously.[27] Tetrabutylammonium acetate (**4**) was purchased from Aldrich and used without further purification. Solvents were purchased from VWR Scientific Products or Sigma Aldrich and dried using standard solvent drying techniques.[28] Other reagents were purchased from Aldrich, Acros or Strem Chemicals and used as received.

II.6.2. Spectroscopy

UV-vis absorption spectra were recorded on a Spectral Instruments 440 Series diode array spectrophotometer with greater than 1 nm accuracy and precision over the course of experimentation. For example, the starting Soret peak positions for all titrations were within 1 nm for a given solvent.

Samples of purpurin-amidinium (**P**) used for absorption spectroscopy were contained within a high-vacuum cell consisting of a 1-cm pathlength clear fused-quartz cell (Starna cells), which was connected to a 10-cm^3 solvent reservoir via a graded seal. The two chambers were isolated from the environment and from each other by high-vacuum Teflon valves. An aliquot of **P** (~6 × 10^{-8} mol) was added to the cell, and an initial aliquot of **1**, **2**, **3**, **4**, **5**, **6** or DMAP was added to the solvent reservoir. The transferring solvent was removed from both compartments on a high-vacuum manifold (10^{-5} Torr). Three milliliters of dry THF, DCM or ACN was subject to at least three freeze-pump-thaw cycles (10^{-5} Torr) and added to the cell by vacuum transfer to make a 20 μM solution of **P**. Both chambers were sealed and removed from vacuum. In this configuration, the first absorption spectrum of **P** was recorded. The valve between the two compartments was then open to expose **P** to the BM while maintaining high vacuum and exactly the same amount of compound and solvent. A second absorption spectrum was recorded. Before a BM was dropped into the vessel, the solvent was transferred into the cuvette with a dry ice/acetone bath and sealed. The solvent reservoir was open and a second addition of BM was added. The same procedure was followed to remove the transferring solvent and expose **P** to a second addition of BM. This procedure was performed for each addition of BM to ensure that the sample remained under vacuum and the solvent volume remained constant.

A Benesi-Hildebrand plot ($1/\Delta A_{Soret}$ vs. 1/[**BM**]) was developed for the spectral shift of the Soret band of **P** upon titration with **2**, **3**, **4**, **5**, **6** and DMAP. An acidity constant, K_a', for **P** is obtained from the ratio of the *y*-intercept and slope of linearly fit data.[29] Linearity of the data points confirms 1:1 binding stoichiometry.

Spectral analysis was performed to aid assignment the end-point configuration of the interface for each **BM** titration: *ionized* or *non-ionized*. The spectral contribution of the unbound **P-am$^+$** species was removed to leave a residual trace indicative of the bound species. In the cases where the residual peaks of the BM titration matched to within 1 nm of the DMAP difference trace, the interface was categorized as *non-ionized*. When the difference spectra showed greater variation compared to the deprotonated standard, DMAP, the interface was characterized at *ionized*.

III.7. References

1. Chang, C. J.; Brown, J. D. K.; Chang, M. C. Y.; Baker, E. A.; Nocera, D. G. In *Electron Transfer in Chemistry*; Balzani, V., Ed.; Wiley-VCH: Weinheim, Germany, 2001; Vol. 3.2.4, pp 409-461.
2. Damrauer, N. H.; Hodgkiss, J. M.; Rosenthal, J.; Nocera, D. G. *J. Phys. Chem. B* **2004**, *108*, 6315-6321.
3. Chang, C. J.; Chang, M. C. Y.; Damrauer, N. H.; Nocera, D. G. *Biophys. Biochim. Acta* **2004**, *1655*, 13-28.
4. Hodgkiss, J. M.; Damrauer, N. H.; Pressé, S.; Rosenthal. J.; Nocera, D. G. *J. Phys. Chem. A* **2006**, *110*, 18853-18858.
5. Yeh, C.-Y.; Miller, S. E.; Carpenter S. D.; Nocera, D. G. *Inorg. Chem.* **2001**, *40*, 3643-3646.
6. Deng, Y.; Roberts, J. A.; Peng, S.-M.; Chang, C. K.; Nocera, D. G. *Angew. Chem. Int. Ed.* **1997**, *36*, 2124-2127
7. Kirby, J. P.; van Dantzig, N. A.; Chang, C. K.; Nocera, D. G. *Tetrahedron Lett.* **1995**, *36*, 3477-3480.
8. Rosenthal, J.; Hodgkiss, J. M.; Young, E. R.; Nocera, D. G. *J. Am. Chem. Soc.* **2006**, *128*, 10474-10483.
9. Izutsu, K. *Acid-base Dissociation Constants in Dipolar Aprotic Solvents*; Blackwell Scientific: Cambridge, USA, 1990.
10. Ireland, J. F.; Wyatt, P. A. H. *Adv. Phys. Org. Chem.* **1976**, *12*, 131-160.
11. Shizuka, H. *Acc. Chem. Res.* **1985**, *18*, 141-147.
12. Arnaut, L. G.; Formosinho, S. J. *J. Photochem. Photobiol. A.* **1993**, *75*, 1-20.
13. Tolbert, L. M.; Solntsev, K. M. *Acc. Chem. Res.* **2002**, *35*, 19-27.
14. Weller, A. *Z. Elektrochem.* **1952**, *56*, 662-668

15. Pranata, J.; Wierschke, S. G.; Jorgensen, W. L. *J. Am. Chem. Soc.* **1991**, *113*, 2810-2819.

16. Uchimaru, T.; Korchowiec, J.; Tsuzuki, S.; Matsumura, K.; Kawahara, S. *Chem. Phys, Lett.* **2000**, *318*, 203-209.

17. Lukin, O.; Leszczynski, J. *J. Phys. Chem. A* **2002**, *106*, 6775-6782.

18. Lukin, O.; Leszczynski, J. *J. Phys. Chem. A* **2003**, *107*, 9251-9252.

19. Schlund, S.; Schmuck, C.; Engels, B. *J. Am. Chem. Soc.* **2005**, *127*, 11115-11124.

20. Hodgkiss, J. M.; Rosenthal, J.; Nocera, D. G. in *Handbook of Hydrogen Transfer. Physical and Chemical Aspects of Hydrogen Transfer*, Hynes, J. T., Klinman, J. P., Limbach H.-H., Schowen, R. L., Eds.; Wiley-VCH: Weinheim, Germany, 2006; vol. 2.4.17, pp 503-562.

21. Rosenthal, J.; Hodgkiss, J. M.; Young, E. R.; Nocera, D. G. *J. Am. Chem. Soc.* **2006**, *128*, 10474-10483.

22. Connors, K. A. In Binding Constants: A Measurement of Molecular Complex Stability; Wiley: New York, 1987.

23. Izutsu, K. *Acid-base Dissociation Constants in Dipolar Aprotic Solvents*; Blackwell Scientific: Cambridge, USA, 1990.

24. The p*K*a range reported for each BM are as follows: acetate (**4**) p*K*a = 20-22; chloroacetate (**5**) p*K*a = 15-19; and, dichloroacetate (**6**) p*K*a = 13-15. The pKa of phenylsulfonate (**3**) is estimated to be 8 from vales for p-toluenesulfonic acid, p*K*a = 8 and 2.5-dichlorobenzenesulfonic acid, p*K*a = 6.2-6.4.

25. Marcus, Y. In *Ion Solvation*; Wiley:Chichester, 1985, pp 136-137.

26. Marcus, Y. In I*on Solvation*; John Wiley: Chichester, 1985, pp 136.

27. Young, E. R.; Rosenthal, J.; Nocera, D. G. *Chem. Commun.* **2008**, 2322-2324.

28. W. L. F. Armarego and D. D. Perrin, in *Purification of Laboratory Chemicals*; Butterworth-Heinmann: Oxford, 4th ed. 1996.

29. Connors, K. A. In *Binding Constants: A Measurement of Molecular Complex Stability*; Wiley: New York, 1987.

Chapter IV

Comparison of ionized versus non-ionized interface architecture in uni-directional PCET systems

Parts of this Chapter have been published:

Young, E. R.; Rosenthal, J.; Hodgkiss, J. M.; Nocera, D. G. *J. Am. Chem. Soc.* **2009**, ASAP article.

Chapter IV

IV.1. Introduction and goals

Insight to the tautomeric configuration of the assembled interfaces provided by the amidinium purpurin, **P**, in Chapter III drives mechanistic studies on PCET kinetics in model systems with special attention to the configuration of the proton interface and the manner in which interface ionization modulates PCET kinetics and parameters. **P** establishes a spectroscopic handle capable of reporting the static tautomeric structure of the proton interface, specifically whether the interface exists as a *non-ionized* amidine carboxylic acid interface or an *ionized* amidinium carboxylate.[1, 2]

The networks established for PCET studies described in this Chapter are formed via association of the protonic groups appended to De and Ae to form a hydrogen bonded interface between a Zn(II) porphyrin De (**D1**) appended with an amidinium functionality and a naphthalene diimide Ae bearing either a carboxylate (**A1**) or sulfonate (**A2**) functionality. In contrast to symmetric interfaces[3,4] or those that cannot support PT,[5,6] the asymmetric nature of the amidine-carboxylic acid (or amidinium-sulfonate) interface underscores the importance of the proton configuration on PCET[7 - 11] by adding a dipole component to the proton interface.[12,13] Proton fluctuations within the asymmetric interface couple to the charge shift accompanying ET through the polarization of the surrounding environment.[14-24] Even in the absence of PT, fluctuations of the proton position within the interface profoundly influence the kinetics of the ET component of PCET.[11,25]

The static configuration of the proton interface in each dyad is at the heart of these kinetic studies. The Zn(II) porphyrin donor, **D1**, is joined to the naphthalene diimide acceptor by a *non-ionized* amidine-carboxylic acid in the case of **A1** and by an *ionized* amidinium-sulfonate interface in the case of **A2**, thus allowing for studies on a homologous De-Ae pair juxtaposed by interfaces of differing ionization. In undertaking kinetic measurements on this De-Ae pair, the influence of interface architecture, specifically the static proton interface configuration, on PCET dynamics is considered. This Chapter augments previous PCET and isotope kinetics measurements performed by Dr. Justin Hodgkiss on **D1**:**A1** in an effort to directly compare the influence of the static interface ionization on PCET.[10,11]

IV.2. Homologous De-Ae assemblies with differing proton interface structures

*IV.2.1. Amidinium-appended Zn(II) porphyrin donor (**D1**) and two naphthalene diimide acceptors appended with a carboxylate or a sulfonate functionality*

The supramolecular D---[H^+]---A dyads designed for comparative PCET kinetics investigations (Scheme IV.1) are formed from the association of a Zn(II) porphyrin-amidinium donor, **D**, to naphthalene diimide acceptors **A1** and **A2**. Synthesis of all three compounds was performed by Dr. Joel Rosenthal following the synthetic protocol outlined his Thesis and were provided for use in these kinetic studies.

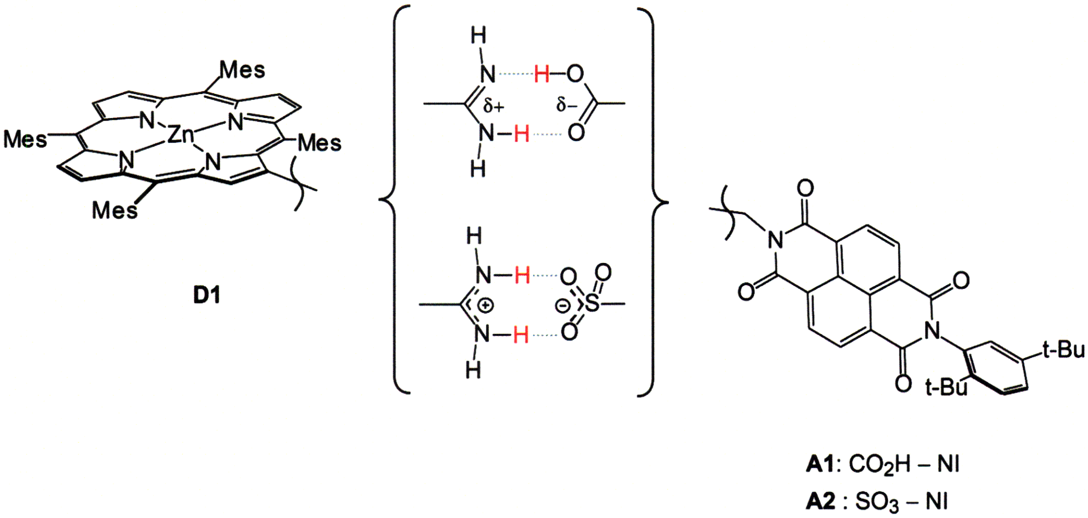

Scheme IV.1. **D1**, **A1**, and **A2**. De-Ae assembly juxtaposed by a *non-ionized* amidine-carboxylic acid interface and an *ionized* amidinium-sulfonate interface.

IV.2.2. Characterization of hydrogen bonding

Supramolecular D---[H$^+$]---A dyads containing **D1** and the two naphthalene diimide acceptors form a well-defined two-point hydrogen bond that possesses favorable primary and secondary electrostatic interactions.[26] A signature of this hydrogen bonding association is the downfield shift of amidinium protons involved in hydrogen bonding (NH_{ax}) and an insensitivity of the chemical shift of the amidinium protons external to the salt bridge (NH_{eq}). As demonstrated by Dr. Joel Rosenthal the ^1H NMR spectrum for the Ni(II) derivative of the **D1**:**A1** complex in 2-MeTHF,[10] the NH_{ax} protons move downfield from 10.6 to 12.4 ppm upon their hydrogen bonding association to the carboxylate, whereas the chemical shift of the NH_{eq} protons changes by <0.05 ppm. A similar downfield shift in the ^1H NMR spectrum of **D1** induced by the addition of **A2** (from 10.6 to 12.1 ppm) in THF confirms that binding in the **D1**:**A2** dyad occurs through the two-point hydrogen bond (as opposed to axial ligation) of the amidinium-sulfonate interface. ^{1}H NMR binding experiments were performed by Dr. Joel Rosenthal and are presented in his Thesis.

Due to the propensity of the amidinium-amidine functionality to bind axially to the Zn(II) porphyrin, the choice of solvent is critical in enforcing a two-point hydrogen bond as the only structure for dyad assembly. The solvent THF binds axially to Zn(II) porphyrins thereby preventing porphyrin aggregation caused by axial ligation of the amidine to the Zn(II) porphyrin. The association of **D1** to **A1** in 2-MeTHF has been demonstrated by Dr. Justin Hodgkiss and is found to have an association constant of K_{assoc}(**D1**:**A1**) = 2.8 × 10^4 M^{-1}. The association constant is obtained from an analysis of the ratio of pre-exponential factors of the fit TE decay curves of **D1** with varying concentrations of **A1**.[11]

*IV.2.3. K_{assoc} for **D1:A** assemblies*

Measurements reported in this Chapter are performed in THF, and association constants for **D1**:**A1** and **D1**:**A2** are dually reevaluated. The static fluorescence quenching from the porphyrin chromophore is monitored upon titration of **D1** with **A1**. A fit of the emission intensity to the Benesi-Hildebrand equation yields K_{assoc}(**D1**:**A1**) = 2.4 × 10^4 M^{-1} (THF, 298 K),[10] which closely matches the value derived from the ratio of pre-exponential factors of the bound:unbound lifetimes of **D1**.[27] As expected, K_{assoc}(**D1**:**A1**) in 2-MeTHF and THF are similar. With the validity of the TE lifetime method established, the binding of **D1** to **A2** is determined by analysis of the pre-exponential factors of

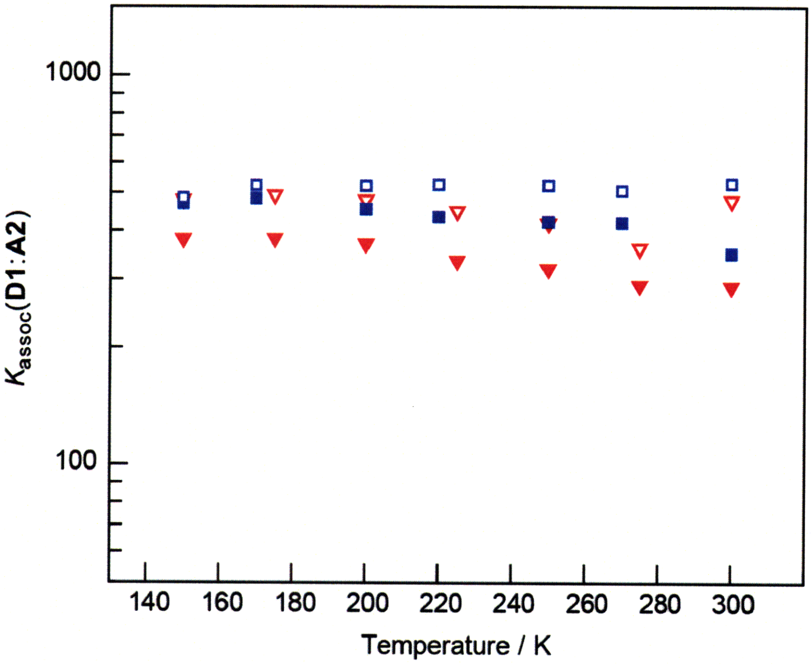

Figure IV.1. Variable-temperature binding constant for **D1**:**A2**. K_{assoc} is plotted for both protonated and deuterated interfaces in THF, **D1-H**:**A2** (▼) and **D1-D**:**A2** (▽), and 2-MeTHF, **D1-H**:**A2** (■), **D1-D**:**A2** (□). Over the operative temperature range, K_{assoc}, remains constant indicating the dyad remains bound.

the emission lifetime decay curves to yield K_{assoc}(**D1**:**A2**) = 2.9 × 10^2 M^{-1} in THF. The ratio of pre-exponential factors remains similar from 150 to 300 K indicating that **A2** remains bound to **D1** throughout the sampled temperature range employed for subsequent kinetics studies (Figure IV.1).

*IV.2.4. Proton interface structure for **D1:A1** and **D1:A2** assemblies*

Characterization of amidinium-appended purpurin, **P**, presented in Chapter III enables assignment of the proton interface configuration in dyads **D1**:**A1** and **D1**:**A2**. **P** has been titrated with a series of carboxylate and sulfonate appended **BMs** to determine the protonation state of the bound amidinium within the assembled interfaces as a function of pK_a value of the BM. The series of **BMs** reveals the manner in which the balance between the pK_a values of the constituent acids and electrostatic interactions within the interface conspire to produce either an ionized or non-ionized interface in THF.[1,2] The results show that **D1**:**A1** dyads are bridged by a *non-ionized amidine-carboxylic acid* interface while **D1**:**A2** dyads are concatenated by an *ionized amidinium-sulfonate* interface (Scheme IV.1).

IV.2.5. Electrochemistry

The electrochemical potentials of **D1** and **A1** in THF (298K) have been reported by Dr. Justin Hodgkiss. Cyclic voltammetry is utilized to yield $E_{1/2}(\mathbf{D1}^{2+/+})$ = 1060 mV and $E_{1/2}(\mathbf{A1}^{-/2-})$ = −520 mV vs. Ag/AgCl. Cyclic voltammetry performed on **A2** yields a one-electron electrochemical potential of $E_{1/2}(\mathbf{A2}^{-/2-})$ = −508 mV vs. Ag/AgCl. The similarity of the reduction potentials obtained for **A1** and **A2** yield ET driving forces that are very similar for the two dyads: ΔG_{ET}(**D1**:**A1**) = −0.58 eV and ΔG_{ET}(**D1**:**A2**) = −0.59 eV.

IV.3. Transient absorption spectroscopy on D1:A2

TA spectroscopy on **D1** and **D1**:**A2** dyads is necessary in order to verify that ET and not energy transfer or other nonradiative mechanisms is operative in the **D1**:**A2** dyads. Following excitation of the $Q_{1,0}$ band of **D1** at λ_{ex} = 560 nm, a broad TA feature of the porphyrin S_1 excited state is superimposed on bleaching features at 562 and 602 nm that arise from the loss of the ground-state Q-band absorptions. Single-wavelength TA kinetics in this region show decay profiles arising from intersystem crossing to the T_1 excited state, which can obscure the spectral signatures of PCET intermediates (specifically, the porphyrin radical cation, λ_{max} = 412 and 637 nm;[11] and the diimide radical anion, λ_{max} = 475 and 610 nm[28]). Clear observation of the ET intermediate is made possible by an isosbestic point in the S_1-T_1 TA spectrum of unbound **D1**, which provides a dynamic-free background for single-wavelength observation of the porphyrin radical cation, as has been demonstrated in early studies of **D1**:**A1**.[10,11] Following on the method established by Dr. Niels Damrauer and Dr. Justin Hodgkiss, the optical TA signature attributed to the CS state for the **D1**:**A2** dyad is monitored at the isosbestic point, λ_{obs} = 654 nm.

Figure IV.2 plots the single-wavelength TA kinetics profiles measured at λ_{obs} = 654 nm for **D1** and dyad **D1**:**A2** in THF. The dynamics of charge separation are superimposed on the flat S_1-T_1 absorption profile arising from unbound **D1**. Based on K_{assoc}(**D1**:**A2**) in THF (K_{assoc}(**D1**:**A2**) =3.5×10^2 M^{-1}), at least 25% of the **D1** is bound by **A2** at the concentrations used for TA experiments. The single-wavelength TA kinetics trace of the **D1**:**A2** dyad shows a small shoulder feature which subsequently decays. A biexponential fit to the data is performed by fixing one lifetime component to the forward ET lifetime (τ_{em} = 420 ps), which was obtained by time resolved fluorescence quenching experiments (Section IV.4). Fitting of the data in this manner yields k_{ET}(forward) = 2.4×10^9 s^{-1} (298 K) for the growth of the transient signal and k_{ET}(back) = 3.3×10^9 s^{-1} (298 K) for the disappearance of the transient signal.

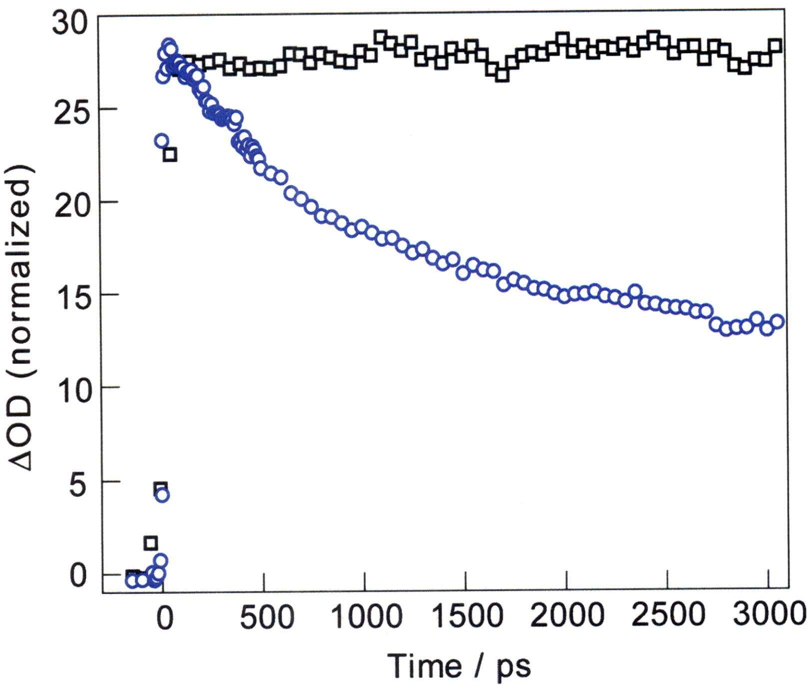

Figure IV.2. Single-wavelength TA profile of **D1** and **D1**:**A2**. The TA profiles for **D1** (□) and **1**:**A2** dyad (○) are taken at the $S_1 \rightarrow T_1$ isosbestic point of **1**, λ_{obs} = 654 nm.

Details of the kinetic analysis are provided in Appendix A. A comparison of the ET rates for the two dyads reveals that both rate constants for **D1**:**A2** are significantly faster than the corresponding rate constants recorded for **D1**:**A1**, k_{ET}(forward) = 0.9 × 10^9 s^{-1} (2-MeTHF, 298 K) and k_{ET}(back) = 1.4 × 10^9 s^{-1} (2-MeTHF, 298 K).[10] For **D1**:**A2**, k_{ET}(back) >> k_{ET}(forward), which leads to a situation in which accumulation of the CS intermediate is not significant. For this reason, the growth component of the TA signal is obscured. Kinetic modeling of the TA signal upon variation of k_{ET}(back) with k_{ET}(forward) fixed to τ_{em} = 420 ps is presented in Appendix B to justify the observed single-wavelength TA signal. At the experimental concentrations employed and for the case in which k_{ET}(back) >>

k_{ET}(forward), the growth of a CT intermediate TA signal appears as a shallow rise with subsequent decay instead of the distinct rise and decay reported for **D1**:**A1**. The shallow rise is a general characteristic of faster ET kinetics with k_{ET}(back) > k_{ET}(forward).

IV.4. Transient emission spectroscopy for variable-temperature and kinetic isotope-dependence measurements in THF

With ET established as the primary excited-state quenching mechanism for the **D1:A2** dyad, TE spectroscopy was employed to perform variable-temperature and isotopic labeling studies on the De-Ae dyads. Exchange of the labile amidinium protons with deuterium enables isotope-dependent studies of PCET. TE experiments provide a more easily employed, modular means of data collection and thus are the method of choice for further kinetics studies on **D1** and **D1:A2**. A temperature range of 300 K to 150 K was employed for variable-temperature studies.

IV.4.1. TE fitting of D---[H$^+$]---A decay traces to establish K_{assoc}

The association constant, K_{assoc}, is determined at ambient temperatures as outlined in Section IV.2.3 as is the validity of the method utilizing pre-exponential components of biexponentially fit data to determine K_{assoc}.[27] Variable-temperature measurements are outlined in this section for the De-Ae dyads and **D1** bound to a non-quenching moiety. However, before analysis of variable-temperature kinetic data, it is critical to verify that the dyads remain bound as the temperature is decreased. To achieve this verification, the binding constant is presented at each temperature by using the ratio of the pre-exponential amplitudes of the fitted TE data method. TE data is fit for **D1**:**A2** in both THF and 2-MeTHF over the temperature range of interest. These same fitting results are utilized in Section IV.4.3 to determine the quenching rate. The results of careful biexponential fitting reveals that the ratio of pre-exponential factors remains similar from 150 to 300 K, yielding similar values for K_{assoc} (Figure II.1) and verifying that **A2** remains bound to **D1** throughout the sampled temperature range discussed.

IV.4.2. TE Control experiments

Prior to PCET kinetic studies on the **D1**:**A2** dyad, control experiments on

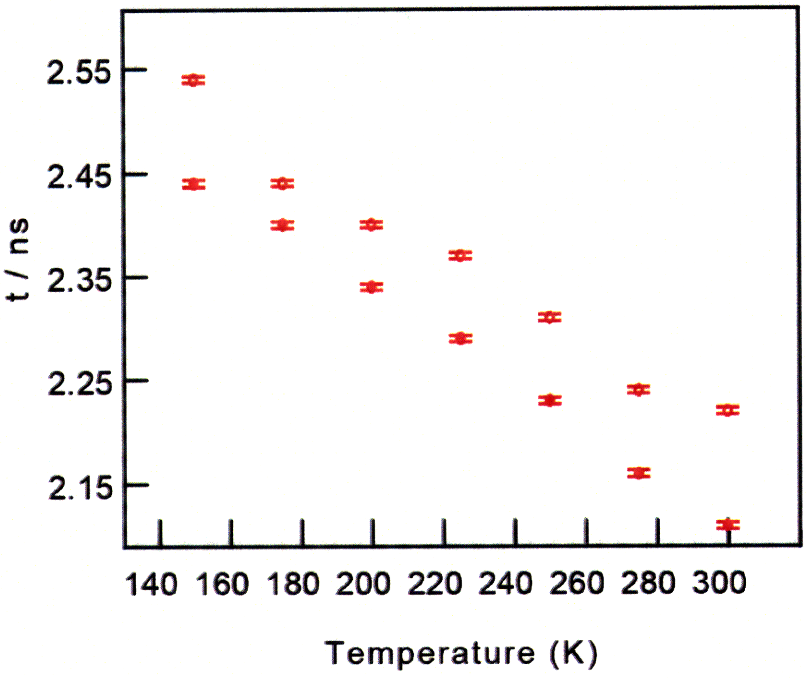

Figure IV.3. Temperature dependence of **D1-H** and **D1-D** lifetimes. The transient emission spectroscopy for **D1-H** (●) and **D1-D** (○) is performed in THF.

D1 and **D1** bound to a non-quenching BM are necessary in THF in order to verify the temperature and kinetic isotope dependence of the **D1**. The emission lifetimes of **D1-H** (protonated amidinium on **D1**) and **D1-D** (deuterated amidinium on **D1**) in THF increase linearly with decreasing temperature as shown in Figure IV.3. At all temperatures, the emission lifetime of **D1-H**(**D**) is shorter than the parent Zn(II) TMP compound (data not shown).[11] These results are in accordance with previous temperature dependence studies on Zn(II) porphyrins in 2-MeTHF.[11, 29] The functional dependence observed for **D1-H**(**D**) and Zn(II) TMP indicates that the ISC process itself is thermally activated. Electronic perturbation to the porphyrin macrocycle introduced by the amidinium functionality leads to shorter emission lifetimes of **D1-H** relative to the reference Zn(II) TMP, which assuming the triplet quantum yield does not change, indicates that the amidinium functionality accelerates ISC in **D1**.[11]

A small kinetic isotope effect (KIE) for unbound **D1** is found in THF where the **D1-D** reveals a slightly longer lived emission lifetime than **D1-H**. The isotope dependence arises from coupling between the nuclear and electronic degrees of freedom of the porphyrin excited state involving the internal vibrations of the amidinium modes. The observed KIE suggests that coupling to internal vibrational modes facilitates ISC to the triplet state or nonradiative decay to the ground state **D1-H**. Measured emission lifetimes depend on the product of the natural radiative lifetime and the quantum yield of fluorescence.

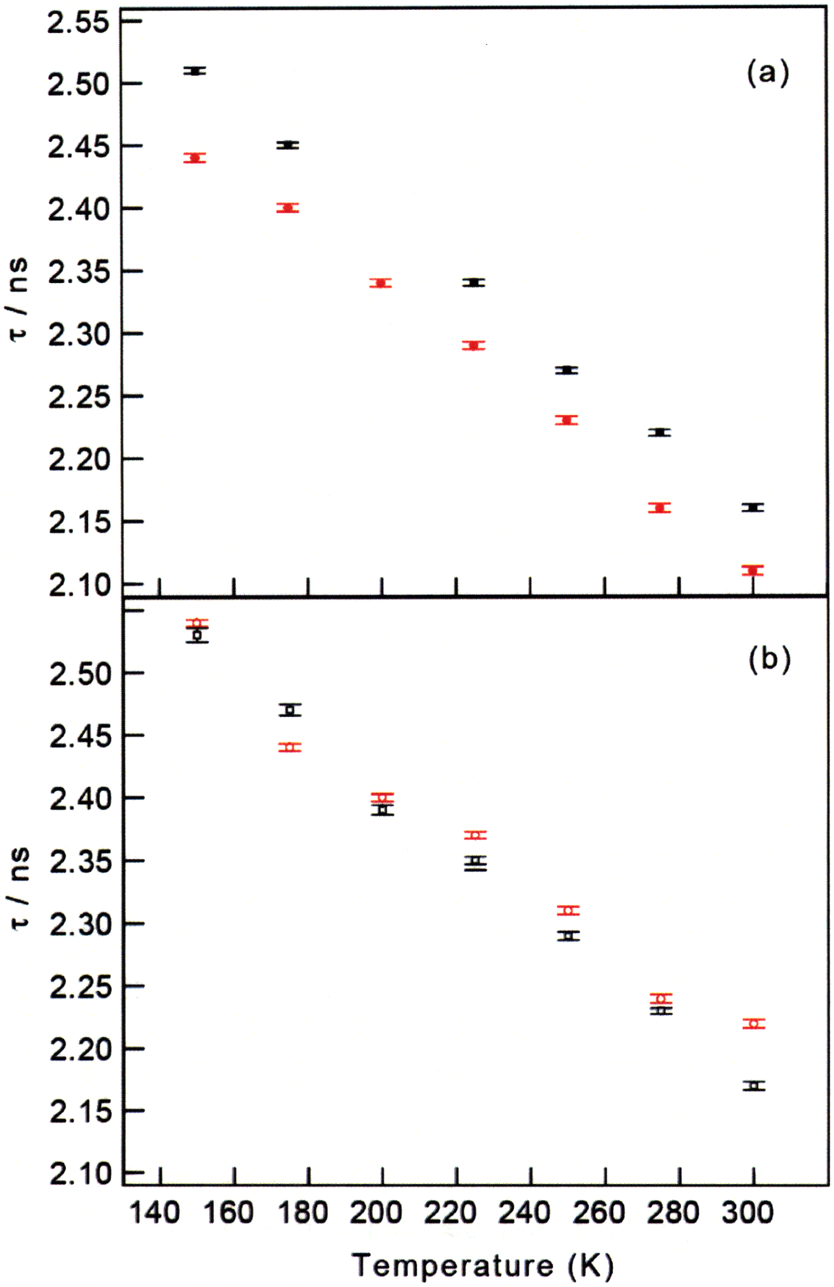

Figure IV.4. Temperature dependence of **D1-H** and **D1-D** lifetimes bound by PS. (a) Temperature dependence of **D1-H** (●) lifetimes compared to that of the bound species **D1-H:PS** (■) in THF, (b) temperature dependence of **D1-D** (○) lifetimes compared to the lifetimes of the bound species **D1-D:PS** (□) in THF

Subsequent control experiments entail introduction of a hydrogen bonding moiety to the amidinium functionality of **D1** in order to form a proton interface for which the bound moiety is not capable of quenching the excited state of **D1**. Both benzoate (**B**) and phenylsulfonate (**PS**) bind efficiently to **D1**, but are not capable of quenching the S_1 excited state of **D1** via electron or energy transfer. The **D1-H(D):B** and **D1-H(D):PS** dyads allow the dynamics of **D1** to be ascertained in the presence of a two-point hydrogen bond but in the absence of excited state deactivation due to PCET dynamics. As a result, either **D1** or **D1:PS** lifetimes can be used to determine the quenching rates. The relatively small shifts in the absorption and emission spectra of **D1** upon binding of **B** or **PS** indicate relatively weak coupling between the porphyrin ring and the appended moiety as a result of the cant angle of the amidinium relative to the plane of the porphyrin ring (~76°).[30]

The temperature dependence of the lifetimes of the **D1-H(D):B** and **D1-H(D):PS** dyads correspond well with the temperature dependence of **D1** alone. All lifetime versus temperature plots show similar slopes, indicating that formation of the two-point hydrogen bond does not affect the excited state dynamics of the Zn(II) porphyrin amidinium. Variable-temperature and kinetic isotope-dependent lifetimes of **D1-H(D):B** were performed by Dr. Justin Hodgkiss and are reported in his Thesis and in published work on this topic.[11] The complementary variable-temperature and kinetic isotope-dependent studies on **D1-H(D):PS** are reported in this Thesis as presented in Figure IV.4. The general behavior displayed in Figure IV.4 is in excellent agreement with the previously reported variable-temperature studies of **D1:B**.[11] In those studies, as in the **D1-H:PS** studies, the emission lifetimes of the bound species are longer. The amidinium protons of the bound porphyrin are restricted, which reduces their contributions to nonradiative decay pathways therefore increasing the emission lifetimes.

The opposite trend is observed for a portion of the **D1-D**:**PS** series, for which some of the bound **D1-D**:**PS** lifetimes are slightly shorter than the unbound species. In the control samples, both bound and unbound **D1** are present and contribute to the observed deactivation of the S_1 state. Because the two lifetimes (bound and unbound) are expected to be very similar, fitting the data to a biexponential decay function, in accordance with typical fitting procedures for cases in which two species are present in a sample, is problematic. For this reason, a monoexponential fit is used for fitting and it must be noted that the reported emission lifetime represents not only the bound **D1**, but also the unbound **D1**. The problematic fitting procedure may contribute to error in the fitting and lead to the unexpected **D1-D**:**PS** results.

IV.4.3. Transient emission experiments on D- - -[H$^+$]- - -A dyads

In contrast to temperature- and kinetic isotope-dependence studies on **D1**, **D1**:**B** and **D1**:**PS**, the TE decay profile is dramatically perturbed when **D1** is bound to **A1** or **A2**. Emission decays of **D1-H**(**D**):**A1** and **D1-H**(**D**):**A2** exhibit a biexponential decay functional, which are fit with one time constant fixed to the unquenched lifetime of **D1-H**(**D**) and the second lifetime varied to obtain the best fit. The lifetime of unbound unquenched **D1** is independently determined as describe in Section IV.3 for all temperatures at which PCET measurements were made. Both the unquenched and the quenched time constants are used to determine the forward rate of PCET using the relation,

$$k_{\mathrm{PCET}} = \frac{1}{\tau_{\mathrm{D1\text{-}H(D):Q}}} - \frac{1}{\tau_{\mathrm{D1\text{-}H(D)}}} \qquad \text{(IV.1)}$$

where **Q** = **A1** or **A2**. Figure IV.5 plots k_{PCET} values versus temperature for the protonated PCET dyads **D1**:**A1** and **D1**:**A2** in THF. Deuterated data plotted in this manner has been omitted for clarity and appears in Figure IV.6. The kinetic data for **D1**:**A1** was collected and analyzed by Dr. Justin Hodgkiss.

IV.5. Semi-classical Marcus analysis

Temperature-dependent kinetic data can be analyzed using the semi-classical Marcus equation,[31]

$$k_{\mathrm{ET}} = \frac{2\pi}{\hbar}|V|^2 \sqrt{\frac{1}{4\pi\lambda_s k_B \mathrm{T}}} \exp\left[\frac{(\Delta G^\circ + \lambda_s)^2}{4\lambda_s k_B \mathrm{T}}\right] \qquad \text{(IV.2)}$$

The activation energy (E_a) of the PCET reaction is furnished by the slope of the kinetics results plotted in the Arrhenius form. The protonated and deuterated PCET kinetic data is presented in Figure IV.6 in an Arrhenius plot of the form $\ln(k_{\mathrm{ET}} \bullet \mathrm{T}^{1/2})$ versus 1/T,

$$\ln(k_{\mathrm{ET}}\sqrt{\mathrm{T}}) = \left[\frac{(\Delta G^\circ + \lambda_s)^2}{4\lambda_s k_B}\right] \bullet \left(\frac{1}{\mathrm{T}}\right) - \ln\left[\frac{2\pi}{\hbar}|V|^2 \sqrt{\frac{1}{4\pi\lambda_s k_B}}\right] \qquad \text{(IV.3)}$$

and is fitted with the semi-classical Marcus formalism. The calculated E_a values (Table IV.1) are small relative to the PCET driving force (ΔG^o), which is known for all systems (Table IV.1). The total solvent reorganization energies, λ_s, are determined from the slope of the linear Arrhenius fit when the driving force for ET is known.[11] The values for the reorganization energy range from λ_s= 0.80 - 0.93 eV for **D1-H**(**D**):**A1** and **D1-H**(**D**):**A2** (THF). These λ_s values match well with a calculated reorganization energy comprising an outer-sphere reorganization energy of λ_o ~ 0.8 eV (r_{DA} distance of 13 Å, and ionic radii of 5 and 4 Å for the donor (**D1**) and naphthalene diimide acceptors **A1** and **A2**, respectively) and inner-sphere solvent reorganization contributions of λ_i ~ 0.2 - 0.3 eV for Zn(II) porphyrin donor-diimide acceptor systems.[32,33] With ΔG^o and λ_s determined, the

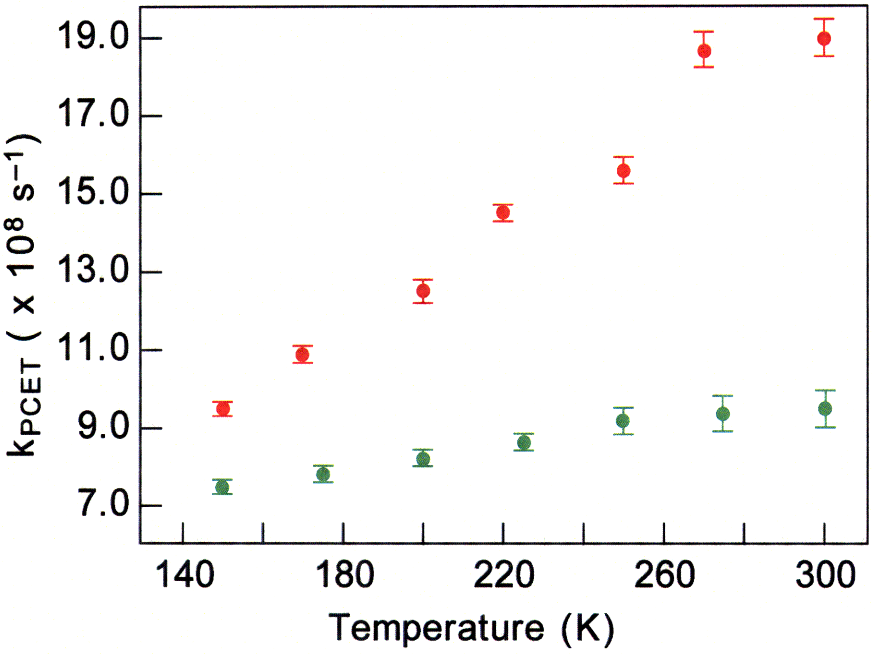

Figure IV.5. Temperature dependence of the PCET rate for **D1-H**:**A1** and **D1-H**:**A2** dyads. The rates for **D1-H**:**A1** (●) and **D1-H**:**A2** (●) are recorded in THF.

electronic coupling matrix element, $|V|$ is evaluated from the y-intercept of the linear fit as per equation IV.3.[11] The values of $|V|$ listed in Table IV.1 ($|V|$ ~1.9 - 4.5 cm^{-1}) are smaller than the corresponding values determined for covalently bound systems of similar architectural design and molecular topology ($|V|$ ~ 10's cm^{-1}).[32,33]

Linear Arrhenius behavior is observed (Figure IV.6) and a distinct isotope effect (KIE) is apparent for each sample. Observation of a KIE indicates that the photo-induced ET is sensitive to nuclear motions within the intervening proton interface. Over the temperature range sampled, **D1-H(D)**:**A1** and **D1-H(D)**:**A2** in THF show an average KIE of 1.07 and 1.22, respectively.

Table IV.1. Thermodynamic and kinetic parameters measured for **D1**:**A1** and **D1**:**A2**.

Dyad	Solvent	ΔG^o /eV^{a,b}	E_a /eV^b	λ_s /eV^b	$\|V\|^b$ /eV [cm–1]	KIE
D1-H:A1	THF	–0.58	$1.56(9) \times 10^{-2}$	0.80(1)	$3.0(2) \times 10^{-4}$ [2.4(2)]	1.07(1)
D1-D:A1	THF	–0.58	$1.72(5) \times 10^{-2}$	0.82(1)	$3.1(2) \times 10^{-4}$ [2.5(2)]	
D1-H:A2	THF	–0.59	$2.8(2) \times 10^{-2}$	0.91(4)	$5.6(9) \times 10^{-4}$ [4.5(8)]	1.22(2)
D1-D:A2	THF	–0.59	$3.1(2) \times 10^{-2}$	0.93(4)	$5.6(9) \times 10^{-4}$ [4.5(8)]	

[a] Calculation using the expression $\Delta G° = E_D^{ox} - E_A^{red} - E_{ex} + \Delta G(\varepsilon_S)$ where E_D^{ox} is the oxidation potential of **D1**, E_A^{red} is the reduction potential of the acceptor, **A1** or **A2**, E_{ex} is the excited state energy of **D1** and $\Delta G(\varepsilon_S)$ is the solvent-dependent Coulombic term. $\Delta G(\varepsilon_S)$ is calculated from the Born equation for $\varepsilon_S = 7.52$ (295 K), a De-Ae distance of 13 Å, and ionic radii of 5 and 4 Å for **D1**, and the acceptors, **A1** and **A2** to yield $\Delta G(\varepsilon_S) = -0.12$ eV. [b] Assuming $\Delta G°$ is temperature-independent, obtained from fitting results to the semi-classical Marcus equation.

IV.6. Discussion and theoretical interpretation

Comparison of variable-temperature and kinetic isotope-dependent PCET kinetics for **D1:A1** and **D1:A2** enable an insightful analysis of ET as mediated by hydrogen bonded interfaces with differing proton configuration. The internal charge of the ionized amidinium-sulfonate interface of **D1:A2** induces a pre-organized solvent structure about the proton interface, leading to stronger coupling of the static proton interface to the solvent prior to ET. Upon ET, larger fluctuations within the interface of the amidinium-sulfonate interface are expected, which contribute to larger solvent reorganization energies. The amidinium-sulfonate interface is, to some extent, able to transiently form an

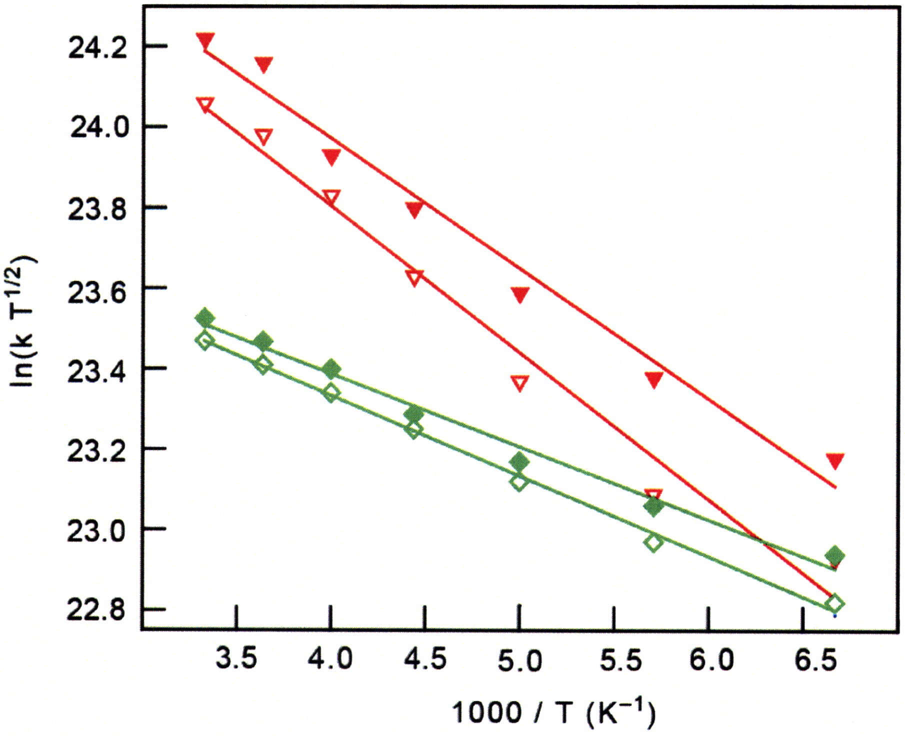

Figure IV.6. Arrhenius plot of PCET rates. The temperature dependence of the PCET rates are plotted in an Arrhenius form for **D1-H:A1** (◆), **D1-D:A1** (◇), **D1-H:A2** (▼) and **D1-D:A2** (▽) in THF.

amidine-sulfonic acid configuration, and in so doing facilitate ET (with larger PT motion). In contrast, the amidine-carboxylic acid interface of **D1:A1** cannot undergo the complementary adjustment to facilitate ET, as carboxylic acid will not accept another proton under these conditions, even transiently. The divergent ability of the two interfaces to transiently adjust the internal proton configuration to accommodate the charge transfer during ET underlies the subtle difference between the two systems, which produces faster PCET rates for **D1:A2**. The enhanced coupling to the solvent is reflected in a larger reorganization energy for **D1:A2** as compared to **D1:A1**. Additionally, the ionized interface may form a tighter De-Ae pair, thus increasing the coupling constant. The larger Franck-Condon term is offset by greater electronic coupling, thus leading to an overall enhancement in the PCET rate constant for **D1:A2**.

The influence of PCET, specifically of the intervening hydrogen bonds, are revealed when **D1:A1** and **D1:A2** are compared to a closely related system in which the donor and acceptor sites are covalently bound. The proton interface between De-Ae moieties retards ET rates by over two orders of magnitude, an effect that is primarily ascribed to attenuation of the electronic coupling constant, $|V|$. The values of $|V|$ tabulated in Table IV.1 (3.0 – 5.6 cm^{-1}) are 10-fold smaller than those inferred for covalently bound analogues.[11,29,34-36] This observation is affirmed by $|V|$ values of ~ 4 cm^{-1} to 12 cm^{-1} reported for other hydrogen bonded D---[H^+]---A architectures involving three point hydrogen bonded Watson-Crick base pairs.[34-38]

Disparate coupling of the two interfaces to the solvent is also revealed by the KIE. Control experiments show the KIE is constant for **D1-H** and **D1-D** over the temperature range sampled, and although the average KIE for **D1-H(D):A1** and **D1-H(D):A2** are 1.07 and 1.22, respectively, the KIE does in fact change slightly with decreasing temperature. Previous studies of the **D1-H(D):A1** dyad in 2-MeTHF performed by Dr. Justin Hodgkiss revealed a KIE behavior for temperature-dependent PCET rates that lead to crossover and inversion of the KIE at lower temperatures[11], a phenomenon that had also been encountered previously by other researchers [39]. This unusual phenomenon was attributed to the freezing out of hydrogen vibrational modes within the interface as temperature decreases. Fluctuations within the hydrogen bonding bridge dynamically modulate electronic coupling for ET, and consequently the rate of charge-separation becomes sensitive to the nature of proton modes within the bridge. The non-parallel slopes in the KIE data of **D1-H(D):A1** and **D1-H(D):A2** in THF show the opposite trend to reports in 2-MeTHF, leading to a ~7% and ~9% increase in KIE over the temperature range sampled. This KIE trend is in contrast to previously reported KIE data reported for **D1-H(D):A1** in 2-MeTHF, which yields a decrease in KIE of ~18% over a similar temperature range.[11] The KIE trend for **D1-H(D):A1** and **D1-H(D):A2** in THF is typical of predictions made by conventional PCET theory.[24,40] The molecular differences between solvents used in these two studies emerges as a contributing factor in dictating the temperature- and KIE-dependent behavior and are the focus of research efforts presented in Chapter V.

IV.7. Conclusion

Variable temperature and kinetic isotope-dependent studies are presented for the hydrogen bonded **D1:A1** and **D1:A2** dyads to contrast PCET occurring between a similar De and Ae pair juxtaposed by either a non-ionized or an ionized interface. Comparison of the PCET dynamics and parameters for **D1:A1** and **D1:A2** underscores the sensitivity of ET through hydrogen bonds to the surrounding environment. Both **D1:A1** and **D1:A2** maintain a specific asymmetric two-point hydrogen bonded interface joined via N---H---O hydrogen bonding that mediates ET between a Zn(II) porphyrin, **D1**, and naphthalene diimide moieties, **A1** or **A2**. The driving force for ET varies by only 0.03 eV among the **D1-H(D)**:**A1** and **D1-H(D)**:**A2** dyads, which precludes the attribution of the observed changes in PCET behavior to a simple driving force effect. The nature of the static interface configuration (*non-ionized* or *ionized*) in **D1:A1** and **D1:A2** emerges as the primary factor towards modulating the observed temperature- and kinetic isotope-dependent behavior of PCET in these systems. The ionized interface is shown to couple more strongly to the solvent in its static configuration, which leads to a higher λ_s upon ET, but through the ability of the ionized amidinium-sulfonate interface to induce greater proton fluctuations or even formal PT concomitant with ET, along with the tighter interface of the ionized charge pair, the electronic coupling is augmented and leads to faster ET rates.

IV.8. Experimental

IV.8.1. Materials

D1[41] and **A1**[10] were prepared by Dr. Joel Rosenthal according to previously published methods and **A2** was synthesized by Dr. Joel Rosenthal as described in his Thesis. Solvents for synthesis were of reagent grade or better and were dried according to standard methods.[42] Spectroscopic experiments employed tetrahydrofuran (THF) (Spectroscopic grade), which was dried using standard methods and stored under vacuum.

IV.8.2. Electrochemistry

Electrochemical experiments were carried out using a Bioanalytical Systems (BAS) Model CV-50W potentiostat/galvanostat. Cyclic voltammetry (CV) and differential pulse voltammetry (DPV) were performed in a two-compartment cell using a glassy carbon disk as the working electrode, a Ag/AgCl reference electrode and a platinum wire auxiliary electrode. The supporting electrolyte used for electrochemistry experiments was either 0.1 M *n*-tetrabutylammonium hexafluorophosphate ($TBAPF_6$) or perchlorate (TBAP). The solution in the working compartment of the cell was deaerated using nitrogen. Background CVs of the electrolyte solution were recorded prior to addition of the solid sample. Redox couples were referenced to SCE by using a ferrocenium/ferrocene internal standard of 0.307 V vs. SCE.[43]

IV.8.3. Spectroscopic sample preparation

Steady-state and TA spectroscopy was performed on samples contained in a high-vacuum cell comprising a 1-cm or 2-mm pathlength clear fused-quartz cuvette (Starna cells) connected to a 10-cm^3 solvent reservoir via a graded seal. High-vacuum Teflon valves were used to seal the cell from the environment and the cuvette from the solvent reservoir.

For TA, one aliquot of **D1** (1×10^{-7} mol) was added to the cuvette and a two-equivalent aliquot of **A2** (2×10^{-7} mol) was added to the solvent reservoir. The cell was evacuated under high-vacuum (10^{-5} Torr) to remove the transferring solvent and to leave the two compounds in their separated compartments. One-half milliliter of dry THF was added to the solvent reservoir by high vacuum transfer and the solvent was subject to three cycles of freeze-pump-thaw. The cell was sealed from the environment and removed from the high vacuum manifold. Single-wavelength TA experiments were first performed on unbound **D1** under vacuum using resonant excitation of the Q-band at 560 nm. The isosbestic point ($\lambda_{\text{isosbestic}}$ = 654 nm) for singlet-triplet conversion yield was verified. At this wavelength, the intensity of the TA spectrum was invariant and thus provided the best wavelength for detecting PCET transients.[10] Subsequently, the Teflon stopper between the cuvette and solvent reservoir was opened and the two compounds were mixed while maintaining vacuum inside the cell to allow for study of the **D1**:**A2** dyad.

Samples for variable-temperature experiments were prepared following a detailed procedure outlined previously.[11] To summarize, one aliquot (1×10^{-7}

mol) of **D1-H** was dissolved in a minimal amount of THF and transferred to a borosilicate short-stem glass ampoule (Kimble-Kontes). Prior to the transfer, a few drops of D_2O were added to samples for deuterium isotopic exchange experiments. The samples were sealed from the atmosphere, shaken and left for 15 minutes before being transferred to the ampoule. The neck of the ampoule had been stretched with a flame to reduce the diameter and allow for easier sealing after high vacuum manipulations. Addition of 4 equivalents of **B**, 4 equivalents of **A1,** 8 equivalents of **PS** or 8 equivalents of **A2** were added for control and quenching experiments. The ampoule containing the sample was attached to a high vacuum adaptor. The transferring solvents were removed on a high vacuum manifold ($< 10^{-6}$ Torr) and the sample remained under vacuum for at least 2 hours to remove any residual water. One milliliter of dry THF was added to the ampoule by vacuum transfer and was subject to at least three cycles of freeze-pump-thaw. The ampoule was then flame-sealed while the solvent remained frozen. The high-vacuum manipulations were necessary to ensured that the samples remained free from exposure the environment or water, which disrupts the hydrogen bonding between the dyads.

IV.8.4. Spectroscopic measurement

Steady-state absorption spectra were obtained using a Spectral Instruments 440 Series spectrophotometer. Steady-state emission spectra were recorded on an automated Photon Technology International (PTI) QM 4 fluorimeter equipped with a 150 W Xe arc lamp and a Hamamatsu R928 photomultiplier tube.

The excitation source for TA and TE measurements was a chirped-pulse amplified Ti:Sapphire laser system that has been described elsewhere.[10] In this experiment, the 150-fs, 800-nm output of the regenerative amplifier was frequency-upconverted in a visible OPA (BMI Alpha-1000) to produce a 1 kHz pulse train of excitation pulses at 560 nm for resonant excitation of the Q-band of **D1**. The excitation was vertically polarized and attenuated to 50 - 250 nJ/pulse.

Single-wavelength TA experiments were performed with the pump beam mechanically chopped at 500 Hz. The probe beam was spectrally resolved in a Jobin-Yvon Triax 320 monochromator, which was used to select a single-wavelength (2 nm) for measurement on an amplified photodiode. The probe beam served as an input signal for a digital lock-in amplifier (Stanford Research Systems SR830) locked to 500 Hz. Data was collected at 10 ps and 50 ps steps over a range of 3 ns and included some negative time points. The results of twenty forward and backwards scans along the stage were collected and averaged.

TE kinetics were measured on a Hamamatsu C4334 Streak Scope streak camera that has been described elsewhere.[44] The emission was collected at the magic angle (θ_m = 54.7°) over a 140-nm window centered on the emission peak. A 10-ns or a 20-ns time base was used.

Temperature-dependent lifetimes of **D1-H(D)** alone and bound to **B**, **PS**, **A1** and **A2** measured over a temperature range of 120-300 K. Experiments were repeated at least 3 times with newly prepared samples. Variable-temperature measurements were carried out based on measurements performed by Dr. Niels

Damrauer and Dr. Justin Hodgkiss in a similar manner.[11] A modular cryogenic refrigeration system (Air Products and Chemicals) consisting of a single stage helium compressor (model 1RO2A) connected via hoses to an expander module (model DE-202) with a heating element and temperature controller (Scientific Instruments, 9600-5) was interfaced with a custom-made computer program in order to automate the temperature control settings. The expander module is housed within in laboratory interface (model DMX-1) consisting of a vacuum shroud with glass windows for fluorescence spectroscopy in a right-angle configuration and is continuously pumped to maintain a vacuum ($\sim 10^{-4}$ Torr). The ampoule containing the sample is mounted on a copper block and the thermocouple was calibrated at three temperatures: liquid nitrogen (77 K), an ice bath (273 K) and ambient temperature (293 K).

Data acquisition was automated for the variable-temperature experiments. The temperature controller and streak camera were synchronized to enable data collection throughout the entire temperature range. Luminescence measurements were made after a 20 minute wait time during which the temperature was adjusted and the sample was allowed to equilibrate. This cycle occurred for each temperature data point, which was typically 10-25 K apart. Each sample was cycled through the entire temperature range 4 times in different sequences to ensure that the data was independent of the sequence

IV.8.5. Data fitting

TE lifetimes were determined from streak camera data analysis by integrating 15-nm or 13-nm, or 40-nm or 50-nm slices of the emission peaks centered at 612 and 655 nm, for **D1**:**A1** and **D1**:**A2** respectively, and fitting to a monoexponential decay function. Temperature dependent lifetimes of **D1-H(D)**:**A1** and **D1-H(D)**:**A2** were measured at the same temperature points and the data was fit in the same manner, except that the data was fit to a biexponential decay function with the longer lifetime component fixed to the lifetime obtained from the control experiment, **D1-H(D)**, at each temperature.

IV.9. References

1. Rosenthal, J.; Hodgkiss, J. M.; Young, E. R.; Nocera, D. G. *J. Am. Chem. Soc.* **2006**, *128*, 10474-10483.
2. Young, E. R.; Rosenthal, J.; Nocera, D. G. *Chem. Commun.* **2008**, 2322-2324.
3. Turró, C.; Chang, C. K.; Leroi, G. E.; Cukier, R. I.; Nocera, D. G. *J. Am. Chem. Soc.* **1992**, *114*, 4013-4015.
4. de Rege, P. J. F.; Williams, S. A.; Therien, M. J. *Science* **1995**, *269*, 1409-1413.
5. Sessler, J. L.; Wang, B.; Springs, S. L.; Brown, C. T. In *Comprehensive Supramolecular Chemistry*; Murakami, Y., Ed.; Pergamon Press: Oxford, 1996; Vol. 4, pp. 311-336 and references therein.
6. Chang, C. J.; Brown, J. D.; Chang, M. C. Y.; Baker, E. A.; Nocera, D. G. In *Electron Transfer in Chemistry*; Balzani, V., Ed.; Wiley-VCH: Weinheim, Germany, 2001; Vol 3.2.4, pp 409-461.
7. Roberts, J. A.; Kirby, J. P.; Nocera, D. G. *J. Am. Chem. Soc.* **1995**, 117, 8051-8052.
8. Roberts, J. A.; Kirby, J. P.; Wall, S. T.; Nocera, D. G. *Inorg. Chim. Acta*, **1997**, 263, 395-405.

9. Roberts, J. A.; Kirby, J. P.; Nocera, D. G. *J. Am. Chem. Soc.* **1997**, 119, 9230-9236.

10. Damrauer, N. H.; Hodgkiss, J. M.; Rosenthal, J.; Nocera, D. G. *J. Phys. Chem. B* **2004**, 108, 6315-6321.

11. Hodgkiss, J. M.; Damrauer, N. H.; Pressé, S.; Rosenthal, J.; Nocera, D. G. *J. Phys. Chem. B.* **2006**; 110, 18853-18858.

12. Cukier, R. I.; Nocera, D. G. *Annu. Rev. Phys. Chem.* **1998**, 49, 337-369.

13. Hodgkiss, J. M.; Rosenthal, J.; Nocera, D. G. In *Hydrogen-Transfer Reactions*; Hynes, J. T.; Klinman, J. P.; Limbach, H.-H.; Schowen, Eds; Wiley-VCH: Weinheim, Germany, 2007; Vol 2.17, pp 503-561.

14 . Cukier, R. I. *J. Phys. Chem.***1996**, *100*, 15428-15443.

15. Cukier, R. I. *J. Phys. Chem.* **1994**, *98*, 2377-2381.

16. Zhau, X. G. Cukier, R. I. *J. Phys. Chem.* **1995**, *99*, 945-954.

17. Cukier, R. I. *J. Phys. Chem. A* **1999**, *103*, 5989-5995.

18. Cukier, R. I. *Biochim. Biophys. Acta* **2004**, *1655*, 37-44.

19. Hammes-Schiffer, S. In *Electron Transfer in Chemistry*; V. Balzani, Ed., Wiley-VCH: Weinheim, Germany, 2001, Vol. 1.1.5, p. 189.

20. Hammes-Schiffer, S. *Acc. Chem. Res.* **2001**, *34*, 273-281.

21. Hammes-Schiffer, S. Iordanova, N. *Biochim. Biophys. Acta* **2004**, *1655,* 29-36.

22. Soudackov, A. Hammes-Schiffer, S. *J. Chem. Phys.* **1999**, *111*, 4672-4687.

23. Soudackov, A.; Hammes-Schiffer, S. *J. Chem. Phys.* **2000**, *113*, 2385-2396.

24. Decornez, H.; Hammes-Schiffer, S. *J. Phys. Chem. A.* **2000**, *104*, 9370-9384.

25. Pressé, S.; Silbey, R. *J. Chem Phys.* **2006**, 124, 164504-164511.

26. Pranata, J.; Wierschke, S. G.; Jorgensen, W. L. *J. Am. Chem. Soc.* **1991**, *113*, 2810-2819.

27. *K*assoc = *Q*(*Q* + 1)/([**A**]0(*Q* + 1) - [**D1**]0Q), where *Q* is the ratio of the pre-exponential factors of the short (bound) and long (unbound) components, which also corresponds to the ratio [**D1**:**A2**]/[**D1**].

28. Rogers, J. E.; Kelly, L. A. *J. Am. Chem. Soc.* **1999**, 121, 3854-3861

29. Winters, M. U.; Pettersson, K.; Martensson, J.; Albinsson, B. *Chem. Eur. J.* **2005**, *11*, 562-573.

30. Damrauer, N. H.; Hodgkiss, J. M.; Rosenthal, J.; Nocera, D. G. *J. Phys. Chem. B* **2004**, 108, 6315-6321.

31. Marcus, R. A.; Sutin, N. *Biochem. Biophys. Acta* **1985**, *811*, 265-322.

32. Archer, M. D.; Gadzekpo, V. P. Y.; Bolton, J. R.; Schmidt, J. A.; Weedon, A. C. *J. Chem. Soc. Faraday Trans. 2* **1986**, *82*, 2305-2313.

33. Gaines, G. L., III; O'Neil, M. P.; Svec, W. A.; Niemczyk, M. P.; Wasielewski, M. R. *J. Am. Chem. Soc.* **1991**, *113*, 719-721.

34. Osuka, A.; Yoneshima, R.; Shiratori, H.; Okada, S.; Taniguchi, S.; Mataga, N. *Chem. Commun.* **1998**, 1567-1568.

35. Harrison, R. J.; Pearce, B.; Beddard, G. S.; Cowan, J. A.; Sanders, J. K. M. *Chem. Phys.* **1987**, *116*, 429-448.

36. Davis, W. B.; Ratner, M. A.; Wasielewski, M. R. *J. Am. Chem. Soc.* **2001**, *123*, 7877-7886.

37. Sessler, J. L.; Wang, B.; Harriman, A. *J. Am. Chem. Soc.* **2003**, *115*, 10418-10419.

38. Sessler, J. L.; Sathiosatham, M.; Brown, C. T.; Rhodes, T. A.; Wiederrecht, G. *J. Am. Chem. Soc.* **2001**, *123*, 3655-3660.

39. Cape, J. L.; Bowman, M. K.; Kramer, D. M. *J. Am. Chem. Soc.* **2005**, *127*, 4208-4215.

40. Hammes-Schiffer, S.; Hatcher, E.; Ishikita, H.; Skone, J. H.; Soudackov, A. V. *Coord. Chem. Rev.* **2008**, *252*, 384-394.

41. Yeh, C.-Y.; Miller, S. E.; Carpenter, S. D.; Nocera, D. G. *Inorg. Chem.* **2001**, *40*, 3643-3646.

42. Armarego, W. L. F.; Perrin, D. D. *Purification of Laboratory Chemicals*, 4th Ed.; Butterworth-Heinmann: Oxford, 1996.

43. Bard, A. J.; Faulkner, L. R. *Electrochemical Methods. Fundamentals and Applications*; John Wiley: New York, 1980.

44. Loh,, Z. H.; Miller, S. E.; Chang, C. J.; Carpenter, S. D.; Nocera, D. G. *J. Phys. Chem. A* **2002**, *106*, 11700-11708.

Chapter V

Molecular variation to the solvent influences PCET: Comparison of ionized versus non-ionized interfaces

Parts of this Chapter have been published:

Young, E. R.; Rosenthal, J.; Hodgkiss, J. M.; Nocera, D. G. *J. Am. Chem. Soc.* **2009**, ASAP article.

V.1. Introduction

ET and PCET processes examined in this Thesis occur within the confines of a solvent environment.[1 - 12] The nature of the surrounding environment, specifically solvent properties such as dielectric constant, refractive index and hydrogen bonding capability are critical in modulating the ET or PCET event.[13-18] In fact, Marcus Theory for ET specifically addresses electrostatic contributions of the solvent to the rate of the ET in the Marcus-Levich equation. The solvent reorganization energy, λ_s, describes the energetic penalty paid to reorient the solvent molecule dipoles in order to accommodate the CS state generated by the ET reaction. The value for λ_s is expressed as a function of the solvent dielectric constant, the solvent refractive index and the distance of charge separation generated between the De and Ae moieties in the CS state as described in equation V.1,

$$\lambda_s = 14.4\left(\frac{1}{2r_D}+\frac{1}{2r_A}-\frac{1}{d_{DA}}\right)\times\left(\frac{1}{\eta}-\frac{1}{\varepsilon_s}\right) \tag{V.1}$$

The variables r_D and r_A are the ionic radii of the donor and acceptor, respectively, d_{DA} is the De-Ae separation, η is equal to the refractive index of the solvent squared, and ε_s is the dielectric constant of the solvent. Thus for ET, when the dielectric constants and refractive indices[19] of two solvents are similar, for a given De-Ae pair, the contribution of λ_s to the ET rate is predicted to be comparable.

PCET occurring through two-point hydrogen bonded networks between **D1** and the pair of acceptors, **A1** and **A2**, is more complex than simple ET because solvent reorganization occurs in response not only the charge separation between the De and Ae, as in ET; but also in response to the transient proton fluctuations within the hydrogen bonded interface that occur in concert with ET (Scheme V.1).[20-31] Additional λ_s contributions arise from pre-existing coupling of the solvent to the proton interface: the *non-ionized* interface for **D1**:**A1** dyads or the *ionized* interface for **D1**:**A2**.

The presence of the proton interface may elicit more complex solvent interactions not accounted for by the typical Marcus dielectric continuum model for ET. Specifically, molecular variation to the solvent may influence PCET more strongly than anticipated based on typical ET theory as a result of the additional interactions between the solvent molecules and the hydrogen bonded interface. Towards this end, a solvent-dependence comparison of PCET is described for the **D1**:**A1** and **D1**:**A2** systems in this Chapter. A set of solvents with comparable dielectric constants that contain a moderate molecular modification are utilized.

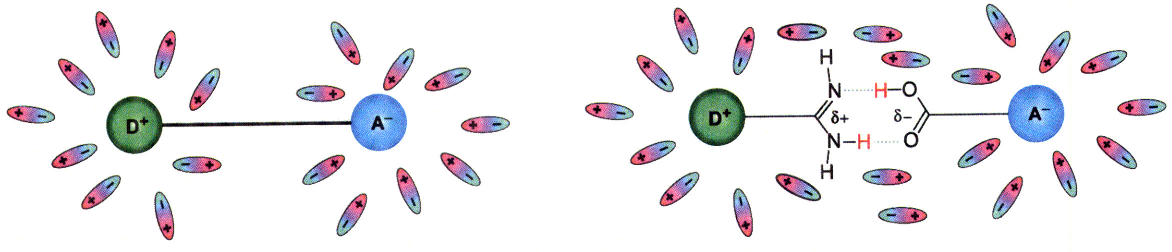

Electron Trasfer CS State

Proton-Coupled Electron Trasfer CS State

Scheme V.1. Solvent dipoles organized around ET or PCET CS state. Cartoon depiction of solvent organization around a typical ET De-Ae CS state (left) compared to the more structured reorganization required to accommodate the CS state of a PCET De-Ae system (right).

The solvent pair is THF and 2-MeTHF. These mechanistic studies extend previous variable-temperature and kinetic isotope measurements on the **D1**:**A1** dyad performed by Dr. Justin Hodgkiss in 2-MeTHF[10,11] and on the **D1**:**A1** and **D1**:**A2** pair in THF[10] (Chapter IV) in presenting variable-temperature and kinetic isotope studies on the **D1**:**A2** dyad in 2-MeTHF. The measurements for **D1**:**A2** in 2-MeTHF enable the influence of molecular variation between two solvents to be compared for the two PCET interface architectures. Surprisingly, the molecular modifications to the solvent produce divergent variable temperature and kinetic isotope behavior for the two D---[H^+]---A dyads indicating that PCET is modulated not only by the dielectric environment of the solvent but also by the molecular structure, particularly the hydrogen bonding ability, of the solvent (Scheme V.2).

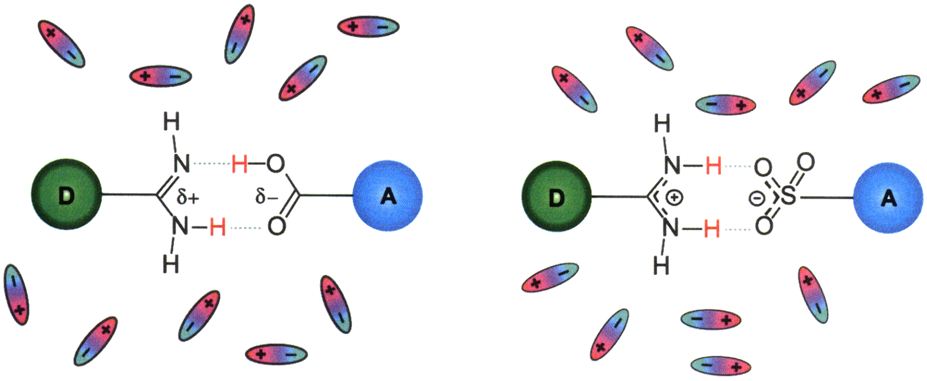

Scheme V.2. Solvent dipoles organized around a non-ionized and ionized proton interface. Cartoon depiction of the pre-existing solvent organization around PCET system joined by a *non-ionized* interface (left) and an *ionized* interface (right). The pre-existing solvent organization is more structured around the internal interface charges in the case of the *ionized* interface.

V.2. PCET dyads reviewed

The **D1**:**A1** and **D1**:**A2** dyads utilized in this Chapter are presented and characterized in Chapter IV. TA spectroscopy has been utilized as presented in Chapter IV to verify CT as the primary deactivation mechanism between the porphyrin donor and the naphthalene diimide acceptors and to provide forward and back ET rates. This Chapter presents TE spectroscopy exclusively to measure excited state decay and CT kinetics. Dr. Justin Hodgkiss has provided kinetic data for the **D1**:**A1** dyad in 2-MeTHF and THF. **D1**:**A2** is presented in Chapter IV (THF) and in this Chapter (2-MeTHF).

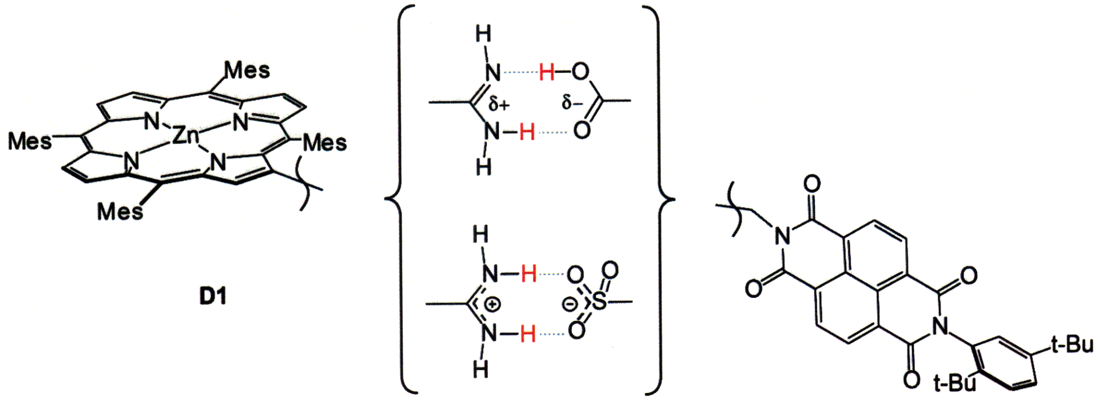

D1

A1: CO_2H – NI
A2 : SO_3 – NI

Scheme V.3. **D1**, **A1**, and **A2**. De-Ae assembly juxtaposed by a *non-ionized* amidine-carboxylic acid interface and an *ionized* amidinium-sulfonate interface for solvent-dependent PCET studies.

V.3. *Solvent-dependent PCET: Temperature- and isotope-dependence*

The solvents chosen for dyad assembly and spectroscopic interrogation are 2-MeTHF (ε_s = 6.97, 298 K) and THF (ε_s = 7.52, 295 K).[32] Both solvents bind axially to Zn(II) porphyrins and prevent porphyrin aggregation due to axial ligation of the amidine to the Zn(II) porphyrin. Using both static emission quenching and the ratio of pre-exponential factors of the fitted **D1** TE decay curves, association constants, K_{assoc}, for two-point bonding of the supramolecular dyads is determined. As reported in Chapter IV, K_{assoc}(**D1-H**:**A1**) = 2.8 × 10^4 M^{-1} (THF) and K_{assoc}(**D1-H**:**A2**) = 2.9 × 10^2 M^{-1} (THF).[10] In 2-MeTHF, K_{assoc}(**D1-H**:**A2**) = 3.5 × 10^2 M^{-1}, which matches closely to the association constant obtained for **D1**:**A2** in THF. As demonstrated by variable temperature TE measurements of the **D1**:**A2** dyad, association constants remains similar over the temperature range sampled indicating that the **D1-H**:**A2** dyads remain bound from 150 to 300 K.[10] Both 2-MeTHF and THF enforce the two-point hydrogen bond as the only structure for dyad assembly over the concentration and temperature ranges sampled in these PCET studies.

V.3.1. *Control experiments*

Transient emission experiments on unbound **D1** are performed at each temperature. The emission decay profile is fit to a monoexponential decay functional. The emission lifetimes of **D1-H** and **D1-D** in both 2-MeTHF and THF increase linearly with decreasing temperature as plotted in Figure V.1. As presented in Chapter IV, phenylsulfonate (**PS**) and benzoate (**B**) are employed to verify that simple binding of a hydrogen-bonding moiety incapable of electron or energy transfer to **D1-H(D)** does not significantly perturb the temperature-dependent behavior of the emission lifetime of **D1-H(D)**. Both **PS** and **B** bind efficiently to **D1** in 2-MeTHF and THF, but are unable to quench the S_1 excited state of **D1** via electron or energy transfer. Dyads of **1-H(D):PS** and **1- H(D):B** thus allow the dynamics of **D1** to be ascertained in the presence of a two-point hydrogen bond but in the absence of excited state deactivation due to PCET dynamics. The lifetime of the **D1-H(D):PS** and **D1-H(D):B** dyads (Figure IV.4) correspond well with the temperature dependence of **D1** alone, indicating that formation of the two-point hydrogen bond does not affect excited state deactivation of **D1**.

V.3.2. Temperature- and isotope-dependent PCET experiments

Binding of **A1** or **A2** to **D1** elicits dramatic quenching of the TE decay dynamics obtained in the control experiments. Emission decay profiles for the dyads of **D1-H(D):A1** and **D1-H(D):A2** exhibit a biexponential decay functionality. Biexponential fitting is performed with one time constant fixed to the unquenched lifetime of **D1-H(D)** at that temperature, and the second lifetime allowed to vary in order to obtain the best fit of the quenched component. Both the unquenched and quenched time constants are used to determine the forward rate of PCET using the relation,

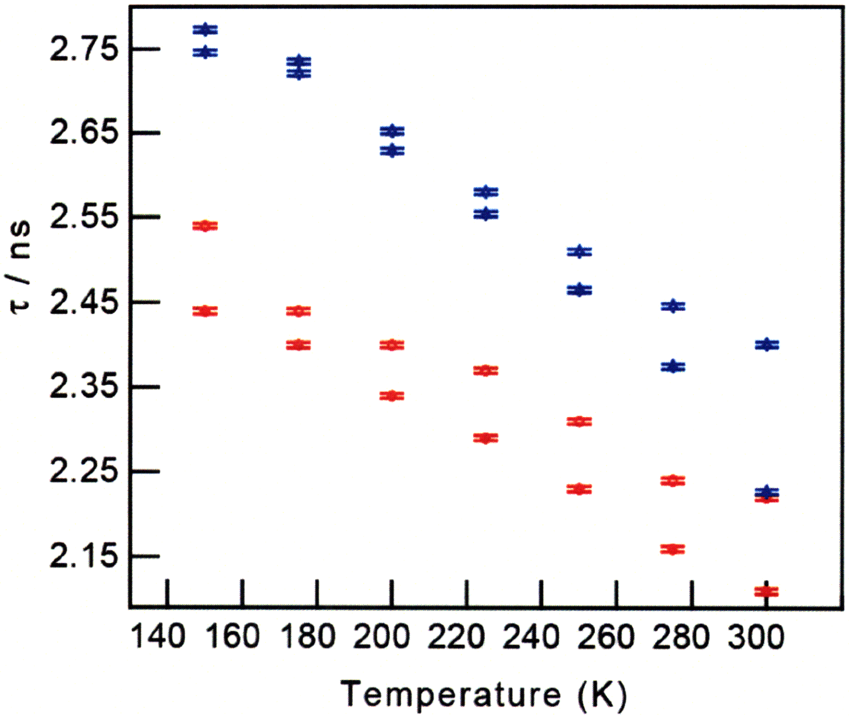

Figure V.1. Temperature dependence of **D1-H** and **D1-D** lifetimes in THF and 2-MeTHF. Transient emission spectroscopy for **D1-H** (▲, ●) and **D1-D** (△, ○) is carried out in 2-MeTHF (▲) and THF (●).

$$k_{\mathrm{PCET}} = \frac{1}{\tau_{\mathbf{D1\text{–}H(D):Q}}} - \frac{1}{\tau_{\mathbf{D1\text{–}H(D)}}} \qquad \text{(V.2)}$$

where **Q** = **A1** or **A2**. Figure V.2 shows a plot of k_{PCET} values versus temperature for protonated PCET dyads **D1**:**A1** and **D1**:**A2** in THF and 2-MeTHF. Deuterated data plotted in the same manner has been omitted from Figure V.2 for clarity and is presented in Figure V.3.

V.4. Semi-classical Marcus Theory analysis

Temperature-dependent kinetic data are analyzed using the semi-classical Marcus equation in a similar manner to the analysis presented in Chapter IV,[33]

$$k_{\mathrm{ET}} = \frac{2\pi}{\hbar}|V|^2 \sqrt{\frac{1}{4\pi\lambda_s k_B \mathrm{T}}}\exp\left[\frac{(\Delta G^\circ + \lambda_s)^2}{4\lambda_s k_B \mathrm{T}}\right] \qquad \text{(V.3)}$$

where E_a is the activation energy of the PCET event, ΔG° is the driving force for PCET, $|V|$ is the electronic coupling matrix element and λ_s is total reorganization energy.

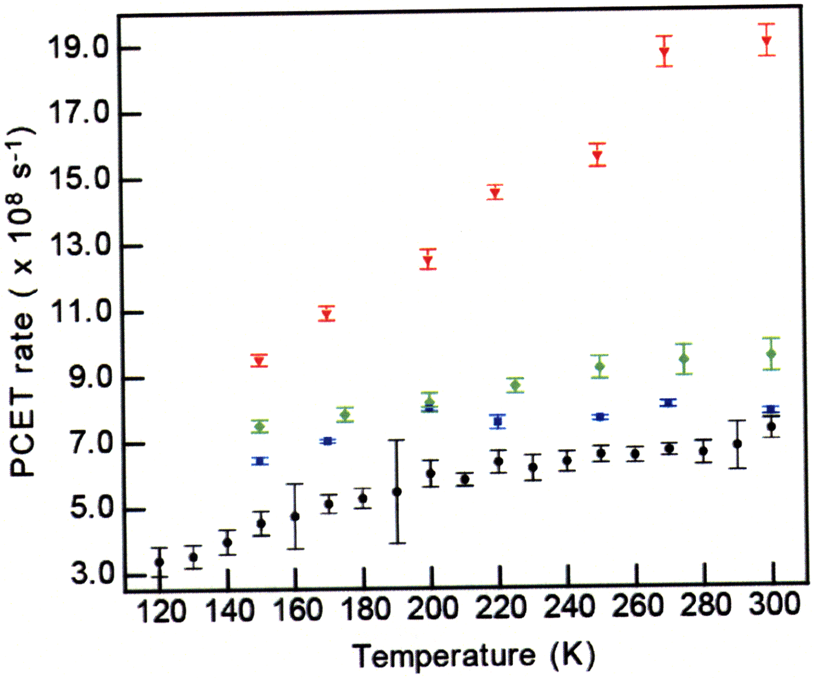

Figure V.2. Temperature dependence of the PCET rate for **D1-H:A1** and **D1-H:A2** dyads in THF and 2-MeTHF. The rates are recorded in 2-MeTHF, **D1-H:A1** (●) and **D1-H:A2** (■), and in THF, **D1-H:A1** (◆) and **D1-H:A2** (▼).

The various PCET parameters for the **D1:A1** and **D1:A2** dyads in 2-MeTHF are determined as outlined in Chapter IV and the values for each parameter are compiled in Table V.1. To summarize, the calculated E_a values (E_a

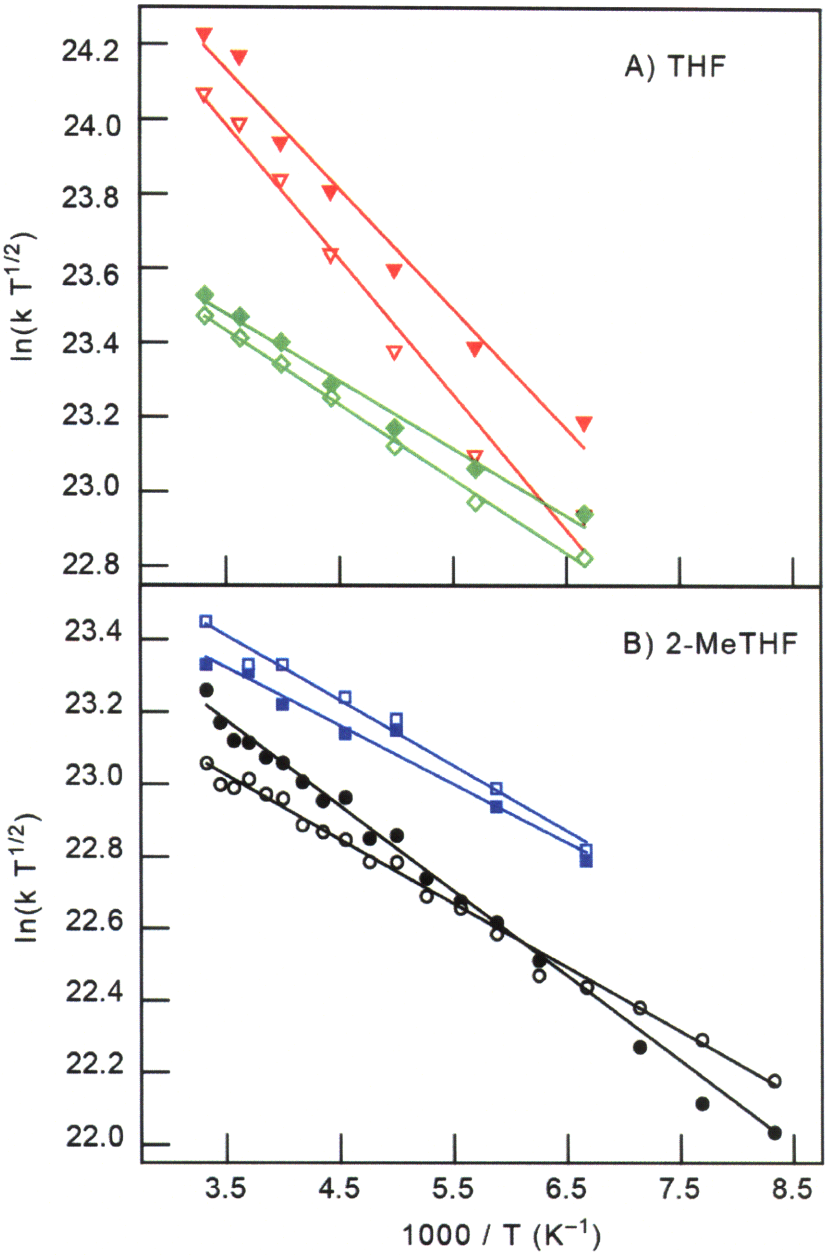

Figure V.3. Arrhenius plots of PCET rates. The temperature dependence of the PCET rates are plotted in an Arrhenius form for (A) **D1-H:A1** (◆), **D1-D:A1** (◇), **D1-H:A2** (▼), **D1-D:A2** (▽) in THF and for (B) **D1-H:A1** (●), **D1-D:A1** (○), **D1-H:A2** (■), **D1-D:A2** (□) in 2-MeTHF.

~ 0.01 – 0.03 eV) (Table V.1) are small relative to the PCET driving force (ΔG^o), which is known for all systems (ΔG^o ~ 0.56 – 0.59 eV). The values for λ_s range from λ_s =0.80 - 0.93 eV and match well with the calculated reorganization energy comprising an outer-sphere reorganization energy of λ_o ~ 0.8 eV (r_{DA} distance of 13 Å, and ionic radii of 5 and 4 Å for **D1** and **A1** and **A2**, respectively) and inner-sphere solvent reorganization contributions of λ_i ~ 0.2 - 0.3 eV for Zn(II) porphyrin donor-diimide acceptor systems.[34,35] With ΔG^o and λ_s determined for each dyad, the electronic coupling matrix element, $|V|$ are evaluated and listed in Table V.1. Values obtained for $|V|$ ($|V|$ ~1.9 - 4.5 cm^{-1}) are smaller than the corresponding values determined for covalently bound systems of similar architectural design and molecular topology ($|V|$ ~ 10's cm^{-1}).[32,33]

Figure V.3 presents the protonated and deuterated data for **D1-H(D):A1** and **D1-H(D):A2**, grouped by solvent, in an Arrhenius plot of the form $\ln(k_{PCET} \cdot T^{1/2})$ versus 1/T. The data is fit with the semi-classical Marcus formalism. The variable-temperature PCET kinetics in the two dyads show divergent behavior in the two solvents, despite similar dielectric constants. The clear variation between the ionized and non-ionized interface in THF is washed out when the two interface ionizations are compared in 2-MeTHF. The results may indicate that modulation of kinetics results from additional dyad-solvent interactions specific to the hydrogen bonds of interface.

Kinetic rates of the two dyads reveal a distinct isotope dependence in each solvent indicating that the photoinduced CT is sensitive to nuclear motions within the intervening proton interface. As reported by Dr. Justin Hodgkiss in his Thesis, **D1-H(D):A1** in 2-MeTHF exhibits disparate KIE behavior with variations

Table V.1. Thermodynamic and kinetic parameters measured for : and : in 2-MeTHF and THF.

Dyad	Solvent	ΔG^o /eV^{a,b}	E_a /eV^b	λ_s /eV^b	$\lvert V\rvert^b$ /eV [cm−1]	KIE
D1-H:A1	THF	–0.58	$1.56(9) \times 10^{-2}$	0.80(1)	$3.0(2) \times 10^{-4}$ [2.4(2)]	1.07(1)
D1-D:A1	THF	–0.58	$1.72(5) \times 10^{-2}$	0.82(1)	$3.1(2) \times 10^{-4}$ [2.5(2)]	
D1-H:A1	2Me-THF	–0.56	$2.03(6) \times 10^{-2}$	0.85	$3.0(2) \times 10^{-4}$ [2.4(1)]	0.87(1), 120 K
D1-D:A1	2Me-THF	–0.56	$1.53(9) \times 10^{-2}$	0.80	$2.4(1) \times 10^{-4}$ [1.9(1)]	1.22(1), 300 K
D1-H:A2	THF	–0.59	$2.8(2) \times 10^{-2}$	0.91(4)	$5.6(9) \times 10^{-4}$ [4.5(8)]	1.22(2)
D1-D:A2	THF	–0.59	$3.1(2) \times 10^{-2}$	0.93(4)	$5.6(9) \times 10^{-4}$ [4.5(8)]	
D1-H:A2	2Me-THF	-0.57	$1.4(1) \times 10^{-2}$	0.80(3)	$2.7(6) \times 10^{-4}$ [2.2(5)]	0.94(1)
D1-D:A2	2Me-THF	–0.57	$1.6(1) \times 10^{-2}$	0.82(3)	$3.0(6) \times 10^{-4}$ [2.4(2)]	

[a] Calculation using the expression $\Delta G^\circ = E_D^{ox} - E_A^{red} - E_{ex} + \Delta G(\varepsilon_S)$ where E_D^{ox} is the oxidation potential of the donor, **D1**, E_A^{red} is the reduction potential of the acceptor, **A1** or **A2**, E_{ex} is the excited state energy of **D1** and $\Delta G(\varepsilon_S)$ is the solvent-dependent Coulombic term. $\Delta G(\varepsilon_S)$ is calculated from the Born equation for 2-MeTHF (ε_S = 6.97, 298 K) and THF (ε_S = 7.52, 295 K), a D–A distance of 13 Å, and ionic radii of 5 and 4 Å for the donor, **D1**, and acceptor, **A1** and **A2** to yield $\Delta G(\varepsilon_S) = -0.10$ eV, 2-MeTHF and $\Delta G(\varepsilon_S) = -0.12$ eV, THF. [b] Assuming ΔG° is temperature-independent, obtained from fitting results to the semi-classical Marcus equation.

in temperature.[11] In the high-temperature regime (300 K), KIE (k_H/k_D) ~ 1.22(1) whereas in the low-temperature regime (120 K), the isotope dependence inverts to KIE ~ 0.87(1). As presented in Chapter IV, the KIE for **D1-H(D):A1** and **D1-H(D):A2** in THF do not invert over the temperature range studied and in fact, the KIE increases slightly with decreasing temperature. In contrast to these previous results, PCET rates for **D1-H(D):A2** in 2-MeTHF yield an inverted KIE at all temperatures visited. To summarize, the average KIE for these samples are: **D1-H(D):A1** (THF) = 1.07(1); **D1-H(D):A2** (THF) = 1.22(2); **D1-H(D):A2** (2-MeTHF) = 0.94(1). All four sets of variable temperature kinetic isotope data produce linear Arrhenius behavior.

V.5. Discussion

V.5.1. Solvent dependent kinetic behavior

Comparison of variable-temperature PCET kinetics for **D1:A1** and **D1:A2** in THF and 2-MeTHF form the basis for a solvent-dependent analysis of ET mediated by hydrogen bonds in interfaces of differing proton configuration. Typical solvent dependent studies for ET involve variation of the solvent dielectric constant to probe the role of the dielectric continuum in modulating CT kinetics. The molecular dyads **D1:A1** and **D1:A2** necessitate use of solvents that axially bind to the Zn(II) amidinium porphyrin in order to discourage axial binding of the amidinium-amidine functionality that lead to deleterious aggregation of **D1**. A different manner of solvent variation is explored for PCET kinetics studies on **D1:A1** and **D1:A2**. The dielectric constant does not change significantly, but significant molecular differences between THF and 2-MeTHF can promote various solvent-dyad interactions. 2-MeTHF and THF both fulfill the restrictive solvent criteria of this system in that both solvents bind axially to the Zn(II) amidinium porphyrin and have similar dielectric constants (THF, $\varepsilon_s = 7.52$, 295 K; 2-MeTHF, $\varepsilon_s = 6.97$, 298 K). The molecular difference between the solvents lies in the presence or absence of the methyl group on the tetrahydrofuran ring. The underlying causes of the divergent behaviors for **D1**:**A1** and **D1**:**A2** in the two solvents may be attributed to this molecular difference. The methyl group in 2-MeTHF sufficiently modifies the specific nature of its intermolecular interactions with the proton interface. For example, the oxygen atom is less available to act as a hydrogen bond acceptor in 2-MeTHF, the lower symmetry makes it a glass-forming solvent at low temperature, and the dielectric relaxation time constant is altered.[36,37]

The results of variable-temperature isotope experiments are summarized in Figure V.2. As presented in Chapter IV, the two static ionization configurations between the De-Ae assembly produce divergent PCET kinetic behavior as a result of strong interactions between the interface and the solvent. The variation in PCET parameters is washed out between the two configurations when the same experiments are performed in 2-MeTHF, such that little difference between the D1:A1 and D1:A2 dyads is observed.

Comparison of the variable-temperature PCET dynamics, which yield values for $|V|$ and λ_s for **D1**:**A1** and **D1**:**A2** (Table V.1), underscores the sensitivity of CT through hydrogen bonds to the surrounding solvent environment and highlight the subtle effects that are brought about by considering the pre-existing structural conformation within the proton interface. The data reveals that PCET is dramatically affected by molecular changes to the solvent even when the dielectric environment is similar. Both **D1**:**A1** and **D1**:**A2** maintain a specific asymmetric two-point hydrogen bonded interfaces joined via N---H---O hydrogen bonding that mediates CT between the Zn(II) porphyrin De and naphthalene diimide Ae. And, the driving force for ET varies by only 0.03 eV among the **D1-(H/D)**:**A1** and **D1-(H/D)**:**A2** dyads, which eliminates simple driving force effects on PCET behavior. Similar dielectric environments presented by the solvents also preclude typical solvent dielectric continuum based reasoning for the divergent behavior of the dyads in the two solvents. In short, the nature of the static configuration (*non-ionized* or *ionized*) of the protonic interface in **D1**:**A1** and **D1**:**A2** and the molecular differences between 2-MeTHF and THF emerge as two prominent factors that modulate the observed solvent-dependent and variable-temperature behavior of PCET in these systems.

Based on the molecular variation between THF and 2-MeTHF, solvent molecules access the proton interface of the D–A dyad to varying degrees thereby modulating their influence on the PCET event. For the amidinium-sulfonate interface of **D1**:**A2**, both the ionization within the interface and the more flexible nature of the De-Ae bridge imparted by tetrahedral sulfur of the sulfonate component may be two factors that augment sensitivity of the PCET rate to molecular changes in the solvent. These effects appear to be attenuated by the more rigid, *non-ionized* amidine-carboxylic acid interface of **D1**:**A1**. The internal charge of the *ionized* amidinium-sulfonate interface of **D1:A2** induces a more structured pre-existing solvent configuration about the proton interface than the *non-ionized* interface of **D1:A1** as depicted by the representation of the solvent dipoles shown in Scheme V.2. Concomitant with ET through the hydrogen-bonded bridge, vibrations within the interface induced by the ET event or even formal PT in the case of **D1:A2** occur within the pre-organized solvent environment. These effects are borne out in THF, but are attenuated in 2-MeTHF. The cause of divergent behavior lies in binding of the solvent to **D1**, but more importantly in the solvent interaction with the proton interface. The appended methyl group, which reduces the hydrogen bond accepting nature of the oxygen atom, limits the exposure of the solvent to the proton interface for the case of 2-MeTHF thereby attenuating pre-existing solvent organization. With the solvent interaction limited in this way, 2-MeTHF does not elicit the differing dynamics for ET between the non-ionized interface of **D1:A1** and the ionized interface of **D1:A2** that are obtained in THF. It is clear that the molecular differences between THF and 2-MeTHF conspire to influence PCET kinetics. A series of plausible explanations are presented, but the exact reasons for the solvent dependent behavior remain unresolved.

V.5.2. Disparate KIE behavior

A distinct KIE emerges for variable-temperature PCET kinetics that reveal differing trends between the two solvents. These trends are likely due to subtle changes within the hydrogen bonded interface and variation of coupling between the interface and the solvent. For **D1-H(D):A1** in 2-MeTHF, the KIE exhibits disparate behavior with temperature.[11] The high-temperature regime (300 K) shows a normal KIE (k_H/k_D) ~ 1.22(1) whereas in the low-temperature regime (120 K), an inverse KIE ~ 0.87(1) is obtained. For the case of **D1-H(D):A2** in 2-MeTHF, no cross-over is observed. Instead, an inverted KIE arises at all temperatures studied (300 K - 150 K). In theoretical undertakings by Dr. Steve Pressé, the KIE cross-over for **D1-H(D):A1** is attributed to the freezing out of hydrogen vibrational modes within the interface with decreasing temperature.[31] The vibrationally assisted contributions to PCET for proton fluctuations decrease more quickly with temperature than the contributions from the deuteron fluctuations, which allows the PCET rate through the deuterated interface to take over with decreasing temperature. In the case of **D1-H(D):A2** in 2-MeTHF the inverted KIE indicates that the deuterated interface facilitates PCET even at higher temperatures. The inverted KIE for **1-H(D):A2** in 2-MeTHF may be a result of the more limited solvent interactions of the 2-MeTHF with the amidinium-sulfonate proton interface, as discussed in Section V.5.1. The static proton configuration of the **D1-H(D):A2** dyads and the limited solvent interaction favor overlap of the deuterated wavefunctions.

Kinetic studies on **D1-H(D):A1** and **1-H(D):A2** in THF reveal a normal KIE and no tendency to invert over the temperature range studied. One possible explanation lies in the observed E_a. For both D–A dyads, PCET in THF yields a higher average activation energy compared to 2-MeTHF. The higher activation energy may contribute to the slight increase to the magnitude of the normal KIE as the temperature decreases. The subtle effects of the vibrational motions in the interface towards assistance of ET may be washed out by the increase in activation energy for PCET, which ends up dominating the variable-temperature KIE behavior of the two systems. Similar studies for the photoinduced oxidation of ubiquinol based systems through a PCET process have reported both normal and inverted KIEs, which have been attributed to equilibrium isotope effects on hydrogen bonding and PT equilibria.[38] Similar factors may be responsible for the disparate kinetic behaviors observed for CT in **D1**:**A1** and **D1**:**A2** and may point to the importance of the effect of the static protonic configuration and hybridization within the interface on PCET.

V.6. Conclusion

In summary, a direct comparison of PCET is facilitated by the similarity of the **D1**:**A1** and **D1**:**A2** PCET systems. The solvent-dependent kinetic differences introduced by molecular variation to the solvent are accentuated. ET through hydrogen bonds established the PCET mechanism for these De-Ae systems and the differing static interface configurations achieved in the **D1**:**A1** and **D1**:**A2** are shown to profoundly influence PCET kinetics.[11,10] The complexity of PCET within the dyads is highlighted by comparison of the kinetic data sets for **D1**:**A1** and **D1**:**A2** in THF and 2-MeTHF where the THF interacts more strongly with the proton interface to modulate PECT. Variation of PCET kinetics, λ_s and $|V|$ obtained in the comparison of **D1**:**A1** and **D1**:**A2** in THF[10], may also have been expected in 2-MeTHF. As shown by the current study, however, surprisingly little variation to the PCET kinetics or fitted PCET parameters between the ionized and non-ionized interface in 2-MeTHF is revealed. Molecular variation between the two solvents emerges as a key contributor to modulating PCET kinetic behavior. Specifically, the presence of the methyl group leads to a reduced hydrogen bonding capacity of the oxygen in 2-MeTHF, which decreases the interaction between the solvent and the interface. Although, the exact reasons for these changes are still unclear and beckon further investigation, possibly including molecular modeling and simulation.

V.7. Experimental

V.7.1. Materials

D1[39] and **A1**[10] were prepared by Dr. Joel Rosenthal according to previously published methods and **A2** was synthesized by Dr. Joel Rosenthal as described in his Thesis. Solvents for synthesis were of reagent grade or better and were dried according to standard methods.[40] Spectroscopic experiments employed tetrahydrofuran (THF) and 2-methyltetrahydrofuran (2-MeTHF) (Spectroscopic grade), which was dried using standard methods and stored under vacuum.

V.7.2. Electrochemistry

Electrochemical experiments were carried out using a Bioanalytical Systems (BAS) Model CV-50W potentiostat/galvanostat. Cyclic voltammetry (CV) and differential pulse voltammetry (DPV) were performed in a two-compartment cell using a glassy carbon disk as the working electrode, a Ag/AgCl reference electrode and a platinum wire auxiliary electrode. The supporting electrolyte used for electrochemistry experiments was either 0.1 M *n*-tetrabutylammonium hexafluorophosphate ($TBAPF_6$) or perchlorate (TBAP). The solution in the working compartment of the cell was deaerated using nitrogen. Background CVs of the electrolyte solution were recorded prior to addition of the solid sample. Redox couples were referenced to SCE by using a ferrocenium/ferrocene internal standard of 0.307 V vs. SCE.[41]

V.7.3. Spectroscopic sample preparation

TA spectroscopy was performed on samples contained in a high-vacuum cell comprising a 2-mm pathlength clear fused-quartz cuvette (Starna cells) connected to a 10-cm^3 solvent reservoir via a graded seal. High-vacuum Teflon valves were used to seal the cell from the environment and the cuvette from the solvent reservoir.

For TA, one aliquot of **D1** (1×10^{-7} mol) was added to the cuvette and a two-equivalent aliquot of **A2** (2×10^{-7} mol) was added to the solvent reservoir. The cell was evacuated under high-vacuum (10^{-5} Torr) to remove the transferring solvent and to leave the two compounds in their separated compartments. One-half milliliter of dry THF or 2-MeTHF was added to the solvent reservoir by high vacuum transfer and the solvent was subjected to three cycles of freeze-pump-thaw. The cell was sealed from the environment and removed from the high vacuum manifold. Single-wavelength TA experiments were first performed on unbound **D1** under vacuum using resonant excitation of the Q-band at 560 nm.

The isosbestic point ($\lambda_{isosbestic}$ = 654 nm) for singlet-triplet conversion yield was verified. At this wavelength, the intensity of the TA spectrum was invariant and thus provided the best wavelength for detecting PCET transients.[10] Subsequently, the Teflon stopper between the cuvette and solvent reservoir was opened and the two compounds were mixed while maintaining vacuum inside the cell to allow for study of the **D1**:**A2** dyad.

Samples for variable-temperature transient emission experiments were prepared following a detailed procedure outlined previously.[11] To summarize, one aliquot (1×10^{-7} mol) of **D1-H** was dissolved in a minimal amount of THF or 2-MeTHF and transferred to a borosilicate short-stem glass ampoule (Kimble-Kontes). Prior to the transfer, a few drops of D_2O were added to samples for deuterium isotopic exchange experiments. The samples were sealed from the atmosphere, shaken and left for 15 minutes before being transferred to the ampoule. The neck of the ampoule had been stretched with a flame to reduce the diameter and allow for easier sealing after high vacuum manipulations. Addition of 4 equivalents of **A1** or 8 equivalents of **A2** were added for control and quenching experiments. The ampoule containing the sample was attached to a high vacuum adaptor. The transferring solvents were removed on a high vacuum manifold ($< 10^{-6}$ Torr) and the sample remained under vacuum for at least 2 hours to remove any residual water. One milliliter of dry THF or 2-MeTHF was added to the ampoule by vacuum transfer and was subject to at least three cycles of freeze-pump-thaw. The ampoule was then flame-sealed while the solvent remained frozen. The high-vacuum manipulations were necessary to ensured that the samples remained free from exposure the environment or water, which disrupts the hydrogen bonding between the dyads.

V.7.4. Spectroscopic measurement

Steady-state absorption spectra were obtained using a Spectral Instruments 440 Series spectrophotometer. Steady-state emission spectra were recorded on an automated Photon Technology International (PTI) QM 4 fluorimeter equipped with a 150 W Xe arc lamp and a Hamamatsu R928 photomultiplier tube.

The excitation source for TE measurements was a chirped-pulse amplified Ti:Sapphire laser system that has been described elsewhere.[10] In this experiment, the 150-fs, 800-nm output of the regenerative amplifier was frequency-upconverted in a visible OPA (BMI Alpha-1000) to produce a 1 kHz pulse train of excitation pulses at 560 nm for resonant excitation of the Q-band of **D1**. The excitation was vertically polarized and attenuated to 50 - 250 nJ/pulse.

TE kinetics were measured on a Hamamatsu C4334 Streak Scope streak camera that has been described elsewhere.[42] The emission was collected at the magic angle ($\theta_m = 54.7^o$) over a 140-nm window centered on the emission peak. A 10-ns or a 20-ns time base was used.

Variable-temperature lifetimes of **D1-H(D)** alone and bound to **A1** and **A2** were measured over a temperature range of 120-300 K. Experiments were repeated at least 3 times with newly prepared samples. Variable-temperature measurements were carried out based on the procedure performed by Dr. Niels Damrauer and Dr. Justin Hodgkiss.[11] A modular cryogenic refrigeration system

(Air Products and Chemicals) consisting of a single stage helium compressor (model 1RO2A) connected via hoses to an expander module (model DE-202) with a heating element and temperature controller (Scientific Instruments, 9600-5) was interfaced with a custom-made computer program in order to automate the temperature control settings. The expander module is housed within in laboratory interface (model DMX-1) consisting of a vacuum shroud with glass windows for fluorescence spectroscopy in a right-angle configuration and is continuously pumped to maintain a vacuum (~10^{-4} Torr). The ampoule containing the sample is mounted on a copper block and the thermocouple was calibrated at three temperatures: liquid nitrogen (77 K), an ice bath (273 K) and ambient temperature (293 K).

Data acquisition was automated for the variable-temperature experiments. The temperature controller and streak camera were synchronized to enable data collection throughout the entire temperature range. Luminescence measurements were made after a 20 minute wait time during which the temperature was adjusted and the sample was allowed to equilibrate. This cycle occurred for each temperature data point, which was typically 10-25 K apart. Each sample was cycled through the entire temperature range 4 times in different sequences to ensure that the data was independent of the sequence

V.7.5. Data fitting

TE lifetimes were determined from streak camera data analysis by integrating 15-nm or 13-nm, or 40-nm or 50-nm slices of the emission peaks centered at 612 and 655 nm, for **D1**:**A1** and **D1**:**A2** respectively, and fitting to a monoexponential decay function. Temperature dependent lifetimes of **D1-H(D):A1** and **D1-H(D):A2** were measured at the same temperature points and the data was fit in the same manner, except that the data was fit to a biexponential decay function with the longer lifetime component fixed to the lifetime obtained from the control experiment, **D1-H(D)**, at each temperature.

V.8. References

1. Turró, C.; Chang, C. K.; Leroi, G. E.; Cukier, R. I.; Nocera, D. G. *J. Am. Chem. Soc.* **1992**, *114*, 4013-4015.

2. de Rege, P. J. F.; Williams, S. A.; Therien, M. J. *Science* **1995**, *269*, 1409-1413.

3. Sessler, J. L.; Wang, B.; Springs, S. L.; Brown, C. T. In *Comprehensive Supramolecular Chemistry*; Murakami, Y., Ed.; Pergamon Press: Oxford, 1996; Vol. 4, pp. 311-336 and references therein.

4. Chang, C. J.; Brown, J. D.; Chang, M. C. Y.; Baker, E. A.; Nocera, D. G. In *Electron Transfer in Chemistry*; Balzani, V., Ed.; Wiley-VCH: Weinheim, Germany, 2001; Vol 3.2.4, pp 409-461.

5. Roberts, J. A.; Kirby, J. P.; Nocera, D. G. *J. Am. Chem. Soc.* **1995**, 117, 8051-8052.

6. Roberts, J. A.; Kirby, J. P.; Wall, S. T.; Nocera, D. G. *Inorg. Chim. Acta*, **1997**, 263, 395-405.

7. Roberts, J. A.; Kirby, J. P.; Nocera, D. G. *J. Am. Chem. Soc.* **1997**, 119, 9230-9236

8. Damrauer, N. H.; Hodgkiss, J. M.; Rosenthal, J.; Nocera, D. G. *J. Phys. Chem. B* **2004**, 108, 6315-6321.

9. Hodgkiss, J. M.; Damrauer, N. H.; Pressé, S.; Rosenthal, J.; Nocera, D. G. *J. Phys. Chem. B.* **2006**; 110, 18853-18858.

10. Young, E. R.; Rosenthal, J.; Hodgkiss, J. M.; Nocera, D. G. *Manuscript submitted.*

11. Cukier, R. I.; Nocera, D. G. *Annu. Rev. Phys. Chem.* **1998**, 49, 337-369.

12. Hodgkiss, J. M.; Rosenthal, J.; Nocera, D. G. In *Hydrogen-Transfer Reactions*; Hynes, J. T.; Klinman, J. P.; Limbach, H.-H.; Schowen, Eds; Wiley-VCH: Weinheim, Germany, 2007; Vol 2.17, pp 503-561.

13. Chang, C. J.; Brown, J. D.; Chang, M. C. Y.; Baker, E. A.; Nocera, D. G. In *Electron Transfer in Chemistry*; Balzani, V., Ed.; Wiley-VCH: Weinheim, Germany, 2001; Vol 3.2.4, pp 409-461.

14. Hodgkiss, J. M.; Rosenthal, J.; Nocera, D. G. In *Hydrogen-Trasfer Reactions*; R. L Schowen, J. P. Klinman, J. T. Hynes, H.-H. Limbach, Eds; Wiley-VCH:Weinheim, Germany, 2006, Vol 2.17, pp. 503-652.

15. Calef, D. F.; Wolynes, P. G. *J. Phys. Chem.* **1983**, *87*, 3387-3400.

16. Lay, P. A. *J. Phys. Chem.* **1986**, *90*, 878-885.

17. Rostov, I. V.; Basilevsky, M. V., Newton, M. D. *AIP Conf. Proced.* **1999**, *492*, 331-349.

18. Marconelli, M. *Proceeding of 19th DOE Solar Photochem. Res. Conf.* **1995**,*BNL 61733*, 76-79.

19. The refractive index of THF is 1.4050 and of 2-MeTHF is 1.4059. Lide, D. R.; Milne, G. W. A., ed. Handbook of Data on Organic Compounds, vol III Compounds 10001-15600 3rd ed.; CRC Press: Ann Arbor, MI, 1994.

20 . Cukier, R. I. *J. Phys. Chem.***1996**, *100*, 15428-15443.

21. Cukier, R. I. *J. Phys. Chem.* **1994**, *98*, 2377-2381.

22. Zhau, X. G. Cukier, R. I. *J. Phys. Chem.* **1995**, *99*, 945-954.

23. Cukier, R. I. *J. Phys. Chem. A* **1999**, *103*, 5989-5995.

24. Cukier, R. I. *Biochim. Biophys. Acta* **2004**, *1655*, 37-44.

25. Hammes-Schiffer, S. In *Electron Transfer in Chemistry*; V. Balzani, Ed., Wiley-VCH: Weinheim, Germany, 2001, Vol. 1.1.5, p. 189.

26. Hammes-Schiffer, S. *Acc. Chem. Res.* **2001**, *34*, 273-281.

27. Hammes-Schiffer, S. Iordanova, N. *Biochim. Biophys. Acta* **2004**, *1655,* 29-36.

28. Soudackov, A. Hammes-Schiffer, S. *J. Chem. Phys.* **1999**, *111*, 4672-4687.

29. Soudackov, A.; Hammes-Schiffer, S. *J. Chem. Phys.* **2000**, *113*, 2385-2396.

30. Decornez, H.; Hammes-Schiffer, S. *J. Phys. Chem. A.* **2000**, *104*, 9370-9384.

31. Pressé, S.; Silbey, R. *J. Chem Phys.* **2006**, 124, 164504-164511.

32. Speight, James G., ed. Lange's Handbook of Chemistry, 16th ed.; McGraw-Hill: New York, NY, 2005.

33. Marcus, R. A.; Sutin, N. *Biochem. Biophys. Acta* **1985**, *811*, 265-322.

34. Archer, M. D.; Gadzekpo, V. P. Y.; Bolton, J. R.; Schmidt, J. A.; Weedon, A. C. *J. Chem. Soc. Faraday Trans. 2* **1986**, *82*, 2305-2313.

35. Gaines, G. L., III; O'Neil, M. P.; Svec, W. A.; Niemczyk, M. P.; Wasielewski, M. R. *J. Am. Chem. Soc.* **1991**, *113*, 719-721.

36. Mizukami, M; Fujimori, H; Oguni, M. *Prog. Theo. Phys. Supp.* **1997**, *126*, 79-82.

37. Garrido, L; Riande, E; Guzman, J. *Makromol. Chem,. Rapid Commun.* **1983**, *4*, 725-9.

38. Cape, J. L.; Bowman, M. K.; Kramer, D. M. *J. Am. Chem. Soc.* **2005**, *127*, 4208-4215.

39. Yeh, C.-Y.; Miller, S. E.; Carpenter, S. D.; Nocera, D. G. *Inorg. Chem.* **2001**, *40*, 3643-3646.

40. Armarego, W. L. F.; Perrin, D. D. *Purification of Laboratory Chemicals*, 4th Ed.; Butterworth-Heinmann: Oxford, 1996.

41. Bard, A. J.; Faulkner, L. R. *Electrochemical Methods. Fundamentals and Applications*; John Wiley: New York, 1980.

42. Loh, Z. H.; Miller, S. E.; Chang, C. J.; Carpenter, S. D.; Nocera, D. G. *J. Phys. Chem. A* **2002**, *106*, 11700-11708.

Chapter VI

Ferrocenyl-amidinium compounds as building blocks for aqueous PCET systems

Chapter VI

VI.1. Introduction and motivation

Ferrocene derivatives have been incorporated into a large number of ET model systems due to their rich redox properties, reversible oxidation and general photostability and thermal stability.[1-9] Accordingly, the use of ferrocenyl moieties appended with hydrogen bonding functionalities is appealing for mechanistic study of PCET. The synthesis of a set of ferrocenyl-amidinium derivatives in which the protonic group is either fused directly to the redox center or bridged by an ethynyl group enables PCET studies to be carried out in aqueous conditions.

Early mechanistic studies of PCET in the literature and in this Thesis have focused primarily on assemblies of De-Ae pairs juxtaposed by hydrogen bonded interfaces[10-12] formed by carboxylic acid dimers,[13,14] and amidinium-carboxylate salt bridges.[15-20] Mechanistic investigation of PCET through hydrogen bonded interfaces addresses the impact of proton motion on through-bond ET in a co-linear PCET arrangement, in which ET and PT occur along the same coordinate. Assembly of these hydrogen bonded systems, however, requires the use of aprotic solvents of low dielectric constant in order to facilitate efficient binding. Mechanistic interrogation of aqueous PCET systems requires an alternative architectural strategy to co-linear PCET in hydrogen bonded systems, as water disrupts formation of amidinium-carboxylate hydrogen bonds and prevents formation of De-Ae dyads. A strategy that can be employed to study PCET that does not necessitate formation of hydrogen bonded De-Ae dyads is the use of a bi-directional PCET motif. Specifically, a bi-directional system of relevance to aqueous studies consists of a covalent De-Ae pair to establish an ET coordinate, which is coupled to a PT coordinate through loss of an amidinium proton to the bulk. The ferrocenyl-amidinium species presented in this Chapter provide such building blocks for aqueous PCET. These systems are akin to the bi-directional PCET systems involving deprotonation of tyrosine to the bulk concomitant with oxidation by a Re polypyridyl photo-oxidant.[21,22]

Prior to the incorporation of the ferrocenyl-amidinium components in a PCET assembly, it is beneficial to characterize the individual ferrocene moieties. Varying degrees of electronic communication between ferrocene and the pendant amidinium are revealed by electrochemistry and UV-vis absorption spectroscopy. pH-dependent absorption spectroscopy yields pK_a values for the amidinium in water, while pH-dependent electrochemistry reveals how the oxidation potentials of the compounds are linked to the protonation state of the amidinium functionality. Formation of the oxidized species is monitored by

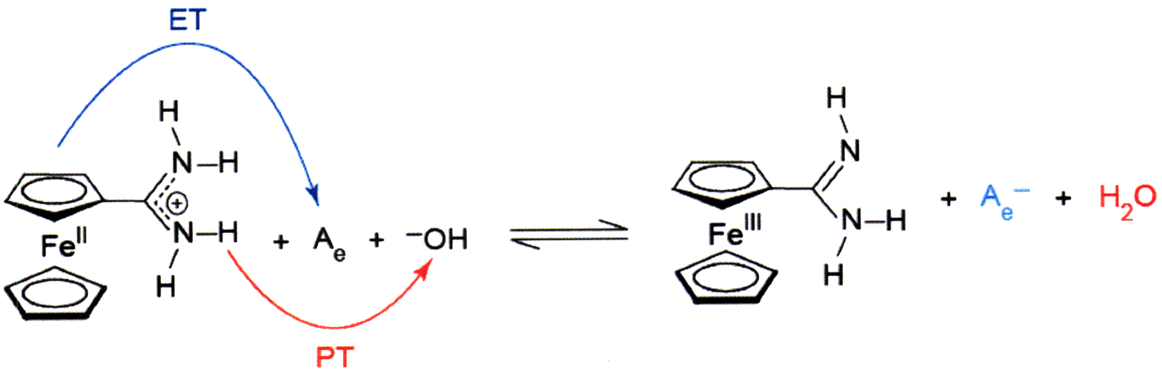

Scheme VI.1. Diffusion-controlled ground-state PCET. Deprotonation of the appended amidinium functionality facilitates loss of an electron to the ET acceptor.

electronic absorption spectroscopy during bulk electrolysis experiments. A proof-of-concept demonstration of diffusion-controlled ground-state ET between the ferrocenyl-amidinium moieties and the electron acceptor hexamine ruthenium (III) chloride (as a function of pH) is presented in Scheme VI.1. In these studies, the assumption is made that the ET event is reversible. Characterization of two ferrocenyl-amidinium moieties according to this Scheme is presented in this Chapter and provides the underpinning for further design of PCET systems.

VI.2. Ferrocenyl-amidinium moieties

An amidinium or an alkynylamidinium functionality was fused to Cp^- ring of ferrocene to yield **Fc1** or **Fc2**, shown in Scheme VI.2. Synthesis and purification of the compounds were performed by Dr. Joel Rosenthal following the synthetic protocol outlined in his Thesis.

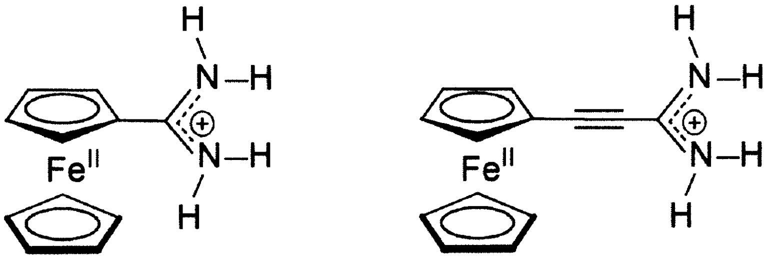

Fc1 **Fc2**

Scheme VI.2. Ferrocene-amidinium, **Fc1**, and ferrocene-alkynylamidinium, **Fc2**.

VI.3. Characterization of Fc1 and Fc2

VI.3.1. pH-dependent electronic absorption spectroscopy

Absorption spectra of ferrocene-amidinium (**Fc1**) and ferrocene-alkynylamidinium (**Fc2**) in aqueous buffered solutions exhibit absorption maxima at 265 nm (ε = 44,300 $M^{-1}cm^{-1}$), 322 nm (ε = 11,400 $M^{-1}cm^{-1}$), and 450 nm (ε = 4,000 $M^{-1}cm^{-1}$) for **Fc1** and 293 nm (ε = 45,500 $M^{-1}cm^{-1}$), 355 nm (ε = 9,700 $M^{-1}cm^{-1}$), and 466 nm (ε = 5,600 $M^{-1}cm^{-1}$) for **Fc2**. Variable-pH absorption spectra are obtained in 10 mM potassium phosphate and 10 mM KCl aqueous solution. The pH-dependent absorption spectra of **Fc1** show a shift of the absorption band at 265 nm (pH 9) to 262 nm (pH 12), a shift of the absorption band at 311 nm (pH 9) to 308 nm (pH 12), and the disappearance of the absorption band at 450 nm (at pH 9) with well anchored isosbestic points at 329 nm, 387 nm, and 418 nm (Figure VI.1). The pH-dependent absorption spectra of **Fc2** show a shift of the absorption band at 291 nm (pH 9) to 273 nm (pH 12), the disappearance of the absorption band at 353 nm (at pH 9), and a shift of the absorption band at 467 nm (pH 9) to 439 nm (pH 12) with well anchored isosbestic points at 273 nm, 317 nm, 339 nm, 405 nm, and 431 nm (Figure VI.2). Figure VI.1 and Figure VI.2 show a plot of absorption versus pH for peak positions corresponding to the initial absorption features. From these plots, pK_a values of pK_a(**Fc1**) > 11.5 and pK_a(**Fc2**) = 10.0 are deduced for the amidinium moiety.

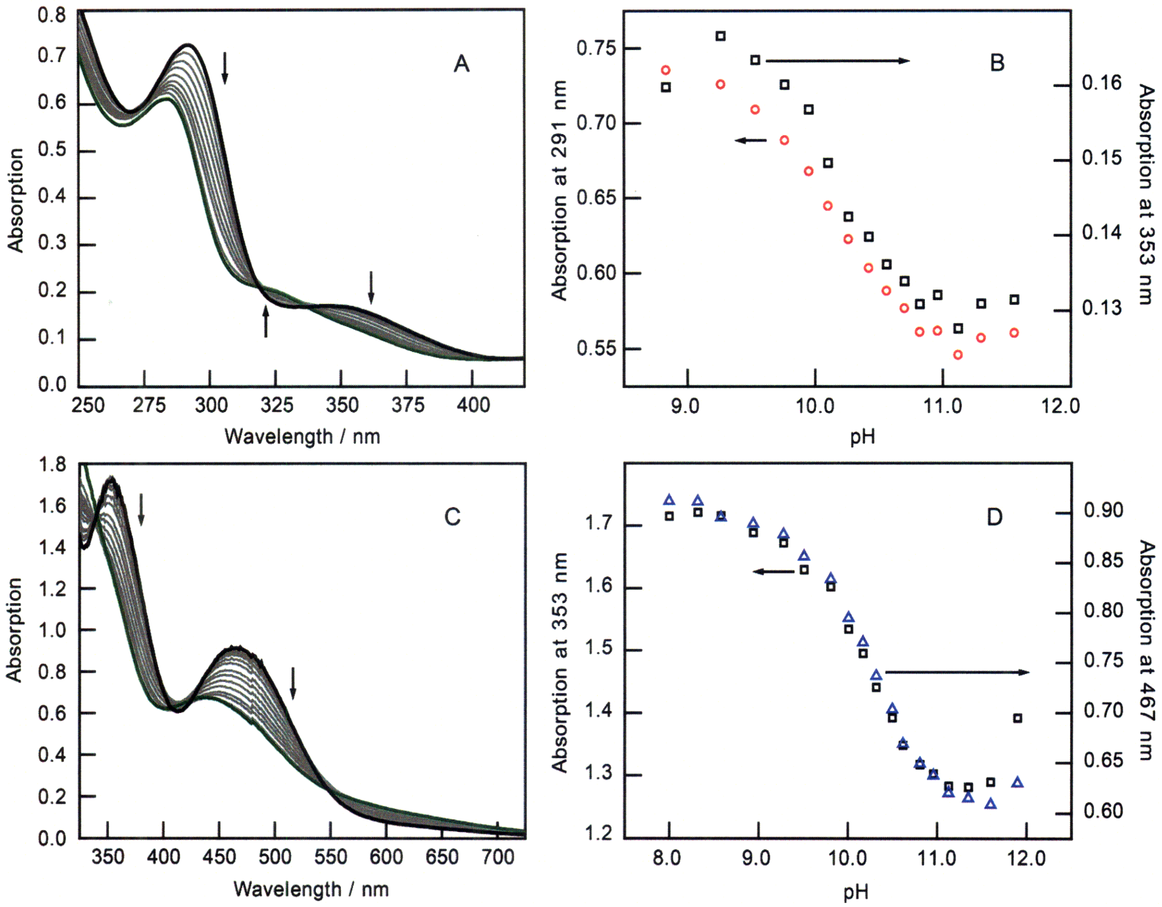

Figure VI.1. Variable-pH absorption spectroscopy on **Fc1**. (A) pH-dependent absorption spectra of a dilute sample of **Fc1** (90 μM) in a 10 mM potassium phosphate and 10 mM KCl solution at 25°. (B) Absorbance at peak maxima as a function of pH at 265 nm (○) and 311 nm (□). (C) pH-dependent absorption spectra of a concentrated sample of **Fc1** (580 μM) in 10 mM potassium phosphate and 10 mM KCl solutions at 25°. (D) Absorbance at peak maxima as a function of pH at 311 nm (□) and 450 nm (△).

In summary, electronic absorption spectroscopy reveals significant spectral shifts upon increase in pH that correspond to deprotonation of the amidinium functionality. The spectral shifts confirm a significant degree of electronic communication between the ferrocene moiety and the amidinium functionality, as been observed previously for amidinium functionalities appended to porphyrin macrocycles.[23-25]

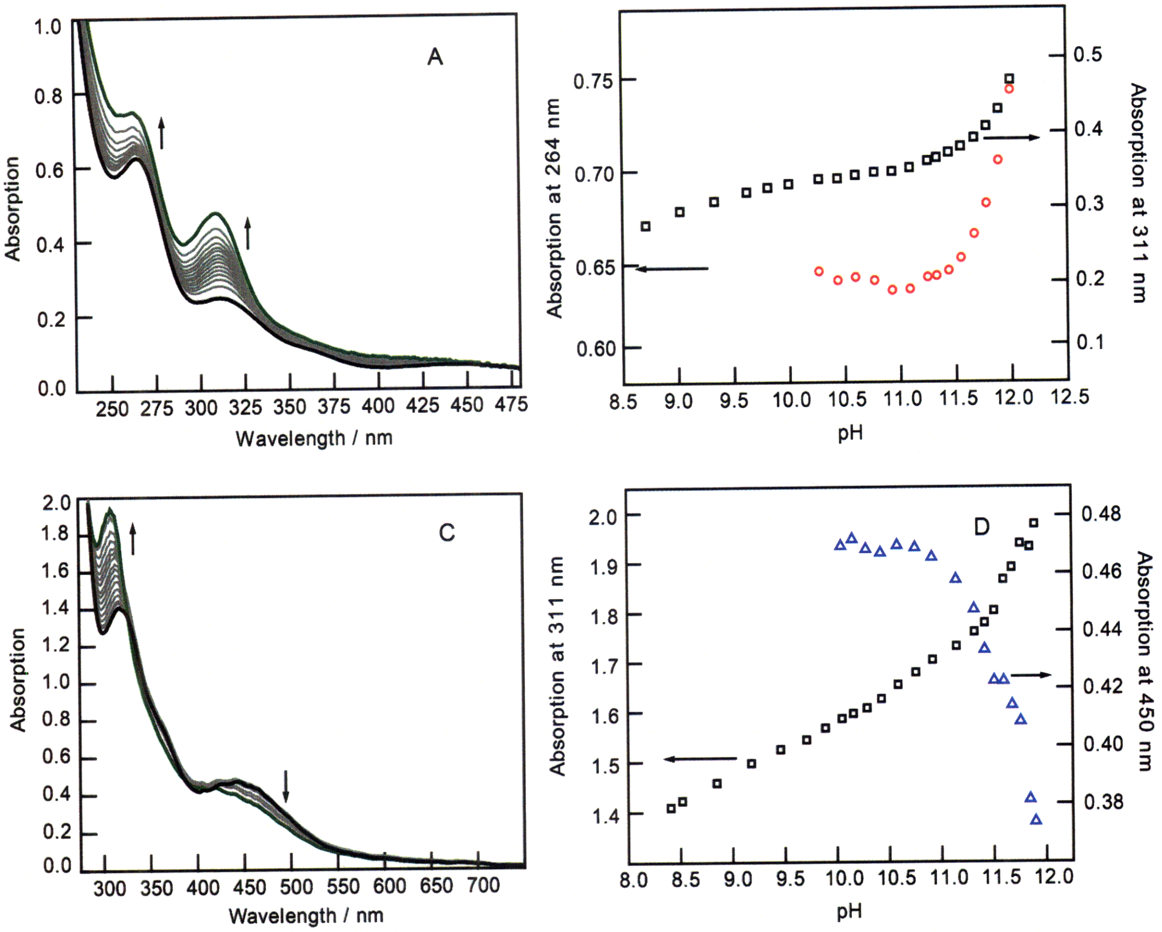

Figure VI.2. Variable-pH absorption spectroscopy on **Fc2**. (A) pH-dependent absorption spectra of spectra of a dilute sample of **Fc2** (90 μM) in a 10 mM potassium phosphate and 10 mM KCl solution at 25°. (B) Absorbance at peak maxima as a function of pH at 291 nm (○) and 353 nm (◻). (C) pH-dependent absorption spectra of spectra of a concentrated sample of **Fc2** (850 μM) in a 10 mM potassium phosphate and 10 mM KCl solution at 25°. (D) Absorbance at peak maxima as a function of pH at 353 nm (◻) and 467 nm (△).

VI.3.2. Bulk electrolysis and spectroelectrochemistry

Spectroelectrochemical experiments on **Fc1** and **Fc2** were undertaken to characterize the spectral signatures associated with formation of the ferrocenium-amidinium species. The spectra collected during the bulk electrolysis are plotted as difference spectra between the initial spectrum and the spectrum at each time point. Plotting the spectra in this manner emphasizes the disappearance of ferrocene-amidinium absorption bands and highlights formation of new absorption bands associated with the ferrocenium-amidinium species. The initial electronic absorption spectrum and a representative difference spectrum obtained during the bulk electrolysis are shown in Figure VI.3. The initial absorption spectrum is overlaid in gray to confirm that the bleaching signals resulting from electrolysis are coincident with absorption peaks of the native ferrocenyl-amidinium moiety. Upon electrolysis, a red-shifted peak at 533 nm for **Fc1** and 555 nm for **Fc2** appears, indicating formation of the oxidized moiety. The growth of these peaks establishes a spectral handle for the ferrocenium-amidinium species for both **Fc1**$^+$ and **Fc2**$^+$. The red-shifted feature can subsequently be used to confirm oxidation of **Fc1** and **Fc2** in ET reactions.

VI.3.3. pH-dependent electrochemistry

Electrochemical experiments were performed in the pH range of 7 to 12 to quantify the effect of pH on the electrochemical oxidation potentials of **Fc1** and

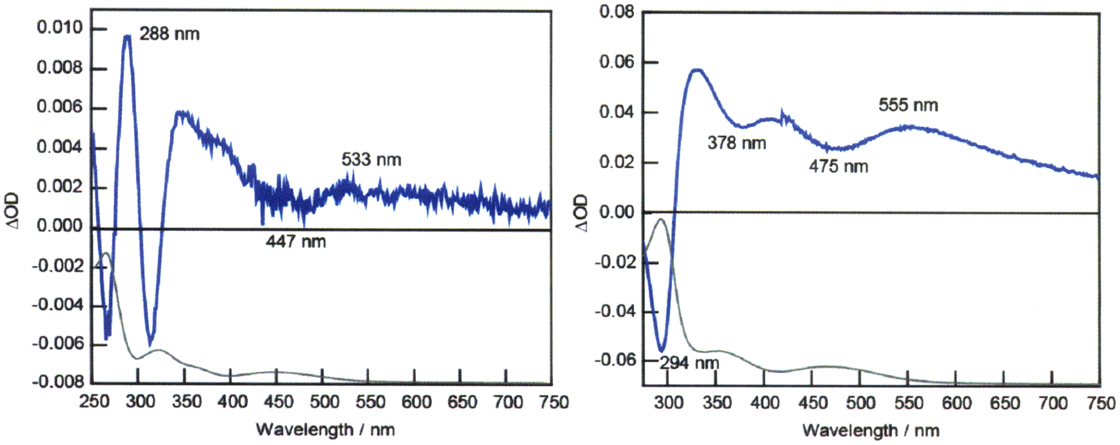

Figure VI.3. Spectral observation of oxidized **Fc1** and **Fc2**. Difference spectra for oxidized ferrocene species (—) with the original absorption spectrum (—) for each compound overlaid shows broad absorption feature centered at (A) 533 nm for **Fc1**, and (B) 555 nm for **Fc2** for the oxidized species.

Fc2. Differential pulse voltammetry (DPV) was utilized to determine oxidation potentials; the peak potential (E_p) is reported at each pH. The oxidation potential of both **Fc1** and **Fc2** decreases with increasing pH, as plotted in Figure VI.4, in a manner that mirrors deprotonation of the amidinium functionality. The electrochemical behavior of **Fc1** and **Fc2** is in accordance with the results of the pH-dependent electronic absorption spectroscopy. The oxidation potentials for **Fc1** vary by 152 mV over the range sampled, from 552 mV at pH 7 to 400 mV at pH 12. Similarly the oxidation potential of **Fc2** varies from 452 mV at pH 7 to 364 mV at pH 12.

UV-vis absorption spectroscopy and electrochemical experiments performed on the ferrocenyl-amidinium compounds reveal marked variation with pH. The spectral and electrochemical behaviors are linked. Oxidation potentials plotted versus pH (Figure VI.4) track the spectral shifts observed in UV-vis spectra and thus confirm oxidation of the **Fc1** and **Fc2** is gated by deprotonation

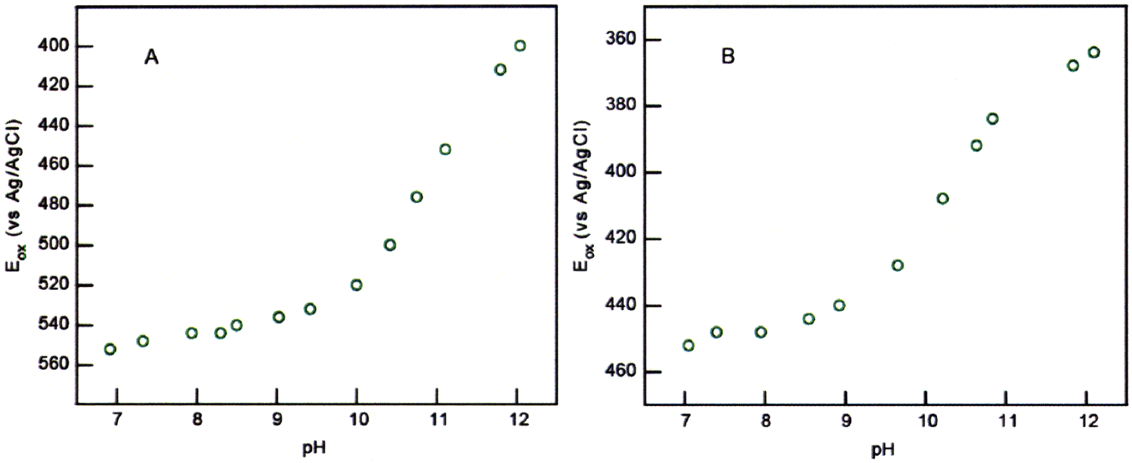

Figure VI.4. Variable-pH electrochemistry on **Fc1** and **Fc2**. Peak potential (E_p) for (A) **Fc1** and (B) **Fc2**, plotted at each pH.

of the amidinium functionality.

VI.3.4. Thermodynamic square scheme

The thermodynamic properties of **Fc1** and **Fc2** are summarized on the square schemes shown in Scheme VI.3, for which complete labeling of acidity constants and oxidation potentials is presented. $\mathrm{p}K_a$ values for the protonated forms of **Fc1** and **Fc2** are experimentally determined as outlined in Section VI.3.1, as are oxidation potentials of both protonated and deprotonated **Fc1** and **Fc2** in Section VI.3.3. With three of the four values in hand, the square can be completed by calculating the $\mathrm{p}K_a$ values for the ferrocenium-amidinium species, **Fc1**$^+$ and **Fc2**$^+$. The values obtained from these calculations are $\mathrm{p}K_a$(**Fc1**$^+$) = 8.9

$$\begin{tikzcd}
\mathrm{Fc1{-}amH^+} \arrow[r, shift left, "\mathrm{p}K_a > 11.5"] \arrow[d, shift left] & \mathrm{Fc1{-}am} \arrow[l, shift left] \arrow[d, shift left, "E_{ox} = 400\ \mathrm{mV}"] \\
\mathrm{Fc1^+{-}amH^+} \arrow[u, shift left, "E_{ox} = 552\ \mathrm{mV}"] \arrow[r, shift right, swap, "\mathrm{p}K_a = 8.9"] & \mathrm{Fc1^+{-}am} \arrow[u, shift left] \arrow[l, shift right]
\end{tikzcd}$$

$$\begin{tikzcd}
\mathrm{Fc2{-}amH^+} \arrow[r, shift left, "\mathrm{p}K_a = 10.0"] \arrow[d, shift left] & \mathrm{Fc2{-}am} \arrow[l, shift left] \arrow[d, shift left, "E_{ox} = 364\ \mathrm{mV}"] \\
\mathrm{Fc2^+{-}amH^+} \arrow[u, shift left, "E_{ox} = 452\ \mathrm{mV}"] \arrow[r, shift right, swap, "\mathrm{p}K_a = 8.5"] & \mathrm{Fc2^+{-}am} \arrow[u, shift left] \arrow[l, shift right]
\end{tikzcd}$$

Scheme VI.3. Thermodynamic square cycle for the **Fc1** and **Fc2**. Horizontal arrows represent $\mathrm{p}K_a$ values for the native and oxidized species, while vertical arrows represent oxidation/reduction of the protonated and deprotonated species.

and pK_a(**Fc2**$^+$) = 8.5. These square schemes from the basis for PCET studies involving **Fc1** and **Fc2**.

VI.4. Ground state ET experiments

*VI.4.1. Ground state ET with **Fc1** and **Fc2***

With the spectroscopic handle for the ferrocenium-amidinium moieties for verified, Diffusion-controlled ground-state ET reactions of **Fc1**$^+$ and **Fc2**$^+$ (via a bi-directional PCET mechanism) were investigated using the electron acceptor hexamine ruthenium (III) chloride. These experiments were performed to establish ET prior to undertaking the task of constructing a covalently bound ET De-Ae system that incorporates the ferrocenyl-amidinium moieties. The diffusion-controlled ground-state PCET reaction is outlined in Scheme VI.1.

The oxidized ferrocenyl-amidinium species was monitored as the pH of the bulk solution was increased. As the pH of the bulk solution increases from pH 6 to pH 10, the reaction is driven to the PCET products. The reaction is monitored by electronic absorption spectroscopy and plotted as difference spectra between the initial spectrum and the spectrum at each pH point. The difference absorption spectra clearly reveal formation of the oxidized species, which becomes more prominent as pH increases for both **Fc1** and **Fc2** (Figure VI.5).

VI.4.2. Analysis of ground state ET: Determining K_{eq}

The observed equilibrium constant for the bimolecular PCET reaction can be expressed as,

$$K_{\mathrm{eq,obs}} = \frac{c_{\mathrm{Fc+}}\, c_{\mathrm{A-}}}{c_{\mathrm{Fc}}\, c_{\mathrm{A}}} \qquad \text{(VI.1)}$$

where c_{Fc} is the ferrocene-amidinium species, $c_{\mathrm{Fc+}}$ is the ferrocenium-amidine species, c_{A} is the hexamine ruthenium(III) chloride, and $c_{\mathrm{A-}}$ is the reduced hexamine ruthenium(II) chloride.

The ET experiments are analyzed by determining the concentrations of each species at all pH points. Extinction coefficients of both the Fc and Fc^{+} moieties at the absorption peak for the ferrocenium species (535 nm for **Fc1⁺**; 555 nm for **Fc2⁺**) are required for this analysis. The extinction coefficients of **Fc1**

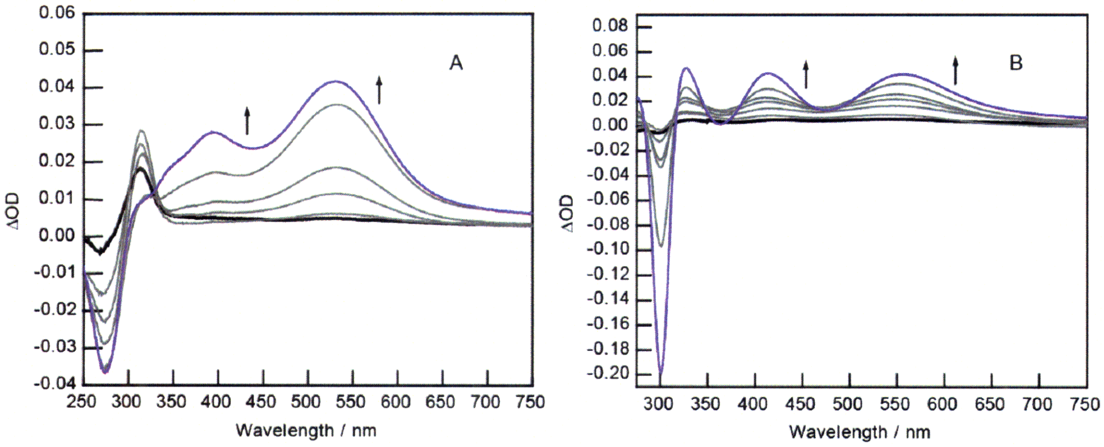

Figure VI.5. Spectral evolution for ground state ET with increasing pH. Difference spectra for (A) **Fc1** and (B) **Fc2** with hexamine ruthenium(III) chloride are shown as a function of pH. For **Fc1**, the pH range was sampled from 6.5 to 10.1, and for **Fc2**, the pH range was sampled from pH 6 to pH 10.4.

and **Fc2** at these wavelengths have been determined in the variable-pH studies (Section VI.3.1), shown in Figure VI.1 and Figure VI.2. These experiments yield ε_{Fc}(535 nm) = 1240 M^{-1} cm^{-1} for **Fc1** and ε_{Fc}(555 nm) = 2000 $M^{-1}cm^{-1}$ for **Fc2**..With extinction coefficients for **Fc1** and **Fc2** in hand, bulk electrolysis experiments were analyzed to determine the extinction coefficients of the oxidized species, Fc^{+}.

The ε_{Fc+}(555 nm) for **Fc2**$^{+}$ is calculated from the absorbance peak at 294 nm (Section VI.3.2). This high energy peak is spectrally removed from the red-shifted absorption feature associated with ferrocenium cation formation and is used to obtain the concentration of depleted **Fc2** upon bulk electrolysis. The bleach feature at 294 nm (ΔOD = −0.055; ε_{Fc}(294 nm) = 45,000 M^{-1} cm^{-1}) yields a depleted **Fc2** concentration of ~6 × 10^{-6} M. With the concentration of **Fc2** loss determined, the extinction coefficient of **Fc2**$^{+}$ at 555 nm is extracted. The ΔOD value from the bulk electrolysis (Figure VI.3) is comprised of the difference in absorption between the loss of **Fc2** and the gain of **Fc2**$^{+}$ at that wavelength, or ΔOD(555 nm) = A_{Fc+}(555 nm) − A_{Fc}(555 nm). With the use of Beer's Law, $A = \varepsilon \ell c$, this relation can be rearranged to obtain,

$$\varepsilon_{Fc+} = \frac{\Delta OD + \varepsilon_{Fc}\ell c_{Fc}}{\ell c_{Fc+}} \qquad (VI.2)$$

to yield a ΔOD at 555 nm of 0.35. It is assumed that the depleted concentration of **Fc2** is the same as the concentration gained for **Fc2**$^{+}$, which is 6 × 10^{-6} M. The pathlength, ℓ, of the sample is 0.2 cm. An approximate extinction coefficient of

Table VI.1. Values for $K_{eq,obs}$ for **Fc1** and **Fc2**.

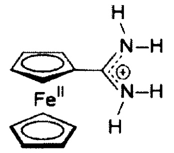		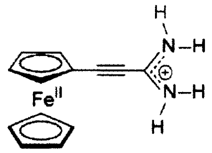	
pH	K_{eq}	pH	K_{eq}
7.60	9.42×10^{-5}	7.48	9.15×10^{-6}
8.08	9.81×10^{-5}	7.64	2.51×10^{-5}
8.60	3.51×10^{-4}	8.41	7.83×10^{-4}
9.08	9.44×10^{-4}	9.16	1.37×10^{-4}
9.52	3.76×10^{-3}	9.30	1.89×10^{-4}
10.10	5.37×10^{-3}	9.90	3.17×10^{-4}
10.60	7.21×10^{-3}	10.40	4.38×10^{-4}

ε_{Fc+}(555 nm) = 4900 M^{-1} cm^{-1} is obtained for **Fc2**$^+$. For **Fc1**, the depleted concentration of **Fc1** during the bulk electrolysis is 6.2×10^{-6} M (ΔOD = −0.055; ε_{Fc}(265 nm) = 44,300 M^{-1} cm^{-1}), which yields ε_{Fc+}(535 nm) = 2050 M^{-1} cm^{-1}.

With experimentally determined extinction coefficients for **Fc1**, **Fc1**$^+$, **Fc2**, and **Fc2**$^+$ in hand, the diffusion-controlled ground-state ET results may be analyzed from the pH-dependent difference spectra obtained for **Fc1** and **Fc2** upon addition of hexamine ruthenium(III) chloride (Figure VI.5). For the ET experiments, the extent of the reaction, *x*, is defined as the extent to which the reaction proceeds to form the oxidized species (**Fc1**$^+$ or **Fc2**$^+$) or,

$$x = \frac{\Delta \text{OD}}{\ell(\varepsilon_{\text{Fc+}} - \varepsilon_{\text{Fc}})} \tag{VI.3}$$

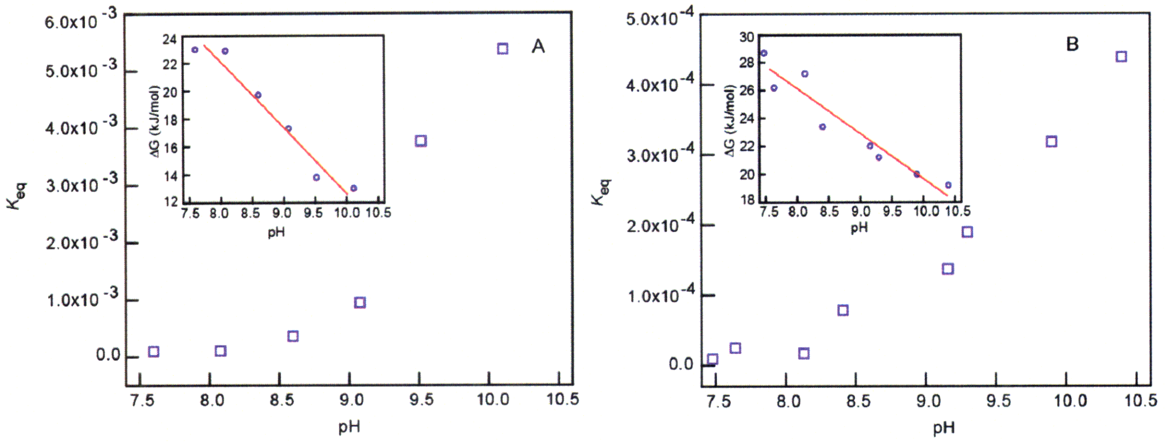

Figure VI.6. Equilibrium constants plotted versus pH for **Fc1** and **Fc2**. Inset: ΔG values plotted versus pH.

with $c_{Fc+} = x$, $c_{Fc} = c_{Fc,initial} - x$, $c_A = c_{A,initial} - x$, and $c_{A-} = x$. The values for ΔOD at 535 nm for **Fc1** and 555 nm for **Fc2** are extracted and the extinction coefficients for the oxidized and native species are utilized to determine the concentrations of donor and acceptor species at all pH points. With the concentrations of all constituents calculated, values for $K_{eq,obs}$ may be computed; these values are tabulated in Table VI.1 and plotted in Figure VI.6. The values for $K_{eq,obs}$ are computed using the relation in equation VI.1. $K_{eq,obs}$ may be converted to a Gibbs free energy for the driving force of the forward reaction depicted in Scheme VI.1 through the relation $\Delta G = -RT\bullet\ln(K_{eq,obs})$, where the gas constant, R, is 8.314 J K^{-1} mol^{-1} and the temperature, T, is 298 K (inset Figure VI.6). Linear fits to the data yield a slope of −4.57 kJ mol^{-1}(pH unit)$^{-1}$ for **Fc1** and −3.17 kJ mol^{-1}(pH unit)$^{-1}$ for **Fc2**. The variation of ΔG with pH is comparable to changes in electrochemical potentials for the ferrocenyl-amidinium species, which implicates a one-proton, one-electron PCET reaction.

VI.5. Conclusion

The spectral and electrochemical properties of two water soluble amidinium-appended ferrocenyl moieties vary with pH. The pH-dependent electronic absorption spectra reveal efficient coupling between the ferrocene moiety and appended amidinium functionality. From pH-dependent spectral shifts of the absorption spectrum, amidinium acidity constants of pK_a(**Fc1**) > 11.5 and pK_a(**Fc2**) = 10 are ascertained. The oxidation potential for each compound moves to lower potential with increasing pH, indicating that oxidation of the ferrocene moiety is facilitated by deprotonation of the acid functionality. Further analysis of the thermodynamic square scheme for each compound yields acidity constants for the ferrocenium-amidinium of pK_a(**Fc1**$^+$) = 8.9 and pK_a(**Fc1**$^+$) = 8.5.

Diffusion-controlled ground-state ET experiments reveal formation of the ferrocenium species. As pH is increased, the extent of the reaction is driven to favor formation of the ET products. This pH-dependent behavior is in line with the PCET scheme (Scheme VI.1), in which deprotonation of the amidinium is correlated to easing of the oxidation event of the ferrocenyl-amidinium species.

The foregoing analysis provides the underpinning for construction of a PCET system through detailed characterization of the ET and PT properties of **Fc1** and **Fc2**. The results provide an imperative for incorporation of **Fc1** and **Fc2** into photoinduced PCET networks of bi-directional character. With the appropriate choice of photo-oxidant, a De-Ae system can be constructed in which the donor and acceptor are covalently linked and for which the driving force for ET is modulated by the pH of the surrounding environment. These water-based bi-directional PCET studies are of particular interest for understanding PCET in various solvent environments for applications of energy storage and the modeling of biological systems.

VI.6. Experimental section

VI.6.1. Materials

Phenyl cyanate (PhOCN)[26] was prepared as described previously. Bromoferrocene (**1**) was purchased and used as received. Amidinium-ferrocene chloride (**Fc1**) and amidiniumethynylferrocene chloride (**Fc2**) were prepared using published methods.[27]

VI.6.2. Electrochemistry

Electrochemical experiments were carried out using a Bioanalytical Systems (BAS) Model CV-50W potentiostat/galvanostat or a CH Instruments Electrochemical workstation.

Bulk electrolysis and spectroelectrochemistry. Bulk electrolysis on **Fc1** and **Fc2** were performed in a solution of 50 mM sodium phosphate (Na_2HPO_4) buffer. The buffer solution was filtered before using. The concentrations employed for bulk electrolysis were 1.4 mg/mL of **Fc1** and 1.6 mg/mL of **Fc2**. The pH of the solution was 9.22. Bulk electrolysis was performed using a 2-mm quartz cuvette. A Pt mesh was used as the working electrode, a silver wire was the reference electrode, and a Pt wire was the auxiliary electrode. The sample in the cuvette was sparged with nitrogen prior to electrolysis. The oxidizing potential for bulk electrolysis was set at 650 mV for **Fc1** and at 750 mV for **Fc2**. All subsequent spectroelectrochemistry spectra were referenced to the initial spectrum of each sample, which was recorded after which the spectrometer was blanked on the initial sample. Difference spectra were collected over ten minutes. The collected spectra are the difference of the initial spectrum and the spectrum at each time point.

pH-dependent electrochemistry. Samples for pH-dependent electrochemical measurements were prepared in a solution of 100 mM potassium phosphate and 100 mM potassium chloride in water. The sample concentration employed for electrochemistry was 0.84 mg/mL for **Fc1** and 0.36 mg/mL for **Fc2**. Aliquots of the stock solution (1 mL) were distributed into small vials and each pH point, from pH 7 to pH 12, was set with a concentrated solution of sodium hydroxide. With all pH points set in individual vials, DPV was performed on each sample. A Pt wire was used as the working electrode, a Ag/AgCl was used as the reference electrode, and a Pt mesh was used as the auxiliary electrode. Redox couples were referenced to SCE by using a ferrocenium/ferrocene internal standard of 0.307 V vs SCE.[28] For **Fc1**, a range of 300 to 800 mV was sampled with a 0.004 step size, 0.1 sec pulse width, 0.0167 sample width, 0.2 sec pulse period and 100 μA sensitivity. For **Fc2**, a range of 100 to 700 mV was sampled with a 0.004 step size, 0.1 sec pulse width, 0.0167 sample width, 0.2 sec pulse period and 10 μA sensitivity.

VI.6.3. Spectroscopy

Absorption spectra were obtained using a Spectral Instruments 440 Series spectrophotometer or a Varian Cary 5000 UV-vis-NIR spectrophotomer. Absorption spectroscopy on samples of ferrocene-amidinium (**Fc1**) and ferrocene-alkynylamidinium (**Fc2**) was performed in a 1-cm pathlength clear fused-quartz cuvette (Starna cells). Samples of **Fc1** and **Fc2** were prepared in a 50 mM sodium phosphate buffer. Peaks in the absorption spectra were observed at 265 nm (ε , 44,300 $M^{-1}cm^{-1}$), 322 nm (ε , 11,400 $M^{-1}cm^{-1}$), and 450 nm (ε , 4,000 $M^{-1}cm^{-1}$) for **Fc1** and 293 nm (ε , 45,500 $M^{-1}cm^{-1}$), 355 nm (ε , 9,700 $M^{-1}cm^{-1}$), and 466 nm (ε , 5,600 $M^{-1}cm^{-1}$) for **Fc2**.

pH-dependent electronic absorption spectroscopy. Amidinium acidity constants were determined in water by performing a pH titration in deionized water with 10 mM KCl and buffered with 10 mM potassium phosphate. A solution of 0.1 M NaOH in 10 mM potassium phosphate and 10 mM KCl was used to set the pH. An absorption spectrum was taken at each pH point in a 2-mm pathlength cuvette. Two different concentration ranges were prepared for each compound in order to clearly monitor the pH-dependence of all three spectral bands. For **Fc1**, 90 μM and 580 μM solutions were prepared; for **Fc2**, 90 μM and 850 μM solutions were used. A stock solution of **Fc1** or **Fc2** in 0.1 M NaOH (in 10 mM KCl/10 mM potassium phosphate) was added to the sample to adjust the pH while maintaining the same **Fc1** or **Fc2** concentrations in the sample throughout the course of the experiment.

Ground state ET experiments. Ground state ET studies were performed using steady-state electronic absorption spectroscopy in a 2-mm pathlength cuvette. Unbuffered solutions of 1.7 mM **Fc1** and 1 mM **Fc2** were prepared with 5 equivalents and 10 equivalents of hexamine ruthenium(III) chloride, respectively. The initial pH of each sample was pH 6.5 for **Fc1** and pH 6.0 for **Fc2**. The pH was adjusted by addition of sodium hydroxide and the electronic absorption spectrum was recorded upon each addition of base (to final pH 10.1 for **Fc1** and pH 10.4 for **Fc2**). The difference spectra clearly reveal formation of the oxidized species as pH is increased for both samples.

VI.7. References

1. Kubo, M.; Mori, Y.; Otani, M.; Murakami, M.; Ishibashi, Y.; Yasuda, M. Hosomizu, K.; Miyasaka, H.; Imahori, H.; Nakashima, S. *Chem. Phys. Lett,* **2006**, *429*, 91-96.
2. Cao, W.; Ferrance, J. P.; Demas, J. Landers, J. P. *J. Am. Chem. Soc.* **2006**, *128*, 7572-7578.
3. Fushimi, T.; Oda, A.; Ohkita, H.; Ito, S. *Langmuir*, **2005**, *21*, 1584-1589.
4. Araki, Y.; Yasumura, Y.; Ito, O. *J. Phys. Chem. B* **2005**, *109*, 8943-9848.
5. Lee, E. J.; Wrighton, M. A. *J. Am. Chem. Soc.* **1991**, *113*, 8562-8564.
6. Fery-Forgues, S.; Delavaux-Nicot, B. *J. Photochem. Photobio. A* **2000**, *132*, 137-159.
7. Siemling, U.; Vor der Bueggen, J.; Vorfeld, U.; Neumann, B.; Stammler, A.; Stammler, H.-G.; Brockhinke, A.; Plessow, R.; Zanello, P.; Laschi, F.; de Biani, F. F.; Fontani, M.; Steenken, S.; Stapper, M.; Gurzadyan, G. *ChemEur. J.* **2003**, *9*, 2819-2833.

8. Delgadillo, A.; Leiva, A. M.; Loeb, B. *Polyhedron* **2005**, *24*, 1749-1754.

9. Heinze, K.; Hempel, K.; Beckmann, M. *European J. Inorg. Chem.* **2006** *10*, 2040-2050.

10. Chang, C. J.; Brown, J. D. K.; Chang, M. C. Y.; Baker, E. A.; Nocera, D. G. In *Electron Transfer in Chemistry*; Balzani, V., Ed.; Wiley-VCH: Weinheim, Germany, 2001; Vol. 3.2.4, pp 409-461.

11. Cukier, R. I.; Nocera, D. G. *Annu. Rev. Phys. Chem.* **1998**, *49*, 337-369.

12. Chang, C. J.; Chang, M. C. Y.; Damrauer, N. H.; Nocera, D. G. *Biochim. Biophys. Acta* **2004**, *1655*, 13-28.

13. Turró, C.; Chang, C. K.; Leroi, G. E.; Cukier, R. I.; Nocera, D. G. *J. Am. Chem. Soc.* **1992**, *114*, 4013-4015.

14. de Rege, P. J. F.; Williams, S. A.; Therien, M. J. *Science* **1995**, *269*, 1409-1413.

15. Damrauer, N. H.; Hodgkiss, J. M.; Rosenthal, J.; Nocera, D. G. *J. Phys. Chem. B* **2004**, *108*, 6315-6321.

16. Roberts, J. A.; Kirby, J. P.; Nocera, D. G. *J. Am. Chem. Soc.* **1995**, *117*, 8051-8052.

17. Roberts, J. A.; Kirby, J. P.; Nocera, D. G. *J. Am. Chem. Soc.* **1997**, *119*, 9230-9236.

18. Roberts, J. A.; Kirby, J. P.; Wall, S. T.; Nocera, D. G. *Inorg. Chim. Acta* **1997**, *263*, 395-405.

19. Kirby, J. P.; Roberts, J. A.; Nocera, D. G. *J. Am. Chem. Soc.* **1997**, *119*, 9230-9236.

20. Hodgkiss, J. M.; Damrauer, N. H.; Pressé, S.; Rosenthal, J.; Nocera, D. G. *J. Phys. Chem. B.* **2006**, *110*, 18853-18858.

21. Irebo, T.; Reece, S. Y.; Sjödin, M.; Nocera, D. G.; Hammarström, L. *J. Am. Chem. Soc.*, **2007**, *129*, 15462-15464.

22. Ishikita, H.; Soudackov, A. V.; Hammes-Schiffer, S. *J. Am. Chem. Soc.*, **2007**, *129*, 11146-11152.

23. Rosenthal, J.; Young. E. R.; Nocera, D. G. *Inorg. Chem.* **2007**, *46*, 8668-8675.

24. Rosenthal, J.; Hodgkiss, J. M.; Young, E. R.; Nocera, D. G. *J. Am. Chem. Soc.* **2006**, *128*, 10474-10483.

25. Young. E. R.; Rosenthal, J. R.; Nocera, D. G. *Chem. Comm.* **2008**, *20*, 2322-2324.

26. Moss, R. A.; Chu, G.; Sauers, R. R. *J. Am. Chem. Soc.* **2005**, *127*, 2408-2409.

27. Young, E. R., Rosenthal, J.; Nocera, D. G. manuscript in preparation

28. Bard, A. J.; Faulkner, L. R. *Electrochemical Methods. Fundamentals and Applications*; John Wiley: New York, 1980.

Chapter VII

Dexter energy transfer through asymmetric hydrogen-bonded interfaces of ferrocenyl-amidinium compounds

Chapter VII

VII.I. Introduction and motivation

Investigations concerning the effect of proton motion on through-bond deactivation have been explored primarily for ET. The influence of proton motion on ET has been investigated by the strategy of photoinduced fixed-distance ET via incorporation of an intervening proton network.[1-3] The inspiration for initial studies of PCET lies in a host of biological systems that employ guanine-cytosine base-pairs[4] and arginine-asparate salt bridges.[5-13] Since these initial studies, PCET has become a generalized mechanism in radical enzymology, enzymatic catalysis and bioenergy conversion.[14-18] The approach to PCET studies relies on the assembly of De-Ae pairs juxtaposed by hydrogen bonded interfaces formed by carboxylic acid dimers,[19,20] and amidinium-carboxylate salt bridges.[21-26] PCET and ET are differentiated from each other by the ability of the charge shift resulting from the motion of the proton to couple to the charge shift of the ET through the polarization of the surrounding environment in PCET.[11,27-37] A recent model suggests that, even in the absence of formal PT, fluctuations of the proton position within the interface may exert significant influence over the ET component of PCET.[20,38] These models for PCET are typically derived from the semi-classical nonradiative decay formalism underlying Marcus Theory for ET.

Both ET and through-bond (Dexter) energy transfer (DEnT) are described by the semi-classical nonradiative decay formalism. It follows then that an intervening proton network should influence processes undergoing not only ET, but DEnT as well. The semi-classical nonradiative decay formalism is distinguished from conventional classical formalisms by the explicit consideration of the electronic coupling constant, |*V*|. The coupling constant of a PCET reaction is attenuated when compared to similar covalently ET reaction.[20] Similarly, attenuation of |*V*| for DEnT systems might be expected upon incorporation of a proton interface. Kinetic isotope studies have revealed sensitivity of PCET rates to substitution of protons within interface with deuterons.[13,20] For DEnT systems juxtaposed by a proton interface, the hydrogen bonds may modulate the kinetics of DEnT based on the protonation or deuteration of the interface.

With judicious choice of donor and acceptor moieties, a De-Ae system is constructed around a proton interface for which ET is not the quenching mechanism, but instead DEnT dominates. As introduced in Chapter VI, ferrocene derivatives have been incorporated into a large number of ET and EnT model systems due to their rich redox properties, reversible oxidation and general photostability stability.[39-47] Accordingly, the use of ferrocenyl moieties appended with hydrogen-bonding functionalities is appealing for PCET and DEnT mechanistic studies. The synthesis of a set of ferrocenyl amidine derivatives in which the protonic group is either fused directly to the redox center or bridged by phenylene or ethynyl groups has enabled these studies to be undertaken. Varying degrees of electronic communication between ferrocene and the pendant amidine are revealed by electrochemistry and UV-vis absorption spectroscopy in the aprotic solvent DCM, which supports efficient hydrogen bonding between the amidine and carboxylic acid functionalities.

For the systems presented in this Chapter, D---[H^+]---A assembly is driven via association of a carboxylic acid pendant on one bpy ligand with the amidine hydrogen bonding functionality of the ferrocenyl-amidine moieties. The two ancillary bpy ligands that comprise the Ru(II) polypyridyl complexes are varied to tune the electronic structure and excited state properties as addressed in the body of this Chapter.[48,49] Ru(II) polypyridyl complexes have been successfully employed as photo-triggers for ET, PCET and EnT reactions.[13,16-18,50,51] This photo-technology is imported here to initiate the PCEnT.

Previous studies involving ferrocene and Ru(II) polypyridyl complexes have established excited state deactivation of Ru(II) polypyridyl complexes by both ET and EnT.[5-9] In many reports, the dominant quenching mechanism has not been unequivocally proven because they have either involved bimolecular quenching pathways or ferrocene moieties tethered to the Ru(II) polypyridyl complex via a floppy alkane or alkene chain.[6-9] Thus, the mechanism may be obscured by diffusion of conformational changes. The D---[H^+]---A dyads formed for these studies represent an improvement over previous work in that they employ a rigid bridge between the donor and acceptor to hold the two moieties apart, thereby defining a fixed De-Ae distance. The design of these systems facilitates characterization of the operative quenching mechanism and the role of the proton interface in influencing deactivation of the Ru(II) bpy complexes.

In this Chapter, a new De-Ae system is presented and a systematic analysis of the possible quenching mechanisms (ET, DEnT, and Förster EnT) is discussed. A series of variable-temperature experiments are performed to unequivocally assign the quenching mechanism. Further, the influence of the hydrogen bonded interface on observed rates is established. The protons of the intervening hydrogen interface are exchanged for deuterium atoms to elucidate the isotopic dependence on emission quenching. In turn, kinetic isotope studies demonstrate that proton fluctuations within the bridge modulate kinetics and that the KIE behavior of the system depends intimately on the excited state electron localization within the Ru(II) bpy photo-trigger. The systems demonstrate modulation of the nonradiative decay kinetics and parameters by the proton interface to allow us to establish a proton-coupled energy transfer (PCEnT) mechanism.

VII.2. Fc and Ru compounds

The supramolecular D---[H$^+$]---A dyads employed for comparative kinetics investigations, displayed in Figure VII.1, are formed from the association of a

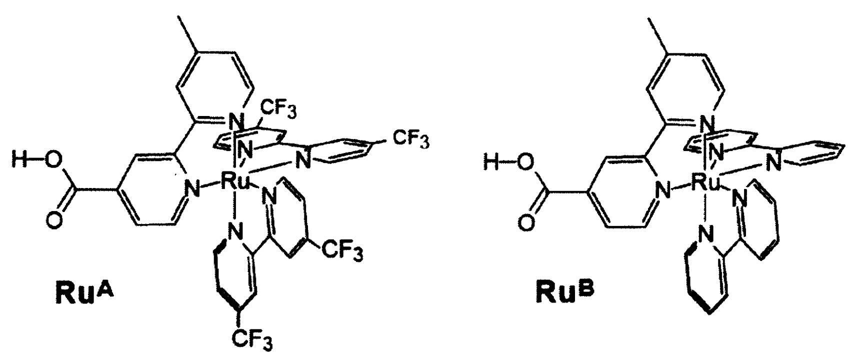

Figure VII.1. Ferrocenyl-amidine and Ru(II) polypyridyl compounds.

ruthenium(II) polypyridyl complex, $\mathbf{Ru^A}$ or $\mathbf{Ru^B}$ to a ferrocenyl-amidine moiety, **Fc1**, **Fc2**, or **Fc3**. Synthesis of all three ferrocenyl-amidine moieties was performed by Dr. Joel Rosenthal following the synthetic protocol outlined his Thesis. $\mathbf{Ru^A}$ and $\mathbf{Ru^B}$, which were prepared from published methods, were also provided by Dr. Joel Rosenthal.

VII.3. Electronic absorption spectroscopy of Fc1, Fc2 and Fc3 in DCM

VII.3.1. pH-dependent electronic absorption spectroscopy

As the amidinium functionality itself has no observable electronic absorption bands in the visible region, its electronic communication with the chromophoric moiety of the molecule is critical. The pH-dependent electronic absorption spectra of **Fc1**, **Fc2** and **Fc3** provide an experimental handle to understanding the electronic delocalization between the ferrocene donor and the amidine functionality. The absorption spectrum of each of the ferrocenyl-amidine moieties is monitored as a function of protonation state (Figure VII.2). Variation of the electronic coupling between ferrocene and the amidinium-amidine functionality results in varying degrees of perturbation to the electronic transitions in ferrocene upon deprotonation of the amidinium functionality. When electronic coupling between ferrocene and the protonic functionality is weak, electronic communication between the two components is attenuated and the absorption bands are less perturbed. The pH-dependent behavior of the electronic absorption spectra of **Fc1**, **Fc2** and **Fc3** show varying degrees of a hypsochromic

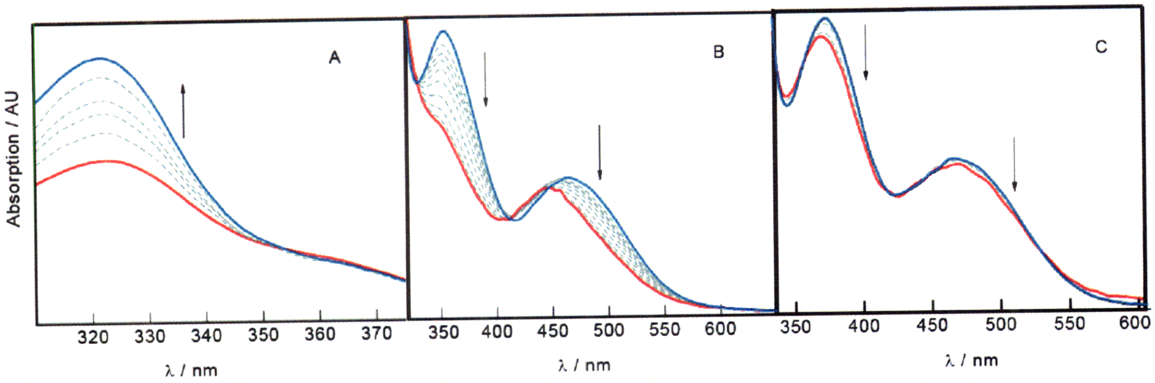

Figure VII.2. Spectral changes associated with amidinium deprotonation of **Fc1**, **Fc2** and **Fc3**. The base DMAP was used to deprotonated the amidinium functionality of (A) **Fc1**, (B) **Fc2** and (C) **Fc3**

shift for the higher energy transitions upon conversion of amidinium to amidine (Figure VII.2). Isosbestic points are maintained between the protonated (amidinium) and deprotonated (amidine) states of the protonic functionality. From these spectral signatures, the pK_a value of the amidinium functionality may be determined as described in Chapters II[52] and III.[53]

The relative degree of electronic communication between the ferrocene chromophore and the protonic interface can be inferred from the extent of the spectral shift upon titration of ferrocenyl-amidinium moieties **Fc1**, **Fc2** and **Fc3** with the base (DMAP). Of the three compounds reported, the ethynyl spacer of **Fc2** imparts the strongest electronic communication between amidine and redox center as supported by a 7 nm shift in the absorption band of **Fc2** at 355 nm (ΔE_{shift} = 567 cm^{-1}) upon deprotonation. Considerable electronic communication is also observed for both **Fc1** and **Fc3**, as both reveal smaller, yet significant shifts of 2 (ΔE_{shift} = 193 cm^{-1}) and 3 nm (ΔE_{shift} = 217 cm^{-1}), respectively (Figure VII.2) to give a trend of increased electronic coupling: directly linked (**Fc1**) ≤ phenylene bridge (**Fc3**) < ethylene bridge (**Fc2**).

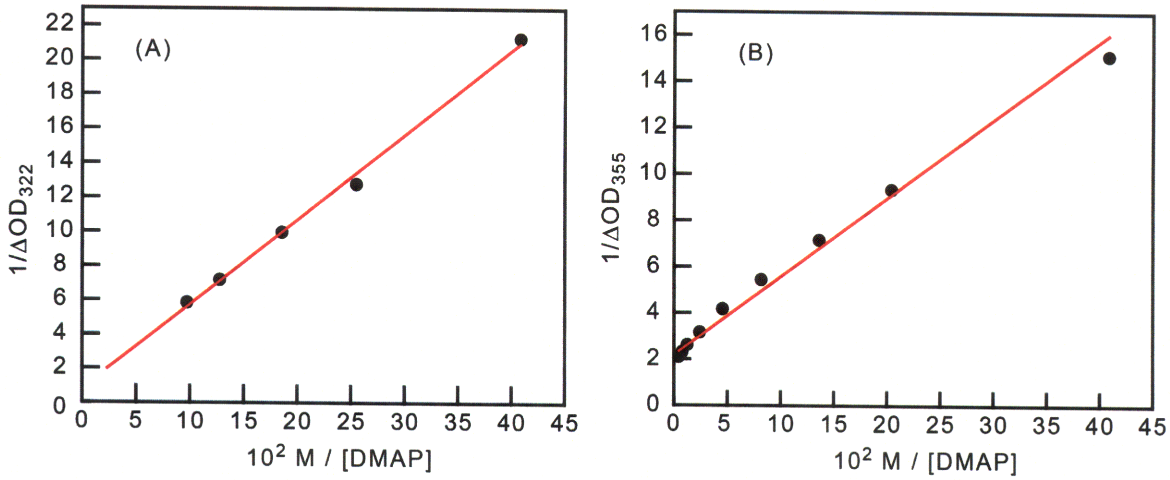

Figure VII.3. Benesi-Hildebrand plots for amidinium deprotonation of **Fc1** and **Fc2**. (A) **Fc1** and (B) **Fc2** are subjected to titration with DMAP to achieve deprotonation.

VII.3.2. *pK_a values for **Fc1, Fc2** and **Fc3***

A Benesi-Hildebrand plot ($1/\Delta A_{MLCT}$ vs. 1/[DMAP]) for the spectral shift of **Fc1** and **Fc2** with DMAP concentration yield acidity constants (K_a') for each species (Figure VII.3). Absorption spectra of **Fc1** were corrected for the contribution of DMAP absorption in the high energy spectral region owing to a DMAP absorption tail that extends to 320 nm. The absorption changes in the spectra of **Fc3** were not subject to a Benesi-Hildebrand analysis because the very small change in extinction coefficients of the protonated and deprotonated forms make such an analysis unreliable. The deprotonation constant, K_a', is obtained from the ratio of the *y*-intercept and slope of the lines shown in Figure VII.3.[54] Values of K_a'(**Fc1**) = 6.44×10^2 M and K_a'(**Fc2**) = 1.65×10^2 M are obtained. Subsequent determination of the ferrocene-amidinium pK_a value is accomplished using the relation,

$$\mathrm{p}K_\mathrm{a}(\mathrm{am}^+) = \mathrm{p}K_\mathrm{a}(\mathrm{DMAP}) - \log(K_\mathrm{a}') \qquad \text{(VII.1)}$$

The $\mathrm{p}K_\mathrm{a}'$ of DMAP in ACN is 12.33,[55] yielding ground-state $\mathrm{p}K_\mathrm{a}$ values of $\mathrm{p}K_\mathrm{a}$(**Fc1**) = 9.52 ± 0.10 and $\mathrm{p}K_\mathrm{a}$(**Fc2**) = 10.11 ± 0.10.

VII.3.3. Proton configuration in Fc-Ru dyad interfaces

Pinning down $\mathrm{p}K_\mathrm{a}$ values for the amidinium functionalities enables the static proton interface configuration to be assigned when **Fc1**, **Fc2** and **Fc3** are bound to **Ru**$^\mathrm{A}$ and **Ru**$^\mathrm{B}$ via the pendant amidine and carboxylic acid functionalities. In the amidinium-purpurin systems of Chapter III, direct observation of the proton interface is observed.[53] In these systems, the electrostatic stabilization afforded by the proton interface allows an ionized amidinium-carboxylate interface to persist in non-aqueous solvents.[53] In ACN, the electrostatic stabilization for the ionized interface is 0.18 eV. For a $\Delta\mathrm{p}K_\mathrm{a}$ difference between the two moieties greater than this stabilization energy, a non-ionized interface is observed. For the **Fc-Ru** systems, the electronic absorptions of the amidinium-bearing **Fc** shown in Figure VII.2 are overwhelmed by absorption of the Ru(II) polypyridyl complexes. Hence, the protonation state of the interface can only be inferred. Based on the $\mathrm{p}K_\mathrm{a}$ values for compounds **Fc1** and **Fc2** in ACN, the $\mathrm{p}K_\mathrm{a}$ of the carboxylic acid functionality of the Ru(II) polypyridyl complexes must be greater than 19 to furnish a non-ionized proton interface. The $\mathrm{p}K_\mathrm{a}$ of benzoic acid in ACN is ~20 and the $\mathrm{p}K_\mathrm{a}$ of acetic acid is

~20-22.[55] In view of these carboxylic acid pK_as, the static interface configuration in the **Fc-Ru** De-Ae systems is likely a non-ionized interface.

VII.4. Electrochemistry

VII.4.1. Electrochemical potentials in DCM

DPV was performed on **Ru**^{A}, **Ru**^{B}, **Fc1**, **Fc2**, and **Fc3** to characterize the electrochemical behavior of each compound and to determine ET driving force for the various dyads. Reduction and oxidation potentials were determined versus a Ag/AgCl reference electrode and are related to an internal ferrocenium/ferrocene standard in DCM with a 0.1 M $(Bu_4N)ClO_4$ electrolyte solution. DPV yields peak potentials are measured to be E_p, (v Fc^+/Fc) of E_p(**Fc1**) = 0.36 V; E_p(**Fc2**) = 0.18 V; E_p(**Fc3**) = 0.03 V; E_p(**Ru**^{A}) = −1.27 V; E_p(**Ru**^{B}) = −1.82 V. From these values, the ET driving force listed in Table III.1 is determined. For all De-Ae dyads, ET is endergonic.

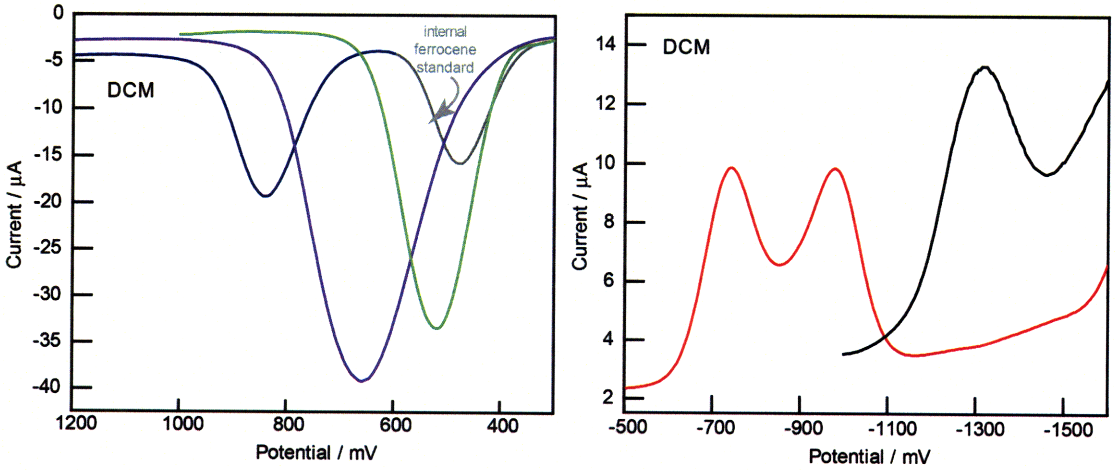

Figure VII.4. Electrochemistry on **Ru**^{A}, **Ru**^{B}, **Fc1**, **Fc2** and **Fc3**. DPV traces for **Ru**^{A} (–), **Ru**^{B} (–), **Fc1** (–), **Fc2** (–), and **Fc3** (–) in DCM shown versus an internal ferrocene standard.

*VII.4.2. Electrochemical behavior of **Ru^A** and **Ru^B** upon binding*

The electrochemical behavior of **Ru**^{A} and **Ru**^{B} upon binding was assessed by monitoring the DPV with the incremental addition of phenylamidine (Pham^0) to solutions of the **Ru** complexes. The phenylamidine provides a good probe for binding since it is unable to participate in EnT or ET reactions. Reduction potentials of E_p(**Ru**^{A}) = −1.30 eV and E_p(**Ru**^{B}) = −1.75 eV, and oxidation potentials of E_p(**Ru**^{A}) = 1.08 eV; E_p(**Ru**^{B}) = 0.84 eV; and E_p(**Fc1**) = 0.27 eV (Figure VII.5) are observed in the absence of Pham^0. THF was used as the solvent for these DPV experiments so that a small-volume electrochemical chamber could be used, as DCM produced high iR compensation values most likely due to the deleterious interaction with the vicor plug separating the two chambers in the small volume electrochemical cell. Incremental addition of Pham^0 produced only a 24 mV increase in E_p for **Ru**^{A} (up to 30 eq) and a 30 mV increase in E_p for **Ru**^{B} (up to 50 eq) (Figure VII.5). These small DPV peak shifts upon binding in a sample of 30 – 50 eq of Pham^0 together with the relatively small number of equivalents used in the sample preparation for transient emission spectroscopy experiments on the De-Ae systems (5-10 eq for Pham^0, **Fc1**, **Fc2**, **Fc3**) indicate that the presence of the binding moiety in the sample and the binding of that moiety to the carboxylic acid functionality of the ruthenium(II) complexes does not significantly perturb the electrochemistry of the **Ru** complexes. Because the electrochemical properties of **Ru**^{A} and **Ru**^{B} do not change upon binding, the ET driving force will remain constant whether **Ru**^{A} or

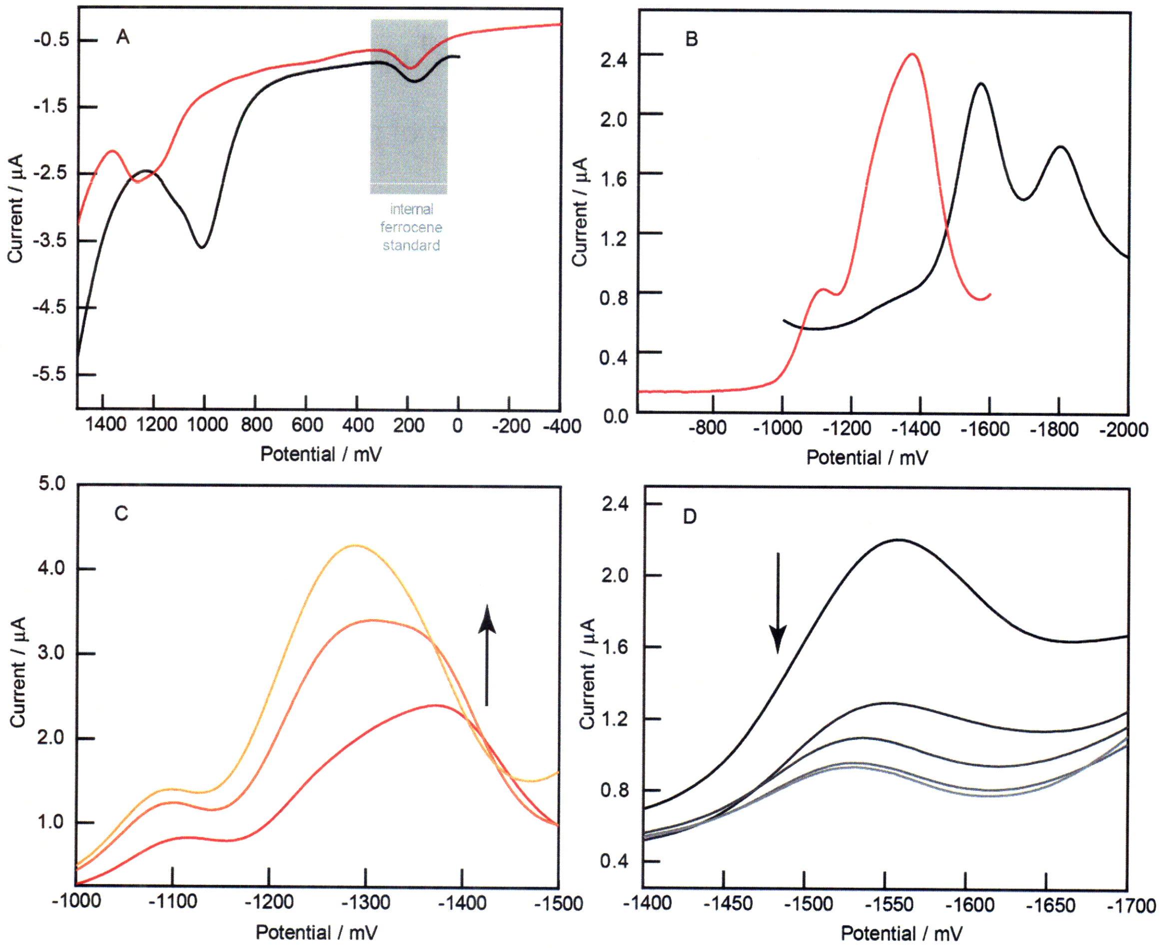

Figure VII.5. DPV for **Ru^A** and **Ru^B** in THF. (A) Oxidation potentials and (B) reduction potentials for (▬) **Ru^A** and (▬) **Ru^B**. (C) and (D) Incremental addition of phenylamidine (**Pham^0**) yielded only a 24 mV increase in E_p for up to 30 equivalents of **Pham^0** to **Ru^A** (C) and a 30 mV increase in E_p for up to 50 equivalents of **Pham^0** to **Ru^B** (D).

Ru^B is unbound or bound in De-Ae dyads. Consequently, a change of the quenching mechanism is not expected over the course of the experiment.

VII.5. Electron density of Ru(II) polypyridyl complex MLCT excited state in relation to the quenching pathway

The quenching pathway between De-Ae systems incorporating **Ru^A** and **Ru^B** is influenced by the nature of the photoexcited **Ru^A** and **Ru^B**. Of specific relevance to these studies is whether the electron density of the excited state is localized on or away from the carboxylic acid-appended bpy ligand that forms the bridge to the ferrocenyl-amidinium moiety.

Substitution on the ancillary bpy ligands of **Ru^{A}** and **Ru^{B}** affects the nature of the MLCT excited states of both compounds. The MLCT excited states in similar Ru(II) bpy complexes are reported to be dependent on the electron donating or withdrawing character of substituents appended to the ancillary bpy ligands.[56] Electron withdrawing groups direct electron localization of the MLCT excited state to those bpy ligands. Conversely, addition of electron donating groups direct the MLCT excited state to other lower lying polypyridyl ligands having no substituents or containing electron withdrawing functionalities. Infrared and resonance Raman studies performed for $Ru(II)(4\text{-}CO_2Et\text{-}4'\text{-}CH_3bpy)_2(bpy)^{2+}$, a complex for which two bpy ligands bear both an electron withdrawing ($-CO_2Et$) and an electron donating ($-CH_3$) group, reveal that electron density in the MLCT excited state resides primarily on the $4\text{-}CO_2Et\text{-}4'\text{-}CH_3$ substituted bpy ligands and *not* on the unsubstituted bpy ligand.[56] For systems of this type, the withdrawing effects of the ester functionality outweigh the electron donating effects of the methyl group. In keeping with these previous observations, the following assumptions are operative for the Ru(II) polypyridyl complexes presented in this Chapter: (i) due to electron withdrawing $-CF_3$ groups, excited state electron density is localized on the low-lying bpy ligands in dyads containing **Ru^{A}** (A = ancillary) and (ii) due to the presence of the electron withdrawing carboxylic acid and absence of groups on the ancillary ligands, excited state electron density is

Table VII.1. Electrochemical potentials for **Ru^A**, **Ru^B**, **Fc1**, **Fc2**, and **Fc3** and ET driving force.

Compound	E°_{red}(**Ru$^{II/I}$**)^a			
Ru^A	−1.27			
Ru^B	−1.82			
Compound		E°_{ox}(**Fc$^+$/Fc**)^a	ΔG_{ET}(**Fc:Ru^A**)^b	ΔG_{ET}(**Fc:Ru^B**)^b
Fc1		0.36	−0.52	−0.06
Fc2		0.18	−0.70	−0.24
Fc3		0.03	−0.85	−0.39

$^{a.}$ in V vs. Fc$^+$/Fc with 0.1 M TBAClO$_4$ as the supporting electrolyte in DCM. $^{b.}$ $\Delta G_{ET} = E_D^{ox} - E_A^{red} - \Delta G_{ES}^\circ + \Delta G(\varepsilon_S)$, ΔG_{ES}° values from Table VII.5, $\Delta G(\varepsilon_S)$, the electrostatic potential, is calculated to be ~ −0.1 for all dyads.

directed onto the bpy ligand adjacent the quenching pathway in dyads containing **Ru^B** (B = bridging). The divergent nature of excited state electron density localization for **Ru^A** and **Ru^B** translates into mechanistic differences for quenching in De-Ae dyads containing **Ru^A** and **Ru^B**. These two cases are depicted schematically in Scheme VII.1.

VII.6. Ambient temperature transient spectroscopy

With the initial characterization of **Ru^A**, **Ru^B**, **Fc1**, **Fc2**, and **Fc3**, TE experiments were undertaken on each of the 6 possible De-Ae combinations. Emission quenching is observed for every dyad. Ambient temperature TE decay profiles were collected and fit as detailed in the experimental section. For each sample, unquenched lifetime of the **Ru^A** or **Ru^B** excited state fits to a the monoexponential decay. In subsequent biexponential fitting of the quenched samples (**Ru**^{A}:**Fc** or **Ru**^{B}:**Fc**) the monoexponential **Ru**^{A} or **Ru**^{B} lifetime is fixed and fitting is performed to obtain the time constant of the quenched component. Both the quenched (τ_q) and unquenched time constants (τ_0) for each sample are compiled in Table VII.2. These lifetimes yield rate constants according to the relation $k_q = \tau_q^{-1} - \tau_0^{-1}$. The quenching rates for each De-Ae dyad are reported in Table VII.3.

Kinetic isotope experiments mat be executed by isotopically labeling the proton interface.. The proton-coupled quenching for dyads containing **Ru**^{A} yields normal KIEs (KIE > 1) when bound to each ferrocene compound (Figure VII.6): KIE(**Fc1**:**Ru**^{A}) = 1.62 ± 0.09, KIE(**Fc2**:**Ru**^{A}) = 1.25 ± 0.08, and KIE(**Fc3**:**Ru**^{A}) = 3.1 ± 0.3, whereas dyads containing **Ru**^{B} reveal inverse KIEs (KIE < 1): KIE(**Fc1**:**Ru**^{B}) = 0.55 ± 0.01, KIE(**Fc2**:**Ru**^{B}) = 0.84 ± 0.02 and KIE(**Fc3**:**Ru**^{B}) = 0.90 ± 0.02.

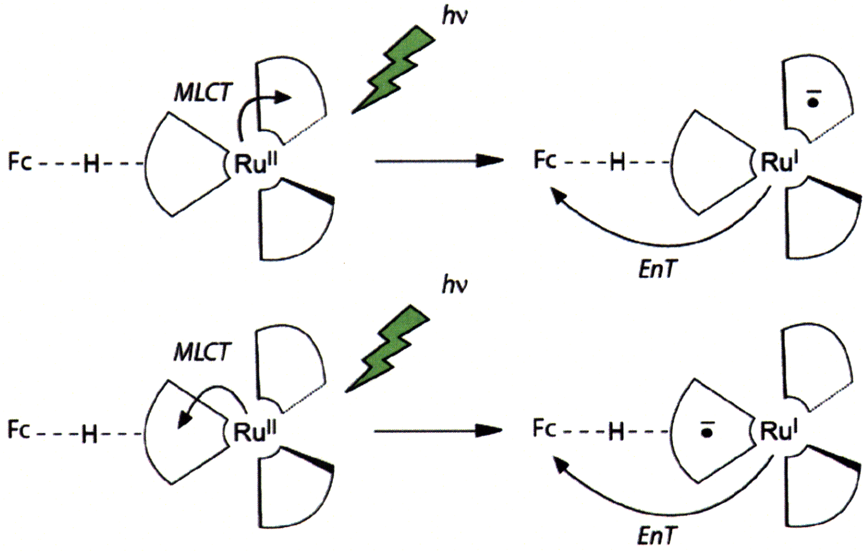

Scheme VII.1. Excited-state electron density with respect to EnT pathway for **Ru**^{A} and **Ru**^{B}. Depiction of MLCT-excited state localization with respect to the hydrogen bonded interface, giving rise to the two distinct pathways that mediate PCEnT in dyads containing **Ru**^{A} (top) and **Ru**^{B} (bottom)

Table VII.2. Ambient temperature time constants for **Ru^{A}**[H/D], **Ru^{B}**[H/D] and each of dyads formed upon binding of **Fc1**, **Fc2**, and **Fc3**.

Moiety	τ[H] / μs	τ[D] / μs
Ru^{A}	1.25	1.1
Ru^{A}:Fc1	0.41	0.26
Ru^{A}:Fc2	0.25	0.20
Ru^{A}:Fc3	0.19	0.16
Ru^{B}	0.84	0.87
Ru^{B}:Fc1	0.27	0.45
Ru^{B}:Fc2	0.34	0.38
Ru^{B}:Fc3	0.33	0.55

These disparate KIE results for the two different Ru complexes prompted additional experiments to be undertaken. In an effort to establish the quenching mechanism at play in these De-Ae systems, TA spectroscopy was undertaken to search for evidence of a CS state, which would be indicative of an ET quenching pathway. Spectral signatures associated with CS however were not observed. The absence of a CS signature does not necessarily exclude ET as the dominant quenching mechanism if the back reaction is significantly accelerated with regard to the forward reaction. For such a case, the CT product will not accrue to an appreciable extent.[49,57] Such a case occurs for the D---[H^{+}]---A porphyrin systems reported in Chapter IV.[57] In these systems, a spectrally distinct porphyrin radical cation signature can be observed with single-wavelength TA experiments at the isosbestic point of the unbound porphyrin. Without the convenience of this

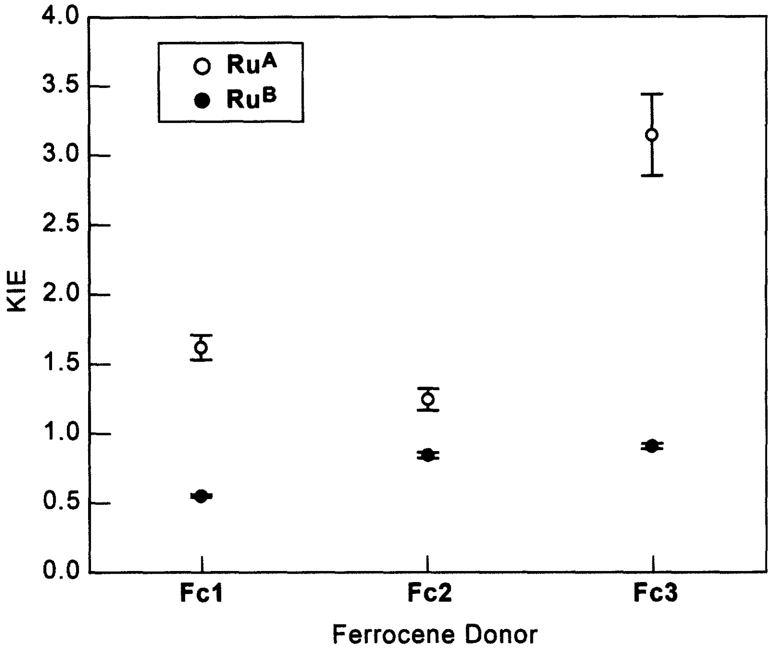

Figure VII.6. KIE for **Ru**^{A} and **Ru**^{B} PCEnT dyads. Graphical representation, including experimental error bars, of the KIE for both photo-oxidant with each ferrocene electron donor. Open circles represent **Ru**^{A}, and filled circles represent **Ru**^{B}.

spectroscopic observable, clear detection of the porphyrin radial cation that enabled quantification of CS and CR rates would not have been possible. Unfortunately, these Ru(II) bpy systems lack the clear spectral signatures for similar straight-forward detection of the CS state as the both the excited state and the CS contain a reduced bpy ligand leading to similar TA signatures in each case.

Other potential quenching mechanisms include EnT via DEnT or Förster resonance energy transfer (FRET). To assist in distinguishing these mechanisms, variable-temperature experiments were undertaken.

Table VII.3. Kinetics for emission quenching in De-Ae dyads.

Donor-Acceptor Dyads:	**RuA** 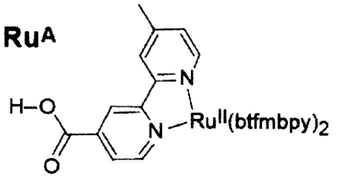		**RuB** 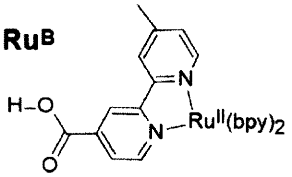	
	$k_q[H]/10^6 s^{-1}$[a]	$k_q[D]/10^6 s^{-1}$[a]	$k_q[H]/10^6 s^{-1}$[a]	$k_q[D]/10^6 s^{-1}$[a]
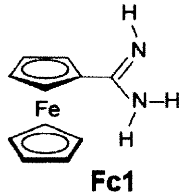 **Fc1**	4.5(2)	2.77(9)	1.79(3)	3.23(4)
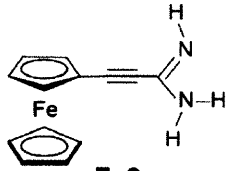 **Fc2**	2.38(9)	1.91(9)	3.45(7)	4.12(5)
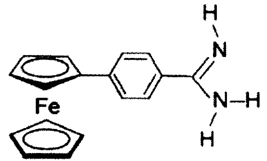 **Fc3**	3.3(3)	1.05(3)	5.21(5)	5.8(1)

VII.7. Excluding Förster resonance energy transfer

The viability of FRET transfer is considered in this section for these De-Ae systems. The intramolecular De-Ae systems in this Chapter are separated by a rigid spacer, and thereby lend themselves well to analysis with FRET theory. The rate of FRET is expressed as follows[58]:

$$k_{ET}(\text{Förster}) = \frac{1}{\tau_D}\left(\frac{R_0}{r}\right)^6 \qquad \text{(VII.2)}$$

where τ_f is the decay time of the fluorescent species in the absence of quencher, r is the donor-to-acceptor distance, and R_0 is the Förster distance, which is defined as the distance at which energy transfer efficiency is 50%. R_0 is defined as,

$$R_0^6 = \frac{900(\ln 10)\kappa^2\phi_D}{128\pi^5 N\eta^4}\int_0^\infty F_D(\lambda)\varepsilon_A(\lambda)\lambda^4 d\lambda \qquad \text{(VII.3)}$$

R_0 is highly dependent on the overlap integral, which expresses the degree of spectral overlap between the donor emission spectra and the acceptor absorption spectra. The quantum yield of the fluorescent species, ϕ_D, the refractive index of the medium, η, and an orientation factor, κ^2, describing the orientation of the transition dipoles for the donor and acceptor are other

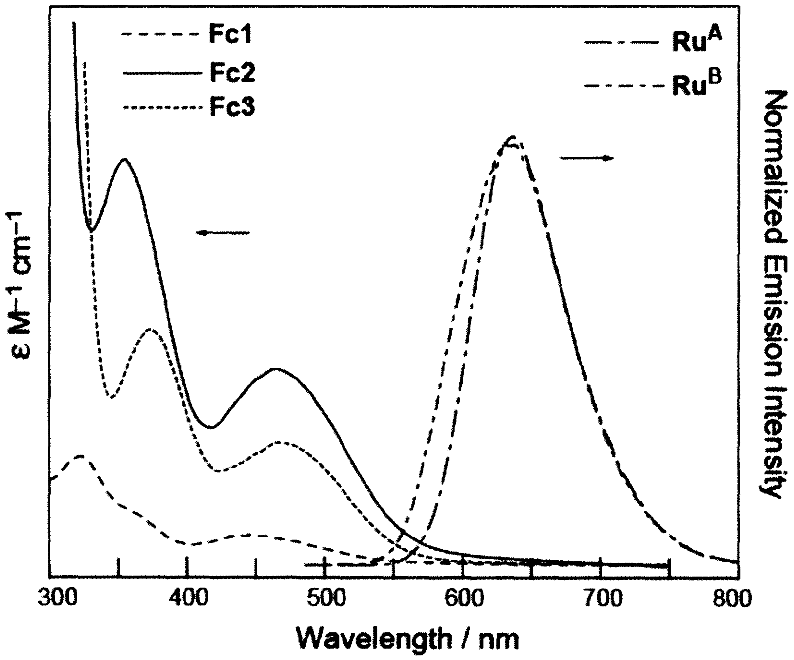

Figure VII.7. Spectral overlap between absorption spectra of **Fc1**, **Fc2**, and **Fc3** and the emission spectra of **Ru**^{A}, **Ru**^{B}.

parameters in the R_0. *N* is Avogadro's number. For these systems, ϕ_D is estimated as 0.03[59], κ^2 is 0.667 for randomly oriented transition dipoles (this value is typically chosen for FRET calculations and will lead to an error of not more than 35%), and η for DCM is 1.4212[60].

The De-Ae systems discussed in these studies show poor spectral overlap between the donor emission and acceptor absorption, as shown in the scaled spectra in Figure VII.7. Poor spectral overlap leads to a small overlap integral and a relatively slow calculated FRET rate. Comparison between calculated FRET rates and the observed quenching rates in Table VII.4 reveal that the predicted FRET rates are more than two orders of magnitude smaller than the observed quenching rates and therefore are not likely to contribute to the reported quenching. The limitation for FRET in these systems is the negligible overlap integral that results in predicted FRET rates 10-200 times slower than observed rates.

Table VII.4. Calculated FRET rates compared to observed quenching rates for De-Ae dyads.

	Fc1: Ru^B	**Fc2: Ru^B**	**Fc3: Ru^B**	**Fc1: Ru^A**	**Fc2: Ru^A**	**Fc3: Ru^A**
$\tau_f \times 10^6$ /sec	1.26	1.26	1.26	8.67	8.67	8.67
$r \times 10^{-8}$ / cm	9.20	11.5	13.3	9.20	11.5	13.3
$R_0^6 \times 10^4$ / Å	5.79	36.2	14.7	5.32	32.1	13.0
k_{ET} calc $\times 10^4$ /sec	7.58	1.24	2.11	1.01	1.60	2.71
$k_{[H]}$ obs $\times 10^4$ /sec	179.	345.	521.	448.	238.	330.
$k_{[D]}$ obs $\times 10^4$ /sec	323.	412.	582.	277.	191.	105.

VII.8. Spectroscopic investigation to determine quenching mechanism

Variable-temperature steady-state emission and transient PL studies were undertaken in an effort to determine the operative quenching mechanism for these systems. The variable-temperature experiments are performed on **Ru^{A}:Fc1** and **Ru^{B}:Fc1** only; assignment of the quenching mechanism is assumed to be the same for **Fc2** and **Fc3**.

VII.8.1. Variable-temperature steady-state emission spectroscopy

Analysis of PL band features can yield insight to the excited state character of Ru(II) complexes and can be employed to differentiate between ET and DEnT. Spectral changes are observed for **Ru^{A}** (or **Ru^{B}**) upon addition of **Pham^{0}** or **Fc1** and upon variation in temperature (Figure VII.8). Absorption of **Ru^{A}** (or **Ru^{B}**) occurs into the singlet state, however emission occurs from the triplet state. For this reason, simple overlap of absorption and emission spectra as predicted by the Franck-Condon principle cannot be used for estimating the excited state energy and a more rigorous fitting method is required. To elucidate the excited state energy, emission spectra were fit by the single mode Franck-Condon functional form shown in equation VII.4, as described previously by Claude and Meyer[61]:

$$\mathrm{I}(\bar{\upsilon}) = \sum_{\nu_m=0}^{5}\left\{\left(\frac{\mathrm{E}_{00}-\nu_M\hbar\omega_M}{\mathrm{E}_{00}}\right)^3 \bullet \left(\frac{S_M^{\nu_M}}{\nu_M!}\right)\times \exp\left(-4(\ln 2)\left(\frac{\bar{\upsilon}-\mathrm{E}_{00}+\nu_M\hbar\omega_M}{\Delta\bar{\upsilon}_{0,1/2}}\right)^2\right)\right\} \tag{VII.4}$$

This spectral fitting method yields the zero-point energy of the ^{3}MLCT state (E_{00}), the electron-vibrational coupling constant (S_M), the vibrational spacing ($\hbar\omega_M$), and the bandwidth ($\Delta\bar{\upsilon}_{0,1/2}$). The energies of the ^{3}MLCT excited states in **Ru^A** and **Ru^B** can then be determined using the following relations:[61,62]

$$\Delta G^{\circ}_{es} = E_{00} + \lambda_o \qquad \text{(VII.5)}$$

$$\lambda_o = (\Delta\bar{\upsilon}_{0,1/2})^2 (16 k_B T \ln 2)^{-1} \qquad \text{(VII.6)}$$

where the excited state energy (ΔG^{o}_{es}) is determined by the energy of the luminescence maximum (E_{00}) and the solvent reorganization energy (λ_o) containing low-frequency modes, which are treated classically and related to the full width at half-maximum ($\Delta\bar{\upsilon}_{0,1/2}$) for a single vibronic component. Conversion of spectroscopic energy to free energy is reasonable because of negligible pressure-volume work and small electronic entropic contributions accompanying excited state production.[62, 63] Corrected emission spectra fit to the standard Franck-Condon functional form[64,65] yield the values for E_{00}, $\hbar\omega_M$, $\Delta\bar{\upsilon}_{0,1/2}$ listed in Table VII.5 for each dyad. With these values, Equations VII.5 and VII.6 furnish ΔG°_{es} for each of the four dyads (Table VII.5).

Of specific interest to this discussion is the temperature-dependence of the full-width at half-maximum, $\Delta\bar{\upsilon}_{0,1/2}$ obtained from the steady-state emission spectra. The temperature-dependence of the square of fitted bandwidth ($\Delta\bar{\upsilon}_{0,1/2}$)^2

is related to the outer sphere reorganization energy of the dyads by equation VII.7:

$$(\Delta\bar{\upsilon}_{0,1/2})^2 = (\Delta\bar{\upsilon}_{0,1/2}{}^{0})^2 + 16(\ln 2)\lambda_o k_B T \qquad \text{(VII.7)}$$

A plot of $(\Delta\bar{\upsilon}_{0,1/2})^2$ versus temperature (Figure VII.9), is constructed for which the slope of the fitted data can be used to determine λ_o, the outer sphere

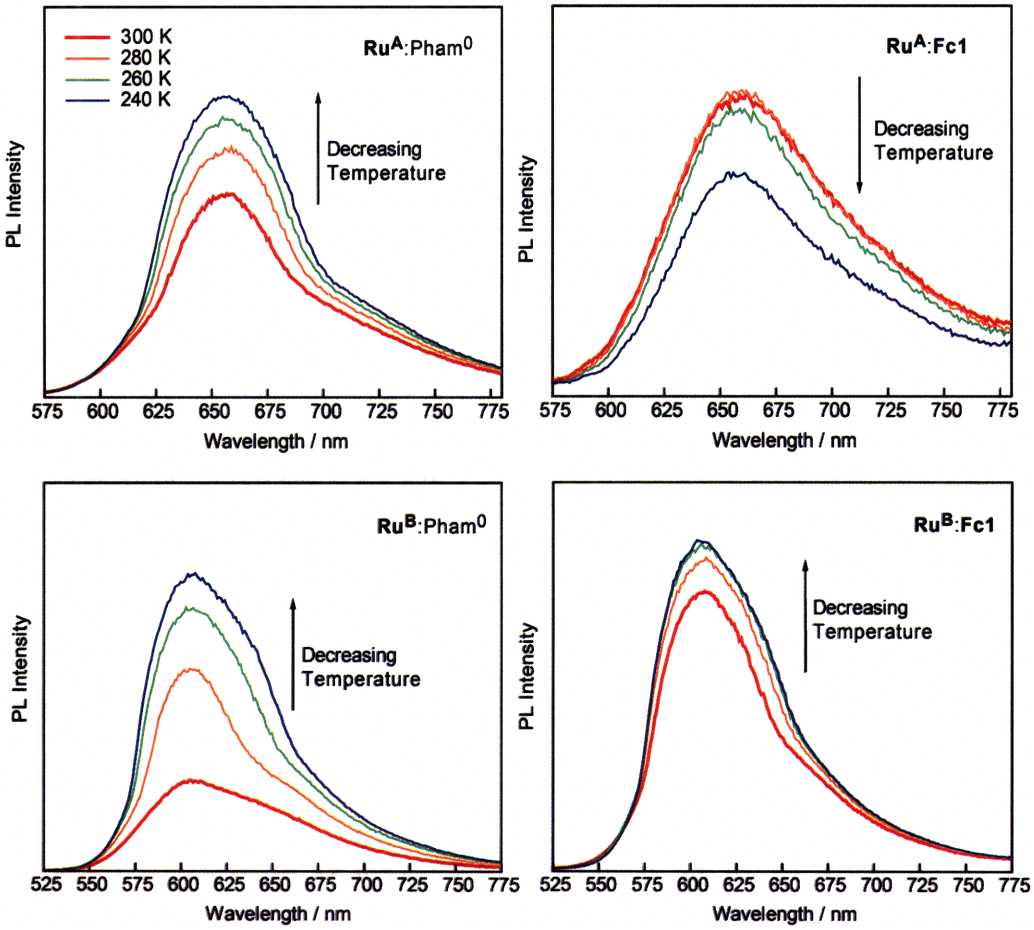

Figure VII.8. Variable-temperature steady-state emission spectra of **Ru^A** and **Ru^B**. **Ru^A** and **Ru^B** (1 × 10^{-4} M) and 10 equivalents of the BM are used. In the case of **Ru^A:Fc1**, 5 eq of **Fc1** were used as significant quenching occurred at higher equivalents of **Fc1**. In contrast to the other dyads, **Ru^A:Fc1** shows a decrease in PL intensity with decreasing temperature.

Table VII.5. Fitting results for steady-state emission spectroscopy.

Dyad	E_{00} [a] / cm^{-1}	$\hbar\omega_M$ [a] / cm^{-1}	$\Delta\bar{\upsilon}_{0,1/2}$ [a] / cm^{-1}	S_M [a]	λ_o [b] / eV	λ_M [c] / eV	□$G°_{es}$ [d] / eV
Ru^A:Pham^0	15,200	1300	1790	0.42	0.12	0.10	2.04
Ru^A:Fc1	15,200	1080	1700	0.56	0.10	0.10	2.03
Ru^B:Pham^0	16,600	1911	1420	0.58	0.11	0.09	2.13
Ru^B:Fc1	16,700	1470	1330	0.81	0.05	0.10	2.16

[a] fitted parameters determined from spectral fitting of steady-state emission spectra at 280K to equation VII.4. [b] determined from the slope of a linear fit to the data in Figure VII.9 as expressed in equation VII.7. [c] $\lambda_M = S_M \bullet \hbar\omega_M$ [d] reported in eV and determined by equations VII.5 and VII.6 in the text.

reorganization energy (Table VII.5). Additionally, the temperature-dependence of E_{00} is plotted versus temperature (Figure VII.10). The change in E_{00} with temperature ($\delta E/\delta T$) represents the entropic change accompanying excited state decay and arises primarily from changes in the solvent librations, ΔS^0_{lib}. ($\delta E/\delta T = \Delta S^0_{lib}$). The values of E_{00} vary negligibly with temperature over the range sampled.

VII.8.2. Variable-temperature time resolved emission spectroscopy

Variable-temperature TE spectroscopy was performed for **Ru^A**, **Ru^B**, **Ru^A:Fc1** and **Ru^B:Fc1** at 20 K intervals from 300 K to 180 K. The emission profiles are fit monoexponentially to yield the MLCT-excited state lifetimes of the unquenched **Ru^A** and **Ru^B**. Lifetimes of **Ru^A** and **Ru^B** increase linearly with decreasing temperature over the entire temperature range (Figure VII.11). The emission profiles of the **Ru^A:Fc1** and **Ru^B:Fc1** dyads are colleted over the same temperature ranges and fit biexponentially with the longer lifetime component fixed to the lifetime obtained from the control experiment at each temperature. Figure VII.12 plots the quenching rates for **Ru^A:Fc1** and **Ru^B:Fc1** versus temperature. A linear dependence of the quenching rate versus temperature is obtained over the temperature range of 300 to 240 K. At temperatures below 240 K, a discontinuity in the linear trend occurs, and it is attributed to dissociation of the De-Ae systems at lower temperatures in DCM. The same type of discontinuity is observed for the system in THF. These TE quenching results are addressed further in Section VII.9.3 under the framework of the semi-classical formalism for nonradiative quenching processes.

VII.9. Quenching mechanism: Electron vs. energy transfer

VII.9.1. Considerations for ET and DEnT

Through-bond super-exchange energy transfer, DEnT, is described by the expression,[66]

$$k_{\mathrm{ET}}(\mathrm{Dexter}) = \frac{2\pi}{\hbar} K^2 e^{\frac{-2r}{L}} \int_0^\infty F_{\mathrm{D}}(\lambda)\varepsilon_A(\lambda) d\lambda \qquad \text{(VII.8)}$$

K is a constant with units of energy, *L* is also a constant value called the effective average Bohr radius, and *r* is the De-Ae distance. As shown by equation VII.8, the DEnT rate constant decreases exponentially with distance.

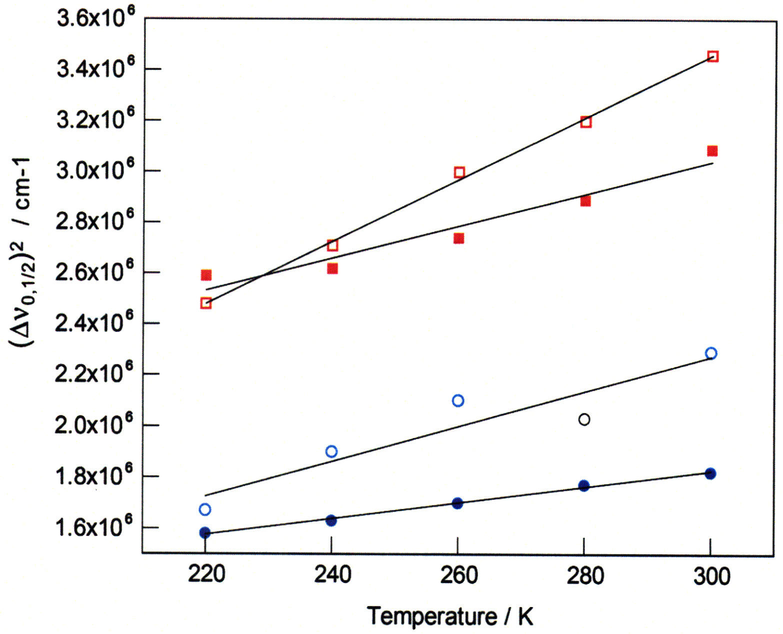

Figure VII.9. Temperature dependence variation of $(\Delta\nu_{0,1/2})^2$ for **Ru^A** and **Ru^B**. **Ru^A**:Pham^0 (□); **Ru^A**: **Fc1** (■); **Ru^B**: Pham^0 (○); **Ru^B**: **Fc1** (●).

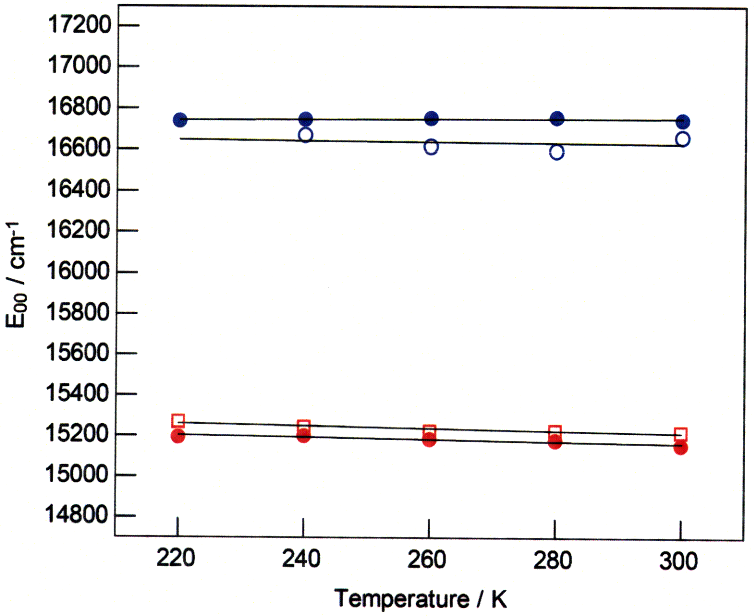

Figure VII.10. Temperature dependence of the energy of the luminescence maximum (E_{00}). **Ru^A**:Pham^0 (□); **Ru^A**: **Fc1** (■); **Ru^B**: Pham^0 (○); **Ru^B**: **Fc1** (●)

The ET rate constant also exhibits an exponential distance dependence that originates from the square of the electronic coupling matrix element H_{RP}[67]:

$$H_{RP} = V_0 e^{\frac{-\beta(r-R_0)}{2}} \qquad \text{(VII.9)}$$

where R_0 is the van der Waals separation and β is a damping term typically on the order of 0.8 – 1.2 $Å^{-1}$. The L value of DEnT is similar to the β value in Marcus Theory. The distance dependence of ET, k_{ET}, can therefore be written as,

$$k_{ET} = k_0 e^{-\beta(r-R_0)} \qquad \text{(VII.10)}$$

The distance dependence of the two quenching mechanisms is difficult to use to distinguish the two mechanisms since DEnT rates falls off at 2r, while ET rates falls off with r. Although ET may have a slight advantage over DEnT, the factor of 2 is difficult to detect experimentally. However, careful analysis of the variable-temperature spectroscopy can be exploited to differentiate between ET and DEnT. The analysis of these results follows.

VII.9.2. Solvent reorganization energy as the key to distinguishing ET and DEnT

Both DEnT and ET processes can be analyzed under the semi-classical formalism to describe rates of nonradiative processes:

$$k_q = \frac{4\pi^2}{h} \bullet \left|V^2\right| \bullet \frac{1}{\sqrt{4\pi\lambda_s k_B T}} \bullet \exp\left(-\frac{(\Delta G_0 + \lambda_s)^2}{4\lambda_s k_B T}\right) \qquad \text{(VII.11)}$$

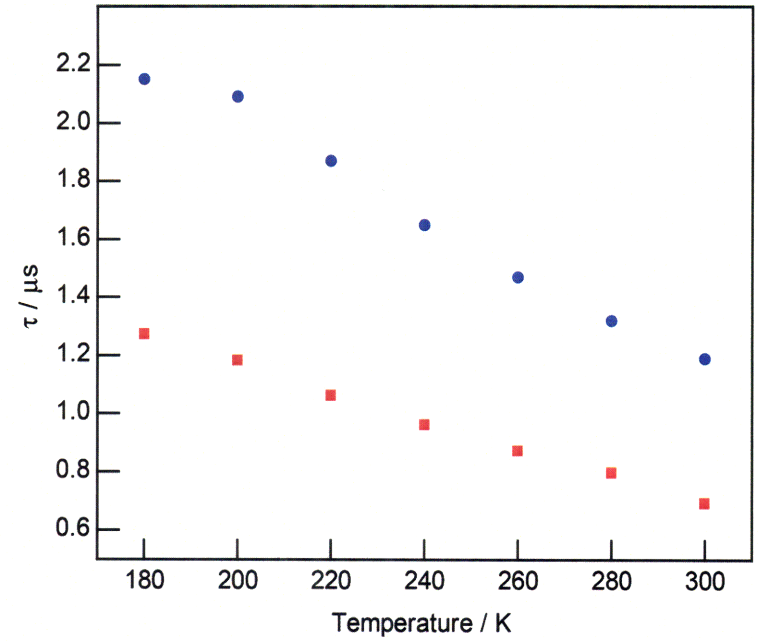

Figure VII.11. Emission lifetime versus temperature for unbound **Ru^A** and **Ru^B**. Lifetimes for **Ru^A** (🟥) and **Ru^B** (●) in DCM upon 400 nm excitation.

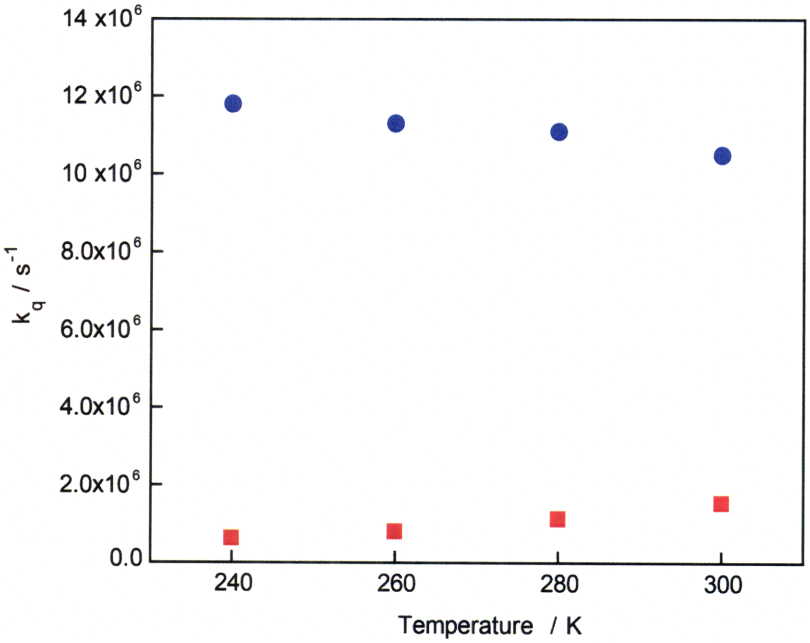

Figure VII.12. Variation of the observed quenching rate for **Ru^A:Fc1** and **Ru^B:Fc1** with temperature. The unexpected increase in k_q with decreasing temperature for **Ru^B:Fc1** is attributed to the complex nature of thermal population equilibrium existing between the lowest MLCT state and the ancillary ligands in **Ru^B**. **Ru^A:Fc1** (🟥); **Ru^B:Fc1** (●) in DCM.

where ΔG_0 is the free energy change associated with the reaction, λ_s is the reorganization energy of the process, and $|V|$ is the electronic coupling constant between the donor and acceptor.

Of particular importance to distinguishing between ET and DEnT is the solvent reorganization energy term. Since no charge is formally transferred in DEnT, the solvent reorganization energy, λ_s, due to the solvent (outer-sphere, λ_o) should be notably less for DEnT as opposed to ET. Typical λ_s values (λ_o and λ_i for inner-sphere contributions) can be on the order of 1-2 eV for ET processes, whereas they are significantly less on the order of 0.1-0.2 eV for DEnT processes.[68 - 71] As demonstrated in Chapters IV and V, variable-temperature time-resolve PL studies may be used to experimentally determine λ_s. Towards this end, such studies on **Ru^A:Fc1** and **Ru^B:Fc1** are presented.

Variable-temperature transient PL studies on **Ru^A** and **Ru^B** yield a linear dependence of the excited state lifetime with temperature (Figure VII.11). Conversely, variable-temperature transient PL measurements on **Ru^A:Fc1** and **Ru^B:Fc1** show a discontinuity in the temperature-dependent quenching rate between 240 K and 220 K; thus only 300 K to 240 K date is presented for analysis. The quenching rates for **Ru^A:Fc1** and **Ru^B:Fc1** dyads are plotted versus temperature (Figure VII.12) and are presented in an Arrhenius plot ($\ln k_q \bullet T^{1/2}$ vs $1/T$) (Figure VII.13). When the data is plotted in the Arrhenius form, the slope of the fitted line is related to λ.

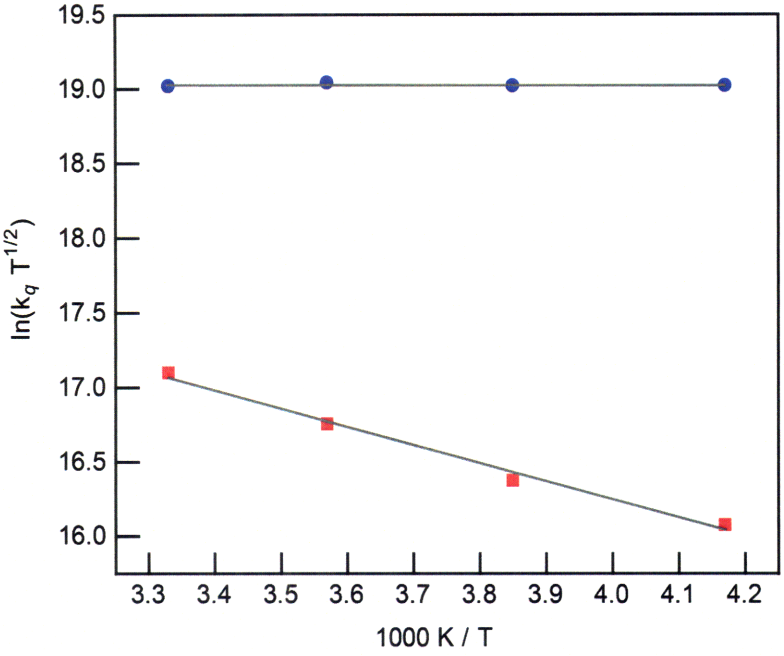

Figure VII.13. TE quenching results interpreted in the framework of the semi-classical formalism for nonradiative quenching processes. Kinetic measurements on **Ru^A:3** (🟥) and **Ru^B:3** (●) are taken in DCM upon 400 nm excitation.

VII.9.3. Failure of transient PL to deliver λ_s

An unexpected trend is obtained for the Arrhenius plot of **Ru^B:Fc1**, which is the complex for which the MLCT excited state resides on the bridging bpy ligand. For **Ru^B:Fc1**, the quenching rate increases slightly with decreasing temperature, in contrast to typical temperature-dependent ET and EnT processes. Conversely, the temperature-dependent rate of **Ru^A:Fc1** decreases with decreasing temperature as expected for typical temperature-dependence studies.

In a system using ruthenium(II) complexes analogous to **Ru^A** and **Ru^B**, Soler and McCusker have presented a thorough and insightful explanation for the temperature-dependence of transient PL data for De-Ae systems involving Ru(II) polypyridyl complexes covalently bound to dinuclear manganese complexes. To summarize their conclusions, Ru(II) polypyridyl complexes exhibit excited state relaxation that may involve low-lying ligand field excited states in addition to CT states within the MLCT manifold.[49,72-74] The thermal accessibility of other MLCT states, close in energy to the lowest-lying MLCT state, impart additional relaxation dynamics to the **Ru^A:Fc1** and **Ru^B:Fc1** dyads that are not associated with the primary De-Ae quenching dynamics of the dyad. With decreasing temperature, the thermal accessibly of the other MLCT states is reduced and the excited state remains more localized on the lowest-lying MLCT state (i.e. on the bridging bpy for **Ru^B** and on the ancillary ligand for **Ru^A**). For the case of **Ru^A:Fc1**, the excited-state localization produces an additional barrier for relaxation via the De-Ae quenching pathway. When the lowest-lying MLCT state resides on the bridging ligand, as in **Ru^B:Fc1**, the excited state remains positioned for efficient relaxation to the acceptor even as the temperature decreases and access to thermally accessible states that otherwise deplete that state is reduced. The temperature-dependent quenching data presented in this Chapter are in excellent agreement with photophysical properties of the system. Notwithstanding, the primary motivation for transient temperature-dependent studies is to determine λ_s associated with the quenching mechanism. The observed results suggest that transient PL measurements are undermined because the data includes other relaxation inherent to the Ru(II) polypyridyl complexes in addition to the desired temperature-dependent dynamics associated with the De-Ae interaction.

VII.9.4. Using steady-state PL to determine λ_s

In order to circumvent the limitation of transient PL in accessing λ_S, steady-state PL experiments were undertaken for the **Ru^A:Fc1** and **Ru^B:Fc1** dyads. Emission spectra of metal polypyridyl complexes have been shown to provide some information about the inner- and outer-sphere reorganization energies when a MLCT excited state is involved.[75-77] Spectral fitting described in equation VII.4 may be applied to variable-temperature steady-state emission spectra of **Ru^A:Pham^0**, **Ru^A:Fc1, Ru^B:Pham^0** and **Ru^B:Fc1** to extract values of the emission peak bandwidth ($\Delta\bar{\upsilon}_{0,1/2}$) (Table VII.5), which is related to the reorganization energy. Values for $\Delta\bar{\upsilon}_{0,1/2}$ are plotted versus temperature in Figure VII.9. Analysis of these data with equation VII.7 provides a reorganization energy for the deactivation process. Such an analysis for **Ru^A:Fc1** and **Ru^B:Fc1** yields λ_o(**Ru^A:Fc1**) = 0.102 eV and λ_o(**Ru^B:Fc1**) = 0.050 eV. These values are very similar to the out-sphere reorganization energies of the control systems, λ_o(**Ru^A:Pham^0**) = 0.12 eV and λ_o(**Ru^B:Pham^0**) = 0.11 eV, and both values of λ are very different from the calculated value for outer-sphere solvent reorganization energy of 0.85 eV for an ET reaction involving these dyads.[78] These results taken together with the lack of a CT state in the TA data, provide a compelling argument to assign the quenching mechanism in **Ru^A:Fc1** and **Ru^B:Fc1** dyads to Dexter EnT.

VII.10. DEnT parameters from variable-temperature experiments

The results from variable-temperature steady-state PL experiments can be analyzed to yield the DEnT parameters for the D---[H$^+$]---A systems. With knowledge of λ_s, $|V|$ for the super-exchange interaction that is responsible for DEnT may be calculated from:

$$|V| = \left[\frac{k_q \bullet h \bullet (4\pi\lambda_s k_B T)^{\frac{1}{2}}}{4\pi^2} \right]^{\frac{1}{2}} \qquad \text{(VII.12)}$$

The λ_s consists of an outer-sphere contribution, λ_o, calculated from the steady state PL experiments as well as an inner-sphere contribution, λ_i. Contributions to λ_i arise from the intramolecular vibrational mode coupled to relaxation of the ^{3}MLCT excited state of the Ru(II) polypyridyl complexes, λ_M, and the inner-sphere effects of the ferrocenyl-amidine acceptor, λ_i. The value of λ_M is calculated from the energy of the dominant mode, $\hbar\omega_M$, and S_M, the Huang-Rys factor, which are both obtained from spectral fitting using equation VII.4 ($\lambda_M = S_M \bullet \hbar\omega_M$) and are found to be ~0.10 eV. The value for λ_i associated with the acceptor is not directly known, however, is likely comparable to or less than λ_i for **Ru^A** and **Ru^B** and is estimated to be roughly ~0.1 eV.[49] Values of λ_s are calculated for **Ru^A:Fc1** and **Ru^B:Fc1** to be 0.3 eV and 0.25 eV, respectively. The λ_s values are applied to equation VII.12 to yield De-Ae coupling constants of 0.096 cm^{-1} and 0.058 cm^{-1} for **Ru^A:Fc1** and **Ru^B:Fc1**, respectively. These values are smaller than DEnT coupling constants calculated by Soler and McCusker in their study using similar Ru(II) polypyridyl complexes covalently bound to dinuclear manganese complexes, which possess coupling constants of 0.15 cm^{-1} and 10 cm^{-1} for the donors similar to $\mathbf{Ru^A}$ and $\mathbf{Ru^B}$, respectively. In the previous study, generation of the MLCT excited state on the bridging bpy ligand increased the coupling constant by two orders of magnitude over the system in which the MLCT state resides on the ancillary ligand. In the hydrogen bonded $\mathbf{Ru^A}$:**Fc1** and $\mathbf{Ru^B}$:**Fc1** dyads, the DEnT coupling constants are smaller than their covalently bound counterparts. The attenuated De-Ae coupling may reflect that DEnT occurs through the hydrogen bonded interface. It is noted that previous studies of PCET have demonstrated that ET is influenced by the intervening hydrogen bonds in similar two-point hydrogen bonded interfaces.[20,57] The present systems establish that in addition to ET, DEnT is influenced by the proton interface between the energy donor and acceptor in a proton-coupled energy transfer (PCEnT) mechanism.

VII.11. KIE uncovers influence of intervening proton interface

VII.11.1. Observation of an inverse KIE for $\mathbf{Ru^B}$

Deuteration of the proton interface yields the quenching rates reported in Table VII.3. The KIE is plotted for each dyad in Figure VII.6. Both small and large KIEs (when KIE >1) are accounted for by the coupling term in PCET theory, which in some situations can lead to very large KIEs.[79],[80] A notable observation is that the KIE is normal (KIE > 1) for dyads of **Ru^A**, but is *inverse* (KIE < 1), for dyads of **Ru^B**. The divergent behavior of the two Ru(II) polypyridyl complexes likely stems from the differing nature of the MLCT excited states of the two systems. As described above, the MLCT excited state of **Ru^B** places electron density on the bridging bipyridine ligand, while excitation to the MLCT state of **Ru^A** produces a system in which electron density is jettisoned onto the lower-lying fluorinated bipyridine ligands, orthogonal to the energy transfer pathway (Scheme VII.1). Additional excited state electron density distributed onto the bridging bipyridine ligand in the ^{3}MLCT excited state of **Ru^B** most certainly influences the pK_a of the appended carboxylic acid and in turn, the nature of the hydrogen-bonding interface on the timescale of the EnT process. Reduction of the bridging bipyridine ligand is expected to increase the pK_a of the appended carboxylic acid and result in the tightening of hydrogen-bonding bridge, based on the additional ionic attraction to the positively charged ferrocenyl-amidinium donor and increased basicity of the hydrogen-bond acceptor.[81-83]

VII.11.2. Application of PCET theory to describe KIEs in PCEnT

A great deal of attention has been paid to interpreting the observed KIEs in PCET. However, little work has been directed to the effect of KIEs on PCEnT reactions. PCET theory can be qualitatively applied to the case of PCEnT. As developed most extensively by Hammes-Schiffer, an ET process coupled to a PT process in which either a proton or a deuteron transfers from the ground donor state to the ground acceptor state depends on the overlap of the ground state proton or deuteron wavefunctions.[79] When large distances between the donor and acceptor states are to be traversed, the tails of the proton or deuteron wavefunctions dictate the efficacy of proton tunneling. In such cases, the overlap of the more diffuse proton wavefunction is greater than the overlap of the more localized deuteron wavefunction and therefore a normal KIE is expected (Figure VII.14). In Hammes-Schiffer's model, inversion of the KIE necessarily involves contributions of the proton or deuteron donor and acceptor excited state in the presence of asymmetric hydrogen bonds.[79] In another PCET model developed by Pressé and Silbey, an inverse KIE can be rationalized for tighter proton interfaces, such as that expected upon excitation to the MLCT excited state of **Ru**^{B}, in the event that ET is induced by small proton fluctuations within the proton or deuteron interface.[25] Provided that only small fluctuations of the hydrogen bond are required to attain the equilibrium configuration for ET, or in this case DEnT, an inverse KIE can be predicted by theory (Figure VII.14). In order for an inverse KIE to occur, the overlap of the deuteron wavefunction at its equilibrium position with the critical displacement for ET or DEnT must be greater than the overlap between the proton wavefunction at its equilibrium point and the corresponding fluctuation necessary to assist ET. Proton interfaces that are not as tightly bound require the proton or deuteron positions to fluctuate by larger amounts in order to induce ET, in which case the proton fluctuation facilitates ET more readily than the deuteron fluctuation, resulting in a normal KIE (KIE > 1). The nature of ET and DEnT as nonradiative processes allows such parallels to be drawn for application the KIE results of proton-coupled electron and energy transfer systems.

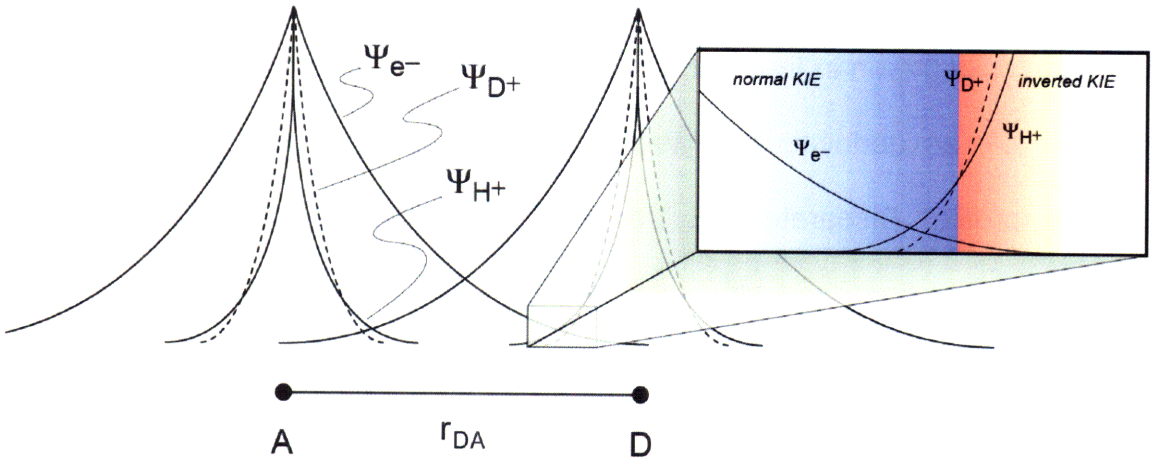

Figure VII.14. Overlap of electron, proton and deuteron wavefunctions. Representative wavefunctions of the electron, Ψ_{e-}; the proton, Ψ_{H+}; and the deuteron, Ψ_{D+} for a D---[H$^+$]---A system are show at a De-Ae distance, r_{DA}. In certain instances, larger proton fluctuations are necessary to induce ET. In such cases the more diffuse Ψ_{H+} exhibits greater overlap with Ψ_{e-} than the more localized Ψ_{D+} leading to a normal KIE (blue region on expanded inset). When the protonic interface contracts and smaller fluctuations are necessary to drive ET, the overlap for Ψ_{D+} at the critical displacement for ET is larger than the overlap for Ψ_{H+} and *inverse* KIE is observed (red region on

VII.12. Conclusions

PCEnT is established in De-Ae dyads comprised of **Ru**$^{\mathbf{A}}$ and **Ru**$^{\mathbf{B}}$ bound to ferrocenyl-amidinium compounds **Fc1**, **Fc2** and **Fc3**. Supramolecular assembly of ferrocenyl-amidinium compounds with two Ru(II) polypyridyl complexes allows for the study of hydrogen-bond mediated quenching through well-defined two-point interfaces. The transient PL results demonstrate that the ferrocenyl-amidinium complexes quench the excited states of the bound Ru(II) polypyridyl complexes, but does not confirm the mechanism by which quenching occurs. TA lends no assistance in confirming the quenching mechanism though it provides the negative result of no CT state. Variable-temperature steady-state PL does provide evidence for DEnT as the dominant quenching mechanism. Influence of the proton or deuteron in the intervening hydrogen-bonded interface is confirmed by small |*V*|, as deduced from temperature dependent band shapes of the emission profile. Disparate KIE trends between the two Ru(II) polypyridyl complexes E is rationalized with current PCET theory, which applies to energy as well as electron transfer. Through these De-Ae systems, the field of proton-coupled studies is expanded to include proton-coupled Dexter energy transfer.

VII.13. Experimental

VII.13.1. Materials

Fc1, **Fc2** and **Fc3** were prepared by Dr. Joel Rosenthal according to synthetic methods described in his Thesis. *Bis*(2,2'-bipyridine)ruthenium(II)(bpy-COOH)](PF_6)$_2$ **(Ru^B)** [84] and *Bis*(4,4'-*bis*(trifluoromethyl)-2,2'-bipyridine)ruthenium(II) dichloride (Ru(BTFMBPY)$_2$Cl$_2$) (**Ru^A**)[85] were prepared using published methods. Solvents for synthesis were of reagent grade or better and were dried according to standard methods.[86] Spectroscopic experiments employed dichloromethane (DCM) and tetrahydrofuran (THF) (Spectroscopic grade), which were dried using standard methods and stored under vacuum.

VII.13.2. Electrochemistry

Electrochemical measurements were performed with a Bioanalytical Systems (BAS) Model CV-50W potentiostat/galvanostat. Differential pulse voltammetry (DPV) was performed using a glassy carbon working electrode, a

Ag/AgCl reference electrode and a platinum wire auxiliary electrode. DPV experiments were performed in DCM with 0.1 M tetrabutylammonium perchlorate $(Bu_4N)ClO_4$ as the supporting electrolyte. Concentrations of ~1 mM were prepared for DPV experiments on **Fc1**, **Fc2**, **Fc3**, **Ru**^{A}, and **Ru**^{B}. A scan rate of 100 mV/sec and a sensitivity of 10 *μ*A/V were used for data acquisition. Prior to each DPV measurement, argon was bubbled through the solution to remove dissolved O_2. All potentials are reported versus an internal standard of Fc^+/Fc. Additional electrochemical measurements were performed on **Ru**^{A} and **Ru**^{B} to determine the effects of addition of a BM to the electrochemical behavior of the complexes. Because amidine-carboxylic acid binding only occurs in dry, aprotic solvents, all experiments were performed in a dry box using a micro-electrochemical cell (BASi Low Volume Cell for C-2 Cell Stand). Limitations imposed by the low volume cell precluded use of DCM as the solvent for these measurements. DCM produced high iR compensation values in the electrochemical set-up most likely due to the deleterious interaction with the vicor plug separating the two chambers in the small volume electrochemical cell. Instead dry THF was employed as the solvent. DPV scans were performed for the oxidative and reductive waves of **Ru**^{A} and **Ru**^{B} and for the oxidation wave of **Fc1** using a glassy carbon working electrode, a $Ag/AgNO_3$ reference electrode and a platinum wire auxiliary electrode in 0.1 M tetrabutylammoinium hexafluorophosphate $(Bu_4N)PF_6$ supporting electrolyte. Concentrations of ~0.3 mM of **Ru**^{A}, **Ru**^{B} and **Fc1** were prepared for the DPV experiments in THF.

Addition of Pham^0 was to concentrations as high as 30 eq for **Ru^A** experiments and 50 eq for **Ru^B** experiments

VII.13.3. Sample preparation for spectroscopic measurements

Absorption spectroscopy titrations with **Fc1**, **Fc2** and **Fc3** were performed in a high-vacuum cell comprised of a 1-cm pathlength clear fused-quartz cuvette (Starna cells) connected to a 10-cm^3 solvent reservoir via a graded seal. High-vacuum Teflon valves were used to seal the cell from the environment and the cuvette from the solvent reservoir. Titrations with a base of known pK_a in acetonitrile (ACN) were monitored by UV-vis spectroscopy to determine the acidity constants for **Fc1**, **Fc2** and **Fc3** in ACN. Titrations with DMAP were performed at 270 μM **Fc1** yielding an absorption band of 0.312 AU at 231 nm, at 670 μM **Fc2** yielding absorption bands of 1.33 AU and 0.643 AU at 355 nm and 464 nm, and at 240 μM **Fc3** yielding absorption bands of 0.456 AU and 0.232 AU at 373 nm and 464 nm. High concentrations of **Fc1**, **Fc2** and **Fc3** were required for UV-vis experiments due to poor extinction coefficients of the three ferrocene compounds: **Fc1** $\lambda_{321\text{ nm}}$ = 1,180 M^{-1} cm^{-1}, **Fc2** $\lambda_{355\text{ nm}}$ = 1,980 M^{-1} cm^{-1}, **Fc3** $\lambda_{373\text{ nm}}$ = 1,900 M^{-1} cm^{-1}. Samples were prepared under high-vacuum. An aliquot of **Fc1** (8.4 × 10^{-6} mol), **Fc2** (2.1 × 10^{-6} mol) or **Fc3** (7.19 × 10^{-7} mol) was added to the cuvette and the cell was evacuated under high-vacuum (10^{-5} Torr), thereby removing the transferring solvent. Three milliliters of dry ACN were vacuum transferred to the solvent reservoir and subject to three cycles of freeze-pump-thaw. The cell was sealed to the environment and removed from the high vacuum manifold. A titration with DMAP was performed to monitor the spectral shifts associated with deprotonation of the amidinium proton. Prior to each addition of DMAP, the ACN was vacuum transferred to the cuvette with a dry ice/acetone bath and sealed from the solvent reservoir and environment. This procedure ensured that the solvent volume remained constant throughout the course of the experiment. A stock solution of DMAP was added to the open solvent reservoir, while preserving the vacuum in the cuvette, and the transferring solvent was removed with a high vacuum manifold (10^{-5} Torr). The solvent reservoir was then sealed from the environment and opened to the cuvette compartment to introduce each new addition of DMAP.

Ambient-temperature TE quenching experiments were performed at concentrations of 3.3 μM of $\mathbf{Ru^A}$ and $\mathbf{Ru^B}$ and 33 μM of **Fc1**, **Fc2** and **Fc3**. One aliquot of $\mathbf{Ru^A}$ or $\mathbf{Ru^B}$ (1×10^{-8} mol) was added to the cuvette and ten equivalents of **Fc1**, **Fc2** and **Fc3** (1×10^{-7} mol) were added to the solvent reservoir. The cell was evacuated under high-vacuum (10^{-5} Torr), thereby removing the transferring solvent, but allowing the two compounds to remain separated. Three milliliters of dry dichloromethane (DCM) were added to the solvent reservoir and subject to three cycles of freeze-pump-thaw. The cell was sealed to the environment and removed from the high vacuum manifold. TE experiments were first performed on unbound $\mathbf{Ru^A}$ (or $\mathbf{Ru^B}$) under vacuum. Subsequently, the Teflon stopper between the cuvette and solvent reservoir was open and the two compounds were mixed while maintaining vacuum inside the cell. MLCT excitation of $\mathbf{Ru^A}$ (or $\mathbf{Ru^B}$) was performed with 460-nm photons and the emission decay profile was recorded at 640 nm.

Variable-temperature transient and steady-state emission experiments were performed following a sample preparation method described previously.[20] One aliquot of $\mathbf{Ru^A}$ or $\mathbf{Ru^B}$ (1×10^{-7} mol) and ten or five equivalents of Pham^0 or **Fc1** (1×10^{-6} mol) were added to a borosilicate short-stem glass ampuole (Kimble-Kontes) using a minimum amount of transferring solvent. The neck of the ampuole had been stretched with a flame to reduce the diameter and allow for easier sealing after high vacuum manipulations. The ampuole containing the sample was attached to a high vacuum adaptor. The transferring solvents were removed on a high vacuum manifold ($< 10^{-6}$ Torr) and the sample remained under vacuum for at least 2 hours to remove any residual water. One milliliter of dry DCM was added to the ampuole by vacuum transfer and was subject to at least three cycles of freeze-pump-thaw. The ampuole was then flame-sealed while the solvent remained frozen. The high-vacuum manipulations were necessary to ensured that the samples remained free from exposure the environment or water, which disrupts the hydrogen bonding between the dyads. The variable temperature experiments were the carried out as described previously.[20]

VII.13.4. Spectroscopic measurements

Absorption spectra were obtained using a Spectral Instruments 440 Series spectrophotometer. Steady-state emission spectra were recorded on an automated Photon Technology International (PTI) QM 4 fluorimeter equipped with a 150 W Xe arc lamp and a Hamamatsu R928 photomultiplier tube.

TE and TA measurements at ambient temperature with nanosecond length excitation pulses were performed with pump light provided by the third harmonic (355 nm) of the 1064-nm fundamental of a pulsed Nd:YAG laser (Spectra-Physics Quanta-Ray PRO-Series). The third harmonic is used to pump an optical parametric oscillator (OPO) at a repetition rate of 10 Hz with pulse energies of ~ 340 mJ/pulse and pulse width of ~ 7 ns. This Spectra-Physics laser has been integrated into an experimental set-up for TE and absorption studies described elsewhere.[87]

Nanosecond luminescence lifetime measurements were performed by exciting the sample at 450 nm and collecting the emission at 640 nm. The emission signal was passed through a SPEX Triax 320 spectrometer where it was amplified in a Hamamatsu R928 photomultiplier tube attached to the lateral exit of the spectrometer. The output from the photomultiplier tube was imaged on a Lecroy 9384 CM digital oscilloscope.

Luminescence lifetime measurements were performed with the picosecond laser system were collected with a Hamamatsu C4334 Streak Scope streak camera that has been described elsewhere.[87] The emission was collected over a 140-nm window centered on the emission peak. A 1-μs, 2-μs or a 5-μs time base was used. Data acquisition was automated for the variable temperature experiments. The temperature controller and streak camera were synchronized to enable data collection throughout the entire temperature range.

Luminescence experiments lasting approximately 20 minutes were followed by a 20 minute wait time during which the temperature was adjusted and the sample was allowed to equilibrate. This cycle occurred for all of the temperature data points, which were 20 K apart. Each sample was cycled through the entire temperature range 4 times in different sequences to ensure that the data was independent of the sequence.

Variable-temperature time resolved emission spectroscopy was performed on the picosecond laser systems using as the excitation source a chirped-pulse amplified Ti:Sapphire laser system that has been described elsewhere.[15] In this experiment, the 100-fs, 800-nm output of the regenerative amplifier was frequency-doubled in a visible OPA (BMI Alpha-1000) to produce a 1 kHz pulse train of excitation pulses at 400 nm for resonant excitation of the MLCT band of **Ru^A** and **Ru^B**. The excitation was vertically polarized and attenuated to 50 - 250 nJ/pulse.

The variable temperature lifetimes of **Ru^A** or **Ru^B** alone and bound to **Fc1** were measured over a temperature range of 200-300 K. Experiments were repeated at least 3 times with newly prepared samples. Luminescence lifetimes were determined from streak camera data analysis by integrating 30-nm slices of the emission peak centered at 660 nm, for **Ru^A** or **Ru^B** respectively, and fitting to a monoexponential decay function. Temperature dependent lifetimes of **Ru^A:Fc1** or **Ru^B:Fc1** were measured at the same temperature points and the data was fit in the same manner, except that the data was fit to a biexponential decay function with the longer lifetime component fixed to the lifetime obtained from the control experiment, **Ru^A** or **Ru^B**, at each temperature. The analysis for **Ru^A:Fc1** or **Ru^B:Fc1** was performed by integrating 30-nm slices of the emission peaks of the bound dyads, which for **Ru^A:Fc1** was centered at 660 nm and for **Ru^B:Fc1** was centered at 600 nm.

Variable temperatures were achieved using a modular cryogenic refrigeration system (Air Products and Chemicals) consisting of a single stage helium compressor (model 1RO2A) connected via hoses to an expander module (model DE-202) with a heating element and temperature controller (Scientific Instruments, 9600-5) that was interfaced with a custom-made computer program in order to automate the temperature control settings. The expander module is housed within a laboratory interface (model DMX-1) consisting of a vacuum shroud with glass windows for fluorescence spectroscopy in a right-angle configuration and is continuously pumped to maintain a vacuum (~10^{-4} Torr). An ampuole containing the sample is mounted on a copper block and the thermocouple was calibrated with three temperatures: liquid nitrogen (77 K), an ice bath (273 K) and ambient temperature (293 K).

VII.14. Reference

1. Chang, C. J.; Brown, J. D. K.; Chang, M. C. Y.; Baker, E. A.; Nocera, D. G. In *Electron Transfer in Chemistry*; Balzani, V., Ed.; Wiley-VCH: Weinheim, Germany, 2001; Vol. 3.2.4, pp 409-461.

2. Cukier, R. I.; Nocera, D. G. *Annu. Rev. Phys. Chem.* **1998**, *49*, 337-369.

3. Chang, C. J.; Chang, M. C. Y.; Damrauer, N. H.; Nocera, D. G. *Biochim. Biophys. Acta* **2004**, *1655*, 13-28.

4. Sessler, J. L.; Wang, B.; Springs, S. L.; Brown, C. T. In *Comprehensive Supramolecular Chemistry*; Murakami, Y., Ed.; Pergamon Press: Oxford, 1996; Vol. 4, pp. 311-336 and references therein.

5. Kumar, S.; Nussinov, R. *ChemBioChem* **2002**, *3*, 604-617.

6. Bosshard, H. R.; Marti, D. N.; Jelesarov, I. *J. Mol. Recog.* **2004**, *17*, 1-16.

7. Puglisi, J. D.; Chen, L.; Frankel A. D.; Williamson, J. R. *Proc. Natl. Acad. Sci. U.S.A.* **1993**, *90*, 3680-3684.

8. Pavletich, N. P.; Pabo, C. O. *Science* **1991**, *252*, 809-817.

9. Berg, J. M. *Acc. Chem. Res.* **1995**, *28*, 14-19.

10. Howell, E. H.; Villafranca, J. E.; Warren, M. S.; Oatley, S. J.; Kraut, J. *Science* **1986**, *231*, 1123-1128.

11. Ramirez, B. E.; Malmström, B. G.; Winkler, J. R.; Gray, H. B. *Proc. Natl. Acad. Sci. U.S.A.* **1995**, *92*, 11949-11951.

12. Crane, B. R.; Siegel, L. M.; Getzoff, E. D. *Science*, **1995**, *270*, 59-67.

13. Brzezinski, P. *Biochemistry* **1996**, *35*, 5611-5615.

14. Reece, S. Y.; Hodgkiss, J. M.; Stubbe J.; Nocera, D. G. *Phil. Trans. Royal Soc. B* **2006**, *361*, 1351-1364.

15. Seyedsayamdost, M. R.; Yee, C. S.; Reece, S. Y.; Nocera, D. G.; Stubbe, J. *J. Am. Chem. Soc.* **2006**, *128*, 1562-1568.

16. Seyedsayamdost, M. R.; Reece, S. Y.; Nocera, D. G.; Stubbe, *J. Am. Chem. Soc.* **2006**, *128*, 1569-1579.

17. Reece, S. Y.; Seyedsayamdost, M, R.; Stubbe, J.; Nocera, D. G. *J. Am. Chem. Soc.* **2007**, *129*, 8500-8509.

18. Reece, S. Y.; Seyedsayamdost, M, R.; Stubbe, J.; Nocera, D. G. *J. Am. Chem. Soc.* **2007**, *129*, 13828-13830.

19. Turró, C.; Chang, C. K.; Leroi, G. E.; Cukier, R. I.; Nocera, D. G. *J. Am. Chem. Soc.* **1992**, *114*, 4013-4015.

20. de Rege, P. J. F.; Williams, S. A.; Therien, M. J. *Science* **1995**, *269*, 1409-1413.

21. Damrauer, N. H.; Hodgkiss, J. M.; Rosenthal, J.; Nocera, D. G. *J. Phys. Chem. B* **2004**, *108*, 6315-6321.

22. Roberts, J. A.; Kirby, J. P.; Nocera, D. G. *J. Am. Chem. Soc.* **1995**, *117*, 8051-8052.

23. Roberts, J. A.; Kirby, J. P.; Nocera, D. G. *J. Am. Chem. Soc.* **1997**, *119*, 9230-9236.

24. Roberts, J. A.; Kirby, J. P.; Wall, S. T.; Nocera, D. G. *Inorg. Chim. Acta* **1997**, *263*, 395-405.

25. Kirby, J. P.; Roberts, J. A.; Nocera, D. G. *J. Am. Chem. Soc.* **1997**, *119*, 9230-9236.

26. Hodgkiss, J. M.; Damrauer, N. H.; Pressé, S.; Rosenthal, J.; Nocera, D. G. *J. Phys. Chem. B.* **2006**, *110*, 18853-18858.

27 . Cukier, R. I. *J. Phys. Chem.***1996**, *100*, 15428-15443.

28. Cukier, R. I. *J. Phys. Chem.* **1994**, *98*, 2377-2381.

29. Zhau, X. G. Cukier, R. I. *J. Phys. Chem.* **1995**, *99*, 945-954.

30. Cukier, R. I. *J. Phys. Chem. A* **1999**, *103*, 5989-5995.

31. Cukier, R. I. *Biochim. Biophys. Acta* **2004**, *1655*, 37-44.

32. Hammes-Schiffer, S. In *Electron Transfer in Chemistry*; V. Balzani, Ed., Wiley-VCH: Weinheim, Germany, 2001, Vol. 1.1.5, p. 189.

33. Hammes-Schiffer, S. *Acc. Chem. Res.* **2001**, *34*, 273-281.

34. Hammes-Schiffer, S. Iordanova, N. *Biochim. Biophys. Acta* **2004**, *1655,* 29-36.

35. Soudackov, A. Hammes-Schiffer, S. *J. Chem. Phys.* **1999**, *111*, 4672-4687.

36. Soudackov, A.; Hammes-Schiffer, S. *J. Chem. Phys.* **2000**, *113*, 2385-2396.

37. Decornez, H.; Hammes-Schiffer, S. *J. Phys. Chem. A.* **2000**, *104*, 9370-9384.

38. Pressé, S.; Silbey, R. *J. Chem Phys.* **2006**, *124*, 164504-164511.

39. Kubo, M.; Mori, Y.; Otani, M.; Murakami, M.; Ishibashi, Y.; Yasuda, M. Hosomizu, K.; Miyasaka, H.; Imahori, H.; Nakashima, S. *Chem. Phys. Lett,* **2006**, *429*, 91-96.

40. Cao, W.; Ferrance, J. P.; Demas, J. Landers, J. P. *J. Am. Chem. Soc.* **2006**, *128*, 7572-7578.

41. Fushimi, T.; Oda, A.; Ohkita, H.; Ito, S. *Langmuir*, **2005**, *21*, 1584-1589.

42. Araki, Y.; Yasumura, Y.; Ito, O. *J. Phys. Chem. B* **2005**, *109*, 8943-9848.

43. Lee, E. J.; Wrighton, M. A. *J. Am. Chem. Soc.* **1991**, *113*, 8562-8564.

44. Fery-Forgues, S.; Delavaux-Nicot, B. *J. Photochem. Photobio. A* **2000**, *132*, 137-159.

45. Siemling, U.; Vor der Bueggen, J.; Vorfeld, U.; Neumann, B.; Stammler, A.; Stammler, H.-G.; Brockhinke, A.; Plessow, R.; Zanello, P.; Laschi, F.; de Biani, F. F.; Fontani, M.; Steenken, S.; Stapper, M.; Gurzadyan, G. *Chem.A Eur. J.* **2003**, *9*, 2819-2833.

46. Delgadillo, A.; Leiva, A. M.; Loeb, B. *Polyhedron* **2005**, *24*, 1749-1754.

47. Heinze, K.; Hempel, K.; Beckmann, M. *European J. Inorg. Chem.* **2006** *10*, 2040-2050.

48. Reece, S. Y.; Seyedsayamdost, M. R.; Stubbe, J.; Nocera. D. G *J. Am. Chem. Soc.* **2006**, *128*, 13654-13655.

49. Soler, M.; McCusker, J. K. *J. Am. Chem. Soc.* **2008**, *130*, 4708-4724.

50. Huynh, M. H. V.; Dattelbaum, D. M.; Meyer, T. J. *Coord. Chem. Rev.* **2005**, *249*, 457-483. and references therein.

51. Balzani, V.; Bergamini, G.; Marchioni, F.; Ceroni, P. *Coord. Chem. Rev.* **2006**, *250*, 1254-1266. and references therein.

52. Rosenthal, J.; Young. E. R.; Nocera, D. G. *Inorg. Chem.* **2007**, *46*, 8668-8675.

53. Young. E. R.; Rosenthal, J. R.; Nocera, D. G. *Chem. Comm.* **2008**, *20*, 2322-2324.

54. Connors, Kenneth A. In Binding Constants: A Measurement of Molecular Complex Stability; Wiley: New York, 1987.

55. Izutsu, K. *Acid-base Dissociation Constants in Dipolar Aprotic Solvents*; Blackwell Scientific: Cambridge, USA, 1990.

56. Omberg, K. M.; Smith, G. D.; Kavaliunas, D. A.; Chen, P.; Treadway, J. A.; Schoonover, J. R.; Palmer, R. A.; Meyer, T. J. *Inorg. Chem.* **1999**, *38*, 951-956.

57. Young, E. R.; Rosenthal, J.; Hodgkiss, J. M.; Nocera, D. G. *manuscript in preparation*.

58. Lackowicz, J. R. In *Principles of Fluorescence Spectroscopy*; Kluwer Academic/Plenum; New York, 1999, pg 367-374.

59. Capser, J. V.; Meyer, T. J. *Inorg. Chem.* **1983**, *22*, 2444-2453.

60. Marcus, Y. In *Ion Solvation*; John Wiley.: Chichester, 1985, pp 136-137.

61. Opperman, K. A.; Mecklenburg, S. L.; Meyer, T. J. *Inorg Chem.* **1994**, *33*, 5295-5301.

62. Kirby, J. P.; Roberts, J. A.; Nocera, D. G. *J. Am. Chem. Soc.* **1997**, *119*, 9230-9236.

63. Hupp, J. T.; Neyhard, G. A.; Meyer, T. J.; Kober, E. M. *J. Phys. Chem.* **1992**, *96*, 10820-10830.

64. Caspar, J. V.; Meyer, T. J. *J. Am. Chem. Soc.* **1983**, *105*, 5583-5590.

65. Chen, P.; Meyer, T. J. *Chem. Rev.* **1998**, *98*, 1439- 1477.

66. Guillet, J. In *Polymer Photophysics and Photochemistry*; Cambridge University Press: New York, 1985, pp 22-23.

67. Barbara, P. F.; Meyer, T. J.; Ratner, M. A. *J. Phys. Chem.* **1996**, *100*, 13148-13168.

68. Barigelletti, R; Flamigni, L.; Guardigli, M.; Juris, A.; Beley, M.; Chodorowski-Kimmes, S.; Collin, J.-P.; Savauge, J.-P. *Inorg Chem.* **1996**, *35*, 136-142.

69. Hamada, T.; Tanaka, S.; Koga, H.; Sakai, Y.; Sakaki, S. *J. Chem. Soc., Dalton Trans.* **2003**, 692-698.

70. Liard, D. J.; Kleverlaan, C. J.; Vlcek, A. *Inorg. Chem.* **2003**, *42*, 7995-8002.

71. Indelli, M. T.; Bignozzi, C. A.; Harriman, A.; Schoonover, J. R.; Scandola, F. *J. Am. Chem. Soc.* **1994**, *116*, 3768-3779.

72. Thompson, D.W.; Fleming, C. N.; Myron, B. D.; Meyer, T. J. *J. Phys. Chem.* **2007**, *111*, 6930-6941.

73. Cooley, L. F.; Larson, S. L.; Elliot, C. M.; Kelley, D. F. *J. Phys. Chem.* **1991**, *95*, 10694-10700.

74. Larson, S. L.; Cooley, L. F.; Elliot, C. M.; Kelley, D. F. *J. Am. Chem. Soc.* **1992**, *114*, 9504-9509.

75. Claude, J. P.; Meyer, T. J. *J. Phys. Chem.* **1995**, *99*, 51-54.

76. Kober, E. M.; Casper, J. V.; Lumpkin, R. S.; Meyer, T. J. *J. Phys. Chem.* **1986**, *90*, 3722-3734.

77. Graff, D.; Claude, J.-P.; Meyer, T. *J. Adv. Chem. Ser.* **1997**, *253*, 183-198.

78. The outer-sphere reorganization energy can be calculated using the Marcus dielectric continuum model for the systems in a solvent of given dielectric constant using the relation: $\lambda_s = 14.4\left(\frac{1}{2r_D}+\frac{1}{2r_A}-\frac{1}{d_{DA}}\right)\times\left(\frac{1}{\eta}-\frac{1}{\varepsilon_s}\right)$ where r_D and r_A are the ionic radaii of the donor and acceptor, respectively, d_{DA} is the De-Ae separation, η is equal to the refractive index of the solvent squared, and ε_s is dielectric constant of the solvent. The refractive index and dielectric

constant for DCM are 1.4212 and 8.93, respectively. The ionic radaii of **3** is 3.2Å; **5** is 7.3 Å; **9** is 5.5 Å; $\mathbf{Ru^A}$ is 6 Å; and $\mathbf{Ru^B}$ is 6 Å. De-Ae separation for $\mathbf{Ru^A}$ and $\mathbf{Ru^B}$ with **3**, **5**, and **9** is 12.6 Å, 16.8 Å, and 14.8, respectively.

79. Decornez, H.; Hammes-Schiffer, S. *J. Phys. Chem. A.* **2000**, *104*, 9370-9384.

80. Huynh, M. H. V.; Dattelbaum, D. M.; Meyer, T. J. *Coord. Chem. Rev.* **2005**, *249*, 457-483.

81. Park, W. J.; Ahn, J.; Lee, C. J. *Photochem. Photobio. A* **1995**, *86* 89-95.

82. Gholamkhass, B.; Koike, K.; Negishi, N.; Hori, H.; Takeuchi, K. *Inorg. Chem.* **2001,** *40,* 756-765.

83. Su, C.-H.; Chen, H.-Y.; Tsai, K. Y. Chang, I-J. *J. Phys. Chem. B* **2007,** *111,* 6857-6860.

84. Roberts, J. A.; Kirby, J. P. ; Nocera, D. G. *J. Am. Chem. Soc.* **1995**, *117*, 8051-8052.

85. Furue, M.; Maruyama, K.; Oguni, T. ; Naiki, M. ; Kamachi, M. *Inorg. Chem.* **1992**, *31*, 3792.

86. Armarego, W. L. F.; Perrin, D. D. *Purification of Laboratory Chemicals*, 4th Ed.; Butterworth-Heinmann: Oxford, 1996.

87. Loh, Z.-H.; Miller, S. E.; Chang, C. J.; Carpentar, S. D.; Nocera, D. G. *J. Phys. Chem. A* **2002**, *106*, 11700-11708.

Appendix

A: Spectral shifts and Benesi-Hildebrand plots for P in THF, DCM, ACN

A1: Spectral shifts and Benesi-Hildebrand plots for titrations in THF

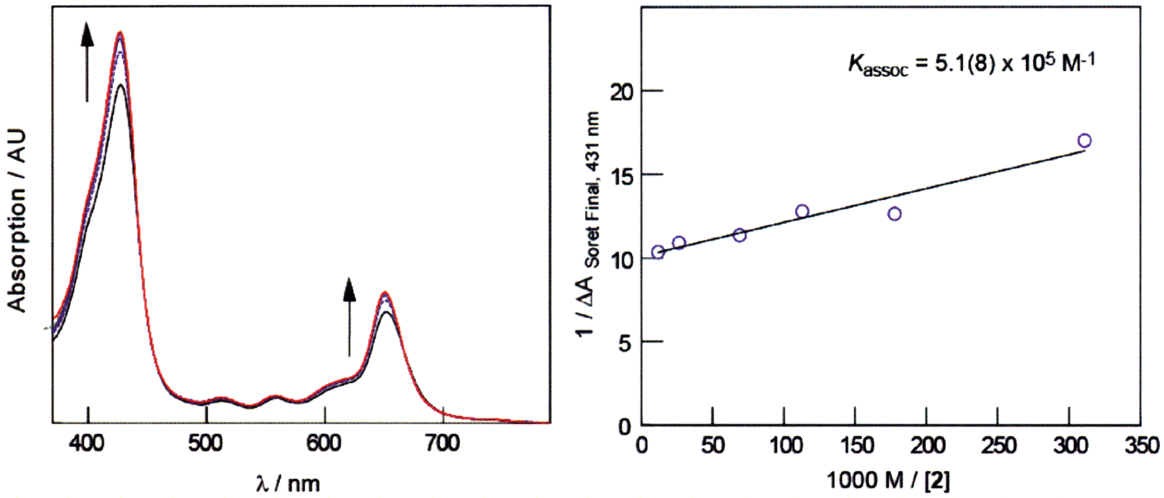

Titration of **P** with **2** in THF a) absorption band shifts upon addition of **2**, b) Benesi-Hildebrant (B-H) Plot. Spectra and B-H shown for addition of 0.4, 0.7, 1.1, 1.8, 4.7 and 10.5 equivalents of **2**.

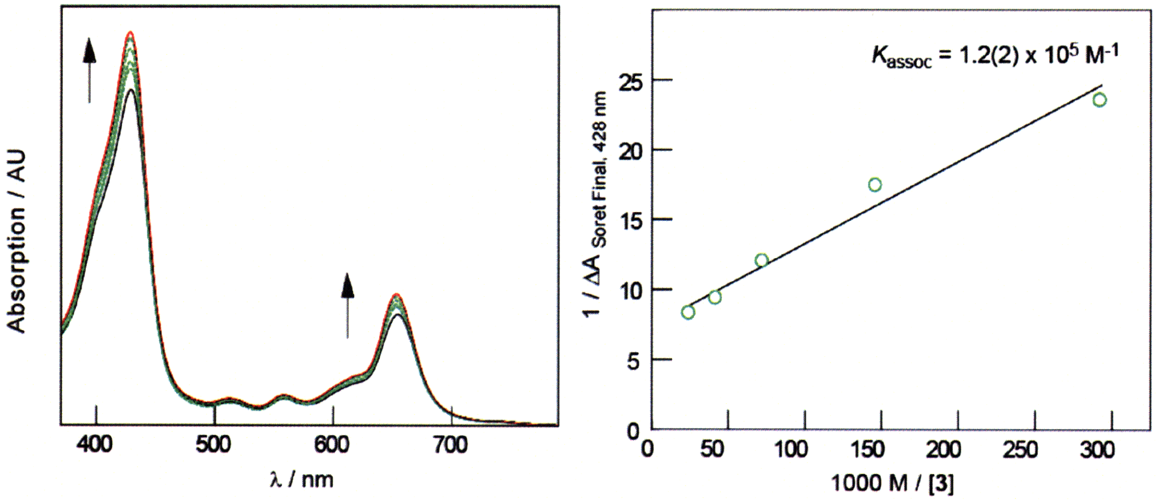

Titration of **P** with **3** in THF a) absorption band shifts upon addition of **3**, b) Benesi-Hildebrant (B-H) Plot. Spectra and B-H shown for addition of 0.4, 0.8, 1.6, 2.8 and 4.8 equivalents of **3**.

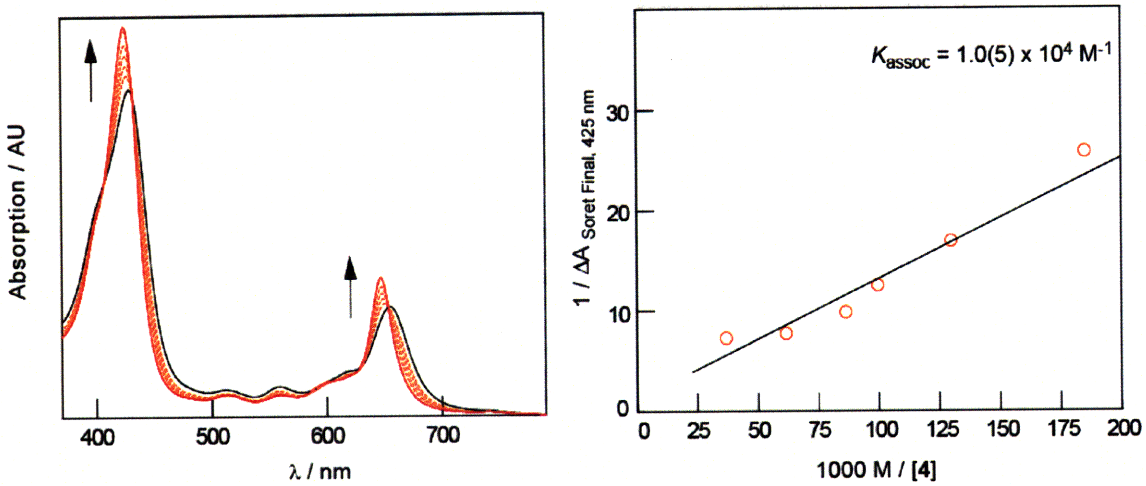

Titration of **P** with **4** in THF a) absorption band shifts upon addition of **4**, b) Benesi-Hildebrant (B-H) Plot. Spectra and B-H shown for addition of 0.7, 1.0, 1.3 , 1.5, 2.1 and 3.5 equivalents of **4**.

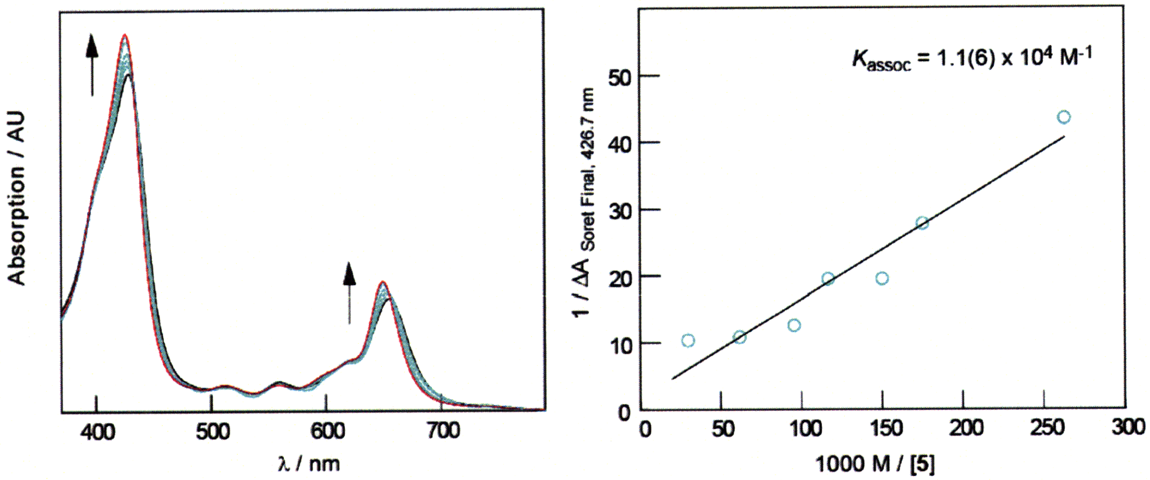

Titration of **P** with **5** in THF a) absorption band shifts upon addition of **5**, b) Benesi-Hildebrant (B-H) Plot. Spectra and B-H shown for addition of 0.4, 0.6, 0.7, 0.9, 1.1, 1.7 and 3.5 equivalents of **5**.

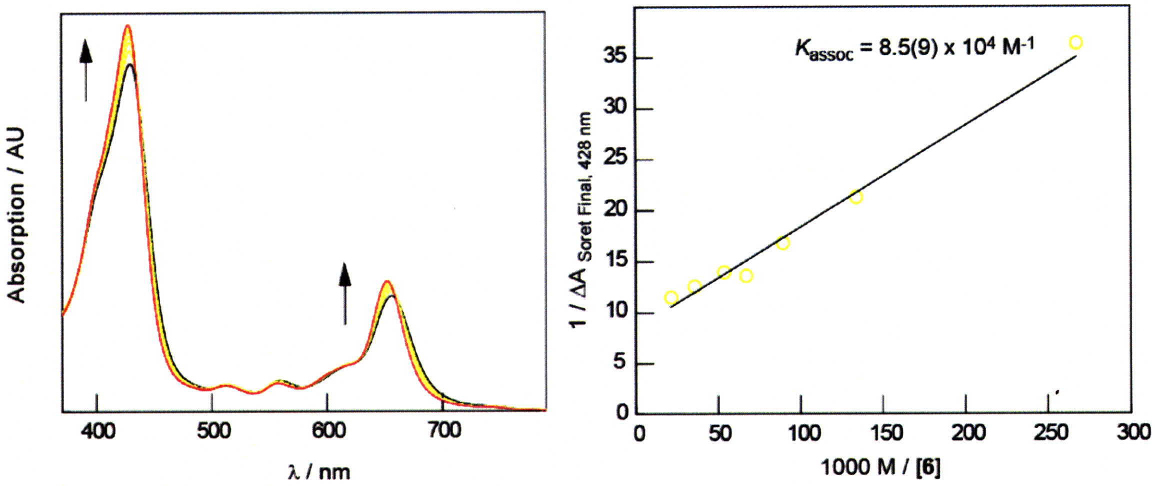

Titration of **P** with **6** in THF a) absorption band shifts upon addition of **6**, b) Benesi-Hildebrant (B-H) Plot. Spectra and B-H shown for addition of 0.4, 0.8, 1.2, 1.6, 2.0, 3.0 and 5.0 equivalents of **6**.

A2: *Spectral shifts and Benesi-Hildebrand plots for titrations in DCM*

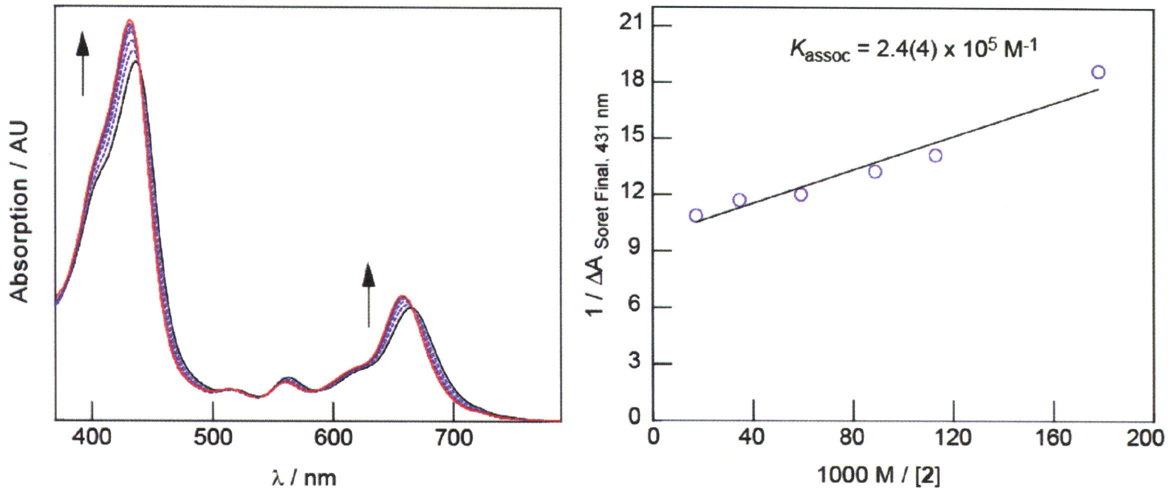

Titration of **P** with **2** in DCM a) absorption band shifts upon addition of **2**, b) Benesi-Hildebrant (B-H) Plot. Spectra and B-H shown for addition of 0.4, 0.7, 1.1, 1.4, 2.1, 3.6 and 7.2 equivalents of **2**.

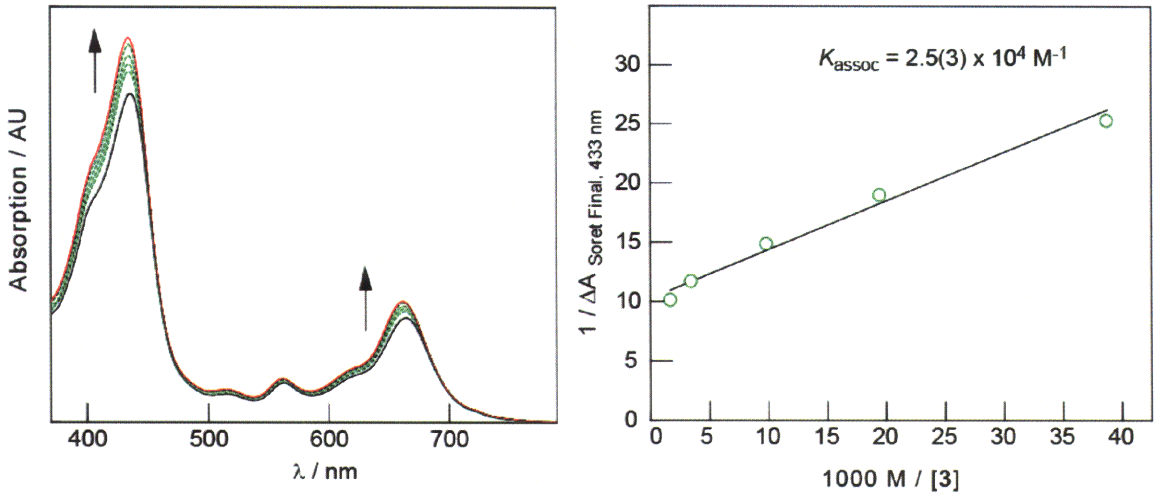

Titration of **P** with **3** in DCM a) absorption band shifts upon addition of **3**, b) Benesi-Hildebrant (B-H) Plot. Spectra and B-H shown for addition of 3.5, 7, 14, 42 and 84 equivalents of **3**.

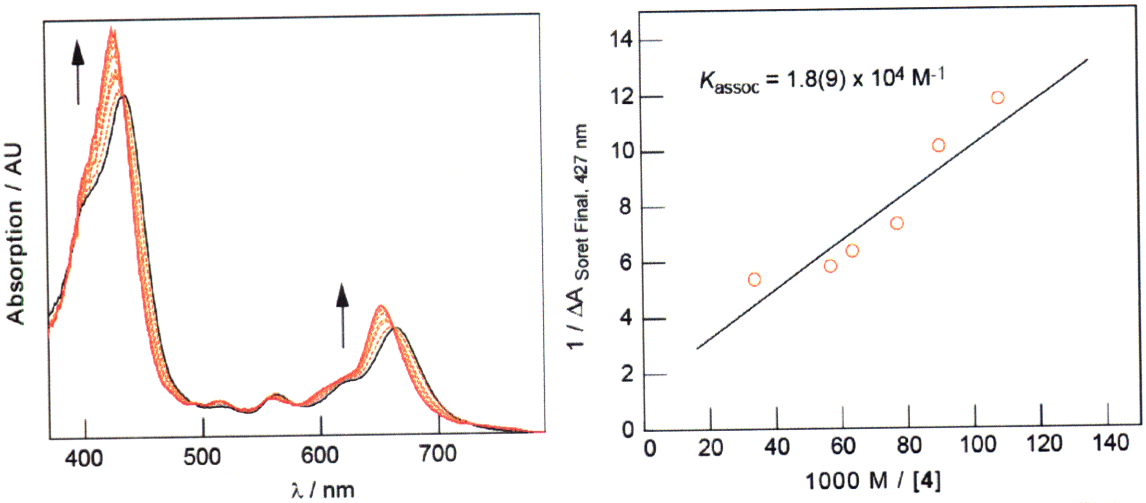

Titration of **P** with **4** in DCM a) absorption band shifts upon addition of **4**, b) Benesi-Hildebrant (B-H) Plot. Spectra and B-H shown for addition of 1.0, 1.2, 1.4, 1.7, 1.9, and 3.2 equivalents of **4**.

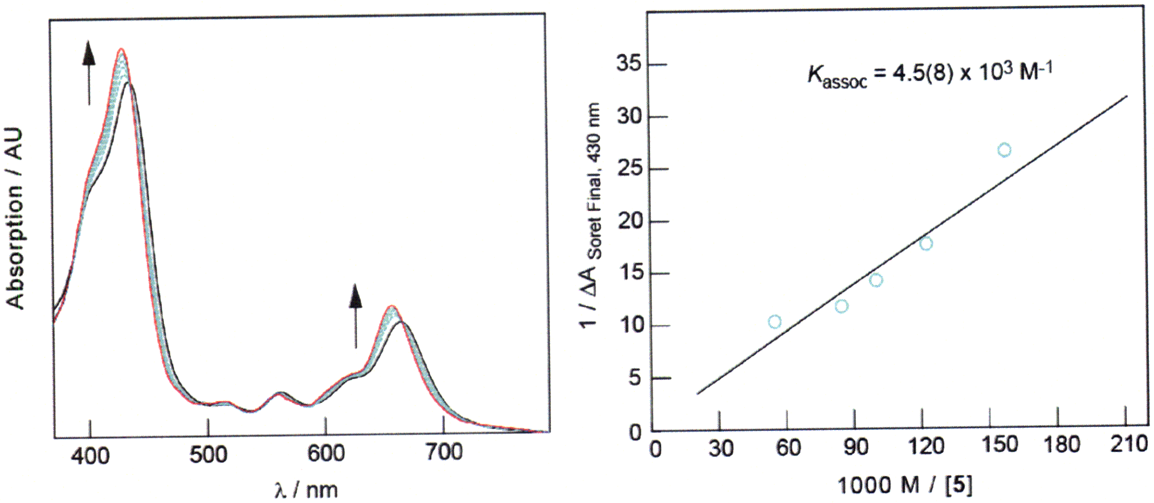

Titration of **P** with **5** in DCM a) absorption band shifts upon addition of **5**, b) Benesi-Hildebrant (B-H) Plot. Spectra and B-H shown for addition of 0.7, 0.9, 1.1 and 1.3 equivalents of **5**.

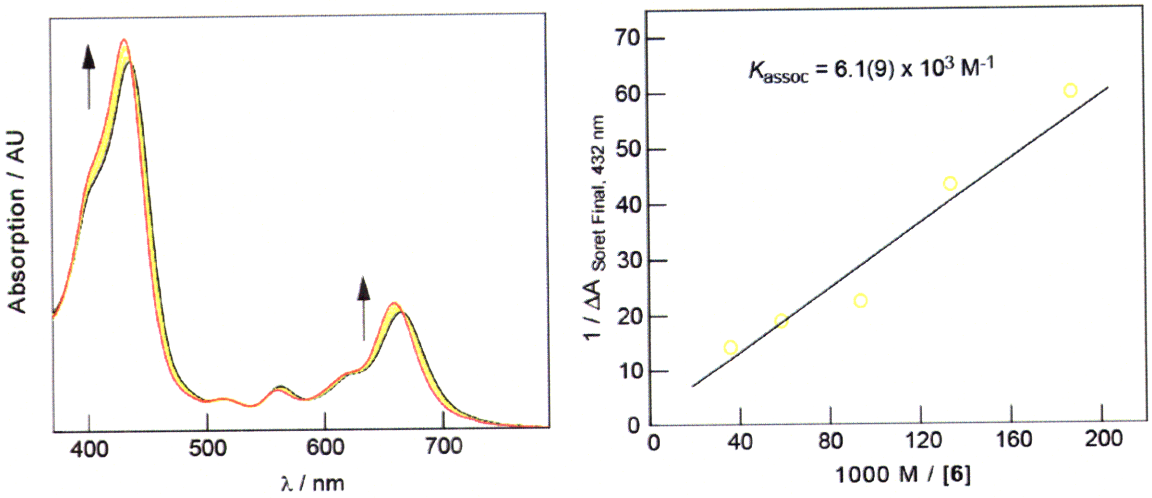

Titration of **P** with **6** in DCM a) absorption band shifts upon addition of **6**, b) Benesi-Hildebrant (B-H) Plot. Spectra and B-H shown for addition of 0.5, 0.7, 1.0, 1.6 and 2.6 equivalents of **6**.

A3: Spectral Shifts and Benesi-Hildebrand plots for titrations in ACN

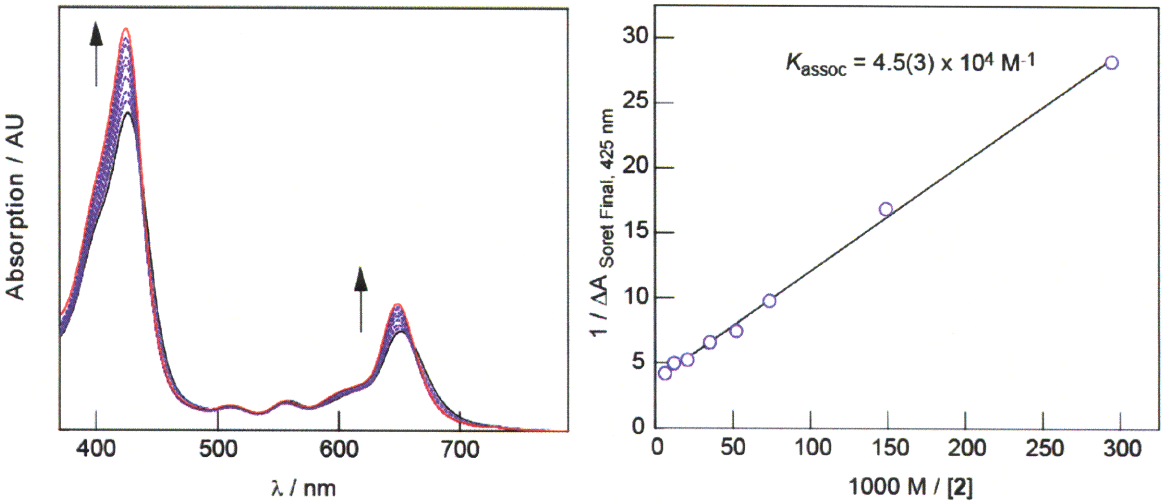

Titration of **P** with **2** in ACN a) absorption band shifts upon addition of **2**, b) Benesi-Hildebrant (B-H) Plot. Spectra and B-H shown for addition of 0.3, 0.6, 1.2, 1.7, 2.6, 4.3, 7.2, and 13 equivalents of **2**.

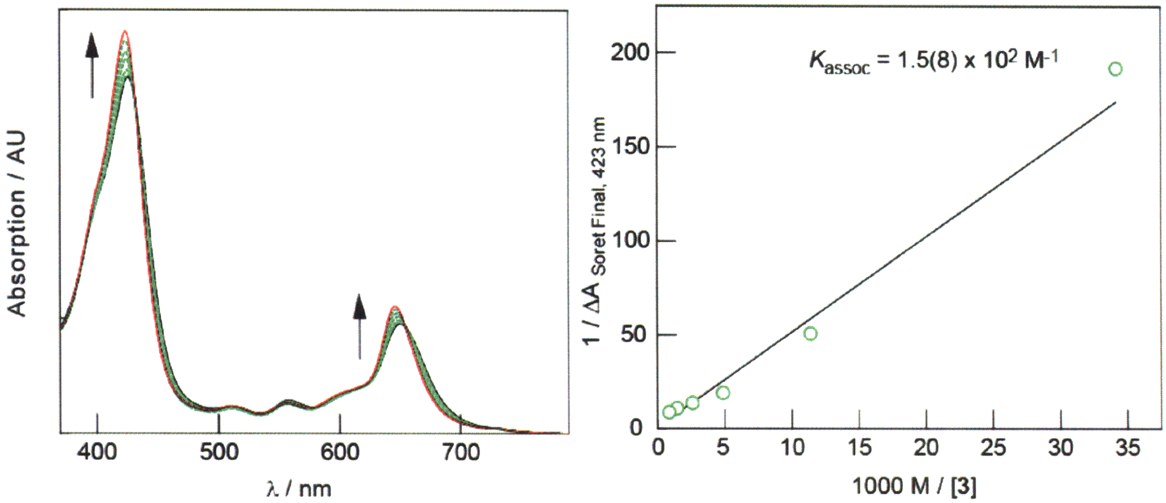

Titration of **P** with **3** in ACN a) absorption band shifts upon addition of **3**, b) Benesi-Hildebrant (B-H) Plot. Spectra and B-H shown for addition of 2.4, 7.2, 16.8, 31.2, 55.2 and 93.5 equivalents of **3**.

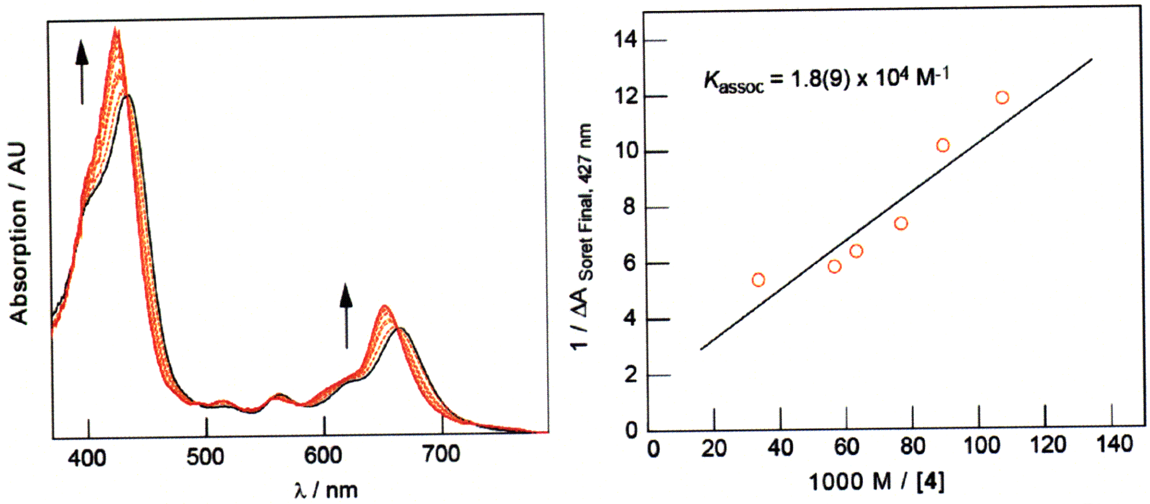

Titration of **P** with **4** in DCM a) absorption band shifts upon addition of **4**, b) Benesi-Hildebrant (B-H) Plot. Spectra and B-H shown for addition of 1.0, 1.2, 1.4, 1.7, 1.9, and 3.2 equivalents of **4**.

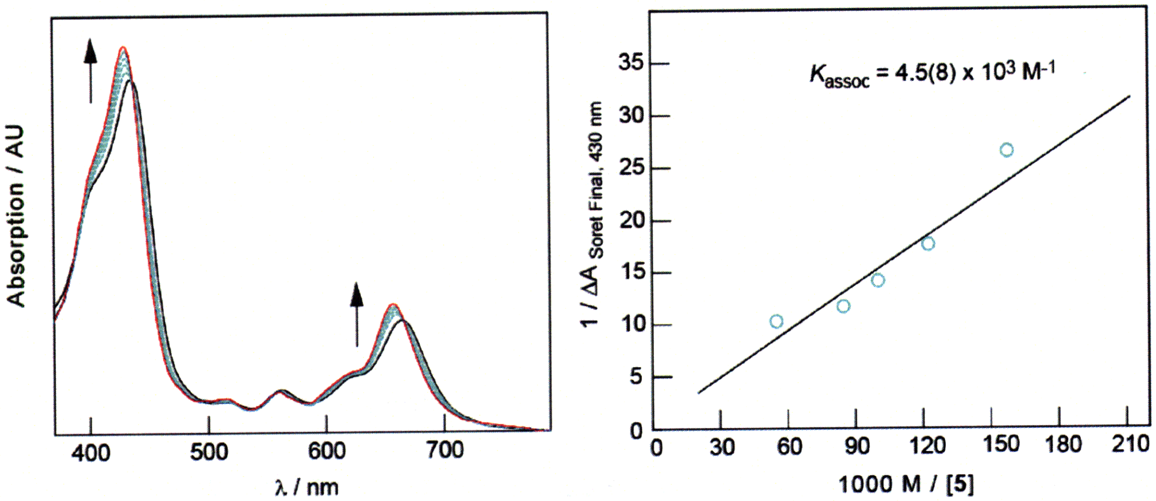

Titration of **P** with **5** in DCM a) absorption band shifts upon addition of **5**, b) Benesi-Hildebrant (B-H) Plot. Spectra and B-H shown for addition of 0.7, 0.9, 1.1 and 1.3 equivalents of **5**.

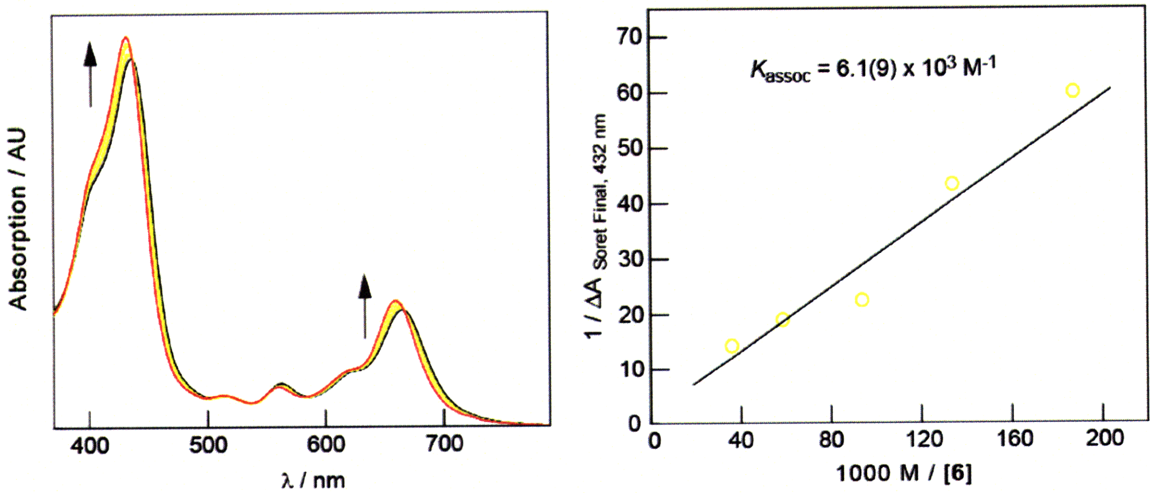

Titration of **P** with **6** in DCM a) absorption band shifts upon addition of **6**, b) Benesi-Hildebrant (B-H) Plot. Spectra and B-H shown for addition of 0.5, 0.7, 1.0, 1.6 and 2.6 equivalents of **6**.

B: Kinetic Modeling of TA Dynamics: Fitting and Simulation of D1 and D1:A2 Dynamics

B1: Motivation for detailed fitting and simulation of D1 and D1:A2 dynamics

A single-wavelength TA kinetic trace of the **D1:A2** dyad at the $S_1 \leftarrow T_1$ isosbestic point of **D1** is shown at early times (up to 1.8 ns) after resonant excitation of the $Q_{1,0}$ absorption band of **D1** with 560-nm photons. TA spectroscopy at the $T_1 \leftarrow S_1$ isosbestic point of **D1** (λ= 654 nm) is performed to establish spectroscopic for evidence of CT products and to resolve forward and back ET rates between the donor and acceptor moieties. Excited state evolution of unbound **D1** (no PCET or external quenching processes) yields a flat background at the isosbestic point (654 nm). Any growth or decay profile observed for single-wavelength TA experiments with the **D1:A2** dyad is due the solely to the **D1:A2** dyad, specifically to the formation and depletion of **D1**$^{\bullet+}$, based on the spectrum of **D1**$^{\bullet+}$ and the absence of other feasible alternatives.[1,2]

---

1. Damrauer, N. H.; Hodgkiss, J. M.; Rosenthal, J.; Nocera, D. G. *J. Phys. Chem. B* **2004**, 108, 6315-6321.
2. Hodgkiss, J. M.; Damrauer, N. H.; Pressé, S.; Rosenthal, J.; Nocera, D. G. *J. Phys. Chem. B.* **2006**; 110, 18853-18858.

secondary lifetime component in the kinetic data that does not match the PL decay lifetime and implicates an intermediate, which contributes to the TA signal and (ii) modeling the data using kinetic rate equations simulates the observed data when the back ET rate is approximately one order of magnitude faster than the forward ET rate.

B2: Various fitting scenarios for TA data

In the scenario where no forward or back ET occurs in **D1:A2** (if energy transfer or some other quenching mechanism were operative), the single-wavelength TA decay would have the same lifetime as the PL decay of the singlet excited state of **D1** observed in complementary PL experiments. Fixing the lifetime to that of the quenched lifetime component in time resolved PL experiments (420 ps) yields a monoexponential decay that fits poorly to the observed data as shown in the figure below.

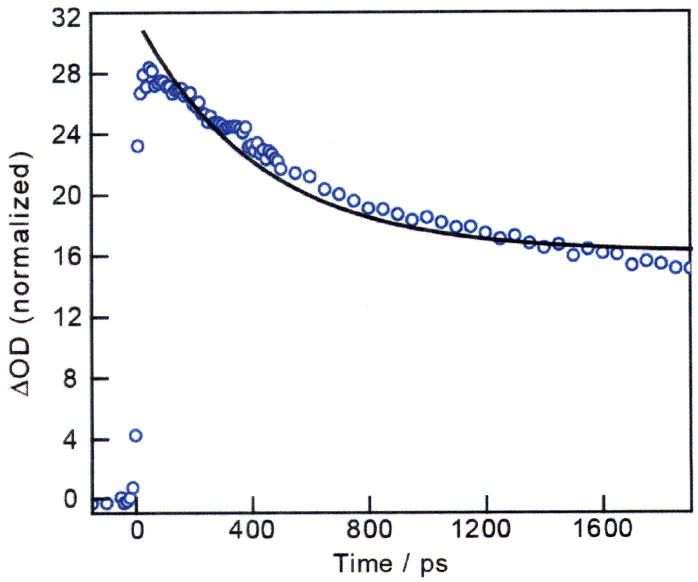

Monoexponential fit of TA data with lifetime fixed to 420 ps (as determined from PL lifetime measurements).

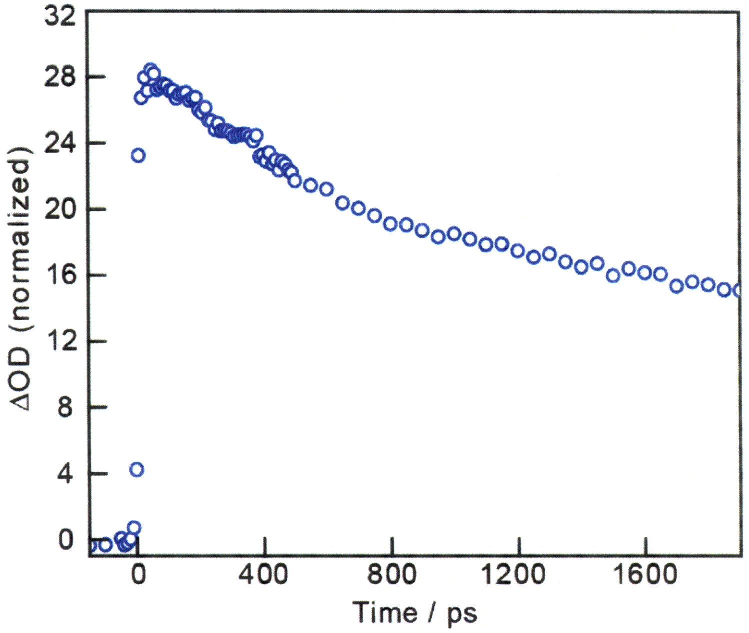

TA trace of **D1:A2** at isosbestic point of **D1** (λ_{obs} = 654 nm)

TA spectroscopy on **D1:A2** shows the kinetic profile in the above figure in which a clear rise and decay of a CT intermediate is attenuated such that the rise feature resemble a shoulder on an apparent decay profile. These results differ slightly from previous single-wavelength TA kinetics traces at the isosbestic point of **D1:A1** which shows a more prominent rise component (build up of a CS intermediate, $\mathbf{D}^{\bullet+}$) and subsequent decay (depletion of CT intermediate, $\mathbf{D}^{\bullet+}$, due to back ET). Previous TA data was fit biexponentially to yield forward and back ET rates. The present data lacks the prominent rise component, but is not in discord with the assertion that ET (and not energy transfer) accounts for the observed TA signal.

We propose that the back ET rate is much faster than the forward rate and therefore does not allow for significant build up of the CT state. The two components supporting this assertion are presented: (i) fitting the data reveals a

An unrestricted monoexponential fit of the data yields a fitted lifetime of 685 ps, which does not correspond to any other lifetime observed for the system. Although a monoexponential function yields a reasonable fit to the data, the lifetime is relatively meaningless in an analysis of the system. At the $T_1 \leftarrow S_1$ isosbestic point, the TA signal should be comprised of two components, which correspond to the growth and decay of a CT intermediate. When fit to a biexponential function, in which one of the lifetime components was fixed to the 420 ps lifetime of the PL decay (corresponding to the forward ET rate), the TA kinetics trace yielded a second lifetime of 300 (100) ps (corresponding to a back ET rate of 3×10^9 s^{-1}). The pre-exponential amplitudes of the fit were positive for 420 ps lifetime and negative for the fitted lifetime (after initial bias in fitting parameters).

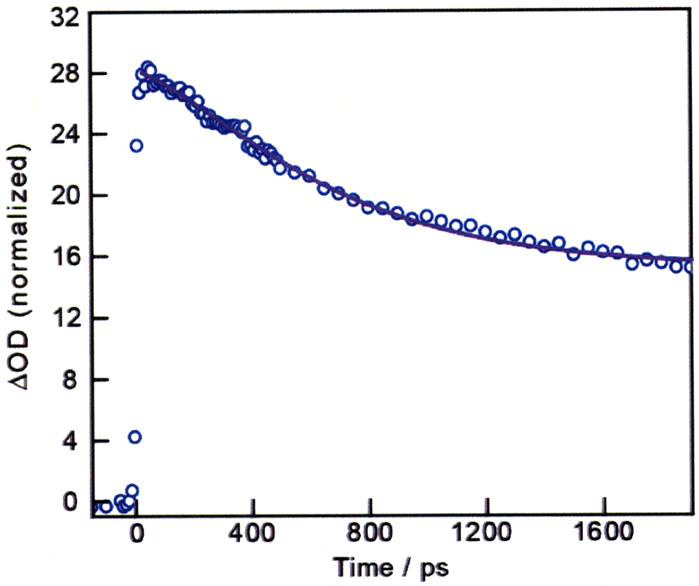

Biexponential fit of TA data with the quenched S_1 lifetime component fixed to that measured by time-resolved PL.

B3: Simulation of TA data

Simulation of the TA data requires an inventory of pertinent species as well as an account of their concentrations, temporal evolution and spectroscopic contributions. Resonant excitation at the Q-band of **D1** yields an initial concentration of **D1** in the singlet excited state, which evolves to produce a TA signal. Deactivation of the singlet excited state of **D1** in the absence of an external quencher (or the unbound species in these experiments) occurs with a rate k_0, which is the sum of radiative relaxation, k_r, nonradiative relaxation, k_{nr}, and intersystem crossing to the first excited triplet state, k_{ISC}.

$$k_0 = k_r + k_{nr} + k_{ISC} \tag{B.1}$$

When bound to an electron acceptor, deactivation of the singlet excited state can occur via ET with a rate of k_{ET}. These two processes yield an expression for the time-dependent concentration of singlet **D1**, ^{1}**D1***, bound to an acceptor, A, to be:

$$[^1D1^* - A](t) = \exp(-(k_{ET} - k_0)t \tag{B.2}$$

Formation of the triplet excited state complex ^{3}**D1***—A occurs from ^{1}**D1***—A with a rate constant k_{ISC}.

$$\frac{d}{dt}[^3D1^* - A] = k_{ISC}[^1D1^* - A] \tag{B.3}$$

Depletion of the triplet state is slow in comparison to the other rates discussed here and is ignored in this treatment. The time-dependent concentration of ^{3}**1***—A is:

$$[^3D1^* -A](t) = \frac{k_{ISC}}{k_{ET} + k_0}(1 - e^{-(k_{ET}+k_0)t}) \quad (B.4)$$

The CT intermediate is formed from ^{1}**D1*** at k_{ET} and is depleted at k_{BET}, the back ET rate.

$$\frac{d}{dt}[D1^+ - A^-] = k_{ET}[^1D1^* -A] - k_{BET}[D1^+ - A^-] \quad (B.5)$$

The time-dependent concentration of **D1**$^+$–A$^-$ is:

$$[D1^+ - A^-](t) = \frac{k_{ET}}{k_{BET} - (k_{ET} + k_0)}(e^{-(k_{ET}+k_0)t} - e^{-k_{BET}t}) \quad (B.6)$$

The TA signal, $\Delta A(t)$, is comprised of the time-dependent concentration of each species and the change in extinction coefficient at the appropriate wavelength, $\Delta\varepsilon_{i\lambda}$.

$$\Delta A(t)\lambda = \sum_{i=\text{species}} \Delta\varepsilon_{i\lambda}[i](t) \quad (B.7)$$

Unbound **D1** and bound **D1:A2** dyads weighted by the appropriate factor contribute to $\Delta A(t)$. Samples are 25% bound at the spectroscopic conditions used for TA.

$$\Delta A(t)_{\lambda,\text{total}} = 0.25 \times \Delta A(t)_{\lambda,\text{bound}} + 0.75 \times \Delta A(t)_{\lambda,\text{unbound}} \quad (B.8)$$

where

$$\Delta A(t)_{\lambda,\mathrm{bound}} =$$

$$\left[\Delta\varepsilon_{{}^1\mathrm{D1^*-A},\lambda} - \Delta\varepsilon_{{}^3\mathrm{D1^*-A},\lambda}\frac{k_{\mathrm{ISC}}}{k_{\mathrm{ET}}+k_0} + \Delta\varepsilon_{\mathrm{D1^+-A^-},\lambda}\frac{k_0}{k_{\mathrm{BET}}-(k_{\mathrm{ET}}+k_0)}\right]e^{-(k_{\mathrm{ET}}+k_0)t}$$

$$-\left[\frac{\Delta\varepsilon_{\mathrm{D1^+-A^-},\lambda}k_{\mathrm{ET}}}{k_{\mathrm{BET}}-(k_{\mathrm{ET}}+k_0)}\right]e^{-k_{\mathrm{BET}}t} + \Delta\varepsilon_{{}^3\mathrm{D1^*-A},\lambda}\frac{k_{\mathrm{ISC}}}{k_{\mathrm{ET}}+k_0}$$

(B.9)

And

$$\Delta A(t)_{\lambda,\mathrm{unbound}} = \Delta\varepsilon_{{}^1\mathrm{D^*-A},\lambda}e^{-k_0 t} - \Delta\varepsilon_{{}^3\mathrm{D^*-A},\lambda}\frac{k_{\mathrm{ISC}}}{k_0}\left[1-e^{-k_0 t}\right] \qquad \text{(B.10)}$$

Matlab was used to simulate ΔA(t) based on k_0, k_{ISC}, k_{ET}, and Δε for each species. k_0 was determined from PL experiments on unbound **D1** and, as the quantum yield for ISC is very high (~ 90%), is largely constituted by ISC. For this reason the estimation of $k_0 \sim k_{ISC}$ was used for these simulations and both were set to 4×10^8 s^{-1}.[3,4] k_{ET} was determined experimentally from PL experiments and set to 1.9×10^9 s^{-1}. Extinction coefficients were estimated and checked with simulations of **D1**:**A1** data to reproduce experimental results with the known experimental rates of k_{ET} and k_{BET}. The following values were employed: $\Delta\varepsilon_{{}^1 1^*-A} = 1000$, $\Delta\varepsilon_{{}^3 1^*-A} = 1000$ and $\Delta\varepsilon_{1^+-A^-} = 2750$ at 654 nm. k_{BET} was varied to simulate different ΔA(t) traces. The simulated data shows ΔA(t) as a function of k_{BET}. The red data points represent $k_{BET} = 3 \times 10^9$ s^{-1}, the green data points represent $k_{BET} = 6 \times 10^9$ s^{-1}, and the blue data points represent $k_{BET} = 1.2 \times 10^{10}$ s^{-1}. The simulated ΔA(t) data affirm that with faster ET kinetics than observed for

---

[3] Gradyushko, A. T.; Tsvirko, M. P. *Opt. Spectrosc.* **1971**, *31*, 291-295.

[4] Rodriguez, J.; Kirmaier, C.; Holten, D. *J. Am. Chem. Soc.* **1989**, *111*, 6500-6506.

D1:A1 and for k_{BET} roughly one order of magnitude faster than k_{ET}, the rise component in the TA signal for systems with kinetics similar to **D1:A2** appears as a shoulder. The discrepancy between the fitted k_{BET} of 3.3 × 10^9 s^{-1} and the simulated k_{BET} of 1.2 × 10^{10} s^{-1} may be attributed to difficulty in fitting the noise inherent in the TA data that arise due to a smaller amount of bound **D1**:**A2** (~25%) and limitations in detection on shorter timescales. At a minimum, this explanation is support for the assertion that ET is the primary mechanism for the singlet excited state quenching of **D1** in the presence of **A2** and that $k_{BET} > k_{ET}$. In addition, due to experimental considerations such as lower to the S/N and detection limitations at shorter times, the fitting the experimental results for k_{BET} provide a lower limit approximation for k_{BET}. The value for k_{BET} may be faster, and thus obscured by limitations is the ability of the program to fit the biexponential decay of the TA trace.

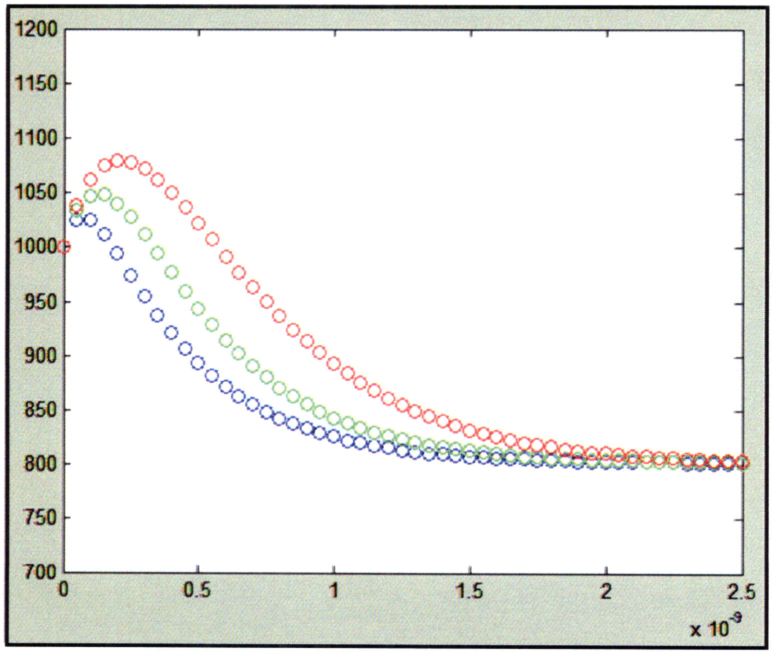

Simulated $\lambda A(t)$ data when varying the back ET rate, k_{BET}.

Acknowledgements

The above work would not have been possible without the help and support of countless individuals. It would be nearly impossible to properly thank every person who contributed to my ability to arrive at this exciting and challenging position at MIT and to somehow make it through this maze in one piece. In the following pages, I will make my best attempt.

I would like to thank my entire family for their support throughout my entire lifetime. My family is truly caring and never ceases to show the deepest concern for each other. I cherish their love and support.

I survived my first year at MIT with the help of a few fellow physical chemistry students. It was not fun, nor was it pretty, but it is over and we survived. Sean Roberts may single-handedly be responsible for my passing grades in both Quantum Mechanics and Statistical Mechanics. Thank you Sean for spending so much time re-explaining QM and helping me with the problem sets. Kathy Stone and Marc Caporini were two other critical companions in working through problem sets and surviving the physical chemistry classes! Additionally, I would like to thank Ziad Ganim, who although he was not in the same courses, was a cheerful and positive source of encouragement that first year. It has been wonderful to see all of my classmates in the neighboring laser labs over the following years as we worked towards our research goals.

The majority of my time in the Nocera group has been spent in the basement laser lab, tuning optics and keeping the Jade happy. Justin Hodgkiss taught me every part of the laser system when I first joined the group and was a truly patient teacher. Even though Justin was involved in what was certainly the most humiliating moment of my life, I will be forever thankful to have worked with him. I would also like to thanks Niels Damrauer for his work in setting up the picosecond system before I arrived. Even though I did not overlap with Niels in the Nocera lab, I have had the privilege of meeting him at various conferences during the past few years. We even starred in a film together along with a few other Nocera group members. In the time after Niels and Justin's departure, Poul Petersen has helped me out a great deal with our laser system. I truly appreciate the time Poul has taken to help me with the routine laser maintenance and in thinking through and designing new experiments. I also wish the best of luck to Andrew Horning and Casandra Cox who will be taking over part the laser lab. Thank you for joining the Nocera lab at just the right time! I know with the two of them working together, the picosecond laser will be in great hands!

Joel Rosenthal is responsible for providing me with all the compounds that I have presented in my thesis work. I am very thankful to him for his synthetic efforts and for his help in thinking through various aspects of our project. For the past few years, Joel has been my only other PCET compatriot in the lab and I appreciated the time he was able to spend on our collaboration.

Julien Bachmann is one of the most inspirational people I have met at MIT. Julien is an excellent, engaging and interested scientist. Not only is Julien talented at his profession, he is one of the most well-rounded people I have ever known. Julien is a true family man – he shows the deepest love and respect for his wife, Sandrine, and his children. Julien has an interest in many extracurricular activities, including outdoor pursuits that allow him to enjoy Nature and to spend time with his friends and family. I know he will maintain this delicate balance throughout his life.

Jenny Yang has been a great friend and positive influence on me during my years in the Nocera lab. Jenny introduced me to ice hockey at MIT and we have had many great times playing hockey together. On the scientific side, I look forward to attending future GRC conferences with her! Becky Somers has also been a great friend. Becky is someone who I have always been able to talk to and confide in. I know our sauna trips did us both a lot of good!! I am thankful to Jenny and Becky for their friendship and companionship in the lab.

Dino Villagrán deserves special recognition as well. Dino has consistently been a great friend and confidant. He has helped me through some rough times and has joked with me through the good times. Dino shares in other people's success unselfishly and keeps a light-hearted attitude in the face of frustration. Thank you, Dino!!!!! (Are five exclamation points enough?)

My time in the Nocera Lab has been made special by all of the other graduate students who were part of the lab when I joined and who have since entered this fraternity we call a research group. I believe that by having weathered the Nocera group, we all share a common experience, or perhaps a common mental problem – depending on Dan's diagnosis, that will forever provide us with ample stories to share or recall in future meetings. Bart Bartlett, Aetna Wun, David Manke were the senior students when I joined the group; I have always appreciated their clear and determined leadership. Steven Reece and Arthur Esswein are the model Nocera group members. They possess a clear dedication to their science and to thoroughly understanding their chemistry. I thank them for being able to show their chemical prowess on a consistent basis. Emily Nytko-Lutz is a classmate and lab member who I will never forget. Glen Alliger … has been thanked. Tim Cook has been instrumental to the Nocera group over the past four years. His artistic flair has elevated the standards of artwork expected for figures and his chalkboard drawings have been the stuff of legend. My favorite memory with Tim, along with Becky Somers, occurred in Western Mass when the three of us discovered we have the same Six Flags strategy. I think we made it onto the Batman ride two times within five minutes! I would like to thank fellow ChemREF, Emily McLaurin, for her help and perspective in the lab. In addition to her scientific contributions, she has been a great social coordinator.

Specifically, she has the important skill of coaxing Nocera out for group dinners these days. Montana Peterson has been the safety officer for most of my time in the group and has done a great job of keeping us all safe. I am happy I got to know Changhoon Lee and am glad he found a good home in the Nocera group. Mike Marshak holds one of the most applicable and telling group job titles. The job called "tool box" was created especially for him and people who know him, know why. Yogi Surendranath is the lab member who is probably the most giving of his time to help out other lab members with their science. I am thankful for our scientific discussions about my proposed future project. Yogi is amazingly driven in his research, which will serve him well in this group and beyond. Arturo Pizano has consistently made me laugh with his antics. Arturo is truly creative as evidenced by the numerous nicknames he devises during Karaoke night at the Thirsty Ear. I am thankful Matt Chambers came do MIT knowing full well he would be called Dorothy for his entire tenure in graduate school. Nothing he does, not even being an awesome hockey goalie can change that! Thomas Teets has shown the greatest hustle of any graduate student I have ever known. He has turned the Organomets team around; under his guidance the team finally brought home the championship. I look forward to hearing about more sports victories under Thomas' managerial eye. I am also thankful that Peter Curtin and Cassandra Newell joined the group this year. I wish them the best of luck.

The post-docs in the Nocera group have added perspective and additional guidance to the group. I am thankful to all the post-docs who spent time in the Nocera lab and shared in my experiences as a graduate student. Matt Shores was a post-doc when I first joined the group. Watching him go through a great deal of discomfort at the hands of some conniving group members was good preparation for what was in store for me. Ted Betley's vocal range is astounding for someone his size! I hope he keeps his students at Harvard amused with his antics, too. I am glad I had the opportunity to work with Andrew Greytak on some of his QD experiments. I have also benefited from my numerous scientific discussions with Andrew. Matt Kanan has introduced the group to some of the finer drinking establishments in Cambridge. I probably would never have been to Grafton St. or Noir otherwise. I wish him the best of luck in his new position at Stanford. It has been fun to have Danny Lutterman join the group. He has great stories from Claudia Turro's days in the Nocera group and he has two of the most athletic children I have ever met. I can't wait to see them on ESPN in the future. I want to thank Alex Radosevich for his bravery during his first year dinner presentation in which, despite my absence, he took a few good shots at my expense. It has been wonderful to finally have a female post-doc in our lab. Dilek (Dee-lek) Dogutan is a great person and an excellent role model for the women in this group. Thank you for being so tough and determined! I would also like to thank Mircea Dinca, Bob McGuire, Matthias Schwalbe, Rick Kelley, Jon Melnick, Thomas Gray, Daniel Grohol, Alex Krivokapic, Shih-Yaun Liu, Preston Snee, Jake Soper, Sebastian Stoian, Adam Viege for their contributions to the group.

Behind the scenes work by Susan Brighton has been instrumental to keeping the whole graduate student program running. Thank you, Susan for all your work translating between the professors and graduate students. Also thank you for support, and those conversations in the hallways. Gretchen Kappelman, Allison Kelsey, Janet MacLaughlin have been instrumental in keeping the Nocera lab functioning. Thank you to all of them for their hard work!

Gary Vaillancourt of Thales lasers has been a great source of help and guidance. His knowledge about the Jade as well as any other laser setup imaginable is amazing. Thank you, Gary, for all the memorable visits to our lab and for being so extremely helpful on the phone whenever I had a question.

During the last year of my graduate work, I collaborated with Yaakov Tischler from the Bulović lab. It has truly been a privilege to work with Yaakov. Yaakov is a positive research collaborator and a driven scientist. I wish him the best of luck in his future endeavors.

Finally, I want to express my deepest thanks to Daniel G. Nocera, Professor of Energy and Chemistry at MIT. Dan has been an excellent research advisor. I have an immense amount of respect for Dan because he places strong emphasis on providing an educational experience for his graduate students. His students do not need to be experts when they join the group, and he gives them ample room to figure out their place in the research program. When I was meeting with Dan to discuss joining his group, I told him I had no experience with time resolved laser spectroscopy and the physical chemistry classes were kicking my butt pretty hard. I wanted him to know what he was getting into if I joined his research group. Dan was unfazed by my self-doubt and told me he was confident I would learn what I needed to know in his group. I am truly thankful to Dan for taking a chance on me and for his subsequent support in his research program.

On a personal note, I would like to briefly thank a few friends who have stood by my side. Elvedin Lukovic has been my friend for the past 11 years – during which we have lived in the same dorm hall or apartment for ten of those years. I would not have made it though the first year of graduate school without Elvedin. Thank you, Elvedin, for your love and support. I am glad we got to experience graduate school and college together and I wish you all the best in your future endeavors. You deserve all the best! I would also like to thank Natalia Rösner. Liebe Natalia, du bist wirklich eine gute Freundin. Ich bedanke mich bei dir sehr herzlich für deine Anstrengungen, diese Freundschaft aufrecht erhalten zu haben. Ich weiß, dass du von deiner Seite des Atlantiks da mehr Arbeit reingesteckt hast, als ich es getan habe und dafür bin ich zu tiefst dankbar. Ich habe mich immer gefreut, mich mit dir in Amerika oder in Europe zu treffen. Wir haben viele, viele gute Zeiten zusammen erlebt und ich freue mich auf die, die noch kommen! Byron, I want to thank you for making the past year a very special one.

Biographical note

The author was born on January 23, 1980 in Allentown, PA to Donald S. and Debra R. Young. Shortly after her birth, she and her parents moved into the house in Macungie, PA where she spent the rest of her childhood and where her parents still reside. Two little sisters, Rebecca and Margaret followed in the next half decade to complete the family of five. During her formative years, the author developed the skills that would later help her survive graduate school at MIT: a love for sports (as a healthy stress outlet) and the aptitude for hard work (garnered from work experience in Pop-pop's junkyard).

The author was driven in her schoolwork at a young age. However in her elementary and junior high school years, the author's interest in science remained undeveloped. It was not until ninth grade biology under the tutelage of Dr. Fran Waller, that her interest in science was piqued. Dr. Waller instilled a respect for biology and the natural sciences in her students. Dr. Waller required her students to fully learn and understand the underlying concepts in biology, thus motivating them to exhaustively comprehend the subject matter. It was not merely the difficult test and homework that drove Dr. Waller's students to engage the material; it was Dr. Waller's clear passion for science and her dedication unlocking the magic of science for her students. From that point on, the author was sold on science – taking only honors and AP science classes for the remainder of high school.

The author attended Haverford College from 1998-2002, majoring in chemistry and minoring in German. While at Haverford, the author met her future graduate student advisor for the first time when he visited the campus to give a seminar. He spoke of pacman porphyrins and the origins of vampire lore. Little did she know then, Professor Nocera's outlandish behavior during his visit was a *milder* version of his true, eccentric self.

Upon graduation from Haverford College, the author participated in a year-long exchange program called the Congress-Bundestag Youth Exchange Program for Young Professionals that allowed her to spend an entire year living in Germany. Her experiences in Germany provided a break from the academic lifestyle and afforded her critical perspective on life in the US and in Europe.

Refreshed from her experiences in Europe, the author entered graduate school for chemistry at MIT in the fall of 2003 and joined the group of Professor Daniel G. Nocera shortly thereafter. The spring of 2009 brings a finish to her Ph.D. work in spectroscopic investigations of PCET. Following a short break, the author will move a few buildings away to join the group of Professor Vladimir Bulović in the Department of Electrical Engineering and Computer Science as a post-doctoral researcher.

Elizabeth R. Young

Chemistry Department, Room 2-045
Massachusetts Institute of Technology
Cambridge, MA 02139

617-258-0444 eyoung@mit.edu

Education

B.S. in Chemistry, Haverford College	*2002*
Ph.D. in Physical Chemistry, Massachusetts Institute of Technology	*2009*

Research Experience

Research Assistant *Massachusetts Institute of Technology, Chemistry Dept.*	*2003-2009*
Research Assistant *University of Heidelberg, Chemistry Dept., Germany,*	*2003*
Research Assistant *Haverford College Chemistry Dept,*	*2002*
Summer Intern *Merck & Co., Merck Research Laboratory,*	*2001*
Summer Research Assistant *University of Pennsylvania Chemistry Dept.,*	*2000*

Teaching Experience

Mentor for High School Student *Student participant in The Catalyst Program*	*2007-2008*
Teaching Assistant *Massachusetts Institute of Technology, Chemistry Dept (Undergraduate Thermodynamics and Kinetics),*	*2004*
Teaching Assistant *Massachusetts Institute of Technology, Chemistry Dept (General Chemistry),*	*2003*
General Chemistry Laboratory Assistant *Haverford College Chemistry Dept., Haverford, PA*	*1999-2002*

Distinctions

Congress-Bundestag Youth Exchange Program for Young Professions Scholarship	*2002*
High Honors in Chemistry Awarded, Haverford College	*2002*
E. Ward Plummer Award, University of Pennsylvania	*2000*
Archibald MacIntosh Award, Haverford College	*1999*

List of publications

Journal articles

Young, Elizabeth R.; Rosenthal, J.; Hodgkiss, J. M.; Nocera, D. G. *J. Am. Chem. Soc.* ASAP Article.

"A Comparative PCET Study of a Donor-Acceptor Pair Linked by Ionized and Non-ionized Asymmetric Hydrogen-Bonded Interfaces."

Young, E. R.; Rosenthal, J.; Nocera, D. G. *Chem. Comm.* **2008**, *20*, 2322-2324.

"Spectral observation of conversion between ionized vs. non-ionized proton-coupled electron transfer interfaces."

Bachmann, J.; Hodgkiss, J. M.; **Young, E. R.**; Nocera, D. G. *Inorg. Chem.* **2007**, *46*, 607-609.

"Ground- and Excited-State Reactivity of Iron Porphyrinogens."

Rosenthal, J.; **Young, E. R.**; Nocera, D. G. *Inorg. Chem.* **2007**, *46*, 8668-8675.

"Structurally Homologous β - and *meso*-Alkynyl Amidinium Porphyrins."

Rosenthal, J.; Hodgkiss, J. M.; **Young, E. R.**; Nocera, D. G. *J. Am. Chem. Soc.* **2006**, *128*, 10474-10483.

"Spectroscopic Determination of Proton Position in the Proton-Coupled Electron Transfer Pathways of Donor-Acceptor Supramolecule Assemblies."

Dunetz, J. R.; Sandstrom, C.; **Young, E. R.**; Baker, P.; Van Name, S. A.; Cathopolous, T.; Fairman, R.; De Paula, J. C.; Åkerfeldt, K. S. *Org. Lett.* **2005**, *7*, 2559-2561.

"Self-Assembling Porphyrin-Modified Peptides."

Schwab, A. D.; Smith, D. E.; Rich, C. S.; **Young, E. R.**; Smith, W. F.; De Paula, J. C. *J. Phys. Chem. B* **2003**, *107*, 11339-11345.

"Porphyrin Nanorods."

Conference presentations

Young, E. R.; Rosenthal, J.; Nocera, D. G.

poster presented at the Gordon Research Conference: Electron Donor Acceptor Interactions, Newport, RI. July, 2008

> "Positioning of Asymmetric Hydrogen-Bonded Interfaces with Respect to MLCT-Excited State Localization Mediates Dexter Energy Transfer Dynamics"

Young, E. R.; Rosenthal, J.; Nocera, D. G.

oral presentation at the 235th ACS National Meeting, New Orleans, LA, April 2008

> "Variation of the Electron-Transfer Pathway to Modulate Proton-Coupled Electron Transfer Kinetics and Kinetic Isotope Effects"

Hodgkiss, J. M.; Damrauer, N. H.; **Young, E. R.**; Rosenthal, J.; Pressé, S.; Nocera, D. G.

poster presented at the Gordon Research Conference: Renewable Energy, Renewable Energy: Solar Fuels, Ventura, CA. Jan, 2007

> "PCET in Hydrogen-Bonded Donor–Acceptor Assemblies: Electronic Coupling and the Role of Proton Fluctuations".

Hodgkiss, J. M.; Damrauer, N. H.; **Young, E. R.;** Rosenthal, J.; Pressé, S.; Nocera, D. G.

poster presented at the Gordon Research Conference: Donor-Acceptor Interactions, Salve Regina University, RI. July, 2006

> "PCET in Hydrogen-Bonded Donor–Acceptor Assemblies: Electronic Coupling and the Role of Proton Fluctuations"

Rosenthal, J.; **Young, E. R.**; Hodgkiss, J. M.; Nocera, D. G.

poster presented at the Gordon Research Conference: Electron Donor Acceptor Interactions, Newport, RI. July, 2006

> "Spectroscopic Determination of Proton Position in the PCET Pathways of Donor-Acceptor Supramolecule Assemblies"

Sandstrom, C.; **Young, E.**; Baker, P.; Dunetz, J.; Fairman, R.; Johnson, K.; de Paula, J.; Akerfeldt, K.

poster presented at the 223th ACS National Meeting, Orlando, FL, April 2002

> "Novel Porphyrin-Peptide Designs for Biomaterials Research"